Acoustical Physics, Vol. 47, No. 1, 2001, pp. 1–2. Translated from Akusticheskiĭ Zhurnal, Vol. 47, No. 1, 2001, pp. 5–6.
Original Russian Text Copyright © 2001 by Editorial Board.

To the Readers of *Acoustical Physics*

The 20th century has gone into history. It was a century of great discoveries, of investigation into the atom, of the exploration of outer space, and of the invention of lasers and computers, a century of molecular biology and genetics. This was a century of scientific and technological revolution and advance. The development of acoustics provides striking evidence of this.

Acoustics is an ancient science. From ancient times its basis was musical and architectural acoustics. The discovery of mechanics by Newton made acoustics an academic science. At the end of the 19th century, after the classical works by Helmholtz and Rayleigh, it seemed that its development had come to an end. However, the discoveries in physics on the eve of the 20th century and in the first years of this century also had an effect on acoustics. Progress in electrical engineering and electrodynamics, aerodynamics and aeronautics, and the invention of the radio stimulated research in new fields, i.e., electroacoustics, atmosphere acoustics, and the acoustics of inhomogeneous moving media. An international program was developed and studies of the atmosphere and stratosphere were conducted in the 1930s with the help of explosions using the effects of long-range propagation of sound. At the same time, fundamental investigations of the physics of ultrasound and its applications for nondestructive testing were started.

After World War I and especially in the course of World War II, the importance of underwater acoustics became evident. The discovery of long-range propagation of sound in the ocean stimulated basic and applied research in this field. Acoustic methods became dominant also in the global study of the ocean. Acoustic tomography of the ocean and acoustic oceanography appeared.

The progress in designing jet aircraft, in rocket technology, and in the construction of ships with nuclear power plants made it necessary to look for ways to control powerful noise of an aerohydrodynamic origin. Extensive study of jet noise, turbulent flows, and hydrodynamic cavitation flows was started. It became evident at the same time that the traditional methods of noise and vibration control based on vibration damping and absorption were almost exhausted. A new rapidly developing field of acoustics, i.e., active methods of noise and vibration control, appeared. Nonlinear acoustics started to develop rapidly.

The appearance of quantum mechanics, the discovery of the wave nature of matter, and the development of the physics of condensed media led to the "birth" of a quasi-particle of sound, a phonon. Like photons, electrons, and other particles, phonons firmly occupied their place in the present-day theories of basic and applied physics. Acoustics "merged" with quantum mechanics. Quantum acoustics, acoustoelectronics, and magnetoacoustics appeared.

The invention of lasers and advances in the physics of elementary particles and accelerator technology stimulated extensive research in the field of photoacoustics and nontraditional sources and receivers of sound. This research became the basis for laser and radiation acoustics.

Important advances were made in "nonphysical" fields of acoustics, i.e., the acoustics of speech, biological and medical acoustics, and also at the interfaces of other fields, e.g., in geoacoustics.

A striking characteristic of the progress in acoustics in the 20th century is its frequency and spatial scales. While at the beginning of the 20th century acoustics embraced only the sound range of 20–20 000 Hz, at the end of the century research was conducted within the frequency interval from deep infrasound ($\sim 10^{-2}$ Hz), where acoustics is contiguous with the hydrodynamics of an incompressible fluid, up to hypersound ($\sim 10^{12}$ Hz), i.e., up to the region of the Debye frequency. It was discovered that sound propagates in the ocean to distances of tens of thousands of kilometers. This has provided the opportunity to introduce and partially realize the idea of acoustic monitoring of the temperature variability of water masses in the ocean over rather long time intervals in order to study changes in the Earth's climate. On a different scale, a scanning acoustic microscope was developed.

Quite often some people in creative professions and sometimes, regretfully, even physicists working in narrow fields identify modern acoustics only with the acoustics of concert halls and audio technology. The results attained in the last century in these very traditional fields are also impressive. There was no objective criterion for the acoustic quality of a concert hall at the beginning of the century apart from the newly introduced characteristics such as the reverberation time. There was also no acoustic basis for the acoustic design of concert halls. At the end of the 20th century, the result of very extensive research was seven scientifically substantiated criteria. During the last decades of this century, in various countries of the world, concert halls and opera houses with acoustic characteristics satisfying the high demands of music-lovers, musicians, singers, and conductors were built.

1063-7710/01/4701-0001$21.00 © 2001 MAIK "Nauka/Interperiodica"

How will acoustics develop in the new 21st century? It is an ungracious task to make predictions. However, considering the logic of the development of science, we can expect that the main stimulus for its progress will be the necessity of solving the global problems of humanity: protection of the environment, provision of resources and good standards of living, health protection, and the development of global communications and information networks.

Scientific discoveries will greatly influence the progress in acoustics in the new century. Indeed, the development of quantum mechanics led physicists to conclude that the world has a quantum nature. This was extremely important for the progress of science.

Nobody could imagine that at the end of the 20th century, 300 years after the development of mechanics by Newton, fundamental discoveries would be made in this field. Chaotic oscillations in nonlinear determinate systems, which are similar to random oscillations, i.e., a determinate or dynamic chaos, were discovered. Chaotic oscillations have a new dynamic property which is called the fractal structure. In other words, chaotic oscillations (phenomena) arise according to regular laws and there is not a formless chaos behind them but a chaos with hidden order, a fractal structure. New concepts have appeared: the fractal and fractal geometry. Chaotic and fractal nonlinear dynamics have been developed. Fractals have attracted the interest of scientists working in many entirely different (as it may seem) fields of science including acoustics. Another discovery is called self-organization. This process is somewhat inverse with respect to dynamic chaos. It means the existence of an ordered behavior or state of a dynamic system regardless of noise and fluctuations in the system. The phenomenon of self-organization is typical of complex nonlinear dynamic systems with many degrees of freedom. Self-organization arises in dynamic systems that are far from the state of thermodynamic equilibrium. Determinate chaos, fractals, and the phenomenon of self-organization are the properties of not only mechanical or even physical nonlinear dynamic systems as it may seem at first glance. They are inherent in processes in biology, ecology, finance, economics, and other fields. We may say figuratively that the world is nonlinear. It is necessary to note by the way that dynamic chaos can be observed also in quantum systems. The discoveries in nonlinear dynamics are comparable to the development of the theory of relativity and quantum mechanics in their revolutionary significance. It is not accidental that fractals and fractal geometry have attracted the attention of many researchers. Their significance is not limited to science. Fractals and their beauty are revealed in the beauty of nature, music, and even in the beauty of intricate hairdos of African women as it has turned out!

The discovery of dynamic chaos, self-organization, and fractals could not have taken place were it not for the development of powerful computers. The construction of the first operational elements of a quantum computer was reported recently. We may expect that real quantum computers will appear in the 2020s to 2030s. There is no doubt that new scientific discoveries, advances in nonlinear dynamics, and the invention of quantum computers will greatly affect the development of acoustics in the coming century.

Humanity has entered the 21st century, the third millennium. The Editorial Board of *Acoustical Physics* and the Scientific Council of the Russian Academy of Sciences on Acoustics congratulate the readers of *Acoustical Physics* with this outstanding event.

Editorial Board of *Acoustical Physics*
and the Scientific Council of the Russian Academy of Sciences on Acoustics

Translated by M. Lyamshev

Acoustical Physics, Vol. 47, No. 1, 2001, pp. 10–15. Translated from Akusticheskiĭ Zhurnal, Vol. 47, No. 1, 2001, pp. 15–21.
Original Russian Text Copyright © 2001 by Akhatov, Khismatullin.

Two-Dimensional Mechanisms of Interaction between Ultrasound and Sound in Bubbly Liquids: Interaction Equations

I. Sh. Akhatov and D. B. Khismatullin

Institute of Mechanics, Ufa Scientific Center, Russian Academy of Sciences, ul. K. Marksa 12, Ufa, 450000 Russia
e-mail: damir-k@anrb.ru

Received December 14, 1999

Abstract—The interaction of long (sound) and short (ultrasound) waves propagating in a rarefied monodisperse mixture of a weakly compressible liquid with gas bubbles is considered. Using the multiscale method, the Davey–Stewartson system of equations is derived as a model of two-dimensional interaction. It is shown that, for some values of parameters, this system is reduced to an integrable form (the Davey–Stewartson I equations) and has localized solutions in the form of dromions (exponentially decaying waves of the short-wave envelope). One of the most important properties of dromions is their ability to move according to the law that governs the variations of the boundary conditions set at infinity for the long wave. It is suggested that these solutions be used for controlling the effects of ultrasound on bubbly liquids. © *2001 MAIK "Nauka/Interperiodica".*

INTRODUCTION

The theoretical studies of nonlinear wave processes in liquids with gas bubbles had been restricted to independent considerations of long and short waves. Specifically, a Korteweg–de Vries (KdV) equation was obtained for describing the evolution of long-wave disturbances in liquids with adiabatic gas bubbles [1]. The existence of a long-wave KdV soliton was confirmed by many experiments [2]. A nonlinear Schrödinger equation was derived for describing the modulation of short waves in polydisperse bubbly mixtures [3]. Modulation equations were constructed for a bubbly mixture on the basis of an incompressible liquid phase [4] and also with allowance for the heat transfer between the phases [5].

It has been known [6] that a dispersion curve for a bubbly liquid consists of two branches: a low-frequency branch and a high-frequency one. Therefore, in such a medium, a simultaneous propagation of long (sound) and short (ultrasound) waves is possible.

Long and short waves can interact. The mechanism of such an interaction was first considered for waves propagating on the surface of water [7]. It was found that, when the group velocity of short waves coincides with the phase velocity of the long wave, the interaction between these waves is maximal (resonant) [8]. Such a long-wave–short-wave resonance requires a special type of dispersion relation, e.g., consisting of two branches [9], and occurs in a limited number of physical systems. Examples of such systems are waves on the surface of water [10] and plasma [11]. In all these systems, the one-dimensional nonresonance interaction is described by a nonlinear Schrödinger equation and the resonance interaction is described by a Zakharov system of equations; the two-dimensional nonresonance dynamics obeys the Davey–Stewartson system of equations [12].

The one-dimensional interaction between long-wave and short-wave pressure perturbations in a liquid with gas bubbles was studied in our previous paper [13]. It was shown that a long-wave–short-wave resonance occurs in this medium, and the aforementioned equations were derived. In addition, the effect of the "degeneration of interaction" was revealed, and new equations describing the resonance interaction in the case of such a degeneration were obtained. An analysis of the effect of dissipation on the "degenerate" long-wave–short-wave interaction was performed [14]. In this paper, we derive and analyze the equations describing the two-dimensional interaction between long and short waves in a bubbly liquid.

BASIC EQUATIONS

A bubbly liquid is a mixture that consists of spherical gas bubbles, the space between which is filled with a homogeneous liquid. For the sake of simplification, we assume that this mixture is rarefied and weakly compressible, all bubbles have the same radius, and the gas pressure in the bubbles varies according to the polytropic law. We neglect the effect of external forces, as

1063-7710/01/4701-0010$21.00 © 2001 MAIK "Nauka/Interperiodica"

well as the dissipative and capillary effects. The motion of such a bubbly liquid is described by the equations [6]

$$\frac{d\rho}{dt} + \rho\,\mathrm{div}\mathbf{v} = 0, \quad \frac{dn}{dt} + n\,\mathrm{div}\mathbf{v} = 0,$$

$$\rho\frac{d\mathbf{v}}{dt} + \mathrm{grad}\,p = 0,$$

$$\rho_l\left[a\frac{d^2a}{dt^2} + \frac{3}{2}\left(\frac{da}{dt}\right)^2\right] = p_g - p, \quad \rho_l - \rho_{l0} = \frac{p - p_0}{C_l^2}, \tag{1}$$

$$\rho = \rho_l(1 - \alpha_g), \quad \alpha_g = \frac{4}{3}\pi a^3 n, \quad \frac{p}{p_0} = \left(\frac{a_0}{a}\right)^{3\kappa}.$$

Here, $\mathbf{v} = u\mathbf{i} + w\mathbf{j}$ is the velocity vector of the mixture; $d/dt = \partial/\partial t + u\partial/\partial x + w\partial/\partial y$ is the substantive derivative with respect to time; p and ρ are the pressure and density of the mixture; ρ_l is the true density of the liquid; C_l is the sound velocity in the bubble-free liquid; p_g, α_g, and a are the pressure, volume content, and radius of bubbles; n is the number of bubbles in a unit volume of the mixture; κ is the polytropic index; and the subscript 0 refers to the unperturbed state of the mixture.

Using dimensionless quantities

$$\tilde{a} = \frac{a}{a_0} - 1, \quad \tilde{p} = \frac{p}{p_0} - 1, \quad \tilde{\rho} = \frac{\rho - \rho_0}{\rho_*},$$

$$\tilde{u} = \frac{u}{v^*}, \quad \tilde{w} = \frac{w}{v^*}, \tag{2}$$

$$\tilde{t} = \frac{t}{t^*}, \quad \tilde{x} = \frac{x}{l^*}, \quad \tilde{y} = \frac{y}{l^*},$$

where

$$\rho_* = \rho_0\alpha_{g0}, \quad v_* = \sqrt{\frac{\alpha_{g0}p_0}{\rho_0}},$$

$$t_* = a_0\sqrt{\frac{\rho_0}{p_0}}, \quad l_* = \frac{a_0}{\sqrt{\alpha_{g0}}} \tag{3}$$

(below, the tilde sign will be omitted), and neglecting the terms of the order of the volume gas content α_g as compared to unity, we reduce the system of Eqs. (1) to the following perturbation equations [3, 13]:

$$\rho_{tt} - p_{xx} - p_{yy} = 0,$$

$$(1 + a)a_{tt} + \frac{3}{2}a_t^2 - (1 + a)^{-3\kappa} + p + 1 = 0, \tag{4}$$

$$\rho - 1 - b^2p + (1 + a)^3 = 0, \quad b = \sqrt{p_0\rho_{l0}^{-1}\alpha_{g0}^{-1}C_l^{-2}}.$$

Let us consider the vector solution to Eqs. (4), $\mathbf{z} = (a, p, \rho)$, in the form of a longitudinal plane harmonic wave propagating along the OX-axis: $\mathbf{z} = \mathbf{z}_0\exp\{i(kx - \omega t)\}$, where $\mathbf{z}_0 = (A, P, R)$ is the constant vector of the solution amplitudes and k and ω are the wave number and the frequency.

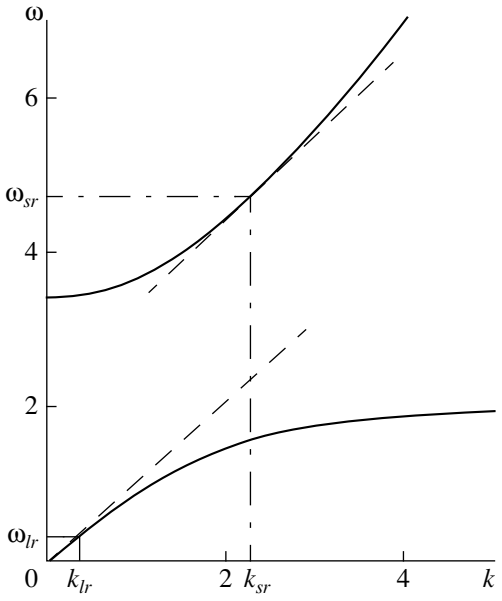

Fig. 1. Dispersion curve for a bubbly liquid.

This solution is valid when k and ω are related by the dispersion relation

$$k^2 = \omega^2[b^2 - 3(\omega^2 - 3\kappa)^{-1}],$$

which can be represented in the form

$$\omega_\pm^2(k) = \frac{1}{2}\left\{3\kappa + (k^2 + 3)b^{-2} \pm \sqrt{[3\kappa - (k^2 + 3)b^{-2}]^2 + 36\kappa b^{-2}}\right\}. \tag{5}$$

Relation (5) falls into two branches, as illustrated in Fig. 1: a low-frequency branch (corresponding to the subscript "–") and a high-frequency branch (corresponding to the subscript "+"). In this case, the long-wave asymptotics of the low-frequency branch, $\omega_l(k_l) = \omega_-|_{k\to 0}$, and the short-wave asymptotics of the high-frequency branch, $\omega_s(k_s) = \omega_+|_{k\to\infty}$, are as follows:

$$\omega_l = c_e k_l - \chi k_l^3 + O(k_l^5) \text{ for } k_l \longrightarrow 0;$$

$$\chi = c_e^5/(6\kappa^2),$$

$$\omega_s = c_f k_s + O(k_s^{-1}) \text{ for } k_s \longrightarrow \infty, \tag{6}$$

$$c_e = \omega_l/k_l\big|_{k_l\to 0} = \sqrt{(b^2 + \kappa^{-1})^{-1}},$$

$$c_f = d\omega_s/dk_s\big|_{k_s\to\infty} = b^{-1},$$

where c_e and c_f are the equilibrium and frozen velocities of sound in the mixture.

Dispersion relation (5) allows the existence of the Benney–Zakharov long-wave–short-wave resonance.

This follows from the fact that, on the one hand, the group velocity of the short wave

$$c_g = d\omega_s/dk_s = k_s\omega_s^{-1}(\omega_s^2 - 3\kappa) \times (2b^2\omega_s^2 - 3\kappa c_e^{-2} - k_s^2)^{-1} \quad (7)$$

is an infinitesimal quantity when k_s tends to zero and, on the other hand, according to Eqs. (6) we have $c_f > c_e$. Then, for any sufficiently small $k_l = k_{lr}$, there exists such a $k_s = k_{sr}$ that provides the fulfillment of the conditions for the Benney–Zakharov long-wave–short-wave resonance (Fig. 1):

$$c_g(k_{sr}) = c_p(k_{lr}). \quad (8)$$

Here, $c_p(k_l) = \omega_l/k_l$ is the phase velocity of the long wave.

In the case of infinitely long waves ($k_l \longrightarrow 0$), the resonance condition (8) is simplified:

$$c_g(k_{sr}) = c_e. \quad (9)$$

For most bubbly media, the frequencies corresponding to the upper branch of the dispersion curve belong to the ultrasonic range. Specifically, if we consider water with air bubbles of radius $a_0 = 0.1$ mm at normal conditions ($p_0 = 0.1$ MPa, $\rho_{l0} = 10^3$ kg/m^3) and with the volume gas content $\alpha_{g0} = 2.22 \times 10^{-4}$, the frequency of the short wave will be $\nu_s = \omega_s/(2\pi t_*) > 32400$ Hz. At the same time, the long wave with the frequency $\nu_l = c_e l_*/(\lambda_l t_*) \approx 110$ Hz (at $\lambda_l = 6.7$ m) represents audible sound. Thus, the long-wave–short-wave interaction in a bubbly liquid can be considered as the interaction of ultrasound and audible sound propagating in this medium.

INTERACTION EQUATIONS

Let us introduce a parameter $\varepsilon \ll 1$ to satisfy the conditions

$$p_l = \varepsilon^l L; \quad p_s = \varepsilon^s S; \quad p = p_l + p_s\exp\{i\Theta\}; \quad L, S = O(1),$$

where p_l and p_s represent the long-wave and short-wave pressure perturbations in the mixture; l and s are some numbers (degrees of smallness); and Θ is the phase of the short wave. In a similar way, we express the perturbations of the bubble radius a and the perturbations of the mixture density ρ. Then, the vector solution $\mathbf{z} = (a, p, \rho)$ to system (2.4) can be represented in the form

$$\mathbf{z} = \varepsilon^l \sum_{m\geq 1} \varepsilon^{m-1}\mathbf{z}_m^{(0)} + \varepsilon^s \sum_{m,n\geq 1}\sum \varepsilon^{(m-1)n+(n-1)s} \times [\mathbf{z}_m^{(n)}\exp[in\Theta] + c.c.]. \quad (10)$$

To derive the equations for the long-wave–short-wave interaction, it is convenient to use the method of multiscale expansions [15], i.e., in addition to expansion (10), to introduce fast (t_0, x_0, y_0) and slow variables $(t_n, x_n, y_n) = \varepsilon^n(t_0, x_0, y_0)$, where $n = 1, 2, \ldots$, by replacing the differential operators with asymptotic series:

$$\frac{\partial}{\partial\psi} \longrightarrow \frac{\partial}{\partial\psi_0} + \sum_{n\geq 1}\varepsilon^n\frac{\partial}{\partial\psi_n}, \quad \psi = t, x, \text{ or } y. \quad (11)$$

Here, we assume that $\Theta = k_s x_0 - \omega_s t_0$ and the long-wave and short-wave components of the solution ($\mathbf{z}_m^{(0)}$ and $\mathbf{z}_m^{(n)}$, where $m, n = 1, 2, \ldots$) depend only on the slow variables. The absence of the fast variable y_0 in the expression for Θ means that the short wave is a plane one.

We select $(l, s) = (2, 1)$; then, we substitute expansions (10) and (11) into Eqs. (4) and split the resulting expressions into the harmonics of the short wave ($\exp\{in\Theta\}$, where $n = 0, 1, 2, \ldots$). We introduce the notation $S = p_1^{(1)}$ and switch to the coordinate system moving in time t_1 with the group velocity of the short waves $c_g(k_s)$; i.e., we assume that

$$p_1^{(0)} = L(\xi, \zeta) + L_0(\eta_1, \eta_2), \quad S = S(\tau, \xi, \zeta), \quad \tau = t_2, \quad \xi = x_1 - c_g t_1, \quad \eta_1 = x_1 \pm c_e t_1, \quad \eta_2 = y_1 \pm c_e t_1.$$

Here, L_0 is the initial profile of the long wave. The choice of the sign in η_1 and η_2 determines the direction of motion of this initial profile along x_1 and y_1: the motion from left to right corresponds to the minus sign, and from right to left, to the plus sign. We also assume that $p_2 = p_2(\xi)$. Then, we obtain the following interaction equations:

$$(c_g^2 - c_e^2)L_{\xi\xi} - c_e^2 L_{\xi\xi} = \alpha(|S|^2)_{\xi\xi}, \quad iS_\tau + \beta S_{\xi\xi} + \varrho S_{\zeta\zeta} + \gamma|S|^2 S = \delta L S, \quad (12)$$

where c_g and c_e are calculated by Eqs. (7) and (6);

$$\alpha = -\frac{c_e^2 c_g^2}{\kappa(\omega_s^2 - 3\kappa)^2}[\omega_s^2 - 9\kappa(\kappa + 1)];$$

$$\beta = \frac{c_g}{2k_s}\left[1 + \frac{c_g}{\omega_s^2 - 3\kappa} \times \{4k_s\omega_s + c_g(k_s^2 + 3(1 + \kappa b^2) - 6b^2\omega_s^2)\}\right];$$

$$\varrho = \frac{c_g}{2k_s}; \quad \delta = -\frac{c_g\omega_s^2}{2\kappa k_s(\omega_s^2 - 3\kappa)^2} \times [\omega_s^2 - 9\kappa(\kappa + 1)];$$

$$\gamma = -\frac{[\omega_s^2 - 3\kappa(3\kappa+1)]\delta}{(\omega_s^2 - 3\kappa)^2} - \frac{c_g(b^2\omega_s^2 - k_s^2)}{4k_s\omega_s^2(\omega_s^2 - 3\kappa)^3}$$
$$\times[-\omega_s^4 + 27\kappa^2(\kappa+1)\omega_s^2 + 27\kappa^2(\kappa+1)^2].$$

We note that the coefficients β and ϱ are positive, and α and δ are of the same sign for all values of k_s, b, and $\kappa > 1$.

From the physical point of view, Eqs. (12) describe the combined evolution of ultrasound and sound with the "slow" time in a layer of the rarefied bubbly mixture enclosed in a rectangular vessel. Sound is generated by the nonmonochromaticity of the ultrasonic signal (the initial component of the long wave propagates independently), the vessel moves with the velocity $C_g = c_g l_*/t_*$ in the direction of wave propagation (the x axis corresponds to one of the sides of the vessel), the wave amplitudes slowly vary in the transverse direction (along the y-axis), and the layer of liquid is assumed to be sufficiently thin to neglect the dependence on the vessel height (the z-axis). It should be noted that such a combined evolution is noninertial, because the sound propagation in a bubbly medium exactly follows the dynamics of the ultrasonic perturbation (because of the absence of time derivatives in the first equation).

System (12) has a spatially homogeneous solution:

$$L = L_0, \quad S = R_0\exp(i\Theta_0),$$
$$\Theta_0 = \gamma R_0^2 - \delta L_0 + \psi_0, \tag{13}$$

where L_0, R_0, and ψ_0 are constants. A linear analysis of the stability of this solution against sinusoidal perturbations

$$\Lambda = \Lambda_0\exp\{i(K_x\xi + K_y\zeta - \Omega\tau)\},$$
$$\Lambda = (L', R', \Theta'), \quad \Lambda_0 = (L_0', R_0', \Theta_0')$$

leads to the dispersion relation

$$\Omega^2 = (\beta K_x^2 + \varrho K_y^2)$$
$$\times\left[\beta K_x^2 + \varrho K_y^2 - 2\gamma R_0^2 - \frac{2\alpha\delta R_0^2 K_x^2}{c_e^2 K_y^2 - (c_g^2 - c_e^2)K_x^2}\right].$$

From this relation, it follows that, for a spatially homogeneous solution (13), a long-wave instability takes place when the following condition is fulfilled (for β, $\varrho > 0$):

$$\gamma + \alpha\delta K_x^2/(c_e^2 K_y^2 - [c_g^2 - c_e^2]K_x^2) > 0. \tag{14}$$

In a bubbly liquid, the coefficients α and δ vanish (the interaction degenerates) when the condition $\omega_s = 3\sqrt{\kappa(\kappa+1)}$ is satisfied [13]. In this case, $p_1^{(0)} = L_0(\eta_1, \eta_2)$, and, hence, the profile of the long wave is $L(\xi, \zeta) = 0$. The equation for the envelope of the short wave $S = p_1^{(1)}$ has the form of a two-dimensional nonlinear Schrödinger equation

$$iS_\tau + \beta S_{\xi\xi} + \varrho S_{\zeta\zeta} + \gamma|S|^2 S = 0. \tag{15}$$

However, when the zero-harmonic terms of the next order in ε are taken into account, an interaction appears between the envelope of the short wave S and the second term of the expansion of the long-wave perturbation $L_1 = p_2^{(0)}$:

$$(c_g^2 - c_e^2)L_{1\xi\xi} - c_e^2 L_{1\zeta\zeta} = i\lambda[SS_\xi^* - S^*S_\xi]_{\xi\xi},$$
$$iS_\tau + \beta S_{\xi\xi} + \varrho S_{\zeta\zeta} + \gamma|S|^2 S = 0.$$

The coefficient $\lambda = (\kappa+1)^{1/2}c_e^2 c_g^3/[3\kappa^{5/2}(3\kappa+2)^2]$ is always nonzero. Thus, in the case of a degenerate interaction, the nonmonochromatic ultrasonic signal will also excite audible sound, but of much lower intensity than in the nondegenerate case.

TWO-DIMENSIONAL LOCALIZED STRUCTURES IN A BUBBLY LIQUID

When $\delta \neq 0$, Eqs. (3.3) can be transformed to a Davey–Stewartson system of equations [10, 12]. For this purpose, we apply the substitution $L \longrightarrow \delta^{-1}\partial\Psi/\partial\xi$ and introduce the notation $\sigma = c_e^{-2}(c_e^2 - c_g^2)$:

$$\sigma\Psi_{\xi\xi} + \Psi_{\zeta\zeta} = -\alpha\delta c_e^{-2}(|S|^2)_\xi,$$
$$iS_\tau + \beta S_{\xi\xi} + \varrho S_{\zeta\zeta} + \gamma|S|^2 S = S\Psi_\xi. \tag{16}$$

The analysis of the coefficients in Eq. (16) shows that, in a bubbly liquid, the two-dimensional interaction can be described by one of the integrable versions of the Davey–Stewartson system, namely, by the Davey–Stewartson I (DS-I) equations:

$$Q_{yy} - Q_{xx} = -2(|A|^2)_x,$$
$$iA_t + A_{xx} + A_{yy} = -|A|^2 A + AQ_x.$$

The passage to this system is possible with the substitutions $Q = \delta^{-1}\partial L/\partial\xi$, $A = \sqrt{\gamma}\,S$, $x = \xi/\sqrt{\beta}$, $y = \zeta/\sqrt{\varrho}$, and $t = \tau$ when the conditions

$$\delta_1 = \varrho/\beta[1 - c_g^2/c_e^2] = -1,$$
$$\delta_2 = \alpha\delta\varrho/(\gamma\sqrt{\beta}c_e^2) = 2 \tag{17}$$

are satisfied (for a bubbly liquid, the coefficients α and δ are of the same sign and, therefore, the second condition (17) holds only for positive values of γ, which means that the aforementioned substitutions are correct).

The evidence for the validity of conditions (17) is the intersection of the curves $\delta_1 = -1$ and $\delta_2 = 2$ (Fig. 2a).

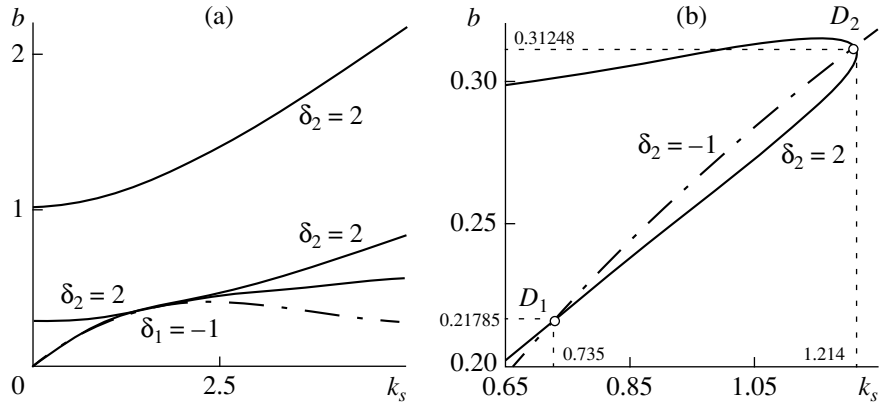

Fig. 2. Curves $\delta_1 = -1$ and $\delta_2 = 2$ in the (k_s, b) plane at $\kappa = 1.4$. At the points D_1 and D_2, the conditions of the existence of two-dimensional localized structures in a bubbly liquid are satisfied.

From Fig. 2b, it follows that the intersection occurs at the points D_1 (k_{s1}, $b_1 \approx 0.74, 0.22$) and D_2 (k_{s2}, $b_2 \approx 1.21, 0.31$), which correspond to the volume gas contents $\alpha_{g01} \approx 1.42 \times 10^{-4}$ and $\alpha_{g02} \approx 2.04 \times 10^{-4}$ and the short wave frequencies $\nu_{s1} \approx 0.14$ MHz and $\nu_{s2} \approx 0.11$ MHz for the bubbly liquid represented by water with air bubbles of radius 0.1 mm at normal conditions.

Among all localized solutions to the DS-I equations, the so-called dromion solution [18] stands out. This solution represents a localized and exponentially decaying structure of the short wave envelope A; in contrast to a conventional soliton, this structure is capable of energy dissipation when interacting with disturbances. A dromion appears when nonzero boundary conditions are set for the long-wave profile Q and exists owing to the energy transfer between the long and short waves. This localized structure has one unique property. The dromion travels along the trajectory determined by the time dependence of the boundary conditions for the long wave. Setting the law that governs the variation of these boundary conditions, one can control the motion of the dromion.

A single-dromion solution can easily be obtained by rotating the coordinate system through 45° ($x \longrightarrow \tilde{x} + \tilde{y}$, $y \longrightarrow \tilde{x} - \tilde{y}$) and by introducing the variables $U \equiv (\partial Q/\partial x - |A|^2)/2$ and $V \equiv (\partial Q/\partial y - |A|^2)/2$ (the tilde sign is omitted). Applying the boundary conditions for U at $y \longrightarrow -\infty$ and for V at $x \longrightarrow -\infty$ in the form

$$U|_{y \to -\infty} = \frac{8k_r^2 \exp(\eta_1 + \eta_1^*)}{[1 + \exp(\eta_1 + \eta_1^*)]^2},$$
$$V|_{x \to -\infty} = \frac{8l_r^2 \exp(\eta_2 + \eta_2^*)}{[1 + \exp(\eta_2 + \eta_2^*)]^2}, \tag{18}$$

we obtain the solution in the form [19]

$$A = \frac{\chi \exp(\eta_1 + \eta_2)}{1 + \exp(\eta_1 + \eta_1^*) + \exp(\eta_2 + \eta_2^*) + \nu \exp(\eta_1 + \eta_1^* + \eta_2 + \eta_2^*)}. \tag{19}$$

Here,

$$\eta_1 = (k_r + ik_i)x + (-2k_rk_i + i\Omega_i)t,$$
$$\eta_2 = (l_r + il_i)y + (-2l_rl_i + i\omega_i)t,$$
$$\Omega_i + \omega_i = k_r^2 + k_i^2 + l_r^2 + l_i^2, \quad \chi = 2\sqrt{2k_rl_r(\nu - 1)},$$

where ν, k_r, k_i, l_r, and l_i are arbitrary real numbers (parameters of the solution).

Figure 3 shows the spatial distributions of the short-wave envelope $|S| = \gamma^{-1/2}|A|$ and of the long-wave profile $L = (U + V + 2|A|^2)/(2\delta)$, which correspond to the single-dromion solution given by Eqs. (18) and (19) with $\nu = 3$, $k_r = l_r = 4/5$, and $k_i = l_i = 1/5$.

Numerical experiments [19] confirm the fact that the motion of the dromion structure occurs along the trajectory determined by the boundary conditions for the long wave. For example, when the variables in Eqs. (18) are given in the form

$$\eta_1 + \eta_1^* = k_r x + \Omega_r \sin(wt),$$
$$\eta_2 + \eta_2^* = l_r x + \omega_r \cos(wt),$$

i.e., when the point of intersection of the peaks of the boundary conditions (point C in Fig. 3) rotates about the origin of the coordinates, the dromion also travels around a circle.

This property can be used for controlling the ultrasonic effect on a bubbly liquid. By producing an ultra-

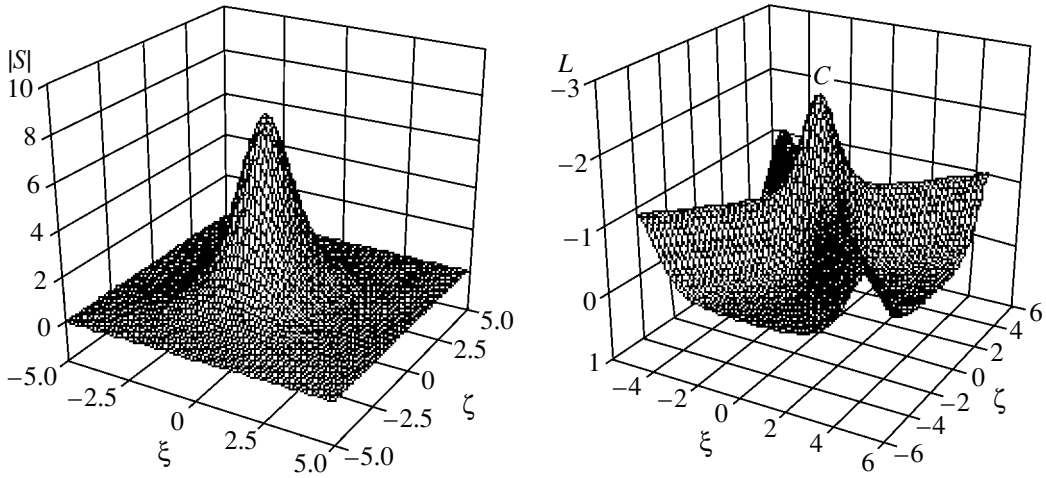

Fig. 3. Spatial distributions of the short-wave envelope $|S|$ and the long-wave profile L that correspond to a single-dromion solution. The parameters of the bubbly liquid are $k_s = 0.74$, $b = 0.22$, and $\kappa = 1.4$.

sonic perturbation in a bubbly liquid whose parameters satisfy the DS-I equation, it is possible not only to focus it at some point in space, but also to control its motion by setting the laws of evolution for the audio-frequency disturbances well away from the focus.

SUMMARY

Using the method of multiscale expansions, we constructed a model of the two-dimensional interaction of ultrasound with audible sound in a bubbly liquid. We considered two cases: the nonresonance case and the degenerate one. In the latter case, the coefficients of interaction between the long and short waves vanish. The degeneration of the interaction occurs at a certain frequency of the short wave.

It was shown that, in the nonresonance case, the interaction can be described by the Davey–Stewartson system of equations and, at some values of the parameters, by the integrable version of this system, namely, by the Davey–Stewartson I equations. The DS-I system has localized solutions in the form of dromions (an exponentially decaying envelope of the short waves) whose specific feature is to travel in space according to the law that governs the variation of the boundary conditions set at infinity for the long wave. The possibility to use this property of dromions for controlling the ultrasonic effects on bubbly liquids was pointed out.

It was found that, in the case of degeneration, a nonmonochromatic ultrasonic signal generates audible sound of much lower intensity than in the nonresonance case.

REFERENCES

1. L. van Wijngaarden, J. Fluid Mech. **33**, 465 (1968).
2. V. E. Nakoryakov, B. G. Pokusaev, and I. R. Shreĭber, *Wave Propagation in Gas- and Vapor-Liquid Media* (Institute of Thermal Physics, Siberian Division, Academy of Sciences of the USSR, Novosibirsk, 1983).
3. N. A. Gumerov, Prikl. Mat. Mekh. **56**, 58 (1992).
4. S. L. Gavrilyuk, Prikl. Mekh. Tekh. Fiz., No. 2, 86 (1989).
5. N. A. Gumerov, in *Bubble Dynamics and Interface Phenomena* (Kluwer Academic, Netherlands, 1994), pp. 131–140.
6. R. I. Nigmatulin, *Dynamics of Multiphase Media* (Nauka, Moscow, 1987), Vol. 2.
7. D. J. Benney, Stud. Appl. Math. **55**, 93 (1976).
8. D. J. Benney, Stud. Appl. Math. **56**, 81 (1977).
9. O. M. Zozulya and S. A. Rybak, Akust. Zh. **44**, 278 (1998) [Acoust. Phys. **44**, 232 (1998)].
10. V. D. Djordjevic and L. G. Redekopp, J. Fluid Mech. **79**, 703 (1977).
11. V. E. Zakharov, Zh. Eksp. Teor. Fiz. **62**, 1745 (1972) [Sov. Phys. JETP **35**, 908 (1972)].
12. A. Davey and K. Stewartson, Proc. R. Soc. London, Ser. A **338**, 101 (1974).
13. I. Sh. Akhatov and D. B. Khismatullin, Prikl. Mat. Mekh. **63**, 980 (1999).
14. I. Sh. Akhatov and D. B. Khismatullin, Izv. Akad. Nauk, Mekh. Zhidk. Gaza, No. 4, 126 (2000).
15. A. Jeffrey and T. Kawahara, *Asymptotic Methods in Nonlinear Wave Theory* (Pitman, London, 1982).
16. V. E. Zakharov and A. B. Shabat, Zh. Eksp. Teor. Fiz. **61**, 119 (1971) [Sov. Phys. JETP **34**, 62 (1971)].
17. T. B. Benjamin and J. E. Feir, J. Fluid Mech. **27**, 417 (1967).
18. A. S. Fokas and P. M. Santini, Physica D **44**, 99 (1990).
19. N. Yoshida *et al.*, J. Phys. A: Math. Gen. **31**, 3325 (1998).

Translated by E. Golyamina

Acoustical Physics, Vol. 47, No. 1, 2001, pp. 102–105. Translated from Akusticheskiĭ Zhurnal, Vol. 47, No. 1, 2001, pp. 119–122.
Original Russian Text Copyright © 2001 by Molevich.

Sound Amplification in Inhomogeneous Flows of Nonequilibrium Gas

N. E. Molevich

Korolev State Aerospace University, Samara, Moskovskoe sh. 34, Samara, 443086 Russia
e-mail: molevich@mb.ssau.ru

Received February 28, 2000

Abstract—The conditions of the acoustic instability of flows of thermodynamically nonequilibrium gas are determined. It is shown that the growth increments of the velocity, temperature, pressure, and density disturbances are different. When the Mach numbers are small, only the velocity and temperature disturbances grow along the flow. © *2001 MAIK "Nauka/Interperiodica".*

The study of the acoustic stability of flows of thermodynamically nonequilibrium gas is of interest in connection with the development of laser engineering and plasma aerodynamics. It is well known that, in a thermodynamically nonequilibrium gas, an amplification of sound is possible. Examples of such media are chemically active mixtures, glow-discharge plasma, gases with a nonequilibrium excitation of molecular internal degrees of freedom, and atmosphere regions with a nonequilibrium condensation. The acoustic instability of these media is associated with the fulfillment of the Rayleigh criterion: in the wave maximums, the heat release from the nonequilibrium degrees of freedom should be greater than in the minimums. As was shown in our previous studies [1], the acoustic increment in all these media can be written in a generalized form as

$$\alpha = \frac{\xi(\omega)\omega^2}{2u_s^3(\omega)\rho}, \qquad (1)$$

where ξ is the second viscosity coefficient, u_s is the sound velocity, both these quantities depend on the frequency ω, and ρ is the density of the medium. The media with $\xi < 0$ are acoustically active.

Expression (1) takes no account of the inhomogeneity of a stationary nonequilibrium medium, which is determined mainly by the type of the heat removal. The heat removal due to the thermal conduction is considered in [2]. It is shown that, for a low degree of nonequilibrium, the region of the acoustic instability (on the pumping power–inverse relaxation time plane) expands, and, for a high degree of nonequilibrium, it contracts, as compared to the homogeneous case. In our previous publication [1], we determined the correction to Eq. (1) that takes into account the refraction losses in the case of a transverse convective heat removal. The propagation of an acoustic pulse or wave in one-dimensional equilibrium media with a periodic inhomogeneity was studied by Grety *et al.* [3].

In this paper, we determine the conditions of the acoustic instability of moving nonequilibrium media relative to the sound propagation along the flow or against it. We consider the two types of gas media: the media with a source of heat whose power Q depends on temperature T and density ρ and molecular media with a vibrational excitation of molecules. The flow velocity W is assumed to be subsonic: the Mach number is $M = W_0/u_s \ll 1$.

For the first type of media, the initial system of one-dimensional equations of gas dynamics can be written as

$$\begin{aligned} \frac{d\rho}{dt} + \rho\frac{\partial v}{\partial x} &= 0, \\ \rho\frac{dv}{dt} &= -\frac{\partial P}{\partial x} + \frac{4}{3}\eta\frac{\partial^2 v}{\partial x^2}, \\ C_{v\infty}\frac{dT}{dt} - \frac{T}{\rho}\frac{d\rho}{dt} &= Q(T, \rho) + \chi C_{p\infty}\frac{\partial^2 T}{\partial x^2}, \\ P &= \frac{\rho T}{m}. \end{aligned} \qquad (2)$$

Here, $d/dt = d/dt + v\,d/dx$, the x axis coincides with the flow direction, v is the velocity of gas, P is the pressure, $C_{p\infty}$ and $C_{v\infty}$ are the heat capacities at constant pressure and volume, m is the molecular mass, χ is the thermal diffusivity, and η is the shear viscosity coefficient. When writing the heat transfer equation and the equation of state, we used the energy units.

We represent the quantities in Eqs. (2) in the form $v = W_0 + v'$, $\rho = \rho_0 + \rho'$, and so on, where the subscript 0 corresponds to stationary values and the prime corresponds to disturbances of these quantities. For small values of the Mach number (but large enough to neglect the heat removal due to the thermal conduction), the

gradients of the stationary quantities in Eqs. (2) are equal to

$$\frac{1}{T_0}\frac{\partial T_0}{\partial x} \approx -\frac{1}{\rho_0}\frac{\partial \rho_0}{\partial x} = \frac{1}{\tau_Q C_{p\infty} M u_\infty}, \tag{3}$$

where $\tau_Q = T_0/Q_0$ is the characteristic time of heat release. In the subsequent consideration, we will use the approximation of linear geometric acoustics, which requires that the inhomogeneity of the medium be weak:

$$\frac{1}{T_0}\frac{\partial T_0}{\partial x} \ll \frac{\omega}{u_s}$$

or, with allowance for Eq. (3), this condition is satisfied only for a high-frequency sound:

$$\omega\tau_Q \gg \frac{1}{C_{p\infty} M}.$$

In the high-frequency limit, the system of Eqs. (2), after linearization and rejection of the terms higher than the second order of smallness, is reduced to closed equations describing the evolution of corresponding disturbances. For instance, for the velocity and density disturbances, the linearized equations take the form

$$\begin{aligned}\frac{\partial^2 v'}{\partial t^2} - u_\infty^2\frac{\partial^2 v'}{\partial x^2} + 2W_0\frac{\partial^2 v'}{\partial x \partial t} \\ = -2\alpha_\infty u_\infty \frac{\partial v'}{\partial t} + \left(\frac{4}{3}\frac{\eta}{\rho_0} + \frac{\chi}{C_{v\infty}}\right)\frac{\partial^3 v'}{\partial x^2 \partial t},\end{aligned} \tag{4}$$

$$\begin{aligned}\frac{\partial^2 \rho'}{\partial t^2} - u_\infty^2\frac{\partial^2 \rho'}{\partial x^2} + 2W_0\frac{\partial^2 \rho'}{\partial x \partial t} = \frac{3u_\infty}{C_{p\infty} M \tau_Q}\frac{\partial \rho'}{\partial x} \\ -2\alpha_\infty u_\infty \frac{\partial \rho'}{\partial t} + \left(\frac{4}{3}\frac{\eta}{\rho_0} + \frac{\chi}{C_{v\infty}}\right)\frac{\partial^3 \rho'}{\partial x^2 \partial t},\end{aligned} \tag{5}$$

where α_∞ is the coefficient of amplification of high-frequency sound in a nonequilibrium medium. According to Eq. (1), it is determined by using the second viscosity coefficient, which in the high-frequency limit is expressed as [1, 4]

$$\xi = \frac{C_{v0}(u_\infty^2 - u_0^2)\rho_0}{\omega^2 \tau_Q C_{v\infty}}.$$

Here, $u_0 = \sqrt{\gamma_0 T_0/m}$ and $u_\infty = \sqrt{\gamma_\infty T_0/m}$ are the velocities of low-frequency and high-frequency sounds; $\gamma_0 = C_{p0}/C_{v0}$; $\gamma_\infty = C_{p\infty}/C_{v\infty}$; $C_{p0} = Q_T - Q_\rho$ and $C_{v0} = -Q_\rho$ are the low-frequency heat capacities at constant pressure and volume for the given type of media [5]; $Q_T = \partial \ln Q_0/\partial \ln T_0$; and $Q_\rho = \partial \ln Q_0/\partial \ln \rho_0$. Taking into account the form of ξ, the high-frequency amplification factor can be represented as

$$\alpha_\infty = -\frac{Q_T + C_{v\infty} Q_\rho}{2\tau_Q C_{p\infty} C_{v\infty} u_\infty}.$$

The actual sound amplification in a homogeneous medium is determined by the condition $\xi < 0$; i.e., the following inequality should be satisfied:

$$Q_T + C_{v\infty} Q_\rho > 0. \tag{6}$$

Note that the sound amplification is also possible in heat absorbing media ($Q_0 < 0$), but, in this case, $\xi < 0$ and inequality (6) is reversed.

We seek the solution to Eq. (4) in the form

$$v' = v_1(x)\exp\left[i\int k dx - i\omega t\right], \tag{7}$$

where v_1 is the slowly changing amplitude of the velocity disturbance ($dv_1/dx \ll kv_1$) and $k = \omega/u_\infty$ is the wave vector. In an inhomogeneous medium, it depends on the spatial coordinate x.

Substituting Eq. (7) into Eq. (4), we obtain a reduced equation for a slowly varying amplitude

$$\frac{dv_1}{dx} = -iMkv_1 - (G_v + \delta)v_1$$

and its solution

$$\begin{aligned}v' = v_1(x=0)\exp\left[-\int_0^x (G_v + \delta)dx\right. \\ \left. + i\int_0^x k(1-M)dx - i\omega t\right],\end{aligned} \tag{8}$$

where

$$G_v = \alpha_\infty - \frac{1}{4C_{p\infty} M \tau_Q u_\infty} \tag{9}$$

is the growth increment of the velocity disturbances (for $G_v < 0$) and

$$\delta = \frac{\omega^2}{2u_\infty^3}\left(\frac{4\eta}{3\rho} + \frac{\chi}{C_{v\infty}}\right)$$

is the coefficient of sound absorption associated with the shear viscosity and the heat conduction.

Additional terms that appear in the increment in the case of a convective heat removal are connected with the fact that the oscillations of the flow velocity lead to oscillations of the heat removal thus determining the feedback between acoustic disturbances and the nonequilibrium heat release [6].

Similarly to Eq. (8), it is possible to obtain the solution for the slowly changing amplitudes of disturbances

of ρ_1, P_1, and T_1. The corresponding increments take the form

$$G_\rho = \alpha_\infty + \frac{5}{4C_{p\infty}M\tau_Q u_\infty},$$
$$G_p = \alpha_\infty + \frac{1}{4C_{p\infty}M\tau_Q u_\infty}, \quad (10)$$
$$G_T = \alpha_\infty - \frac{3}{4C_{p\infty}M\tau_Q u_\infty}.$$

All other quantities in Eq. (8) remain unchanged.

Unlike homogeneous media, in an inhomogeneous flow, the disturbances of the gas dynamic quantities have different increments. Earlier, a similar property was observed for nonstationary nonequilibrium media [7–10]. The increments may differ in both magnitude and sign. For instance, for $\alpha_\infty < 0$ and small values of the Mach number

$$M < \frac{C_{v\infty}}{2(Q_T + C_{v\infty}Q_\rho)},$$

only the velocity and temperature disturbances grow along the flow. However, this kind of flow is unstable for the density and pressure disturbances propagating against the flow. Obviously, for heat-absorbing media ($Q_0 < 0$), the situation will be reverse. Note that the increments G for small values of M_0 may far exceed the value of α_∞.

We consider now the second type of nonequilibrium media—a flow of vibrationally excited molecular gas. In this case, in Eqs. (2) only the equation of heat transfer will change:

$$C_{v\infty}\frac{dT}{dt} + \frac{dE_v}{dt} - \frac{T}{\rho}\frac{d\rho}{dt} = Q(T,\rho) + \chi C_{p\infty}\frac{\partial^2 T}{\partial x^2}, \quad (11)$$

where E_v is the vibrational energy (calculated per one molecule) the change of which is described by the relaxation equation

$$\frac{dE_v}{dt} = \frac{E_v^e - E_v}{\tau_v(T,\rho)} + Q. \quad (12)$$

Here, E_v^e is the equilibrium value of the vibrational energy, τ_v is the vibrational relaxation time, and Q is the power of the source maintaining the nonequilibrium excitation of molecule vibrations $E_v > E_v^e$. For simplicity, we consider the quantity Q as independent of T and ρ. In such a formulation of the problem, the dependence on these quantities would lead only to a more complex form of the second viscosity coefficient.

From Eqs. (11) and (12) for $M \ll 1$, it follows that

$$\frac{1}{T_0}\frac{dT_0}{dx} = -\frac{1}{\rho_0}\frac{d\rho_0}{dx} = \frac{S}{\tau_v C_{p\infty} W_0}.$$

Thus, in this case, the condition of geometric acoustics is satisfied when

$$\omega\tau_v \gg \frac{S}{C_{p\infty}M}, \quad (13)$$

where $S = (E_{v0} - E_{v0}^e)/\tau_v$ is the steady-state value of the degree of nonequilibrium.

For media with high degrees of nonequilibrium $S > 1$, the condition (13) is fulfilled only in the high-frequency limit. For small values of $S \ll 1$, Eq. (13) can also hold for low-frequency sound ($\omega\tau_v \ll 1$).

At the next step, we can use the above technique for finding the growth increments for the disturbances in an inhomogeneous flow. As a result, for high-frequency disturbances, we obtain G in the form of Eqs. (9) and (10) with τ_Q being replaced by τ_v/S in the second terms of these expressions. The coefficient α_∞ retains the form of Eq. (1) but with the second viscosity coefficient is expressed as

$$\xi = \frac{C^2_{v0}(u_\infty^2 - u_0^2)\rho_0}{\omega^2\tau_v C_{v\infty}} = \frac{C_v + S(\tau_T + C_{v\infty}\tau_\rho)}{C_{v\infty}C_{p\infty}u_\infty},$$

where, as before, $u_0 = \sqrt{\gamma_0 T_0/m}$ is the velocity of low-frequency sound, $\gamma_0 = C_{p0}/C_{v0}$; $C_{p0} = C_{p\infty} + C_v + S(\tau_T + \tau_\rho)$; and $C_{v0} = C_{v\infty} + C_v + S\tau_T$ are the low-frequency heat capacities at constant pressure and volume in a vibrationally excited gas [1], C_v is the equilibrium vibrational heat capacity, $\tau_T = \partial\ln\tau_v/\partial\ln T_0$, and $\tau_\rho = \partial\ln\tau_v/\partial\ln\rho$.

Thus, we have

$$\alpha_\infty = \frac{C_v + S(\tau_T + C_{v\infty}\tau_\rho)}{2\tau_v C_{v\infty}C_{p\infty}u_\infty},$$

and the condition of sound amplification in a homogeneous vibrationally excited gas is $\xi < 0$; i.e.,

$$S(\tau_T + C_{v\infty}\tau_\rho) < -C_v. \quad (14)$$

In an inhomogeneous flow of vibrationally excited gas, it is necessary to use the increments determined by Eqs. (9) and (10).

In the low-frequency limit, instead of increments (9) and (10), one has to use the expressions

$$G_v^0 = \alpha_0 - \frac{S}{4C_{p0}M_0\tau_v u_0},$$
$$G_\rho^0 = \alpha_0 + \frac{5S}{4C_{p0}M_0\tau_v u_0},$$
$$G_p^0 = \alpha_0 + \frac{S}{4C_{p0}M_0\tau_v u_0},$$
$$G_T^0 = \alpha_0 - \frac{3S}{4C_{p0}M_0\tau_v u_0},$$

where $M_0 = W_0/u_0$, $\alpha_0 = \omega^2\xi_0/2u_0^3\rho$ is the low-frequency amplification factor, and

$$\xi_0 = \frac{(u_\infty^2 - u_0^2)\tau_v C_{v\infty}\rho_0}{C_{v\infty}}$$

is the low-frequency second viscosity coefficient [1, 4]. For small values of S, the value of α_0 is negative when condition (14) is satisfied. Note that, for small values of S, we have $C_{p0} \approx C_{p\infty}$, $u_0 \approx u_\infty$ and the second terms in Eqs. (15) practically coincide with the corresponding terms of the high-frequency approximation.

Thus, in this paper, the growth increments of the gas dynamic disturbances that occur in nonequilibrium gas flows are determined, and it is shown that the velocity, density, pressure, and temperature disturbances have different increments. For heat releasing media and vibrationally excited gases (which are active in the homogeneous approximation), in the case of small Mach numbers, the velocity and temperature disturbances grow along the flow and the pressure and density disturbances grow in the opposite direction. For endothermic media, the situation is reversed. The growth increments in flows may far exceed the increments in homogeneous media.

REFERENCES

1. N. E. Molevich and A. N. Oraevskiĭ, Tr. Fiz. Inst. im. P. N. Lebedeva, Ross. Akad. Nauk **222**, 45 (1993).
2. E. V. Kol'tsova, A. I. Osipov, and A. V. Uvarov, Akust. Zh. **40**, 969 (1994) [Acoust. Phys. **40**, 859 (1994)].
3. N. Crety, P. P. Delsanto, G. Nita, *et al.*, J. Acoust. Soc. Am. **104**, 57 (1998).
4. L. D. Landau and E. M. Lifshitz, *Course of Theoretical Physics*, Vol. 6: *Fluid Mechanics* (Nauka, Moscow, 1986; Pergamon, New York, 1987).
5. N. E. Molevich and A. N. Oraevskiĭ, Zh. Eksp. Teor. Fiz. **94** (3), 128 (1988) [Sov. Phys. JETP **67** (3), 504 (1988)].
6. A. V. Nedospasov and V. D. Khaĭt, *Oscillations and Instabilities of Low-Temperature Plasma* (Nauka, Moscow, 1979).
7. J. P. Patureau, T.-Y. Toong, and C. A. Garris, in *16th Symposium (International) on Combustion, Pittsburgh, 1977*, p. 929.
8. G. E. Abouseif, T.-Y. Toong, and J. Cinverti, in *17th Symposium (International) on Combustion, University of Leeds, England, 1978*, p. 1341.
9. R. H. Detsch and H. E. Bass, J. Acoust. Soc. Am. **77**, 512 (1985).
10. N. E. Molevich and A. N. Oraevskiĭ, Akust. Zh. **35**, 482 (1989) [Sov. Phys. Acoust. **35**, 282 (1989)].

Translated by A. Svechnikov

Acoustical Physics, Vol. 47, No. 1, 2001, pp. 106–111. Translated from Akusticheskiĭ Zhurnal, Vol. 47, No. 1, 2001, pp. 123–129.
Original Russian Text Copyright © 2001 by Prokhorov.

Formation of a Deep Scattering Layer in a Stratified Flow behind a Two-Dimensional Obstacle

V. E. Prokhorov

Institute of Problems of Mechanics, Russian Academy of Sciences,
pr. Vernadskogo 101 (1), Moscow, 117526 Russia
e-mail: prohorov@ipmnet.ru

Received January 18, 2000

Abstract—A stratified stationary flow around a circular cylinder is accompanied by the formation of a thin, acoustically contrasting layer extending along the horizontal axis of the flow. The theoretical and experimental studies show that the pressure differential and the backscattering coefficient of the layer can be quantitatively estimated in the framework of the problem on a stratified ideal incompressible liquid flow around a cylinder. *© 2001 MAIK "Nauka/Interperiodica".*

Experimental modeling of stratified flows around two-dimensional obstacles is of great practical importance, because the elements of such flows often occur behind extended irregularities of the sea bottom in the open ocean, as well as in coastal and shelf zones. The models of two-dimensional flows behind bodies are convenient for studying the effects of the sound scattering by isolated forms of motion, such as eddies, waves, and layered and turbulent structures. In modeling, the effect of each of the above forms of motion can be artificially emphasized by choosing the corresponding flow characteristics.

In the context of acoustical tomography and thermometry, where the average values of the sound velocity [1], the refractive index [2], and the propagation time [3] are of primary importance, the scattering by internal waves and turbulence is often considered as a forward scattering.

According to experimental data, backscattering is caused to a considerable extent by turbulence. This is particularly true in the anisotropic case, for example, in the vertical echo sounding of a turbulent wake behind a body moving in stratified water [4]. The level of volume scattering estimated for an isotropic turbulence is several orders of magnitude less than the scattering level caused by the discrete suspension (plankton) occurring everywhere in the ocean [5]. According to Stanton *et al*. [6, 7], turbulence additionally plays the role of the marking suspension in the echo sounding of internal waves. In this case, waves are visualized in the echograms as two-layer periodic structures and every layer is clearly seen only for the sounding waves of a certain frequency range. This behavior is explained by the combined effect of two kinds of scatterers, namely, zooplankton and turbulence [6].

Generally, the contribution of internal waves to the backscattering is small, because the local density gradients characteristic of internal waves are too small for causing any noticeable sound reflection at the frequencies used in full-scale and laboratory studies.

However, internal waves can produce considerable pressure differentials in the wake behind a body. Indeed, a stratified flow around a two-dimensional obstacle is accompanied by the formation of thin interlayers in the wake, and local density gradients in these layers can exceed those characteristic of an unperturbed liquid by a factor of several dozen [8]. Experimental data point to a close causal link between the interlayers and the field of attached internal waves. The experiments with the shadow visualization demonstrated that the wake is subdivided into two regions: the outer region occupied by internal waves, and the inner region adjacent to the wake axis and free from internal waves [9, 10]. A similar situation occurs for a turbulent flow around a thin vertical plate, when a density boundary separates the turbulent wake from the field of secondary internal waves generated by this wake [11]. Such boundaries can be observed in the backscattered field by sounding the water column. This fact was supported by laboratory experiments, in which the measured scattering coefficients agreed well with the coefficients calculated in the approximation of the reflection from a plane transition layer [10, 12]. In this connection, a theoretical and experimental investigation of the role played by the attached internal waves in the formation of acoustically contrasting boundaries in the stratified flow behind a two-dimensional obstacle is of interest.

From the standpoint of experimental testing, the optimal theoretical model of the flow is the model that has an exact solution free of restrictions on the amplitude of internal waves, is reproducible in laboratory conditions, and allows one to control the flow using optical and echo-sounding methods.

Let a horizontal flow with a constant velocity $\mathbf{v}_0 = \{U, 0\}$ be incident on a two-dimensional cylinder of

radius R located in a basin in which the liquid is characterized by the vertical profiles of density and buoyancy frequency $\rho_0(z)$ and $N = (g\rho^{-1}d\rho/dz)^{1/2}$, respectively. Within a time interval τ, new distributions of the flow velocity and density will be formed: $\mathbf{v}_0 + \mathbf{v} = \{U + u, w\}$ and $\rho(x, z) = \rho_0(z) + \rho'(x, z)$. These distributions are described by the complete system of fluid mechanics equations and the boundary conditions at the body surface. In our consideration, we assume that the z-axis is directed downward, the x-axis is opposite to the flow direction, and $R \ll L$, where L is the smallest linear size of the basin.

It was shown [13] that, in the case of two-dimensional steady-state flow of an ideal liquid, the system of fluid mechanics equations can be reduced to a single equation whose exact solution is known. For a homogeneous stratification characterized by a depth-independent buoyancy frequency N, the introduction of the stream function ψ for the disturbances of the velocity, $u = \partial\psi/\partial z$ and $w = -\partial\psi/\partial x$, and density, $\alpha = \rho'/\rho = -\psi N^2/gU$, results in the following final equation [14]:

$$\Delta\psi + N^2/U^2\psi = 0. \tag{1}$$

This equation together with the boundary condition $\mathbf{v}n - \mathbf{v}_0 n = 0$ (n is the outer normal to the cylinder surface) completely defines the problem. Aksenov *et al.* [14] replaced the boundary condition by force sources thus transforming Eq. (1) to an inhomogeneous equation and obtained the solution to the latter in the form

$$\psi\frac{NR^2}{2} \times\left(-\pi Y_1(y)\sin\varphi + \sum_1^M \frac{8m}{4m^2-1} J_{2m}(y)\sin 2m\varphi\right), \tag{2}$$

where Y and J are the Neumann and Bessel functions of the argument $y = r/Rf$, $r = (x^2 + z^2)^{1/2}$ and $\varphi = \arctan(z/x)$ are the polar coordinates, and $f = U/NR$ is the Froude number. The integer number M is infinite in the limit; however, for flows with $f > 0.1$, the value $M = 5$ is sufficient [14].

Taking into account Eq. (2), we can represent the disturbed density α in the form

$$\alpha = \frac{R}{\Lambda}\frac{1}{f}\left(-0.5\pi Y_1(y)\sin\varphi + \sum_{m=1}^{M} J_{2m}(y)\sin 2m\varphi 4m/(4m^2-1)\right), \tag{3}$$

from which it follows that, at every point of the space, the quantity α is a function of two dimensionless parameters: the Froude number f and the ratio of R to the stratification scale $\Lambda = g/N^2$.

As was mentioned above, the model determined by Eqs. (1) and (3) holds for steady-state flows. The transient flow begins at the instant when the stream is turned on (or the cylinder starts to move) and lasts to the instant τ when the disturbed density takes on the form of Eq. (3). For a laminar flow of a homogeneous liquid about a cylinder, the value of τ coincides with the time required for the liquid to flow from the front zone to the wake and is of the order of R/U. On the contrary, in stratified flows, the duration τ can multiply exceed the ratio R/U. The reason is that a zone of blocked liquid (blocked zone) is formed in front of the body, and the kinetic energy of liquid in this zone is insufficient for overcoming the buoyancy forces and flowing into the wake. According to experimental data [15], the length of this zone relative to the body center is $L = R\mathrm{Re}/20f^2$, where $\mathrm{Re} = UR/\nu$ is the Reynolds number and $\nu \approx 0.01$ cm^2/s is the kinematic viscosity. Correspondingly, the dimensionless time of reaching the steady state is about

$$N\tau = NL/U = \mathrm{Re}/20f^3. \tag{4}$$

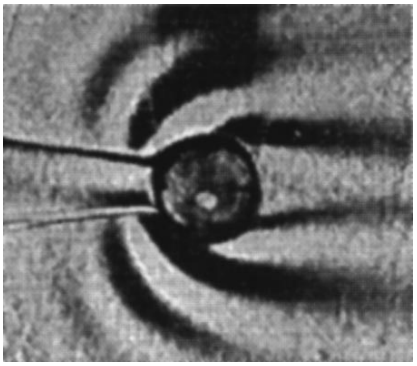

Fig. 1. Nonstationary flow behind the cylinder ($f = 0.05$, $\mathrm{Re} = 20$, $R = 1.3$ cm, $N = 0.5$ s^{-1}, and $Nt = 180$). Two inclined boundaries and the adjacent alternating curved beams of attached internal waves are clearly seen in the wake. The light triangular region in front of the body is the blocked zone.

The effect of the blocked zone is the most prominent for the Froude numbers $f < 0.1$. Figure 1 shows the shadow pattern of the flow, where the blocked zone appears as the light triangle with the vertex on the axis of the cylinder motion (here and below, we consider laboratory experiments in which the water is stratified in salinity and the cylinder is moved rather than the liquid: this is equivalent from the viewpoint of the theory, but essentially simplifies the experiment). The wake has two boundaries (its external envelopes), and the wave beams are adjacent to them. As can be seen, waves propagate only in the external region of the flow and cannot penetrate into the wake.

The blocked zone has the form of an elongated isosceles triangle with the vertex located at the axis of motion. Due to this fact, the zone plays the role of an inclined plane that favors the motion of the adjacent liquid layers and their transfer into the wake even in weak flows. The smaller the velocity of the oncoming stream,

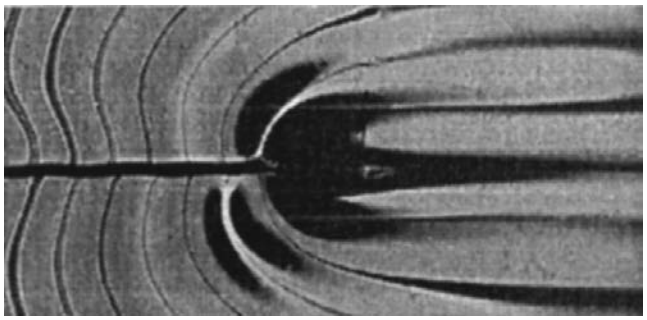

Fig. 2. Stable stationary flow behind the cylinder ($f = 0.3$, Re = 20, $R = 0.75$ cm, $N = 1.2$ s^{-1}, and $Nt = 72$). Wave beams are adjacent to the single axial boundary in the wake. The dark triangular region in front of the body is the blocked zone.

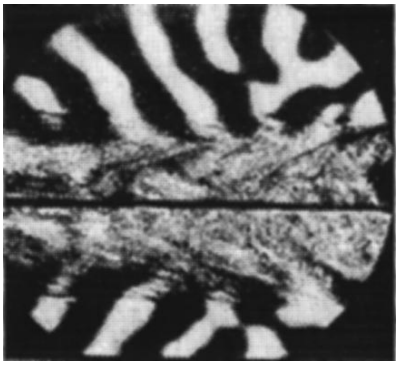

Fig. 3. Stationary flow behind the cylinder ($f = 0.3$, Re = 90, $R = 2.5$ cm, $N = 0.6$ s^{-1}, and $Nt = 180$). The microstructural instability is seen in the wake. The cross-sections of the wave beams of internal waves (the inclined strips) are interrupted in the unstable zone.

the smaller the slope of the blocked zone and the greater its length, which ensures that the inertia forces overcome the buoyancy forces. The nonstationary stage begins immediately after the flow is turned on (or the cylinder starts to move): first, the liquid particles that are closest to the top and the bottom of the cylinder flow into the wake, then, the more distant particles, and, finally, the liquid particles adjacent to the vertex of the blocked zone. Because of this process, the density of particles forming the near-wall layer will steadily vary tending to the density of the liquid at the axis of motion ($z = 0$). The separation of the layer from the cylinder surface is governed by the buoyancy of the near-wall layer relative the surrounding wake and, to a lesser extent, by the viscosity. The first factor causes the point of separation to move steadily toward the wake axis during the nonstationary stage. The effect of the viscosity manifests itself in the fact that the layer will be separated with some delay relative to the instant when it reaches the height of the steady-state density. During the nonstationary stage, all these processes bring into existence two boundaries—the upper and lower envelopes of the wake (Fig. 1), which slowly move toward each other. Figure 1 clearly shows that the starting points of wave beams are adjacent to these boundaries, which means that the density boundaries separate the wave region from the internal region of the wake. If we place an immobile microcontact sensor in the path of the boundary motion, then, at the moment the envelope reaches the sensor, it will fix the envelope thickness and the density differential. This approach was used in [12] to measure the parameters of the boundaries. For the flow regime used ($f = 0.05$, Re = 20), the duration of the nonstationary stage exceeds two hours, which goes beyond the duration of a single experiment.

As follows from Eq. (4), the time required for reaching the steady-state regime steeply decreases with increasing Froude number. Figure 2 shows the flow pattern ($f = 0.3$, Re = 20) at the instant $Nt = 72$ relative the onset of the body motion, which is almost twice the duration of the nonstationary stage $N\tau = 37$. The top and bottom envelopes approach each other near the motion axis and form a thin transition layer from which wave beams originate both above and below the layer. Note that the decrease in the duration of the nonstationary stage due to the increase in the Froude number is limited by the condition $f < 2$; with further increase in the Froude number, a shear instability can appear [16].

An increase in the Reynolds number produces the opposite result, i.e., an increase in the duration of the nonstationary stage. In addition, the flow loses its laminar structure for the Reynolds numbers exceeding the critical value Re = 20 and, with further increase in the Reynolds number, the flow becomes unstable [17]. Figure 3 shows the flow pattern ($Nt = 180$, $N\tau = 160$) for the Froude number coincident with the foregoing case ($f = 0.3$) and the Reynolds number (Re = 90) exceeding the stability threshold by a factor greater than two. As can be seen, on average (with respect to large-scale elements), the flow is stable and shows the basic stationary features (an axis-type boundary and the adjacent internal waves); however, in the wake, one can see a zone of microscale instability that masks the internal waves.

The flow shown in Fig. 2 is the most appropriate for experimental study of the scattering by the structures formed by internal waves. The Reynolds number Re = 20 is optimal in this case, because such choice ensures the maximal suppression of the viscosity effects without loss of stability. For the given Froude number $f = 0.3$, the pattern with clearly defined internal waves and the density boundary is observed in the wake (Fig. 2). In addition, the time required for reaching the steady-state pattern is quite acceptable ($\tau = \mathrm{Re}/(20f^3N) = 30$ s).

The interlayer at the wake axis (Fig. 2) can be considered as a horizontal layer of constant thickness with the density differential $\delta\rho = \delta\rho(x)$ varying in the horizontal direction with the spatial period equal to a half wavelength of the attached internal wave $\lambda_i/2 = \pi U/N$. For sounding such a boundary with a vertical acoustic beam whose cross-section is much smaller than λ_i, the

scattering coefficient of sound $n(x)$ can be represented for every x in the form [12, 18]

$$n = n_a|\sin(kdR)|, \tag{5}$$

where

$$n_a = 0.5\eta(1 + \beta_c/\beta_\rho)/kdR, \tag{6}$$

$\eta(x) = |\delta\rho/\rho_0|$, $k = 2\pi/\lambda$, λ is the sound wavelength, d is the envelope thickness normalized by the cylinder radius, and the parameters $\beta_\rho = \rho^{-1}\partial\rho/\partial S = 0.8 \times 10^{-3}(‰)^{-1}$ and $\beta_c = c^{-1}\partial c/\partial S = 0.7 \times 10^{-3}(‰)^{-1}$ are the coefficients in the linearized equations of state relating the density differential $\delta\rho/\rho = \beta_\rho\delta S$ and the sound velocity differential $\delta c/c = \beta_c\delta S$ to the salinity differential δS.

As follows from Eq. (3), the density differential at the wake axis is

$$\begin{aligned}\delta\rho &= \rho(x, d/2) - \rho(x, -d/2)\\ &\approx \rho_0[\alpha(x, d/2) - \alpha(x, -d/2)].\end{aligned} \tag{7}$$

Expressions (3), (5)–(7) determine the scattering coefficient as a function of the distance x, the Froude number, and the ratio R/Λ. Thus, they present the theoretical solution of the problem.

The oscillating factor $\sin(kdR)$ appearing in Eq. (5) drastically depends on small variations in the thickness d in the vicinity of $kdR = m\pi$ where the sine takes on small values. This region is often reached in the experiments because of the fluctuations of the layer thickness. As a result, the scattering level exhibits uncontrollable sharp oscillations. Usually, these fluctuations occur at higher frequencies (above the buoyancy frequency) and can be filtered out in the course of the processing.

Figure 4 shows the behavior of n_a as a function of the dimensionless distance x/R for $f = 0.3$ and Re = 20. The period $x/R = 1$ is prominent in this behavior, and it corresponds to a half of the wavelength of the internal wave $\lambda_i(2R) = \pi f \approx 1$. In the calculations, we specified $d = 0.45$, which corresponds to the scattering layer of thickness 0.33 cm and coincides with the average thickness of the dark horizontal interlayer at the wake axis (Fig. 2).

In order to consider an actual case rather than the idealized situation (Fig. 4), we should take into account the averaging of the backscattered signals over the width D of the sound beam. As a result, a practicable approximation to n_a will be the expression

$$n_0(x) = D^{-1}\int_x^{x+D} n_a(\xi)d\xi. \tag{8}$$

In the experiment, the sound beam remains immobile and the coordinate x varies due to the fact that the whole pattern of attached internal waves (together with the structural inhomogeneities formed by these waves) follows the body with the velocity $-U$.

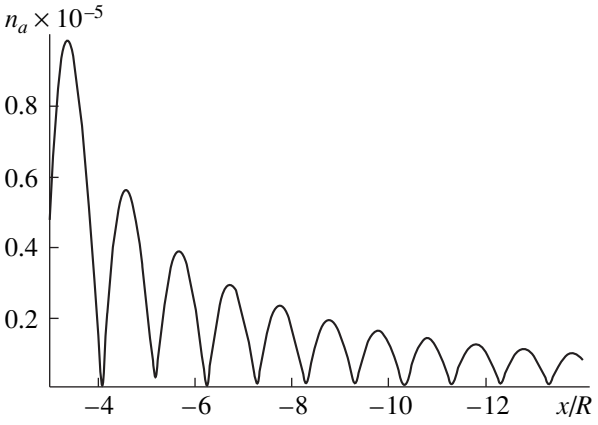

Fig. 4. Theoretical scattering coefficient n_a versus the dimensionless distance x/R for $f = 0.3$ and Re = 20.

The experiment was carried out in a $240 \times 40 \times 60$-cm^3 basin filled with water with a stratified salinity. The buoyancy frequency, the cylinder radius, and its velocity were $N = 1.2$ s^{-1}, $R = 0.75$ cm, and $U = 0.3$ cm/s, respectively. We used the acoustic sounding with the following parameters: the sound wavelength $\lambda = 0.15$ cm (the operating frequency of echo sounder 1 MHz), the pulse duration 30 μs, and the pulse repetition period 0.16 s. In this case, the wavelength and the layer thickness are such that the oscillating factor in Eq. (5) is $\sin(kdR) \approx 1$, and one can correlate the measured scattering coefficient with quantity n_0 calculated by Eq. (6) taking into account Eq. (8).

The acoustic antenna had the form of a circular piezoceramic disc of radius $a = 2.5$ cm. The antenna was placed in a damping screen (a rubber tube 8 cm long and 2 cm in diameter), which improved its directivity property. The antenna was mounted at the height $h = 25$ cm relative the wake axis. This height essentially exceeds the length of the near zone $a^2/4\lambda = 10.5$ cm [18], and we can assume that the wake is located in the far zone. The sound beam axis was directed along the vertical, and its angular half-width measured by the shadow image was 2°. The transverse size of the insonified zone observed on the display was about 4 cm at the point where it intersected the wake axis [12]. However, the peripheral part of the beam practically did not contribute to the formation of the backscattering, because the power of the incident beam is mainly confined in the first Fresnel zone whose diameter is $(h\lambda)^{1/2} \approx 2$ cm. Actually, the diameter of the active cross-section of the sound cone forming the backscattering is still smaller because of the angular divergence of the beam, owing to which only a small central portion of the insonified circular spot scatters in the vertical direction. Outside the spot, the angle of incidence of the sound wave is such that reflected rays are deflected and bypass the antenna.

Immediately before towing the cylinder, we measured the voltage amplitude V_0 obtained at the output of

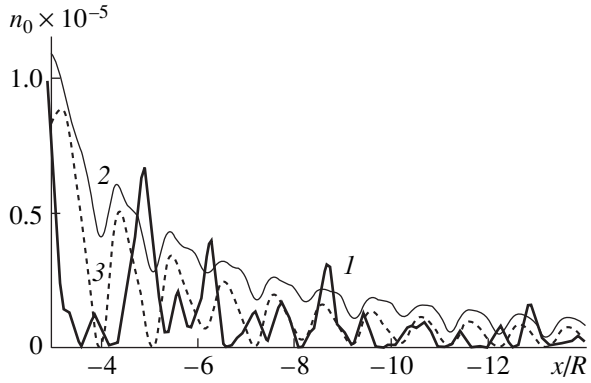

Fig. 5. Average amplitude of the scattering coefficient n_0 versus the dimensionless distance for $f = 0.3$ and Re = 20: (*1*) the experimental curve and (*2*), (*3*) the theoretical dependences calculated with the length of averaging D/R = (*2*) 2 and (*3*) 0.5.

the echo sounder from a plane horizontal plate made of organic glass. We used the amplitude V_0 to determine the amplitude of the incident signal $V_i = V_0/b$, where $b = 0.3$ is the empirical coefficient that takes into account the losses related to the propagation of the acoustic pulse and its reflection from the plate [10]. Then, we used echo signals V obtained by sounding the wake to calculate the scattering coefficient

$$n = V/V_i = bV/V_0. \quad (9)$$

The starting point of the cylinder motion was at a distance of 20 cm from the sound beam axis. Sixty seconds after the start, the cylinder entered the insonified zone; here, the flow pattern corresponded to that shown in Fig. 2. We started to measure the desired echo signal immediately after the cylinder left the sound beam. At this moment, the intense reflection from the cylinder disappeared, and the antenna of the echo locator was reset to the sensitive reception of weak echo signals from the wake.

During the measurements, the signals from the antenna output were sent to the computer memory through a special interface unit. The data were arranged as voltage–depth–time three-dimensional arrays. The array of the current values of the scattering coefficient determined by Eq. (9) was calculated for the fixed depth at which the wake axis was located. Then, from this array, we filtered out the high-frequency components, which could appear because of the random fluctuations of the reflecting layer thickness and orientation.

Figure 5 shows the measured scattering coefficient versus the dimensionless distance x/R (curve *1*). For comparison, this figure contains additional curves obtained by averaging the ideal theoretical curve (Fig. 4) over a moving window according to Eq. (8). Curve *3* obtained with the averaging interval $D/R = 0.5$ appeared to be closest to the experimental curve. This averaging interval corresponds to the diameter of the active part of the sound beam ($D = 0.4$ cm), which is much less than the total width of the beam observed in the shadow image.

The features of the experimental curve coincide with those of the theoretical one. The curves exhibit a half-wave spatial period and a decay with distance. The general agreement between curves *1* and *3* is evidence in favor of the fact that the theoretical model determined by Eqs. (3), (6), and (7) with consideration for Eq. (8) adequately describes the sound scattering from the boundary.

Thus, using the stationary laminar flow behind a two-dimensional cylinder as an example, we showed that an acoustically contrasting layer of density differential is formed in the wake. Two facts dictated the choice of the flow regime. The first fact is that an exact solution is known for this particular type of flow, which allows one to calculate the magnitude of the density differential. The second fact is that a stable and practically plain layer is formed in such a wake, which allows one to calculate the theoretical scattering coefficient of the layer and test it experimentally using the data of the optical measurements and echo sounding. Note that Eq. (1) is a linear equation, and the boundary conditions represent a linear combination of the velocities of the undisturbed (main) flow v_0 and the attached internal waves v. In these terms, the horizontal boundary of the density differential given by Eq. (7) is a result of the superposition of internal waves and the main flow in the wake behind the body.

As was mentioned above, boundaries with a similar of higher contrast are also formed in nonstationary (Fig. 1), in partially unstable (Fig. 3), and even in totally turbulent ($f \sim 1$, Re ~ 5000) [11] wakes. In each of these cases, the flow pattern is characterized by a sharp density differential between the region of internal waves and the zone adjacent to the wake axis, which is evidence in favor of the fact that, in these cases, the boundary is also formed as a result of a combined action of internal waves and the main flow. It is not unlikely that, although the flows behind obstacles in the ocean are highly turbulent and nonstationary, a similar mechanism should be present in the ocean. This means that isolated sound-reflecting boundaries can appear in the wakes in the ocean and act in parallel with the turbulent sources of scattering.

The following conclusions can be made from this study.

An acoustically contrasting density differential is formed near the horizontal axis of the wake in a stationary stratified flow around a cylinder.

The measured values of the sound-scattering coefficient of the layer agree well with the theoretical value calculated for a plain transition layer whose density differential can be expressed analytically as the wave solution to the problem of the flow around a cylinder.

In flows behind obstacles, the attached internal waves together with the main flow form a mechanism for the generation of deep scattering layers.

ACKNOWLEDGMENTS

This work was supported by the Russian Foundation for Basic Research, project no. 97-01-01013.

REFERENCES

1. M. Wolfson and J. Spiesberger, J. Acoust. Soc. Am. **106**, 1293 (1999).
2. D. Di Iorio and D. M. Farmer, J. Acoust. Soc. Am. **103**, 321 (1998).
3. J. Colosi and E. K. Scheer, J. Acoust. Soc. Am. **105**, 3202 (1999).
4. I. Pelech, G. Zipfel, and R. Holford, J. Acoust. Soc. Am., **73**, 528 (1983).
5. J. Proni and J. Apel, J. Geophys. Res. **80**, 1147 (1975).
6. T. Stanton, J. Warren, P. Wiebe, *et al.*, in *Internal Solitary Wave Workshop, Victoria, B.C., Canada, 1998*.
7. T. K. Stanton, P. H. Wiebe, D. Chu, and L. Goodman, ICES J. Mar. Sci. **51**, 4469 (1994).
8. I. V. Voeĭkov and Yu. D. Chashechkin, Izv. Akad. Nauk, Mekh. Zhidk. Gaza, No. 1, 20 (1993).
9. I. V. Voeĭkov, V. E. Prokhorov, and Yu. D. Chashechkin, Izv. Akad. Nauk, Mekh. Zhidk. Gaza, No. 3, 3 (1995).
10. V. E. Prokhorov and Yu. D. Chashechkin, Akust. Zh. **41**, 908 (1995) [Acoust. Phys. **41**, 804 (1995)].
11. B. R. Sutherland and P. F. Linden, J. Fluid Mech. **377**, 223 (1998).
12. V. V. Mitkin, V. E. Prokhorov, and Yu. D. Chashechkin, Akust. Zh. **45**, 380 (1999) [Acoust. Phys. **45**, 336 (1999)].
13. R. R. Long, Tellus **7**, 341 (1955).
14. A. V. Aksenov, V. A. Gorodtsov, and I. V. Sturova, Preprint No. 282, IPM RAN (Moscow Inst. for Problems in Mechanics, Russian Academy of Sciences, 1986).
15. D. L. Boyer, P. A. Davies, H. Fernando, and X. Zhang, Philos. Trans. R. Soc. London, A **328**, 501 (1989).
16. J. Turner, *Buoyancy Effects in Fluids* (Mir, Moscow, 1977).
17. L. M. Brekhovskikh and V. V. Goncharov, *Introduction to Mechanics of Continua* (Nauka, Moscow, 1982).
18. V. A. Shutilov, *Foundations of the Physics of Ultrasound* (Leningr. Gos. Univ., Leningrad, 1980).

Translated by A. Vinogradov

Acoustical Physics, Vol. 47, No. 1, 2001, pp. 112–114. Translated from Akusticheskiĭ Zhurnal, Vol. 47, No. 1, 2001, pp. 130–132.
Original Russian Text Copyright © 2001 by Lyamshev.

The 7th International Congress on Sound and Vibration

The 7th International Congress on Sound and Vibration was held July 4–7, 2000, in Garmish-Partenkirchen (Germany). The Congress was sponsored by the International Institute of Acoustics and Vibration, the Bavarian State Ministry for Regional Development and Environmental Affairs, and other institutions and companies. Professor Hanno Heller was the General Chairman of the Congress. It was a regular congress of a series of congresses started in 1990. The previous congresses were held in the United States (twice), Canada, Russia, Australia, and Denmark.

The congresses were initiated by the International Institute of Acoustics and Vibration (IIAV) which was officially founded in 1995 as a public noncommercial international institution. Members of IIAV are researchers and experts whose priority in academic and applied research is acoustics and vibrations. Acoustic societies and associations from many countries are collective members of the Institute. IIAV has the status of a branch of the Union of Theoretical and Applied Mechanics at UNESCO. Professor Sir James Lighthill, who is well known in the international scientific community, was elected the first President of IIAV. Starting from June 2000, Professor Colin Hansen (Australia) has been the President of the Institute. Professor Malcolm Crocker (United States) is the Executive Director of IIAV. He was the initiator and one of the founders of IIAV together with other acousticians from many countries. Professor Crocker is a permanent chairman of scientific committees and congresses. IIAV publishes the International Journal of Acoustics and Vibration.

The 7th International Congress on Sound and Vibration was a vast and representative scientific forum. Forty-six researchers participated in its Scientific Committee. About 450 papers were presented at the Congress. They were distributed in 34 fields: keynote (plenary) lectures, aeroacoustics, architectural and building acoustics, adaptronics, aerospace measurements, active noise control, arrays, active vibration control, biological acoustics, boundary-element methods, finite-element methods, condition monitoring and diagnostics, duct-acoustics, environmental and outdoor noise, instrumentation and transducers, musical acoustics, modal methods, machinery noise and vibration, measurement techniques, nonlinear vibrations, noise propagation, passive control of noise and vibration, sound perception, rotating systems, solids and continuous media, statistical energy analysis, signal processing, structural vibrations, tuned absorbers, trains and railways, underwater acoustics, ultrasonics, vehicle noise and vibration, and wavelets.

Eight keynote (plenary) lectures were delivered at the congress.

A lecture by G. Lilley (Great Britain) “On the Relation between Classical Theories of Acoustic and Electromagnetic Wave Propagation” primarily treated the particular features of the fields of moving sources of sound and electromagnetic waves. The paper was devoted to the memory of Sir James Lighthill, the author of fundamental works on the theory of aerodynamic turbulent noise. Professor G. Lilley together with J. Lighthill were among the founders of this theory.

A paper by L. Beranek (United States) “Concert Halls and Opera House Acoustics: 2000” discussed the criteria characterizing the acoustic quality of a concert hall or opera house and the application of these criteria in the process of the design and construction of such halls. The author noted that one of the best concert halls, the Symphony Hall in Boston (United States), was the first one constructed taking into account the requirements determined by acoustic criteria. The hall was built in 1900. W. Sabine, the founder of architectural acoustics, was the advisor on the hall acoustics. Only one criterion of the acoustic properties of halls from the six criteria recognized nowadays and discussed in the paper was known at that time, namely, the reverberation time. It was noted in the paper that the acoustic criteria of halls adopted now were applied in the process of the design of the Tokyo Opera City Concert Hall. The acoustic rating of 23 opera houses all over the world made up by conductors and its correlation with the acoustic parameters (criteria) of these halls are given in the paper.

A paper by V. Bolotin (Russia) “Dynamic Instabilities and Postcritical Vibrations of Structures” presented and discussed fundamental problems of the behavior of dynamic structures in the conditions of loss of stability. The parametric excitation of vibrations in a structure, structure vibrations in a flow of a gas or fluid, the instability of a dynamic system under the effect of an impact load, and vibrations and instabilities arising in rotating systems were considered. All these problems were treated within a unified approach.

J. Bento Coelho (Portugal) delivered a paper “On Silencer Design Techniques.” Noise silencers are widely used in very different devices including powerful blowers and air ducts, internal combustion engines for suppression of the exhaust noise, and other devices. A review of silencers of various types was given, namely, resonance and dissipative silencers and silencers employing the technique of active suppression of

1063-7710/01/4701-0112$21.00 © 2001 MAIK “Nauka/Interperiodica”

noise and vibrations. The advantages and possible applications of various silencers were indicated. The methods of testing of silencers and the possibilities for the comparison and evaluation of their efficiency were described.

C. Morfey (Great Britain) presented a paper "Fundamental Problems in Aeroacoustics." The paper discusses the state of the art in aeroacoustics starting from 1970. Basic information on aeroacoustics in the 1950s and 1960s was given. The question of whether all fundamental problems of aeroacoustics have been solved was raised. A critical review of four topical problems was given. The conclusion was made that the modern concept of the source of aerodynamic noise is incomplete. According to the lecturer, the four problems indicated above are sound emission by a turbulent jet at high Reynolds numbers and low Mach numbers; sound radiation by turbulence at a plane boundary and the role of wall fluctuations of viscous strain at the boundary; the problem of the interaction of sound with a flow; and wide-band noise of blowers as an aerodynamic problem of their design.

The studies conducted in the 1980s and 1990s showed that the existence of aerodynamic sound sources of the monopole type is possible in a turbulent flow with dissipation and a shift of velocity. It was noted that the role of monopole sound sources in many cases can be dominant because of the high efficiency of monopole sound sources in comparison with quadrupole sources. However, experiments demonstrated that the monopole sources play a secondary role. At the same time, this problem cannot be considered completely solved and further investigations (first of all experiments) are necessary.

Up to now experts in aeroacoustics from the United States and Europe have adhered to the opinion that there are no dipole sources of aerodynamic noise at a plane unlimited rigid wall in a turbulent flow. Some papers were published at the end of the 1990s in which this point of view was called into question, and according to the lecturer, this is one more question that needs additional investigation. Note that Russian (Soviet) researchers almost always supported the opinion that dipole sources of sound exist. However, their Western colleagues apparently did not notice the papers devoted to this problem and published in Soviet journals and probably just ignored them since the results of these studies contradicted the "common" or "settled" point of view that there are no and cannot be dipole sources at a plane wall. Meanwhile, as was indicated in the papers by Soviet researchers, one of the mechanisms of the formation of the sources of the dipole type is connected with reflection of viscous waves born by a turbulent flow and existing in the viscous sublayer of the turbulent boundary layer from a plane surface (wall). A longitudinal (sound) wave arises from the reflection of a viscous wave from the boundary.

A lecture "Modal Testing 2000" was delivered by D. Ewins (Great Britain). The major contents of the paper refer to the problem of the measurement of the characteristics of the vibrations of dynamic structures including the precision of the measurement of these characteristics and their repeatability. This is necessary for a more substantiated representation, calculation, and evaluation of vibrational and acoustic fields of dynamic structures (real objects).

G. Pavic (France) presented a paper "Power and Energy in Vibroacoustic Systems." The paper exposed a method of utilization of the relationship between the input power and vibroacoustic characteristics of a dynamic system as a characteristic of vibroacoustic properties of a dynamic system from the point of view of noise suppression. The possibility of the employment of this relationship was discussed. This approach is close in its concept to the so-called statistical energy analysis. Two fields of application of the criterion proposed by the lecturer (the ratio of input power to energy in a dynamic system) were considered: optimization of vibroinsulation and suppression of vibrations and noise by active methods.

The problem of noise borne by the operation of axial wind turbines and helicopter rotors was discussed in the paper "Aeroacoustics of Wind Turbines and Helicopter Rotors" by S. Wagner (Germany). Analysis of noise sources was conducted. Possibilities were discussed and examples were given of a computer simulation of noise that was based on application of the finite-element method. Examples of the calculation of noise characteristics were given that were based on numerical solution of nonlinear equations, the Euler equation, and the Navier–Stokes equation.

It is necessary to note in conclusion that papers devoted to two relatively new fields deserve special attention. One of these fields is called "adaptronics" and the other one, "wavelets."

A characteristic example of a paper in the first field is the paper "Overview of Adaptronics in Aerospace and Traffic Engineering" by D. Sachau and E. Breitbach. It was noted that new structural systems were designed and found their application in the first half of the 1980s. The systems got the name of "smart," "intelligent," or "adaptive" systems. At first the studies were started in the United States and Japan and then continued in Europe beginning in Germany. Adaptive structures consist of various elements and materials including sensors and materials with piezoelectric, electrostrictive, magnetostrictive, and electro- and magnetorheological properties. The application of sensors and the indicated materials provides an opportunity to design structures and dynamic systems adaptive to environment and external loads and their changes. Characteristic examples of the design and application of such materials, structures, and systems were given in the paper. An adaptive wing is one of them. Usually the profile of an aircraft wing is designed to be optimal for certain preset

conditions. As a rule, these are the conditions of take-off and landing of an aircraft. In practice, the wing turns out to be nonoptimal in other conditions during a flight. "Smart" and "adaptive" materials open opportunities and offer ways to design an adaptive wing with the profile changing together with changing conditions of a flight. Adaptive wing profiles may be useful and effective for the solution of the problem of the reduction of aerodynamic noise and vibration.

An example of the papers devoted to the field of "wavelets" that were presented at the Congress is the paper "Computation of Time-Varying Cross-Spectra" by D. Newland. The author is a well-known expert in the field of wavelet analysis. Wavelet analysis is a relatively new type of signal processing that has essential advantages over traditional techniques and is applicable to the analysis of nonstationary signals. The first papers on wavelet analysis were published in the middle of the 1980s. A wavelet is a function describing a damped vibration. Some Russian mathematicians prefer to use the term "splash analysis" instead of "wavelet analysis" since the Russian word for "splash" corresponds to the English word "wavelet" best of all. The average value of a wavelet function is equal to zero. Wavelet functions can form a complete orthonormal system of functions. A wavelet function can be the kernel of an integral transformation, and in this case we can talk about an integral wavelet transformation. An integral wavelet transformation, or in the terms of some Russian mathematicians, an integral splash transformation, is convenient for the analysis of nonstationary signals. In contrast to the integral Fourier transformation, it is possible to monitor the variability of the fine time structure of a process with the help of a wavelet transformation. An original technique of the computation of the cross-spectral power of nonstationary (transient) signals was described in the paper by Newland. The author showed that it was possible to solve the fundamental problem of the processing of nonstationary signals, i.e., to determine in the process of analysis of two simultaneously detected nonstationary signals the peak of the amplitude and phase variation in time from the power cross-spectrum. It was noted that the suggested technique might be applied for the analysis of chaotic oscillations in nonlinear dynamic systems and structures.

The 7th International Congress on Acoustics and Vibration was well organized. An excursion program was offered to the participants and those accompanying them. The decision was made to have the 8th International Congress on Acoustics and Vibration in Hong Kong (China).

L. M. Lyamshev

Translated by M. Lyamshev

Acoustical Physics, Vol. 47, No. 1, 2001, pp. 16–21. Translated from Akusticheskiĭ Zhurnal, Vol. 47, No. 1, 2001, pp. 22–28.
Original English Text Copyright © 2001 by Barja, Mansanares, Silva, Magalhães, Alves.

Photosynthesis in Eucalyptus Studied by the Open Photoacoustic Technique: Effects of Irradiance and Temperature[1]

P. R. Barja*, A. M. Mansanares*, E. C. da Silva*, A. C. N. Magalhães, and P. L. C. A. Alves*****

** Instituti de Fisica Gleb Wataghin, Universidade Estadual de Campinas, Unicamp, Cx.P.6165, 13083-970, Campinas, SP, Brazil*
e-mail: barja@ifi.unicamp.br; manoel@ifi.unicamp.br; ecorrea@ifi.unicamp.br

*** Instituto de Biologia, Universidade Estadual de Campinas, Unicamp, Cx.P.6109, 13083-970, Campinas, SP, Brazil*

**** Depto. de Biologia Aplicada, FCAVJ-Unesp, 14870-000, Jaboticabal, SP, Brazil*
e-mail: plalves@fcav.unesp.br

Received March 10, 2000

Abstract—This work demonstrates the usefulness of the Open Photoacoustic Cell Technique to study the effects of irradiance and temperature on photosynthesis. *In vivo* and *in situ* photosynthetic induction measurements were performed in three different species of eucalyptus plants (*E. grandis*, *E. urophylla*, and *E. urograndis*) previously dark-adapted at different temperatures. Photosynthetic activity curves were built as a function of light intensity, indicating the occurrence of photosynthesis saturation. *E. urograndis* presented higher photosynthetic activity than the other species, especially at low temperature, indicating its tolerance to stress conditions. The incidence of background saturation light of various intensities allowed the *in situ* study of photoinhibition in eucalyptus plants through open photoacoustics. *© 2001 MAIK "Nauka/Interperiodica".*

INTRODUCTION

In the past few years, the photoacoustic technique has been employed in the study of photosynthesis [1, 2]. In this method, a leaf is usually enclosed in a cell and exposed to a monochromatic, modulated light beam. The principle of the photoacoustic technique relies on the light absorption by the sample (plant leaf) with consequent release of heat and oxygen at the same frequency of the light beam, as the photoacoustic signal reflects the pressure oscillation in the cell. Detected by a microphone, this pressure oscillation is a consequence of (i) the gas–sample interface temperature oscillation (which produces a periodic variation of the gas temperature inside the cell) and (ii) the gas exchange between the sample and the cell (due to the photosynthetic activity of the leaf). The sample expansion because of gas production can also change the gas pressure inside the cell, with the leaf acting as an acoustic piston itself [3].

As the absorbed light energy is converted into chemical energy and heat in the photosynthetic process, the quantum yield determination is an important application of the technique in photosynthetic investigations. This capability of the technique was predicted by Malkin and Cahen [4], with experimental results in both chloroplast suspensions [5] and leaf sections [6]. Recent applications include measurements of energy storage in Photosystems I and II [7] and photosynthetic activities of plants under chemical stress [8–11].

The photoacoustic signal carries information on optical and thermal properties of the sample, parameters which appear on both the amplitude (magnitude) and the phase (delay with respect to the light absorption) of the signal. The signal phase carries information about the delay between light excitation and pressure change, which depends on the coefficients of heat and oxygen diffusion. Moreover, the signal phase also depends on the time constants of the various steps in the electron transfer chain (delayed generation of heat). Poulet *et al.* [12] determined the oxygen diffusion coefficient and estimated the limiting time constant on the donor side of Photosystem II. A more complete model on mass diffusion was discussed by Korpium and Osiander [13]. Photosynthetic induction in dark-adapted plants was also investigated, and fast photoacoustic transients were registered [14, 15].

In the first works using photoacoustics to study plant photosynthesis, the leaf was cut and closed in the cell. This began to change with the development of the Open Photoacoustic Cell (OPC) [16–18], a compact device formed by a commercial electret microphone that uses its own chamber as the acoustic cell, with the sample acting as one of the walls. As the sample itself closes the chamber, it is not necessary to cut a leaf disc nor to detach the leaf from the plant for measurements. Therefore, the OPC avoids dehydration of the sample and minimizes changes in the photoacoustic chamber atmosphere, because part of the leaf remains exposed to the outside, capturing external CO_2. These advantages

[1] This article was submitted by the authors in English.

make the OPC detection a direct way to study the effects of parameters like temperature and irradiance in the photosynthesis of plant leaves. Several studies on photosynthesis were already performed with the OPC, such as energy storage determination [19], the effect of dehydration in soybean leaves [20], and evidence of heterosis in maize hybrids through photosynthetic induction measurements [21].

Eucalyptus is an important culture due to its potential value in the paper and cellulose industries. *Eucalyptus grandis* is the most cultivated species in Brazil, followed by *E. urophylla*, which has a lower growing rate but is more tolerant to water-limited conditions [22]. The crossing of these two species generated the fast growing *E. urograndis*, apparently efficient in dry environments [23]. However, since it was recently developed, this hybrid has not been fully characterized until now [24] in terms of adaptation to stressing conditions, particularly high irradiance and chilling temperatures. As the adaptability of a plant to different conditions can be evaluated through its photosynthetic parameters and considering that stress can affect the productivity of eucalyptus, the study of its adaptability to stressing conditions is justified by the necessity of improving eucalyptus agriculture [25, 26].

This work shows the influence of temperature and irradiance on the photosynthesis of *E. grandis*, *E. urophylla*, and *E. urograndis* leaves *in vivo* and *in situ* using the Open Photoacoustic Cell Technique. As far as we know, it was the first time that the OPC technique was applied to study the photosynthesis of tree leaves like eucalyptus leaves.

MATERIALS AND METHODS

Photoacoustic Setup

The experimental setup used for photoacoustic measurements has two light sources: a xenon arc lamp (Oriel, mod. 6128, 1000 W) and a tungsten lamp (Ushio/ELC, 250 W). A chopper (PAR, mod. 192) and a monochromator (Oriel, mod. 77250) are used in front of the xenon lamp in order to obtain modulated light of a determined wavelength (680 nm). Optical filters limit the light of the tungsten lamp to the visible part of the spectrum. A double-branched optical cable is used to guide each light beam up to the photoacoustic cell. The chopper and the photoacoustic cell microphone are connected to a lock-in amplifier (PAR-EG&G, mod. 5210) that measures the amplitude and phase of the microphone signal. The lock-in is connected through a GPIB interface to a microcomputer for data acquisition. The typical lock-in time-constant used is one second, which gives a time response of the setup clearly sufficient for our purposes.

The OPC has already been described in the literature [17–20]. The device is essentially an electret microphone, with the photoacoustic (microphone) chamber being closed by the leaf itself. This microphone is composed by a metallized electret diaphragm and a metal plate separated by an air gap. A resistor connects the metallic part of the membrane to the metal backplate. Pressure oscillation in the air chamber deflects the membrane, thus generating a voltage across the resistor. The sensitivity is of about 10 mV/Pa.

Plant Material

Eucalyptus plants were cultivated in small pots under 50% shade conditions. Fifty-day-old seedlings were transferred to the laboratory where they were dark-adapted at two different temperatures, 10 and 25°C (ambient), for 24 h. After this period, plants were taken to the experimental setup and a selected part of an undetached leaf was fixed to the OPC and exposed to the modulated light beam (680 nm, 17 Hz, 8 W/m^2) coming from the optical cable. Fully expanded leaves of the second pair were selected for measurements (performed at ambient temperature). The photoacoustic signal (amplitude and phase) was recorded as a function of time, with intervals of two seconds between points. About 30 plants were measured for each species and temperature in the photosynthetic induction experiment. Measurements were performed in plants previously adapted at two temperatures to investigate the influence of the temperature treatment on the readaptation to light conditions.

Performing induction measurements for different light intensities, the steady-state photosynthesis rate was used to build photosynthetic activity curves, which give the amplitude of the oxygen evolution component as a function of irradiance. Five measurements were performed for each species (all plants previously adapted to 25°C) and for a given irradiance.

In the photoinhibition experiment, for a given species adapted to one temperature, about five measurements were performed for each light intensity. The effects of irradiance were evaluated by comparing the photoacoustic signal before and after plant exposure to different intensities of background saturation light for about 15 min.

RESULTS AND DISCUSSION

Photosynthetic Induction

A typical photosynthetic induction curve for eucalyptus is presented in Fig. 1. This figure shows that the photoacoustic amplitude presents initially a fast transient ($0 < t < 20$ s), followed by a slower one, reaching the steady state after about two minutes. The first transient expresses a rapid increase in the signal amplitude, followed by a fast decrease back to the initial level, while the second transient represents a continuous increase of the signal until the steady state is reached.

Since seedlings were dark-adapted for a long period (24 h) before measurements, their photosynthetic reaction centers were deactivated [2]. Therefore, the initial

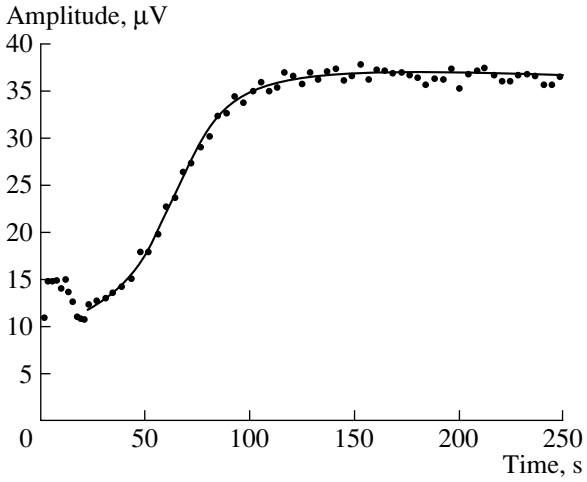

Fig. 1. Typical photosynthetic induction curve obtained for *E. grandis* previously treated at 10°C for 24 h. Measurement was carried out at ambient temperature. Modulated light characteristics: λ = 680 nm, modulation frequency of 17 Hz, and intensity of 8 W/m^2. Dots represent measured points and the solid line the best fit to Eq. (1) (many data points were suppressed to avoid overcrowding).

level of the photoacoustic signal corresponds to temperature oscillation (thermal component) [6]. As the reaction centers readapt to light conditions, photosynthesis starts and the production of oxygen takes place. The corresponding variation in the photoacoustic signal is the gas component.

Concerning the fast transient, this behavior has been reported in the last twenty years [27]. The initial stage of the photosynthetic induction seems to be limited by metabolite levels mainly related to the inorganic phosphate availability in the intercellular medium. Actually, the literature reports two possible explanations for this transient: the first one is based on a rapid photoreduction of both glycerate-3-P and inorganic phosphate stored during the dark period [28], while the second relates the transient to an initial gas uptake immediately after light incidence [14]. The fast transient was also observed when similar measurements were performed in spinach leaves [28]; it did not appear in the photosynthetic induction of maize leaves [21].

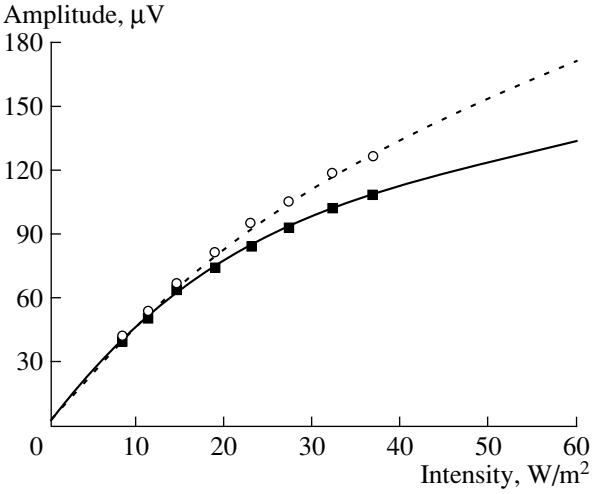

Fig. 2. Photosynthetic activity saturation curves for *E. urophylla* (solid line) and *E. urograndis* plants (dotted line). Each data set corresponds to the average over 5 measurements. *E. grandis* saturation curve is similar to *E. urophylla* curve. All plants were adapted to ambient temperature (25°C). Modulated light characteristics: λ = 680 nm, modulation frequency of 17 Hz.

Since the gas component of the photoacoustic signal is related to the photosynthetic rate, an analysis of the signal amplitude and the time needed to achieve the steady state becomes appropriated. To do this, the measured induction curves (removing the fast transient) were adjusted by the logistic function [21]

$$S(t) = S_0 + \Delta S \frac{\exp[(t - t_0)/\Delta t]}{[1 + \exp[(t - t_0)/\Delta t]]}, \qquad (1)$$

where S_0 is the initial value of the photoacoustic signal, ΔS is the signal excursion to the saturation value which takes place during the time interval Δt, and t_0 is the instant at which $(S - S_0)/\Delta S = 0.5$.

The table shows values obtained for these parameters. The results reveal important characteristics of the eucalyptus leaves. In particular, Δt and t_0 are very short for eucalyptus in comparison with other plants like maize [21] and coffee [data not published]. For both maize and coffee leaves, Δt is in the range of a few minutes and t_0 can be as high as 45 min, while the same parameters in eucalyptus leaves reach values around 20 s (Δt) and 2 min (t_0). These differences may be associated to the efficiency of the Light Harvesting Complex (LHC II). Since eucalyptus plants were grown under 50%-shade conditions, their light collecting systems tend to be more efficient than those of maize and coffee (cultivated under full sunlight).

Comparison among the three species of eucalyptus shows that, especially for 10°C adaptation, ΔS is superior for *E. urograndis*. This result confirms the superiority of this species and its higher tolerance to low temperature. Regarding that the *E. urograndis* hybrids originate from the crossing of the other two (*E. urophylla* and *E. grandis*), this result resembles that observed by da Silva *et al*. [21] for maize hybrids when compared to their imbreds. In that case, maize hybrids had shown superior photosynthetic performance than imbreds.

Saturation Curves

Figure 2 shows curves of the photosynthetic activity as a function of irradiance for *E. urograndis* and *E. urophylla* samples adapted to 25°C. The *E. grandis* curve is similar to the curve for *E. urophylla*. From these data, it can be seen that *E. urograndis* plants present a much higher photosynthetic activity than

plants of the other species. These results corroborate those obtained in photosynthetic induction measurements in which the superiority of *E. urograndis* was less clear due to the low irradiance (8 W/m^2) then employed. The fact that photosynthetic activity in *E.urograndis* plants saturates at a higher light intensity indicates that this is the species that can best adapt to high irradiance environments.

Photoinhibition

It is known that photoinhibition occurs when the plant is unable to dissipate excessive light energy and starts accumulating highly oxidizing free radicals. Photoinhibition is commonly associated with a decrease in the photosynthetic quantum efficiency; as a consequence, there is a reduction in the production of carbohydrates. The association of high irradiance and low temperature or other kinds of stress makes the plant more susceptible to photoinhibition [29].

Figure 3 shows a typical measurement performed to investigate photoinhibition in eucalyptus plants. These measurements followed the same procedure adopted in photosynthetic induction. Once the steady state was achieved, continuous white light with a high intensity was added to the monochromatic modulated light in order to saturate photosynthesis. The conversion efficiency of modulated light to chemical energy then goes to zero and the oxygen starts to be liberated continuously (Fig. 3, $t > 350$ s). White light was switched off after 1000 s, while modulated light was kept on continuously. Figure 3 shows the modulated oxygen evolution being restored (partially or totally) after $t \simeq 1350$ s.

After the white light was interrupted, the gas component increased slowly up to a steady state, with a time-constant of about 100 s. This slow recovering capability to respond to modulated light indicates the existence of a readaptation mechanism to low light intensity. This mechanism might be related to the consumption of products accumulated during exposure to white light, as well as to the recombination of free radicals hence produced. When compared to the photoacoustic signal amplitude immediately before the white light incidence, the amplitude after achieving the new steady state depends on the white light intensity itself. For low intensities, this relative photosynthetic rate is about one (dashed curve in Fig. 3), which means that photoinhibition was not observed. For high intensities, however, the ratio is lower than one (solid curve in Fig. 3), characterizing photoinhibition.

Figure 4 shows the results for the relative photosynthetic rate, as defined above, for the three species and two temperatures. Each point represents the average over about five measurements. It is known that low temperature and high irradiance are concurrent stress conditions to produce photoinhibition. No differentiation was observed between species. From Fig. 4 one can see that all measured eucalyptus samples were photoinhibited for irradiances of about 350 W/m^2 or higher. This value corresponds to full sunlight incidence in an open field. Actually, Long *et al.* [29] have shown that exposure to full sunlight can result in a slowly reversible diurnal decrease in PSII efficiency of plants even in near-optimal conditions. Furthermore, our results are compatible with values found in the literature for other plants [8] and for eucalyptus species [30].

Finally, it can be observed that the relative rate is even higher than one for 100 and 200 W/m^2 background light intensities—values which do not fully saturate photosynthesis. Under such conditions, photoinhibition does not take place, and indeed an optimization of the photosynthetic process is achieved. This result indicates that, when photosynthesis is induced by irradiances below the assimilation capacity of the sample,

Mean values of the adjusted parameters by Eq. (1) S_0, ΔS_0, t_0, and Δt for the three eucalyptus species treated at 25 and 10°C for 24 h before measurement. The average was taken over about thirty ($n = 30$) measurements for each species and temperature. The error was determined as the standard sample deviation σ_{n-1} divided by $n^{1/2}$.

Parameter	*E. grandis*		*E. urophylla*		*E. urograndis*	
	25°C	10°C	25°C	10°C	25°C	10°C
S_0, μV	8 ± 1	7 ± 1	11 ± 1	11 ± 1	10 ± 1	9 ± 1
ΔS, μV	31 ± 2	29 ± 2	28 ± 3	26 ± 2	33 ± 2	34 ± 2
t_0, s	89 ± 4	64 ± 2	96 ± 3	78 ± 4	88 ± 4	72 ± 3
Δt, s	22 ± 2	18 ± 1	22 ± 1	26 ± 2	21 ± 2	23 ± 2

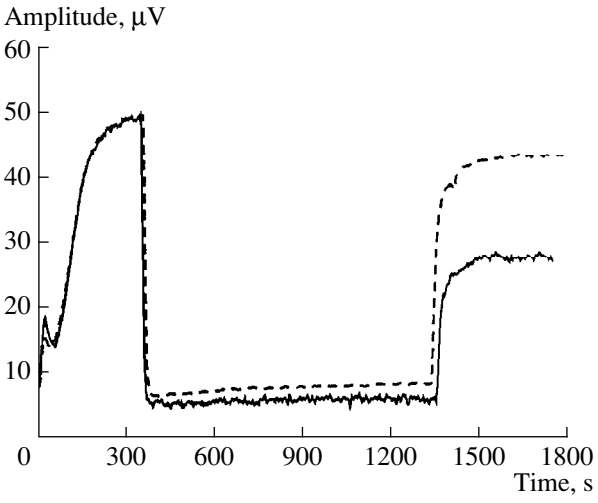

Fig. 3. Typical measurement carried out to evaluate the photoinhibition phenomenon (two *E. grandis* plants maintained at 25°C before measurements). Photosynthesis is induced on a dark-adapted plant until the steady state is reached. Continuous white light is then switched on at $t \simeq 350$ s (off at $t \simeq 1350$ s). Modulated light characteristics: $\lambda = 680$ nm, modulation frequency of 17 Hz, and intensity to 8 W/m^2. White light intensities: 670 W/m^2 for the solid curve and 360 W/m^2 for the dashed one.

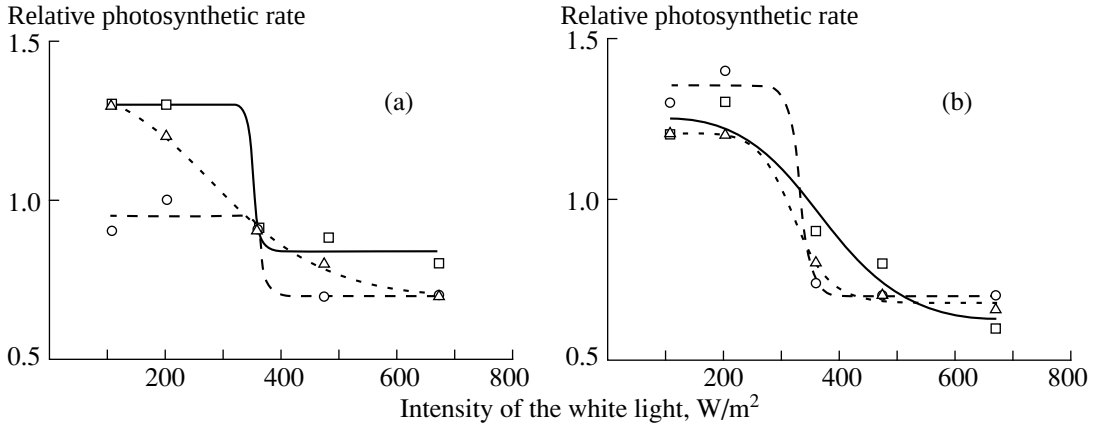

Fig. 4. Photosynthetic activity after 1000 s of white light irradiation, divided by the photosynthetic activity before the white light incidence, as a function of the white light intensity. Each point represents the average of about 5 measurements. *E. grandis*: squares and solid lines, *E. urophylla*: circles and dashed lines; *E. urograndis*: triangles and dotted lines; (a) plants treated at 10°C for 24 h; (b) plants maintained at 25°C. The lines represent the best fit to a logistic S-shaped curve. The photoinhibition threshold can be observed around 350 W/m^2 for all species at both temperatures.

the steady state does not correspond to the maximal photochemical quantum efficiency.

SUMMARY

This study shows the usefulness of the Open Photoacoustic Technique in investigating the photosynthetic behavior of tree leaves. Eucalyptus leaves showed a faster photosynthetic induction when compared to that reported for plants like maize and coffee. The results obtained reveal that *E. urograndis* samples presented a higher photosynthetic activity than plants of the other eucalyptus species studied; this is supported by their photosynthesis saturation curves. The higher activity observed for *E. urograndis* plants is more pronounced after adaptation to 10°C.

Comparison between the photosynthetic activity before and after exposure to high intensities of white light allowed the determination of the threshold for photoinhibition, which is of about 350 W/m^2 for all species studied.

This work shows that the Open Photoacoustic Cell is an adequate technique for the study of photosynthesis in living plant samples. With the OPC, one can perform comparative analysis between plants from different species, as well as the study of plants submitted to different stress conditions. Besides the dependence on the temperature and light treatment of the samples, the photoacoustic signal may also depend on other experimental parameters such as leaf morphology, gas atmosphere, etc., allowing a wide range of investigations. Such measurements must be performed *in vivo* and *in situ*, for suspensions of chloroplasts cannot reproduce the behavior of living samples and the response of detached leaves can be distorted by dehydration.

ACKNOWLEDGMENTS

The authors thank the Brazilian agencies CAPES, CNPq, and FAPESP for financial support and Votorantim Celulose e Papel Ltda. for supplying the samples.

REFERENCES

1. D. C. Fork and S. K. Herbert, Photochem. Photobiol. **57**, 207 (1993).
2. S. Malkin and O. Canaani, Annu. Rev. Plant Physiol. Plant Mol. Biol. **45**, 493 (1994).
3. F. A. McDonald and G. C. Wetsel, Jr., J. Appl. Phys. **49**, 2313 (1978).
4. S. Malkin and D. Cahen, Photochem. Photobiol. **29**, 803 (1979).
5. N. Lasser-Ross, S. Malkin, and D. Cahen, Biochim. Biophys. Acta **593**, 330 (1980).
6. G. Bults, B. A. Horwitz, S. Malkin, and D. Cahen, Biochim. Biophys. Acta **679**, 452 (1982).
7. K. Veeranjaneyulu, M. Charland, D. Charlebois, and R. M. Leblanc, Photosynth. Res. **30**, 131 (1991).
8. M. Havaux and M. Eyletters, Z. Naturforsch. C **46**, 1038 (1991).
9. G. Ouzounidou, R. Lannoye, and S. Karataglis, Plant. Sci. (Limerick, Irel.) **89**, 221 (1993).
10. J. Szurkowski and Z. Tukaj, Arch. Environ. Contam. Toxicol. **29**, 406 (1995).
11. G. Ouzounidou, Plant. Sci. (Limerick, Irel.) **113**, 229 (1996).
12. P. Poulet, D. Cahen, and S. Malkin, Biochim. Biophys. Acta **724**, 433 (1983).
13. P. Korpiun and R. Osiander, in *Springer Series in Optical Science, Photoacoustic and Photothermal Phenomena III*, Ed. by D. Bicanic (Springer, Berlin, 1992), pp. 619–627.
14. S. Malkin, Planta **171**, 65 (1987).
15. W. J. Vredenberg, J. F. H. Snel, W. F. Buurmeijer, and H. Boumans, Photosynthetica **27**, 207 (1992).

16. L. F. Perondi and L. C. M. Miranda, J. Appl. Phys. **62**, 2955 (1987).
17. M. V. Marquezini, N. Cella, A. M. Mansanares, *et al.*, Meas. Sci. Technol. **2**, 396 (1991).
18. A. C. Pereira, G. de O. Neto, H. Vargas, *et al.*, Rev. Sci. Instrum. **65**, 1512 (1994).
19. P. R. Barja and A. M. Mansanares, Instrum. Sci. Technol. **26** (2–3), 209 (1998).
20. A. C. Pereira, M. Zerbetto, G. C. Silva, *et al.*, Meas. Sci. Technol. **3**, 931 (1992).
21. W. J. da Silva, L. M. Prioli, A. C. N. Magalhães, *et al.*, Plant. Sci. (Limerick, Irel.) **104**, 177 (1995).
22. S. T. Blake, Austrobaileya **1**, 7 (1977).
23. M. T. Inoue and S. Oda, in *Proceedings of the International Symposium on Forest Tree Physiology, Nancy, 1988*, p. 69.
24. L. D. Pryor, E. R. Williams, and B. V. Gunn, Aust. Syst. Bot. **8**, 57 (1995).
25. T. Blake, E. Bevilacqua, and M. M. Barbosa, IPEF **40**, 5 (1988).
26. M. T. Inoue, J. D. Vieira, and G. Correa, in *VI Congresso Florestal Brasileiro, Campos de Jordão, 1990*, p. 493.
27. Y. Inoue, A. Watanabe, and K. Shibata, FEBS Lett. **101**, 321 (1979).
28. R. T. Prinsley and R. C. Leegood, Biochim. Biophys. Acta **849**, 244 (1986).
29. S. P. Long, S. Humphries, and P. G. Falkowski, Annu. Rev. Plant Physiol. Plant Mol. Biol. **45**, 633 (1994).
30. E. Ögren and J. R. Evans, Aust. J. Plant Physiol. **19**, 223 (1992).

Acoustical Physics, Vol. 47, No. 1, 2001, pp. 22–28. Translated from Akusticheskiĭ Zhurnal, Vol. 47, No. 1, 2001, pp. 29–36.
Original Russian Text Copyright © 2001 by Vershubskiĭ, Parygin, Rezvov.

Acousto-Optic Interaction of Diverging Gaussian Beams in Anisotropic Media

A. V. Vershubskiĭ, V. N. Parygin, and Yu. G. Rezvov

Moscow State University, Vorob'evy gory, Moscow, 119899 Russia
e-mail: parygin@osc162.phys.msu.su

Received May 16, 2000

Abstract—A strong acousto-optic interaction of bounded light and sound beams of a Gaussian shape is considered for different geometries permitting long-term interaction. The anisotropic spreading of an acoustic beam in the course of its propagation is taken into account. The spectra of light beams are described by a Gaussian-polynomial expression, and a set of differential equations is derived which allows one to describe various geometries of acousto-optic diffraction. It is demonstrated that the transmission function of an acousto-optic cell essentially depends on the ratio between the dimensions of the light and sound beams and on the angle between the propagation direction of the diffracted beam and that of the incident beam. The degree of spreading of the acoustic beam noticeably affects the suppression of the transmission side lobes. © *2001 MAIK "Nauka/Interperiodica".*

INTRODUCTION

One of interesting problems of acousto-optics is the collinear diffraction of light by a traveling acoustic wave, because this kind of propagation creates the conditions for obtaining very large lengths of interaction of light and sound. A long-term interaction can be observed in acoustically anisotropic media with a pronounced drift of a sound beam even in the case of a noncollinear propagation of light and sound when only the directions of the energy propagation in the incident beams coincide. Such a geometry of the acousto-optic interaction is called quasi-collinear. Today, it is widely used in designing acousto-optic filters.

The theory of acousto-optic interaction usually operates with plane sound and light waves [1–3]. As a rule, a bounded acoustic beam is assumed to have a plane wavefront and the light wave is considered to be unbounded. At the same time, experimental acousto-optic devices (modulators, deflectors, filters, and spectrum analyzers) are designed utilizing acoustic and light beams of finite dimensions with a considerable inhomogeneity over the cross-section and along the propagation direction. The propagation of such beams is connected with changes in the phase distribution in the plane of the wavefront.

There is a series of papers devoted to the investigation of the particular features of weak and strong interactions of wave beams and packets in the case of the drift and spreading of beams in an anisotropic medium [4–7]. These effects become significant in the case of a large interaction length, which is characteristic of collinear and quasi-collinear geometries of interaction. In the case of a collinear interaction, the wave vectors and the group velocities of all interacting beams coincide. A high selectivity is attained in this case, but such an interaction is possible only along certain directions in crystals, which limits the variety of materials suitable for designing effective acousto-optic devices. In the case of the quasi-collinear geometry, which was first considered by Parygin *et al*. [8] and Voloshinov [9], the group velocities of sound and incident light are parallel, whereas the wave vectors of all interacting waves are not collinear in the general case. This form of diffraction can be efficiently realized in many different directions. However, in this case, a diffracted light beam can propagate at a noticeable angle to the incident beam.

This paper is devoted to the theoretical study of the effect of the indicated particular feature on the characteristics of the collinear and quasi-collinear diffraction of Gaussian beams with allowance made for their drift and divergence.

THEORY OF ACOUSTO-OPTIC INTERACTION OF WEAKLY DIVERGENT BEAMS

Let the region of interaction be a plane layer, $0 \le z \le l$, of a nonmagnetic transparent dielectric. Here, z is the coordinate measured along the unit vector of the normal $\mathbf{n}$. The electric field strength $\mathbf{E}(\mathbf{R}, t)$ within the layer is consistent with the equation following from the Maxwell equations:

$$\left[\nabla^{\times}\nabla^{\times} + \frac{1}{c^2}\varepsilon^0\frac{\partial^2}{\partial t^2}\right]\mathbf{E}(\mathbf{r}, t, z) = -\frac{1}{c^2}\frac{\partial^2}{\partial t^2}[\Delta\varepsilon(\mathbf{r}, t, z)\mathbf{E}(\mathbf{r}, t, z)], \quad (1)$$

1063-7710/01/4701-0022$21.00 © 2001 MAIK "Nauka/Interperiodica"

where c is the light velocity in vacuum; ε^0 is the permittivity tensor of an unperturbed medium; $\Delta\varepsilon(\mathbf{r}, t, z)$ is its perturbation in the acoustic field; and $\mathbf{r} = -\mathbf{n}^{\times}\mathbf{n}^{\times}\mathbf{R}$ is the two-dimensional vector representing the tangential component of the radius-vector $\mathbf{R}$ and, hence, satisfying the condition $\tilde{\mathbf{r}}\,\mathbf{n} = 0$.

We use the following symbols to denote the operations with vectors and tensors: $\nabla^{\times}\mathbf{a}$ means curl $\mathbf{a}$, $\mathbf{a}^{\times}\mathbf{b}$ means the vector product of the vectors $\mathbf{a}$ and $\mathbf{b}$, and $\tilde{\mathbf{a}}\,\mathbf{b}$ is their scalar product, where $\tilde{\mathbf{a}}$ is the row vector, as distinct from the column vector $\mathbf{a}$. The notation $\tilde{\mathbf{a}}\,\mathbf{T}\mathbf{a}$ shows that the second-rank tensor $\mathbf{T}$ is contracted with the vectors $\tilde{\mathbf{a}}$ and $\mathbf{a}$. Finally, the notation of the type $\tilde{\mathbf{T}}\,\mathbf{a}^n$ means that the n-rank tensor $\mathbf{T}$ is contracted with n vectors $\mathbf{a}$. Such a notation was introduced in the monograph by Balakshiĭ *et al.* [2].

Let us apply the Fourier transform to Eq. (1) with respect to the variable $\mathbf{r}$:

$$\left[\left(j\mathbf{k}_\tau + \mathbf{n}\frac{\partial}{\partial z}\right)^{\times}\left(j\mathbf{k}_\tau + \mathbf{n}\frac{\partial}{\partial z}\right)^{\times} + \frac{\varepsilon^0}{c^2}\frac{\partial^2}{\partial t^2}\right]\mathbf{E}(\mathbf{k}_\tau, t, z) = -\frac{1}{c^2}\frac{\partial^2}{\partial t^2}[\Delta\varepsilon(\mathbf{k}_\tau, t, z)] \otimes [\mathbf{E}(\mathbf{k}_\tau, t, z)], \tag{2}$$

where $\mathbf{k}_\tau = -\mathbf{n}^{\times}\mathbf{n}^{\times}\mathbf{k}$ is the tangential component of the wave vector, j is the imaginary unit, and the sign $\otimes$ means the convolution operation with respect to the variable $\mathbf{k}_\tau$ (in this case, the functions in square brackets are subjected to the convolution).

In the case of an anisotropic diffraction, each spectral component of the field is a sum of two plane waves of different polarizations and frequencies:

$$\mathbf{E}(\mathbf{k}_\tau, t, z) = \mathbf{e}_t(\mathbf{k}_\tau)E_t(\mathbf{k}_\tau, z)\exp(jk_{tz}z - \omega_t t) + \mathbf{e}_d(\mathbf{k}_\tau)E_d(\mathbf{k}_\tau, z)\exp(jk_{dz}z - \omega_d t). \tag{3}$$

Here, $\mathbf{e}_t$ and $\mathbf{e}_d$ are the unit vectors of polarization and ω_t and ω_d are the frequencies of the light wave. The subscripts t and d correspond to transmitted and diffracted light, respectively.

The dependence of the amplitude of each partial wave in Eq. (3) on z expresses the essence of the coupled-mode approach. According to this approach, the spectra of transmitted and diffracted light are assumed to change slowly in the course of the propagation, which allows us to omit the second-order derivatives with respect to z in our calculations. Following this concept, we assume that the wave vectors $\mathbf{k}_\alpha = \mathbf{k}_\tau + k_{\alpha z}\mathbf{n}$ (where $\alpha = t, d$) satisfy the dispersion relation for an unperturbed medium, so that $(-\mathbf{k}_\alpha^{\times}\mathbf{k}_\alpha^{\times} - c^{-2}\omega_\alpha^2\varepsilon^0)\mathbf{e}_\alpha^0 = 0$. We also assume that, in a perturbed medium, the polarization vectors change weakly, and this change can be ignored. Therefore, we will set $\mathbf{e}_\alpha(\mathbf{k}_\tau)$ equal to $\mathbf{e}_\alpha^0(\mathbf{k}_\tau)$. The perturbation of the permittivity tensor under the effect of the sound field has the form $\Delta\varepsilon(\mathbf{r}, t, z) = -0.5\varepsilon^0\mathbf{p}\nabla(\mathbf{A} + \mathbf{A}^*)\varepsilon^0$, where $\mathbf{A}(\mathbf{r}, z, t)$ is the field of displacements of the sound beam, $\mathbf{p}$ is the tensor of elastooptic constants, and $\mathbf{A}^*$ is a complex-conjugate expression.

The spectral transformation for $\Delta\varepsilon(\mathbf{r}, t, z)$ yields

$$\Delta\varepsilon(\mathbf{k}_\tau, t, z) = -0.5\varepsilon^0\mathbf{p}\left(j\mathbf{k}_\tau + \mathbf{n}\frac{\partial}{\partial z}\right) \times [\mathbf{A}(\mathbf{k}_\tau, z)e^{-j\omega_s t} + \mathbf{A}^+(\mathbf{k}_\tau, z)e^{j\omega_s t}]\varepsilon^0. \tag{4}$$

Here, $\omega_s = 2\pi f_s$, f_s is the ultrasonic frequency, and the superscript "+" has the following meaning: $\mathbf{F}^+(\mathbf{k}_\tau) = \mathbf{F}^*(-\mathbf{k}_\tau)$.

Taking into account the weak absorption of sound in the medium, we write the sound spectrum in an arbitrary plane z in the form $\mathbf{A}(\mathbf{k}_\tau, z) = \mathbf{a}(\mathbf{k}_\tau)A(\mathbf{k}_\tau)\exp((jk_{sz} - \delta)z)$, where $\mathbf{a}$ is the unit vector of the polarization of the plane sound wave, k_{sz} is the projection onto the normal of the wave vector, and δ is the parameter determining the sound attenuation.

Both sound and optical fields have narrow spectral distributions in many problems of acousto-optics. We introduce the centered spectrum of a sound field of unit amplitude $U(\mathbf{f}) = A_0^{-1}A(\mathbf{k}_{s0\tau} + \mathbf{f})$. Here, $\mathbf{f} = \mathbf{k}_\tau - \mathbf{k}_{s0\tau}$, $\mathbf{k}_{s0\tau}$ is the tangential component of the central sound wave in a crystal, and A_0 is the amplitude of the sound shift at $z = 0$. Let the coordinate z be normalized to the cell length l (along the normal to the input plane) so that the interaction region lies within the interval $0 \le z \le 1$.

A detailed theory of the acousto-optic interaction of beams is given in our previous paper [10]. Substituting Eqs. (3) and (4) into Eq. (2) and omitting the intermediate mathematical transformations, we obtain the system describing a strong acousto-optic interaction (the +1 diffraction order):

$$\frac{\partial U_d(\mathbf{f}, z)}{\partial z}\Gamma_d = \frac{q_{d0}l}{2}[U(\mathbf{f})\exp[-0.5jzl\tilde{\mathbf{f}}\mathbf{w}\mathbf{f}]] \otimes [U_t(\mathbf{f}, z)\Gamma_t]\exp[(j\eta - \delta)lz],$$
$$\frac{\partial U_t(\mathbf{f}, z)}{\partial z}\Gamma_t = -\frac{q_{t0}l}{2}[U^+(\mathbf{f})\exp[0.5jzl\tilde{\mathbf{f}}\mathbf{w}\mathbf{f}]] \otimes [U_d(\mathbf{f}, z)\Gamma_d]\exp[(-j\eta - \delta)lz], \tag{5}$$

where $\Gamma_\alpha = \exp[-jzl((\tilde{\mathbf{s}}_\alpha - \tilde{\mathbf{s}})\mathbf{f} + 0.5\tilde{\mathbf{f}}\,\mathbf{w}_\alpha\mathbf{f})]$ and $\alpha = t, d$.

In Eqs. (5), the acousto-optic mismatch is $\eta = k_{t0z} + k_{s0z} - k_{d0z}$, $\mathbf{k}_{d0\tau} = \mathbf{k}_{t0\tau} + \mathbf{k}_{s0\tau}$, and $\omega_d = \omega_t + \omega_s$; the coefficients $q_{\alpha 0}$ determine the acousto-optic coupling between the central plane waves. The vectors $\mathbf{s}$ and $\mathbf{s}_\alpha$ and the matrices $\mathbf{w}$ and $\mathbf{w}_\alpha$ determine the dependences $k_{sz}(\mathbf{f})$ and $k_{\alpha z}(\mathbf{f})$ in the parabolic approximation: $k_{sz} = \tilde{\mathbf{s}}\,\mathbf{f} + 0.5\tilde{\mathbf{f}}\,\mathbf{w}\mathbf{f}$ and $k_{\alpha z} = \tilde{\mathbf{s}}_\alpha\,\mathbf{f} + 0.5\tilde{\mathbf{f}}\,\mathbf{w}_\alpha\mathbf{f}$.

Let the distribution of the displacements at the transducer surface ($z = 0$) have the Gaussian form: $A(\mathbf{r}) = A_0\exp\left\{-\frac{1}{2}\tilde{\mathbf{r}}\mathbf{b}^{-1}\mathbf{r}\right\}$, where $\mathbf{b}$ is the symmetric real positively determined 2×2 matrix characterizing the dimensions of the piezoelectric transducer. The spectrum of sound of unit amplitude can be written in the form

$$U(\mathbf{f}) = (2\pi)^{-3/2}\int A_0^{-1}A(\mathbf{r})\exp\{-j\tilde{\mathbf{f}}\mathbf{r}\}d\mathbf{r} = |\mathbf{b}|^{\frac{1}{2}}\exp\left\{-\frac{1}{2}\tilde{\mathbf{f}}\mathbf{b}\mathbf{f}\right\}. \quad (6)$$

Let the light amplitude at $z = 0$ have the distribution of an arbitrary form with the Gaussian envelope: $E_i(\mathbf{r}) = E_0E'(\mathbf{r}')\exp\left\{-\frac{1}{2}\tilde{\mathbf{r}}'\mathbf{b}_i^{-1}\mathbf{r}'\right\}$, $\mathbf{r}' = \mathbf{r} - \mathbf{r}_0$. Here, E_0 is the amplitude at the center of the light spot shifted by the two-dimensional vector $\mathbf{r}_0$ from the center of the sound spot and $E'(\mathbf{r}')$ is the function that does not exceed unity and describes the transverse distribution of the amplitude within the envelope. The matrix $\mathbf{b}_i$ characterizes the transverse dimensions of the light spot in the input plane.

Let us proceed to the dimensionless variables $\hat{\mathbf{f}} = \mathbf{b}^{\frac{1}{2}}\mathbf{f}$ and $\hat{\mathbf{r}} = \mathbf{b}^{-\frac{1}{2}}\mathbf{r}$. In the following calculations, we will omit the sign "^." Then, we obtain $A(\mathbf{r}) = A_0\exp\left\{-\frac{1}{2}\tilde{\mathbf{r}}\mathbf{r}\right\}$, $U(\mathbf{f}) = \exp\left\{-\frac{1}{2}\tilde{\mathbf{f}}\mathbf{f}\right\}$. The implication of such a substitution is the normalization of the characteristic transverse dimensions to the transverse dimension of the sound spot.

Let the spectrum of incident radiation at $z = 0$ be approximated by the Gaussian-polynomial expression of the sixth order: $U_i(\mathbf{f}) = \zeta_i\exp\left\{-j\tilde{\mathbf{A}}_i\mathbf{f} - \frac{1}{2}\tilde{\mathbf{B}}_i\mathbf{f}^2\right\}$, where $\mathbf{B}_i = \mathbf{b}^{-\frac{1}{2}}\mathbf{b}_i\mathbf{b}^{-\frac{1}{2}}$ is the matrix characterizing the transverse dimensions of the light beam with respect to the sound beam, $\mathbf{A}_i = \mathbf{b}^{-\frac{1}{2}}\mathbf{r}_0$ is the dimensionless shift of the beams with respect to each other in the plane $z = 0$, and $\zeta_i = C_i + \tilde{\mathbf{F}}_i\mathbf{f} + \frac{1}{2!}\tilde{\mathbf{G}}_i\mathbf{f}^2 + \frac{1}{3!}\tilde{\mathbf{H}}_i\mathbf{f}^3 + \frac{1}{4!}\tilde{\mathbf{L}}_i\mathbf{f}^4 + \frac{1}{5!}\tilde{\Pi}_i\mathbf{f}^5 + \frac{1}{6!}\tilde{\mathbf{T}}_i\mathbf{f}^6$. The complex quantities $(C, \mathbf{F}, \mathbf{G}, \mathbf{H}, \mathbf{L}, \Pi, \mathbf{T})_i$ determine the difference of the spectrum of the light beam from the Gaussian form.

Let the spectra of transmitted and diffracted light be described by analogous expressions:

$$U_d(\mathbf{f}, z) = \sqrt{\frac{q_{d0}}{q_{t0}}}\zeta_d\exp\left\{-j\tilde{\mathbf{A}}_d\mathbf{f} - \frac{1}{2}\tilde{\mathbf{B}}_d\mathbf{f}^2\right\},$$
$$U_t(\mathbf{f}, z) = \zeta_t\exp\left\{-j\tilde{\mathbf{A}}_t\mathbf{f} - \frac{1}{2}\tilde{\mathbf{B}}_t\mathbf{f}^2\right\}. \quad (7)$$

Here, $\mathbf{A}_\alpha = \mathbf{A}_\alpha(z)$, $\mathbf{B}_\alpha = \mathbf{B}_\alpha(z)$, and $\alpha = t, d$ are the dependences initially determined in an explicit form. The parameters $(C, \mathbf{F}, \mathbf{G}, \mathbf{H}, \mathbf{L}, \Pi, \mathbf{T})_\alpha$ also vary in the course of the beam propagation. They will be determined in solving the simplified set of differential equations. We note that, in Eq. (7), $A_t = A_i$, $B_t = B_i$, $X_t = Y_t = 0$, $A_d = (1 + B_i)^{-1}A_i + \frac{1}{2}z(N_t - N_d)$, $X_d = \frac{1}{2}(N_t - N_d)$, $B_d = B_i(1 + B_i)^{-1} + z^2(N_t - N_d)^2$, and $Y_d = 2z(N_t - N_d)^2$. These are the dependences set initially. The quantities N_α determine the relative drift of the light beams (see Appendix). Selecting a specific model of long-term interaction, we obtain simplified expressions.

Such a representation of the spectra of transmitted and diffracted light is based on the following considerations. An incident light beam is usually several times thinner than a sound beam or is comparable to it in width. Therefore, in the case of the (quasi-)collinear interaction, the width of a transmitted light beam must not change significantly. If the transmitted and diffracted light beams propagate in diverging directions, the beam size increases and the transmitted light spectrum will not be narrowed. Therefore, its change can be described by the product of the Gaussoid, which gives the characteristic width of the spectrum, by a polynomial which describes the accumulated amplitude-phase changes. The width of the diffracted beam increases, while the spectrum does not expand. If, at $z = 0$, the spectra of both beams are similar in shape, then, in the course of the propagation, the part of the energy near the spectrum center U_d increases because of the selective energy transfer. Hence, it is possible to select several models of the spectrum variation for the diffracted light.

The representation of the light spectra in the form of Eq. (7) makes it possible to take into account additional information on widening or narrowing of the spectrum and on the position of the beam center. Therefore, the dependences $\mathbf{A}_\alpha(z)$ and $\mathbf{B}_\alpha(z)$ must be set up initially. On the contrary, the tensors of the polynomial factors must be determined in the process of solving the simplified set of differential equations. Below, for simplicity, we consider the one-dimensional case.

Substituting Eqs. (6) and (7) into Eq. (5), expanding the exponential terms into a series in powers of $\mathbf{f}$, and

equating the expressions multiplying equal powers of **f**, we obtain a set of differential equations for the coefficients describing the problem of strong acousto-optic interaction of divergent beams (see Appendix).

The relative part of the energy transmitted from the incident light to the diffracted light (with the change of polarization) is of most interest. According to the Parseval theorem, this coefficient can be represented in two ways:

$$P_d = \frac{q_{t0}\int E_d(r)E_d^*(r)dr}{q_{do}\int E_i(r)E_i^*(r)dr} = \frac{q_{t0}\int U_d(f)U_d^*(f)df}{q_{do}\int U_i(f)U_i^*(f)df} = \frac{\Lambda_d}{\Lambda_i}, \quad (8)$$

where

$$\Lambda_\alpha = B_\alpha^{-\frac{1}{2}}\left\{C_\alpha C_\alpha^* + \frac{1}{4}[C_\alpha G_\alpha^* + C_\alpha^* G_\alpha + 2F_\alpha F_\alpha^*]B_\alpha^{-1}\right.$$

$$+ \frac{1}{32}[C_\alpha L_\alpha^* + C_\alpha^* L_\alpha + 4(F_\alpha H_\alpha^* + F_\alpha^* H_\alpha) + 6G_\alpha G_\alpha^*]$$

$$\times B_\alpha^{-2} + \frac{1}{384}\Big[C_\alpha T_\alpha^* + C_\alpha^* T_\alpha + 6(F_\alpha \Pi_\alpha^* + F_\alpha^* \Pi_\alpha)$$

$$\left. + 15(G_\alpha L_\alpha^* + G_\alpha^* L_\alpha) + 20H_\alpha H_\alpha^*\Big]B_\alpha^{-3}\right\}, \quad \alpha = i, d.$$

DISCUSSION

The theory given above is suitable for calculating the diffraction characteristics at various geometries of acousto-optic interactions. For example, the condition $N_t = N_d = 0$ corresponds to a collinear diffraction of light. In the case of a quasi-collinear geometry, the incident optical beam is directed along the sound beam, $N_t = 0$, and the diffracted light beam can propagate in a somewhat different direction, $N_d \neq 0$. Finally, a geometry of the interaction is possible with both transmitted and diffracted light beams propagating at a certain angle to the sound column. We conducted calculations for all these possible geometries of long-term interaction of light and sound.

The dependences of the intensity of diffracted light on the Raman–Nath parameter $Q = ql/2$ were calculated for various ratios between the radii of the light and sound beams for the case of collinear diffraction ($N_t = N_d = 0$). The values of the relative power of diffracted light near the maximum of the energy transfer are presented in Fig. 1. Curve *1* corresponds to the case of equal radii of the light and sound beams (r and R, respectively) at the input of the cell. The maximal level of the power conversion does not exceed 73% in this case and is attained at $Q = 2.62$. The low percentage of light conversion is explained by the fact that different parts of the light beam interact with sound whose amplitude decreases toward the beam edges according to the Gaussian law. The maximal conversion is determined in this case not by the instant when the central part of the light beam is completely converted, but by a somewhat later time when the lateral components of light are efficiently diffracted.

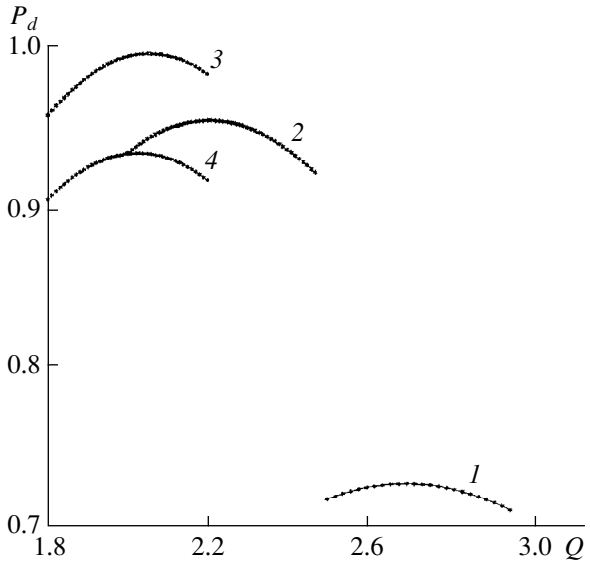

Fig. 1. Relative power of the diffracted light P_d near the maximum of the energy transfer versus the Raman–Nath parameter Q for different ratios between the radii of the light and sound beams (r and R, respectively) at the cell input: r/R = (*1*) 1, (*2*) 0.3, (*3*) 0.1, and (*4*) 0.01; $N_t = N_d = 0$; $D = 0.2$.

In the case of the radius ratio $r/R = 0.3$ (Fig. 1, curve *2*), light propagates within a more homogeneous sound beam and the diffraction efficiency reaches 96%, while the optimal value of Q decreases down to 2.15. At $r/R = 0.1$ (Fig. 1, curve *3*), light propagates within an almost homogeneous sound column, and the power maximum reaches 100% at $Q = 2$. A further decrease in the diameter of the light beam leads to the growth of its divergence with respect to the divergence of sound. In this case, only the part of light that propagates near the axis of the acousto-optic cell can be diffracted. The diffraction efficiency again decreases (Fig. 1, curve *4* corresponding to $r/R = 0.01$). The optimal value of Q almost does not change in this case.

Figures 2 and 3 illustrate the case of the quasi-collinear geometry. The effect of the divergence of the sound beam on the shape of the transmission curve of the acousto-optic cell $P_d(\Theta)$, where $\Theta = \eta l/2$, is demonstrated in Fig. 2. In this case, the incident light beam

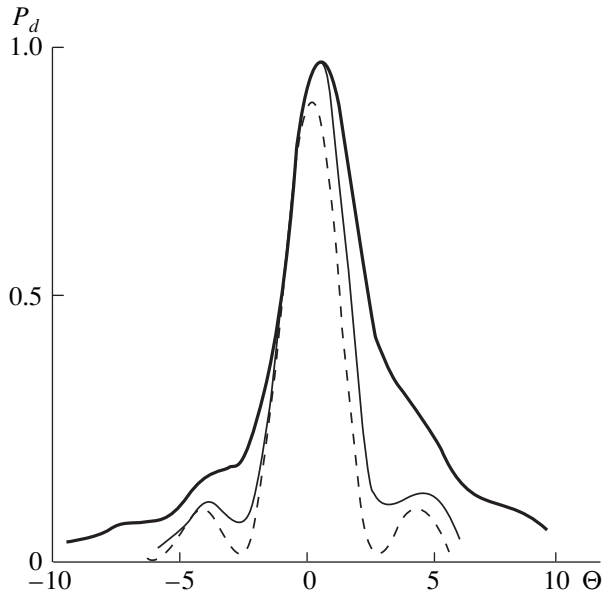

Fig. 2. Effect of the sound beam divergence on the shape of the transmission curve of the acousto-optic cell in the case of the quasi-collinear geometry of interaction: $N_t = 0$, $N_d = 0.2$; $D = 5$ (thick curve), 2 (solid curve), and 0.2 (dashed curve).

propagates along the axis of the sound beam and the diffracted beam at the output is shifted with respect to the cell center. The divergence of the sound beam is characterized by the quantity D, which shows to what extent the radius of the sound beam at the cell output R_{out} exceeds its input radius ($R_{\text{out}} = R\sqrt{1 + D^2}$). The dashed curve in Fig. 2 corresponds to the case of a weak divergence of sound ($D = 0.2$), and the solid and thick curves correspond to large values of the parameter D. One can see that the growth of the sound beam divergence somewhat widens the transmission band of the cell and increases the level of the side lobes, while the latter become smoothed and merge with the principal maximum of the transmission function. Naturally, the indicated curves were calculated for different values of the Raman–Nath parameter Q, which sharply increases with growing D.

Figure 3 demonstrates the effect of the diffraction angle on the transmission function of the cell in the case of the quasi-collinear interaction ($N_t = 0$, $N_d \neq 0$). The thick, dashed, and solid curves correspond to the shifts of the diffracted beam at the output by $0.2R$, $0.6R$, and R, respectively. All curves were calculated for the same value of Q. One can notice that an increase in the exit angle of the diffracted beam leads to a considerable decrease in the diffraction efficiency. A certain smoothing of the side lobes of the transmission band of the cell occurs simultaneously.

Figure 4 corresponds to the case of oblique ($N_t \neq 0$, $N_d \neq 0$) propagation of both light beams with respect to the axis of the sound column. For comparison, the solid curve in the plot describes the case of collinear geometry ($N_t = N_d = 0$) and the dashed curve corresponds to the shift of the incident and diffracted beams by R at the

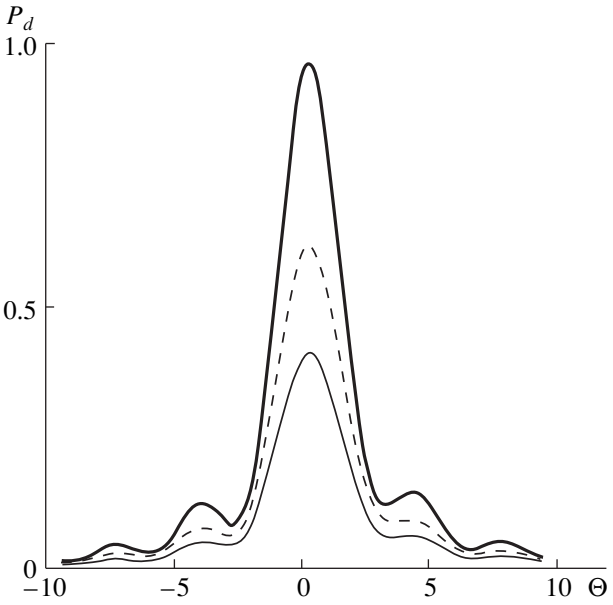

Fig. 3. Effect of the diffraction angle in the case of the quasi-collinear interaction ($N_t = 0$; $N_d \neq 0$) on the transmission function of the cell for a weak divergence of the acoustic beam $D = 0.2$: $N_d = 0.2$ (thick curve), 0.2 (dashed curve), and 1 (solid curve).

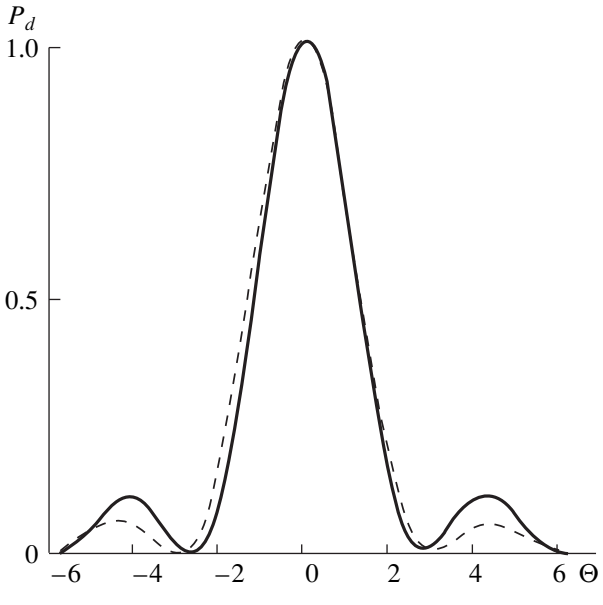

Fig. 4. Transmission function of the cell in the case of the oblique ($N_t = N_d = 1$) propagation of both light beams with respect to the axis of the sound column for a weak divergence of the acoustic beam $D = 0.2$ (the dashed curve). The solid curve corresponds to the collinear geometry of acousto-optic interaction ($N_t = N_d = 0$).

cell output. This curve testifies to an approximately twofold suppression of the side lobes in the case of such a diffraction geometry.

CONCLUSION

The study described above has shown that, in the case of the collinear geometry of interaction, the ratio between the radii of the light and sound beams considerably affects the efficiency of diffraction. However, its influence on the form of the transmission function of the acousto-optic cell and on the level of the side lobes is almost unobservable. On the contrary, the divergence of the acoustic beam noticeably affects the width of the transmission function and the degree of suppression of the side lobes, which leads to a considerable distortion of the transmission function of the cell. At the same time, in the case of quasi-collinear geometry, an increase in the angle with which the diffracted light beam exits from the sound column only reduces the diffraction efficiency. An oblique propagation of light with respect to the axis of a Gaussian acoustic beam can reduce the level of the side lobes of the transmission function.

APPENDIX

Substituting Eqs. (6) and (7) into Eq. (5), expanding the exponential factors in powers of **f**, and equating the expressions multiplying equal powers of **f**, we obtain a set of differential equations:

$$\frac{dC_t}{dz} = -Q\beta_d\Psi_{d0},$$

$$\frac{dF_t}{dz} = jX_tC_t - Q\beta_d[\Psi_{d1} - j\Omega_d\Psi_{d0}],$$

$$\frac{dG_t}{dz} = 2jX_tF_t + Y_tC_t$$

$$- Q\beta_d[\Psi_{d2} - 2j\Omega_d\Psi_{d1} - (\Omega_d^2 + \Phi_d)\Psi_{d0}],$$

$$\frac{dH_t}{dz} = 3jX_tG_t + 3Y_tF_t - Q\beta_d[\Psi_{d3}$$

$$- 3j\Omega_d\Psi_{d2} - 3(\Omega_d^2 + \Phi_d)\Psi_{d1} + j(\Omega_d^3 + 3\Omega_d\Phi_d)\Psi_{d0}],$$

$$\frac{dL_t}{dz} = 4jX_tH_t + 6Y_tG_t - Q\beta_d[\Psi_{d4} - 4j\Omega_d\Psi_{d3}$$

$$- 6(\Omega_d^2 + \Phi_d)\Psi_{d2} + 4j(\Omega_d^3 + 3\Omega_d\Phi_d)\Psi_{d1}$$

$$+ (\Omega_d^4 + 6\Omega_d^2\Phi_d + 3\Phi_d^2)\Psi_{d0}],$$

$$\frac{d\Pi_t}{dz} = 5jX_tL_t + 10Y_tH_t - Q\beta_d[\Psi_{d5} - 5j\Omega_d\Psi_{d4}$$

$$- 10(\Omega_d^2 + \Phi_d)\Psi_{d3} + 10j(\Omega_d^3 + 3\Omega_d\Phi_d)\Psi_{d2}$$

$$+ 5(\Omega_d^4 + 6\Omega_d^2\Phi_d + 3\Phi_d^2)\Psi_{d1}$$

$$- j(\Omega_d^5 + 10\Omega_d^3\Phi_d + 15\Omega_d\Phi_d^2)\Psi_{d0}],$$

$$\frac{dT_t}{dz} = 6jX_t\Pi_t + 15Y_tL_t - Q\beta_d[\Psi_{d6} - 6j\Omega_d\Psi_{d5}$$

$$- 15(\Omega_d^2 + \Phi_d)\Psi_{d4} + 20j(\Omega_d^3 + 3\Omega_d\Phi_d)\Psi_{d3}$$

$$+ 15(\Omega_d^4 + 6\Omega_d^2\Phi_d + 3\Phi_d^2)\Psi_{d2}$$

$$- 6j(\Omega_d^5 + 10\Omega_d^3\Phi_d + 15\Omega_d\Phi_d^2)\Psi_{d1}$$

$$- (\Omega_d^6 + 15\Omega_d^4\Phi_d + 45\Omega_d^2\Phi_d^2 + 15\Phi_d^3)\Psi_{d0}],$$

$$\frac{dC_d}{dz} = -Q\beta_t\Psi_{t0},$$

$$\frac{dF_d}{dz} = jX_dC_d + Q\beta_t[\Psi_{t1} - j\Omega_t\Psi_{t0}],$$

$$\frac{dG_d}{dz} = 2jX_dF_d + Y_dC_d$$

$$+ Q\beta_t[\Psi_{t2} - 2j\Omega_t\Psi_{t1} - (\Omega_t^2 + \Phi_t)\Psi_{t0}],$$

$$\frac{dH_d}{dz} = 3jX_dG_d + 3Y_dF_d + Q\beta_t[\Psi_{t3}$$

$$- 3j\Omega_t\Psi_{t2} - 3(\Omega_t^2 + \Phi_t)\Psi_{t1} + j(\Omega_t^3 + 3\Omega_t\Phi_t)\Psi_{t0}],$$

$$\frac{dL_d}{dz} = 4jX_dH_d + 6Y_dG_d + Q\beta_t[\Psi_{t4} - 4j\Omega_t\Psi_{t3}$$

$$- 6(\Omega_t^2 + \Phi_t)\Psi_{t2} + 4j(\Omega_t^3 + 3\Omega_t\Phi_t)\Psi_{t1}$$

$$+ (\Omega_t^4 + 6\Omega_t^2\Phi_t + 3\Phi_t^2)\Psi_{t0}],$$

$$\frac{d\Pi_d}{dz} = 5jX_dL_d + 10Y_dH_d + Q\beta_t[\Psi_{t5} - 5j\Omega_t\Psi_{t4}$$

$$- 10(\Omega_t^2 + \Phi_t)\Psi_{t3} + 10j(\Omega_t^3 + 3\Omega_t\Phi_t)\Psi_{t2}$$

$$+ 5(\Omega_t^4 + 6\Omega_t^2\Phi_t + 3\Phi_t^2)\Psi_{t1}$$

$$- j(\Omega_t^5 + 10\Omega_t^3\Phi_t + 15\Omega_t\Phi_t^2)\Psi_{t0}],$$

$$\frac{dT_d}{dz} = 6jX_d\Pi_d + 15Y_dL_d + Q\beta_t[\Psi_{t6} - 6j\Omega_t\Psi_{t5}$$

$$- 15(\Omega_t^2 + \Phi_t)\Psi_{t4} + 20j(\Omega_t^3 + 3\Omega_t\Phi_t)\Psi_{t3}$$

$$+ 15(\Omega_t^4 + 6\Omega_t^2\Phi_t + 3\Phi_t^2)\Psi_{t2}$$

$$- 6j(\Omega_t^5 + 10\Omega_t^3\Phi_t + 15\Omega_t\Phi_t^2)\Psi_{t1}$$

$$- (\Omega_t^6 + 15\Omega_t^4\Phi_t + 45\Omega_t^2\Phi_t^2 + 15\Phi_t^3)\Psi_{t0}].$$

Here, $X_\alpha = \dfrac{dA_\alpha}{dz}$ and $Y_\alpha = \dfrac{dB_\alpha}{dz}$ are the initially determined functions;

$$\beta_\alpha = U_0 M_\alpha^{\frac{1}{2}} \exp\left\{\pm 2j\Theta z - \Delta z - \frac{1}{2} M_\alpha V_\alpha^2\right\},$$

$$\Phi_t = M_t D_t (B_t + jzK_t) - (B_d + jzK_d),$$
$$\Phi_d = M_d D_d (B_d + jzK_d) - (B_t + jzK_t),$$

$$\Omega_d = M_d D_d V_d - V_t, \quad \Omega_t = M_t D_t V_t - V_d,$$
$$V_\alpha = A_\alpha + zN_\alpha,$$

$$M_\alpha = [D_\alpha + B_\alpha + jzK_\alpha]^{-1}, \quad D_\alpha = 1 \pm jzD,$$

$$\Psi_{\alpha n} = n!\left\{\Psi_{n0}^{(\alpha)} C_\alpha + \Psi_{n1}^{(\alpha)} F_\alpha + \frac{1}{2!}\Psi_{n2}^{(\alpha)} G_\alpha + \frac{1}{3!}\Psi_{n3}^{(\alpha)} H_\alpha \right.$$

$$\left. + \frac{1}{4!}\Psi_{n4}^{(\alpha)} L_\alpha + \frac{1}{5!}\Psi_{n5}^{(\alpha)} \Pi_\alpha + \frac{1}{6!}\Psi_{n6}^{(\alpha)} T_\alpha \right\},$$

$$\Psi_{n;\,kl}^{(\alpha)} = \sum_{i=0}^{n} (-1)^{n-i} C_{2k}^{n-i} D_\alpha^i S_{2k+l-n+i,\,i}^{(\alpha)}$$

$$= \sum_{i=0}^{n} (-1)^i C_{2k}^i D_\alpha^{n-i} S_{2k+l-i,\,n-i}^{(\alpha)};$$

the sign "+" corresponds to $\alpha = t$, and the sign "–" corresponds to $\alpha = d$.

The quantities involved in the last expression are determined by the recurrence formula

$$S_{k+1,\,p}^{(\alpha)} = (p+1) S_{k,\,p+1}^{(\alpha)} + M_\alpha S_{k,\,p-1}^{(\alpha)} - jM_\alpha V_\alpha S_{k,\,p}^{(\alpha)},$$
$$0 \le k \le 12, \quad 0 \le p \le k,$$

the process starting from the value $S_{00}^{(\alpha)} = 1$. Additionally, it is necessary to set $S_{kp}^{(\alpha)} = 0$ for $k < p$ and for $k, p < 0$.

In the equations, $Q = \dfrac{1}{2}\sqrt{q_{d0} q_{t0}}\, l$, $\Theta = \dfrac{1}{2}\eta l$, and $\Delta = \delta l$ are the dimensionless mismatch, acousto-optic coupling, and sound attenuation; $D = b^{-1} w l$ is the real parameter describing the spreading of the sound beam within the cell length; the quantities $K_\alpha = b^{-1} w_\alpha l$ represent the measure of the spreading of light packets; and $N_\alpha = b^{-\frac{1}{2}}(s_\alpha - s)l$ is the dimensionless drift of light beams with respect to the sound beam within the interaction length (the drift is expressed in parts of the sound beam radius).

The given set of equations should be solved with the initial conditions (at $z = 0$): $(C, F, G, H, L, \Pi, T)_t = (C, F, G, H, L, \Pi, T)_i$, $(C, F, G, H, L, \Pi, T)_d = 0$. By setting up the nonzero quantities $(F, G, H, L, \Pi, T)_i$, it is possible in the general case to describe various forms of the spectrum of incident light.

REFERENCES

1. A. Korpel, *Acousto-Optics* (Marcel Dekker Inc., New York, 1997).
2. V. I. Balakshiĭ, V. N. Parygin, and L. E. Chirkov, *Physical Foundations of Acousto-Optics* (Radio i Svyaz', Moscow, 1985).
3. C.-W. Tarn, R. S. Huang, and C.-W. Hsieh, Appl. Opt. **37**, 7496 (1998).
4. Chieu D. Tran and Geng-Chen Huang, Opt. Eng. (Bellingham) **38** (7), 1143 (1999).
5. V. N. Parygin and A. V. Vershubskiĭ, Akust. Zh. **44**, 32 (1998) [Acoust. Phys. **44**, 23 (1998)].
6. V. N. Parygin and A. V. Vershubskiĭ, Radiotekh. Elektron. (Moscow) **43**, 293 (1998).
7. V. N. Parygin, A. V. Vershubskiĭ, and Yu. G. Rezvov, Opt. Spektrosk. **84**, 1005 (1998) [Opt. Spectrosc. **84**, 911 (1998)].
8. V. N. Parygin, A. V. Vershubskiĭ, and E. Yu. Filatova, Izv. Akad. Nauk, Ser. Fiz. **62** (12), 2409 (1998).
9. V. B. Voloshinov, Opt. Eng. (Bellingham) **31** (10), 2089 (1992).
10. V. N. Parygin, A. V. Vershoubskiy, and Yu. G. Resvov, Proc. SPIE **3581**, 118 (1998).

Translated by M. Lyamshev

Acoustical Physics, Vol. 47, No. 1, 2001, pp. 29–34. Translated from Akusticheskiĭ Zhurnal, Vol. 47, No. 1, 2001, pp. 37–43.
Original Russian Text Copyright © 2001 by Goncharov.

Acoustic Tomography of Currents in the Ocean by the Linearized Method of Matched Nonreciprocity

V. V. Goncharov

Shirshov Oceanology Institute, Russian Academy of Sciences, Nakhimovskiĭ pr. 36, Moscow, 117851 Russia
e-mail: gvv@rav.sio.rssi.ru

Received December 30, 1999

Abstract—The matched nonreciprocity method recently developed for acoustic diagnostics of ocean currents is based on matching the nonreciprocity of a sound field propagating along the current and against it. In this paper, the possibilities for linearizing this method are studied on the basis of numerical experiments. In contrast to the strict limitations of the linear approach in the tomography of the field of sound velocity by the matched field methods, in the method of matched nonreciprocity, the linearity is provided by the smallness of the Mach number M of currents and by the fact that the terms quadratic in M are partially suppressed in the course of the nonreciprocity calculation. The linear approach makes it possible to speed up the procedure of calculation (including calculations in higher dimensional parametric spaces) and to efficiently use nonlinear procedures for the localization of the main minimum. © *2001 MAIK "Nauka/Interperiodica"*.

The new approach to acoustic tomography of ocean currents, which is called the method of matched nonreciprocity, has received wide acceptance [1–4]. It is based on matching the experimentally measured and theoretically predicted nonreciprocities of acoustic fields for sound propagation in opposite directions. In the cited papers [2–4], the efficiency of various value functions whose minimization gives the desired profile of the current was investigated. In particular, good results were obtained in the case of matching the nonreciprocity of the phase of the sound field, which leads to the value functions of the form

$$F_c(\mathbf{q}) = 2\{1 - [\langle A\cos\Delta\vartheta(\mathbf{q})\rangle^2 - \langle A\sin\Delta\vartheta(\mathbf{q})\rangle^2]/\langle A\rangle^2\}, \quad (1)$$

$$F_a(\mathbf{q}) = \langle A[\vartheta_e - \vartheta_t(\mathbf{q})]^2\rangle/(A\pi^2). \quad (2)$$

Here, the angular brackets mean averaging, e.g., $\langle A\rangle = J^{-1}\sum_{j=1}^{J} A_j$, $\Delta\vartheta_j(\mathbf{q}) = \vartheta_{ej} - \vartheta_{tj}(\mathbf{q})$, $\vartheta_{ej} = \arg[P_{ej}^{+}P_{ej}^{-*}]$, and $\vartheta_{tj} = \arg[P_{tj}^{+}P_{tj}^{-*}]$ are the phase nonreciprocities between the sound fields obtained at the jth element of the array (and/or the frequency in the case of reception of a wide-band signal) for the direct P^+ and opposite P^- propagation of sound; the index e corresponds to the measured field; the index t corresponds to the calculated field; the normalization coefficient is $A_j = |P_{ej}^{+}P_{ej}^{-*}|$; and the vector $\mathbf{q}$ parametrizes the reconstructed field of currents.

This paper investigates the possibilities for linearizing the method of matched nonreciprocities on the basis of numerical experiments. It should be noted that attempts to linearize the conventional method of sound field matching in the tomography of the field of sound velocity were made more than once (e.g., in [5]). However, as it was shown, in this case linearization is possible only for sufficiently small variations of the sound velocity ($\Delta c < 1$ m/s). Therefore, in many practically important cases, exact nonlinear calculations are necessary. There are a lot of possibilities for linearization in the case of the reconstruction of the field of currents by the method of matched nonreciprocity where nonlinearity is provided by the smallness of the Mach number M of currents and by the fact that the terms quadratic in M are partially suppressed in the course of the nonreciprocity calculation.

In the linear approximation in the vector $\mathbf{q} - \mathbf{q}_0$ ($\mathbf{q}_0$ is a certain selected point), the nonreciprocity of the calculated phase has the form

$$\vartheta_t(\mathbf{q}) = \vartheta_t(\mathbf{q}_0) + \nabla\vartheta_t(\mathbf{q}_0)(\mathbf{q} - \mathbf{q}_0). \quad (3)$$

Substitution of this expression into Eq. (2), for example, leads to a value function quadratic in $\mathbf{q} - \mathbf{q}_0$:

$$F_l(\mathbf{q}) = \langle A[\vartheta_e - \vartheta_t(\mathbf{q}_0) - \nabla\vartheta_t(\mathbf{q}_0)(\mathbf{q} - \mathbf{q}_0)]^2\rangle/(\langle A\rangle\pi^2). \quad (4)$$

In the case of the value function given by Eq. (1), such an expression can be obtained by additional linearization of the trigonometric functions involved in this value function. As a result, the value function becomes quadratic and completely analogous to the one obtained in Munk's linear tomographic scheme, where a linearized nonreciprocity of the phase of the total field is used instead of times of propagation along rays. This fact noticeably speeds up the procedure of inversion and, according to the developed technique [6], allows one to estimate its error, attainable precision, etc.

1063-7710/01/4701-0029$21.00 © 2001 MAIK "Nauka/Interperiodica"

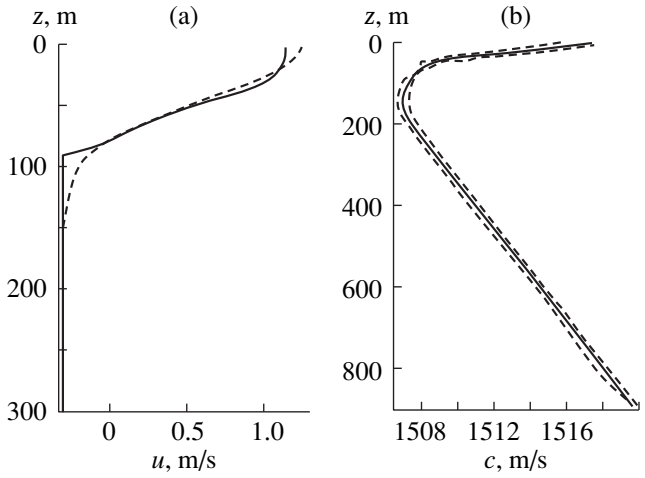

Fig. 1. Typical profiles of (a) the current and (b) the sound velocity for the conditions of the 1996 experiment in the Strait of Gibraltar. Solid lines correspond to measurements and dashed lines correspond to (a) the approximation of the current by empirical orthogonal functions and (b) the effective profiles of the sound velocity.

However, in our case the situation is complicated by the fact that, in contrast to variations in the signal propagation times used in Munk's tomography and monotonic with respect to the variations of the sound velocity, the values of the nonreciprocity of the phase of the sound field $\Delta\vartheta_j(\mathbf{q})$ from Eqs. (1) and (2) are determined in the interval $(-\pi, \pi)$. This leads to the appearance of additional minimums in the function $F_a(\mathbf{q})$, which form a periodic structure in the **q**-space, primarily along the barotropic component of the current. Equating the phase difference of the sound field propagating along and against the current to 2π, we obtain the estimate of the variation of the characteristic current's velocity, which is necessary for proceeding to the next minimum of the function $F_a(\mathbf{q})$:

$$\Delta u_m = c_0^2(2fR)^{-1}, \tag{5}$$

where c_0 is the characteristic sound velocity, f is the sound frequency, and R is the distance between emitting–receiving systems. For example, for the conditions of the Strait of Gibraltar at R = 21.18 km and frequencies f = 100, 500, and 1000 Hz, this estimate yields the values Δu_m = 0.5, 0.1, and 0.05 m/s, respectively. Hence, a complete linearization of the function $F_a(\mathbf{q})$ leading to its quadratic dependence on the variations of $(\mathbf{q} - \mathbf{q}_0)$ is possible in the region where the corresponding variations of the characteristic velocity of the current do not exceed $\Delta u_m/2$. Moreover, in contrast to the linear scheme of Munk's tomography by the arrival times of signals, everywhere in this region the exact function $F_a(\mathbf{q})$ is not quadratic, because it has inflection points close to its maximum. This leads to noncoincidence of the minimum of the corresponding quadratic function with the true minimum if the initial point $\mathbf{q}_0$ is set after an inflection point. Therefore, an adequate reconstruction of velocity of the current, which is obtained by inversion of a system of algebraic equations as in Munk's scheme, is possible in the case of the determination of the point of linearization within the limits of an even smaller region of the **q**-space. In this case it is necessary to use the iteration procedure in such inversions with the calculation of a new linear approximation after each iteration.

A possible way of calculating $F_l(\mathbf{q})$ consists in substituting the calculated values of nonreciprocity of the phase $\vartheta_t(\mathbf{q})$ from Eq. (3) into Eq. (4) with preliminarily recalculating them to $\vartheta_t^{(1)}(\mathbf{q}) = \vartheta_t(\mathbf{q}) \pm 2n\pi$ lying within the interval $(-\pi, \pi)$:

$$F_l^{(1)}(\mathbf{q}) = \langle A[\vartheta_e - \vartheta_t^{(1)}(\mathbf{q})]^2\rangle/(\langle A\rangle\pi^2). \tag{6}$$

We will call this approach the calculation of the linear limited phase. In this case, the value function becomes nonlinear but easily computable. We note that a similar result is obtained with the use of the value function

$$F_{c1}(\mathbf{q}) = 1 - \langle A\cos\Delta\vartheta(\mathbf{q})\rangle^2/\langle A\rangle^2, \tag{7}$$

where linear Eq. (3) is substituted into $\Delta\vartheta(\mathbf{q})$.

We also note that the function $F_c(\mathbf{q})$ is strongly degenerate with respect to the barotropic component of the current. This effect is caused by the invariance of the function $F_c(\mathbf{q})$ with respect to the addition of a constant shift to the value of $\Delta\vartheta_j(\mathbf{q})$ and by an approximately constant phase shift of all sound modes in the case when the velocity of the current changes by a constant value.

Numerical studies were conducted in the case of matching of the fields P^+ and P^- received by vertical arrays and for various hydrological conditions typical of various regions of the open ocean and straits where the velocities of currents may reach relatively large values, including one of the routes (T1–T2 with the length 21.18 km) of the 1996 experiment in the Strait of Gibraltar [7] (see also Fig. 1 and the Web site http://atocdb.ucsd.edu.gibraltar). Solid lines in Fig. 1 show typical measured profiles of (a) the current and (b) the sound velocity in this experiment. The current's profile $u_e(z)$ was approximated by empirical orthogonal functions: the barotropic function $u_{e1}(z) = a_1$ = const and the baroclinic function $u_{e2}(z) = a_2\{\exp[-(z/z_0)^2] - a_3\}$, where the constants a_1 were determined from the orthonormalization conditions $\int_0^H u_{em}(z)\,u_{en}(z)dz = H\delta_{mn}$, z_0 = 60 m, and H is the depth of the approximation interval (in the case under study, the oceanic depth was equal to 890 m). The integrals were calculated exactly for the piecewise-linear interpolation of the empirical orthogonal functions by 27 points of their setting; the effective profiles of the sound velocity corresponded to sound radiation along and against the current. Vertical arrays (85 hydrophones) were positioned at the depth of 10 to 850 m.

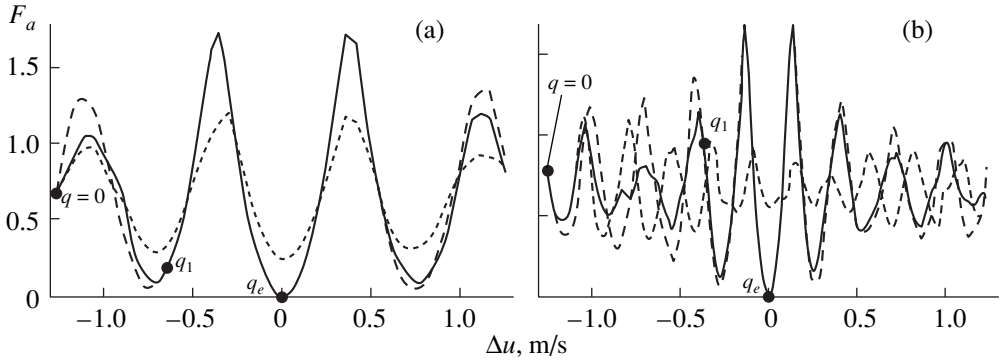

Fig. 2. Calculation of the functions $F_a(\mathbf{q})$ for the frequencies (a) 400 and (b) 1150 Hz. Solid lines correspond to the exact calculation, and other lines correspond to partial linearization for various points of linearization $\mathbf{q}_0$: long dashes are for $\mathbf{q}_0 = \mathbf{q}_e$ and short ones are for $\mathbf{q}_0 = 0$.

An adiabatic mode code was used for the computation of sound fields. The velocities of the current were taken into account using the approximation of the effective field of the sound velocity $c_{\text{eff}} = c + u$. We note that the layered-homogeneous medium model used for calculating the eigenvalues of sound modes ξ_m allows one to calculate exactly (by analytical formulas) both ξ_m and their derivatives with respect to the components of the two-dimensional vector $\mathbf{q}$, as well as the corresponding gradient of mode phases at the reception points: $\nabla\varphi_m(\mathbf{q})$. Now, we calculate these expressions at a certain point $\mathbf{q}_0$ and form linear approximations for the phases of the sound modes:

$$\varphi_m(\mathbf{q}) = \varphi_m(\mathbf{q}_0) + \nabla\varphi_m(\mathbf{q}_0)(\mathbf{q} - \mathbf{q}_0). \qquad (8)$$

Then, we substitute the latter into the expressions for the sound fields $P_{tj}^{+}(\mathbf{q})$, $P_{tj}^{-*}(\mathbf{q})$ through the sum of the sound modes and calculate the functions $F_c(\mathbf{q})$ and $F_a(\mathbf{q})$ (Eqs. (1) and (2)). As a result, we obtain the so-called partial linearization of the matched nonreciprocity method. In this case, the functions $F_c(\mathbf{q})$ and $F_a(\mathbf{q})$ stay nonlinear in $\mathbf{q}$, but the time for their calculation is considerably reduced (ten times or more). The domains of validity of such a linearization depending on the sound frequency were investigated. It turned out that, at the frequencies $f \approx 100$ Hz and lower, independently of the choice of the vector $\mathbf{q}_0$, the partial linearization describes with high accuracy both the positions of all minimums in the $\mathbf{q}$-space (with the error $\Delta u_e \le 0.03$ m/s) and the values of the functions $F_c(\mathbf{q})$ and $F_a(\mathbf{q})$ up to the variations of $(\mathbf{q} - \mathbf{q}_0)$ corresponding to the maximal values of the real velocities of the currents ($\Delta u \le 2$ m/s). It is natural that errors in the linear expression (3) for the phase nonreciprocity increase with the increase in distance and frequency, and the domain of validity of this expression becomes narrower. For example, for the conditions of the Strait of Gibraltar at the distance 21.18 km, the current's velocities corresponding to admissible variations of $(\mathbf{q} - \mathbf{q}_0)$ must not exceed 1 m/s at the frequency 250 Hz, 0.6 m/s at the frequency 500 Hz, and 0.4 m/s at the frequency 1 kHz. Similar results were obtained for the case of calculation of the value function (6) (the calculation of the linear limited phase) when the values of linear phase (3) were normalized to the interval $(-\pi, \pi)$.

Figure 2 shows the comparison of such calculations of the function $F_a(\mathbf{q})$ for the frequencies (a) 400 and (b) 1150 Hz as an example. In the $\mathbf{q}$-space, sections are made through the points $\mathbf{q} = 0$ and $\mathbf{q}_0 = 2\mathbf{q}_e$ in such way that all the current's profiles are similar to $u(\mathbf{q}_e)$ (the dashed line in Fig. 1a): $u(\mathbf{q}) = su(\mathbf{q}_e)$, $0 \le s \le 2$. The argument of Δu in the figure is equal to the maximal deviation of the current's velocity from $u(\mathbf{q}_e)$: $\Delta u = \max u(\mathbf{q}) - \max u(\mathbf{q}_e) = (s-1)u(\mathbf{q}_e)|_{z=0}$. Therefore, the vector $\mathbf{q}_e = (-0.21017, 0.30611)$ corresponds to the point $\Delta u = 0$; the lines originate from the left ($\mathbf{q} = 0$, no current). The calculation in the approximation of the linear limited phase was close to the corresponding calculation with partial linearization, and it is not given in Fig. 2. One can easily see that the distance between the minimums of the function $F_a(\mathbf{q})$ corresponds to estimate (5) given above (in this case, it is necessary to take into account that the barotropic component of the current is approximately four times less than the maximal variation in the current's profile, which is used as the argument in Fig. 2). We should also note that the interval of validity of the approximation of partial linearization decreases as the frequency grows, and, therefore, the interval of validity for the linear limited phase also decreases. Thus, it follows from the behavior of the dashed lines corresponding to the linearization point $\mathbf{q}_0 = \mathbf{q}_e$ ($\Delta u = 0$) that, at the frequency 400 Hz, the maximal admissible variations of the current's profile are $\Delta u_{lm} \approx 1$ m/s and, at the frequency $f = 1150$ Hz, $\Delta u_{lm} \approx 0.4$ m/s. This is confirmed also by the behavior of the lines of partial linearization corresponding to $\mathbf{q}_0 = 0$ in Fig. 2a, which are noticeably different from the exact calculation. At the same time, analogous calculations corresponding to $\mathbf{q}_0 = \mathbf{q}_1$ (at the frequency 400 Hz, $\mathbf{q}_1 = (-0.103, 0.150)$ and $\Delta u = 0.64$ m/s and, at 1150 Hz,

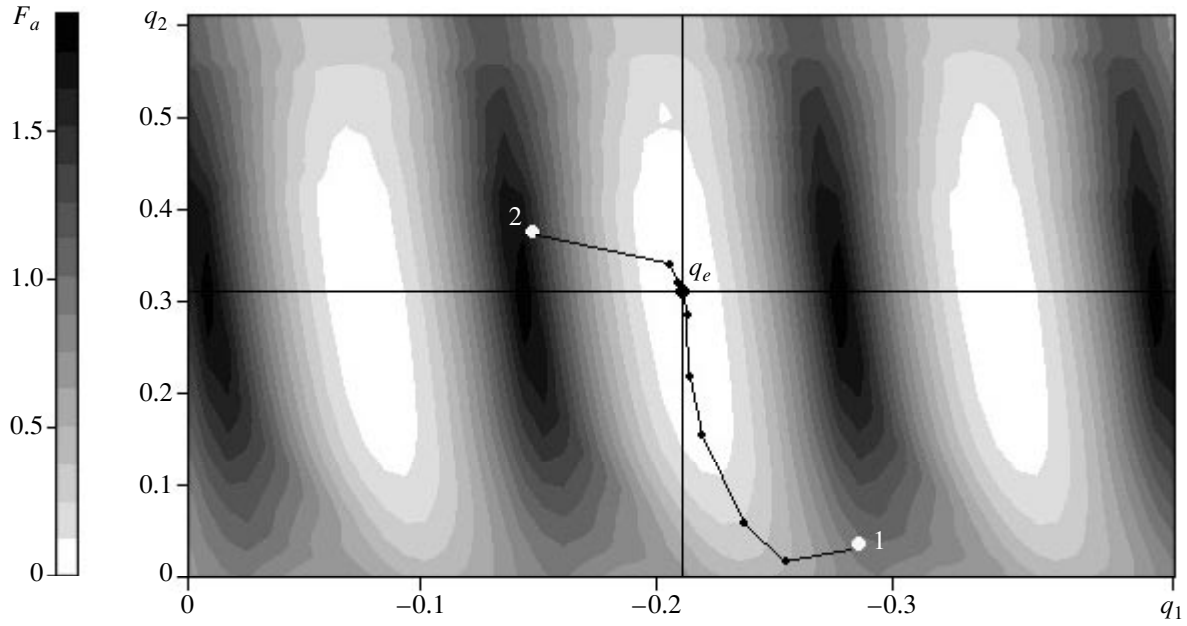

Fig. 3. Pattern of convergence of the iteration procedure for two starting points, 1 and 2.

$\mathbf{q}_1 = (-0.148, 0.215)$ and $\Delta u = 0.37$ m/s) almost completely coincide with the exact calculation.

Thus, a rough estimate of the admissible maximal variation of the current's profile with the use of the approximations of partial linearization and the linear limited phase for the conditions of the 1996 experiment in the Strait of Gibraltar has the form

$$\Delta u_{lm}\ [\text{m/s}] \approx 400/f\ [\text{Hz}]. \qquad (9)$$

The procedure of complete linearization was also simulated numerically for the conditions of the Strait of Gibraltar. The results of such a simulation fully agree with the estimates given above. In the case of selecting the linearization point $\mathbf{q}_0$ in the vicinity of the boundaries of the region influenced by the main minimum of the functions $F_a(\mathbf{q})$ and $F_c(\mathbf{q})$, from two to seven iterations were necessary (depending on the selection of the initial point $\mathbf{q}_0$) for the convergence to the exact solution. Recall that the ith iteration consists of two steps: (i) calculation of the coefficients of the quadratic target function for the initial point $\mathbf{q}_i$; (ii) determination of the next point $\mathbf{q}_{i+1}$ minimizing this function. The exact calculation of the two-dimensional function $F_a(\mathbf{q})$ at a frequency of 400 Hz is shown in Fig. 3. In the case of setting the initial (starting) point "1," the determination of the exact value $\mathbf{q}_e$ requires six iterations; for the point "2," three iterations are necessary. The process of convergence and the position of the intermediate points $\mathbf{q}_i$ are also shown in Fig. 3.

The influence of errors in setting both the field of the sound velocity in the medium and the parameters of bottom sediments on the result of the reconstruction of the field of currents was also studied. It was found that, although the values of the functions $F_c(\mathbf{q})$ and $E_a(\mathbf{q})$ at the points of the main minimum increased, the position of the minimum in the $\mathbf{q}$-space remained close to the true one with the rms errors in the field of the sound velocity in water less than 0.5 m/s, and in sediments in the shallow sea conditions, up to 10 m/s.

A similar situation was observed at higher frequencies, but, in this case, according to estimate (5), the region of influence of the main maximum rapidly decreased, which made it difficult to perform this procedure in practice. Naturally, it is always possible to complete the linearization in practice in the process of a relatively frequent monitoring of the variations of the current $\Delta u(z)$. Namely, it is necessary to measure $u_0(z)$ at the beginning of the experiment; select its parameters as the initial point; and then, at the time intervals when it is *a priori* known that $\Delta u(z)$ remains within the region of influence of the main minimum of the functions $F_c(\mathbf{q})$ and $F_a(\mathbf{q})$, reconstruct a new profile $u_m(z)$, take it as the initial one, and so on.

In the cases when such a procedure is impossible for some reasons, e.g., at high frequencies at which, according to estimate (5), the region of influence of the main minimum is about several centimeters per second (i.e., lies within the errors of the current's parameter measurement), it is apparently necessary to develop more complex procedures of nonlinear inversion. An additional difficulty arises here, which is connected with the presence of a large number of equivalent minimums of the function $F_a(\mathbf{q})$ and the independence of $F_c(\mathbf{q})$ from the barotropic component, which follows, e.g., from the form of the two-dimensional value functions $F_a(\mathbf{q})$ and $F_c(\mathbf{q})$ in Fig. 4. As a result, the determination of the main minimum $\mathbf{q}_e = (-0.21017, 0.30611)$ becomes impossible. The so-called multifrequency ver-

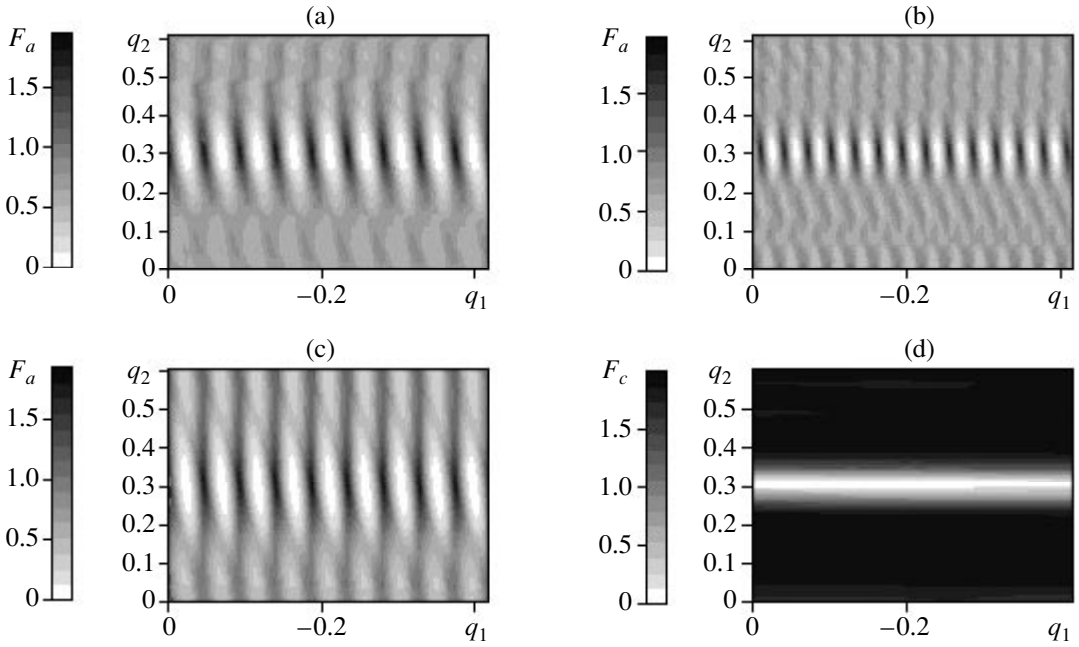

Fig. 4. Form of the value functions $F_a(\mathbf{q})$ and $F_c(\mathbf{q})$: (a) exact calculation of $F_a(\mathbf{q})$ at a frequency of 1150 Hz, (b) exact calculation of $F_a(\mathbf{q})$ at a frequency of 1750 Hz, (c) calculation of $F_a(\mathbf{q})$ at a frequency of 1150 Hz in the approximation of partial linearization, and (d) exact calculation of $F_c(\mathbf{q})$ at a frequency of 1750 Hz.

sion of the method of matched nonreciprocity for the reception by vertical arrays was proposed by Godin and Mikhin [3, 4] in order to overcome this difficulty. Since the main minimum of the value functions $F_a(\mathbf{q})$ and $F_c(\mathbf{q})$ does not move with the change of frequency while other minimums change their positions, one can expect that even a simple summation of such functions at different frequencies will lead to a resultant value function that is more acceptable for the inversion. If the main goal of such a procedure is the estimation of the position of the main minimum, one can expect that approximate calculations using partial linearization or linear limited phase will also lead to the desired result. This follows, e.g., from the comparison of Figs. 4a, 4c, where the general behavior of the functions is the same.

From the comparison of the dependences $F_a(\mathbf{q})$ at different frequencies (Figs. 4a, 4b), it follows that their general structure differs basically by the period in the barotropic component q_1. Therefore, one can expect a successful localization of the main minimum in the case of utilization of the following scheme considerably reducing the time of calculation. Calculating the spectrum $S(k; q_2)$ of the function $F_a(q_1)$ for each fixed q_2, shifting it by $\Delta k = k_{0n} - k_0$, and performing the inverse Fourier transformation, we obtain the estimate of the dependence $F_a(\mathbf{q})$ at a shifted frequency. In fact, this procedure is equivalent to calculating the envelope of the function $F_a(q_1)$ and filling it with a higher frequency. However, it is necessary to take into account that, in the case of such a shift, the higher harmonics of the fundamental component k_0 of the spectrum of the function $F_a(q_1)$ as a rule do not pass into the corresponding harmonics of the shifted spectrum and distort the result. Therefore, it is necessary to limit the spectrum making it sufficiently narrow-band. Moreover, the procedure of shifting the spectrum, which preserves the position of the main minimum q_{e1} of the function $F_a(q_1)$, needs a corresponding change of phases of the spectral components by $\Delta\varphi = (k_{0n} - k_0)q_{e1}$, which can be easily accomplished when the position of the main minimum is known, e.g., in the case of numerical simulation, but may be impossible if one works with measured signals.

All such approaches were simulated using the experimental conditions of 1996 in the Strait of Gibraltar as an example. The spectrum of the sound signal emitted in this experiment was within the frequency range 1136.36–3409.09 Hz. The frequency band 1150–1750 Hz within this range was selected for simulation. The studies demonstrated that all these approaches give value functions quite acceptable for estimating the position of the main minimum. Good results were obtained already with the averaging of five functions uniformly distributed within the band (1150–1750 Hz). Their further increase provided only smoothing of the resultant function beyond the region of the main minimum and two neighboring ones. The examples of such calculations are given in Fig. 5. We note a rather high degree of coincidence of the resultant functions obtained by approximate and exact calculations.

Thus, the conducted study demonstrates that partial linearization and the linear limited phase adequately describe the effect of the field of the current's velocities on the functions $F_c(\mathbf{q})$ and $F_a(\mathbf{q})$. This makes it possible

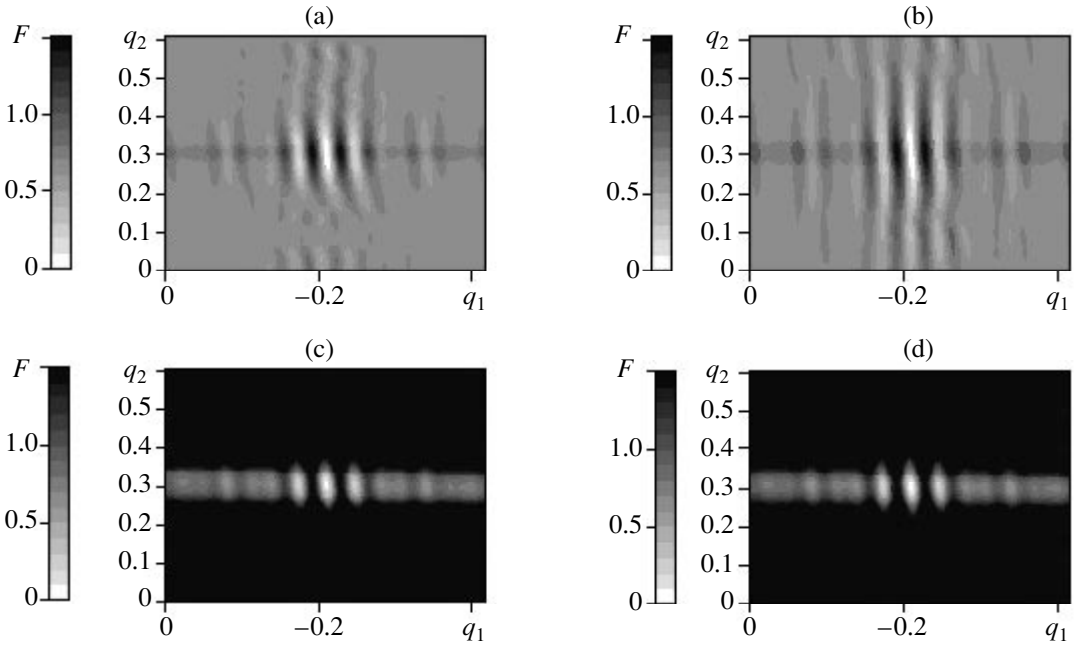

Fig. 5. Results of the averaging procedure for the value functions at different frequencies: (a) averaging of 21 functions $F_a(\mathbf{q})$, 19 of which are obtained by way of shifting and linearly interpolating the spectra of two exact functions at the frequencies 1150 and 1750 Hz (Figs. 4a, 4b); (b) analogous result for initial functions in the approximation of partial linearization (Fig. 4c); (c) sum of the function shown in Fig. 5a and the function $F_c(\mathbf{q})$ at a frequency of 1750 Hz (Fig. 4d); and (d) analogous result for the function shown in Fig. 5b.

to speed up the procedure of their calculation (including the calculation in the higher-dimensional parametric spaces) and efficiently use nonlinear procedures for the localization of the main maximum. After that, it is possible to determine more precisely the desired solution by using a complete linearization and solving a linear problem of inversion, as well as to obtain the estimate of the inversion error simultaneously with its result, the answer to the question about the attainable precision of measurements of currents with the help of the method of matched nonreciprocity, etc.

ACKNOWLEDGMENTS

This study was supported in part by the INTAS with the Russian Foundation for Basic Research (project no. 95-1002) and the Russian Foundation for Basic Research (project no. 99-05-65243).

REFERENCES

1. O. A. Godin, D. Yu. Mikhin, and A. V. Mokhov, in *Full Field Inversion Methods in Ocean and Seismo Acoustics*, Ed by O. Diachock *et al.* (Kluwer, Dordrecht, 1995), pp. 261–266.
2. O. A. Godin, D. Yu. Mikhin, and A. V. Mokhov, Akust. Zh. **42**, 501 (1996) [Acoust. Phys. **42**, 441 (1996)].
3. O. A. Godin and D. Yu. Mikhin, in *Proceedings of the 3rd European Conference on Underwater Acoustics*, Ed. by J. S. Papadakis (FORTH-IACM, Heraklion, 1996), Vol. 2, p. 785.
4. D. Yu. Mikhin and O. A. Godin, in *Theoretical and Computational Acoustics'97*, Ed. by Yu-Chiung Teng *et al.* (World Scientific, Singapore, 1999), pp. 499–513.
5. A. Tolstoy, J. Acoust. Soc. Am. **91**, 781 (1992).
6. W. Munk, P. Worcester, and C. Wunsch, *Ocean Acoustic Tomography* (Cambridge Univ. Press, Cambridge, 1995).
7. P. F. Worcester, U. Send, B. D. Cornuelle, and C. O. Tiemann, in *Proceedings of the International Conference on Shallow Water Acoustics, Beijing, China, 1997*, Ed. by R. Zhang and J. Zhou (China Ocean, Beijing, 1997), p. 471.

Translated by M. Lyamshev

Acoustical Physics, Vol. 47, No. 1, 2001, pp. 3–9. Translated from Akusticheskiĭ Zhurnal, Vol. 47, No. 1, 2001, pp. 7–14.
Original Russian Text Copyright © 2001 by Andronov, Belinskiĭ.

On the Uniqueness of the Problem of Acoustic Diffraction by an Infinite Plate with Local Irregularities

I. V. Andronov* and B. P. Belinskiĭ**

** St. Petersburg State University (Petrodvorets Branch), Ul'yanovskaya ul. 1/1, Petrodvorets, 198904 Russia*
e-mail: iva@aa2628.spb.edu

*** University of Tennessee at Chattanooga, USA*

Received March 20, 2000

Abstract—The question concerning the uniqueness of the solution to the problem of the acoustic diffraction by an immersed and isolated thin infinite plate with a finite scatterer is studied. It is shown that, to provide the uniqueness of the solution, the conditions at the scatterer must lead to an energy inequality for a source-free field, which determines the absence of the energy-carrying field components at infinity. A formula that generalizes the Sommerfeld formula is obtained and is used to prove the uniqueness of the solution to the problem of diffraction by a plate immersed in an acoustic medium. For the problem of diffraction of a flexural wave by an irregularity of the plate, the uniqueness theorem is proved only for the case of a fixed or hinged edge. When boundary conditions of a general form are imposed on the scatterer in an isolated plate, the uniqueness of the solution is generally lost, which is also corroborated by an example. © *2001 MAIK "Nauka/Interperiodica".*

The boundary-value problems with generalized impedance conditions occur in the mechanics of thin shells, in hydroacoustics, and in the problems of electromagnetic wave diffraction by bodies with dielectric coatings. The geometry of the studied regions becomes increasingly complex, and, unlike the first works [1–4], in which explicit formulas for the diffracted field were obtained, the problems are reduced to integral equations or infinite sets of algebraic equations [5–11]. For such diffraction problems, it is necessary to verify whether they are well-posed problems. This is usually accomplished by calculating the outward energy flux. In the presence of infinite baffles with generalized boundary conditions imposed on them, one should consider not only the flux transferred in the medium, but also the energy flux carried by the waves concentrated near the baffle. Note that, in this case, the variables in the spherical coordinates cannot be separated in the far-field region and the classical proof of uniqueness [12] cannot be applied. Therefore, the following technique is used [13]. Consider an expanding region containing the scatterer and write Green's formula for the solution. The conditions set at the boundary of the scatterer cause integrals along the boundary to be zero. Then, the integral over an arc (in the two-dimensional case) or over a hemisphere (in the three-dimensional case) of a large radius must also be zero, which means that the energy flux and the radiation pattern of the scattered field are zero. In particular, when the impedance boundary conditions at the surface contain tangential derivatives, it is necessary to impose additional, so-called contact, conditions at the salient points or lines of the boundary or at the points or lines where the curvature of the boundary or the coefficients in the generalized impedance conditions have a jump. These conditions must comply with the differential operator of the generalized impedance. Thus, a problem is considered well-posed if it is stated so that, in the absence of sources, the radiation pattern is zero and the number of conditions is minimal.

In a number of problems, the condition that the scattering pattern be zero provides uniqueness of the solution. This was first was proved for the problems that allow an explicit solution [13] or from the analysis of the Fredholm integral equation, to which the problem was reduced [14]. In a more general case, the question concerning the uniqueness of the two-dimensional boundary-value contact acoustic problems in the presence of an infinite plate was studied in [15] with the help of the Sommerfeld formula (see [17]), which expresses the solution to the Helmholtz equation in terms of an analytical extension of the radiation pattern. A similar analysis for the three-dimensional case is given below.

The condition that the far-field radiation pattern be zero does not entail the uniqueness of the solution to the diffraction problem for flexural waves in an isolated plate, because, for the Kirchhoff operator, a formula similar to the Sommerfeld formula does not exist. Below, we consider particular cases when the uniqueness can be established; we also consider an example of the formulation of a problem with a nonunique solution.

Consider acoustic vibrations in a liquid bounded by an infinite elastic plate (at $z = 0$) in the presence of a compact scatterer Ω. Let the wave process be station-

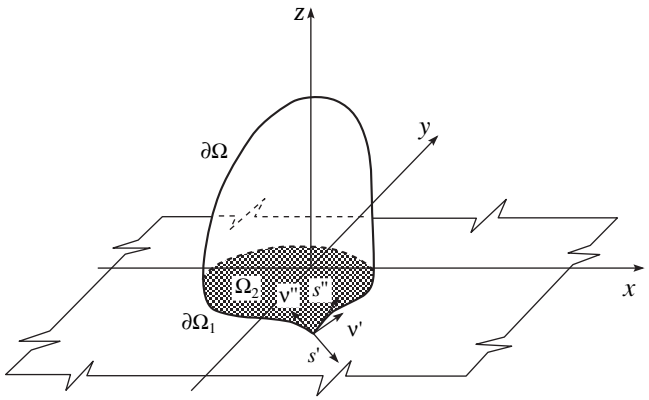

Fig. 1. Geometry of the problem.

ary and have the circular frequency ω. The pressure in the liquid is described by the Helmholtz equation

$$\Delta U(x, y, z) + \frac{\omega^2}{c^2} U(x, y, z) = 0, \quad z > 0. \tag{1}$$

Here, $\Delta = \partial^2/\partial x^2 + \partial^2/\partial y^2 + \partial^2/\partial z^2$ is the three-dimensional Laplacian and c is the velocity of sound. Vibrations of a thin plate obey the Kirchhoff theory

$$(D\Delta_\perp^2 - \rho_0 h\omega^2)\xi(x, y) + U(x, y, 0) = 0. \tag{2}$$

Here, $\Delta_\perp = \partial^2/\partial x^2 + \partial^2/\partial y^2$ is the two-dimensional Laplacian and D, ρ_0, and h are the parameters of the plate: the flexural rigidity ($D = \frac{1}{12} Eh^3(1 - \sigma^2)^{-1}$, where E is the Young modulus and σ is the Poisson ratio), the density, and the thickness. The function $\xi(x, y)$ describes the flexural displacements and is related to the acoustic pressure through the continuity condition

$$\xi(x, y) = \frac{1}{\rho\omega^2} \frac{\partial U(x, y, 0)}{\partial z}, \tag{3}$$

where ρ is the density of the acoustic medium.

We introduce the wave numbers of the acoustic waves $k = \omega/c$, the flexural waves in the isolated plate $k_0 = (\rho_0 h\omega^2/D)^{1/4}$, and the flexural waves for a plate in the medium κ; i.e., κ is a positive root of the dispersion equation

$$(\kappa^4 - k_0^4)\sqrt{\kappa^2 - k^2} = \frac{\rho\omega^2}{D}. \tag{4}$$

The radiation condition is imposed, which requires that the scattered field U^s cannot carry the energy from infinity. This condition can be represented in the form of two asymptotic expansions:

$$U^s \sim \frac{2\pi}{kr} \exp[ikr - i\pi/2]\Psi(\varphi, \vartheta), \quad r \longrightarrow +\infty, \tag{5}$$

$$U^s \sim \sqrt{\frac{2\pi}{\kappa r_\perp}} \exp[i\kappa r_\perp - i\pi/4]\Psi_\perp(\varphi)\exp[-\sqrt{\kappa^2 - k^2}\, z], \quad r_\perp \longrightarrow +\infty. \tag{6}$$

Here, $r = \sqrt{x^2 + y^2 + z^2}$ and $r_\perp = \sqrt{x^2 + y^2}$ are the radii in the spherical and cylindrical coordinate systems, respectively, and $\vartheta = \arccos(r_\perp/r)$ and φ are the azimuth and polar angles. Asymptotics (5) describes a diverging spherical wave with the pattern $\Psi(\varphi, \vartheta)$ propagating from the irregularity. It is valid in the cone $\vartheta \geq \vartheta_0$, where ϑ_0 is some constant angle, $\vartheta_0 > 0$. Asymptotics (6) describes a surface wave and is valid near the plate for a limited z. As a particular case, asymptotics (6) yields the asymptotics for the flexural displacements of the plate

$$\xi^s \sim \sqrt{\frac{2\pi}{\kappa r_\perp}} \exp[i\kappa r_\perp - i\pi/4]\Psi_\xi(\varphi), \quad r_\perp \longrightarrow +\infty, \tag{7}$$

which serves as the radiation condition in the problems on the vibrations of an isolated plate.

The scattering obstacle Ω may be of an arbitrary nature and may consist of one or several elastic or rigid bodies fixed on the plate or positioned separately (see Fig. 1). At the boundary of the region Ω, the boundary conditions (for example, the Dirichlet or Neumann conditions for a perfectly rigid or perfectly elastic body Ω, respectively) are imposed. If the body is fixed on the plate, contact conditions are imposed at the boundary $\partial\Omega_\perp$ of the contact region $\Omega_\perp$.

The scatterer Ω is assumed to be passive; i.e., it does not generate fields. The zero value of the energy generated by the scatterer is checked on the basis of the boundary and contact conditions, which leads to the inequality (derived below)

$$\mathrm{Im}\left(\int\int_{\partial\Omega} U \frac{\partial \bar{U}}{\partial n} dS + \rho\omega^2 \int_{\partial\Omega_\perp} \left(f\bar{\xi} + m\frac{\partial \bar{\xi}}{\partial \nu} \right) ds + \rho\omega^2 \sum_i F_i \bar{\xi}(x_i, y_i) \right) \geq 0. \tag{8}$$

Here and below, the overbar symbol means complex conjugation, n is the inner normal to the surface $\partial\Omega$ of the scattering obstacle, $\partial\Omega_\perp$ is the boundary of the region where the obstacle is fixed to the plate (Fig. 1), and ν is the inner normal to this boundary in the plane of the plate. The quantities f (the shearing force) and m (the bending moment) are represented as [18]

$$f = -D\left(\frac{\partial \Delta_\perp \xi}{\partial \nu} + (1 - \sigma)\left(\frac{\partial^3 \xi}{\partial \nu \partial s^2} - \frac{\partial}{\partial s} K(s) \frac{\partial \xi}{\partial s} \right) \right), \tag{9}$$

$$m = D\left(\Delta_\perp \xi - (1 - \sigma)\left(\frac{\partial^2 \xi}{\partial s^2} + K(s) \frac{\partial \xi}{\partial \nu} \right) \right). \tag{10}$$

Here, s and $K(s)$ are the arc length of the contour $\partial\Omega_\perp$ and its curvature. The summation in formula (8) is per-

formed over all corner points of $\partial\Omega_\perp$, and the quantities F_i have the meaning of the "corner" forces [19]

$$F = D(1-\sigma)$$
$$\times\left(\frac{\partial^2\xi}{\partial\nu'\partial s'} - K(s')\frac{\partial\xi}{\partial s'} - \frac{\partial^2\xi}{\partial\nu''\partial s''} + K(s'')\frac{\partial\xi}{\partial s''}\right).$$

The "corner" forces have the form of a jump at the salient point of the boundary, s' and ν' referring to the part of the boundary before the salient point and s'' and ν'', to the part after this point.

We will not consider particular boundary and contact conditions; in the following analysis, it will be sufficient to assume that condition (8) is satisfied.

Condition (8) provides that the energy-carrying field components are zero in the source-free problem; i.e., if the total field satisfies asymptotic formulas (5) and (6), the radiation patterns $\Psi(\vartheta, \varphi)$ and $\Psi_\perp(\varphi)$ are identically zero on the hemisphere and the circle, respectively. To verify this statement, we use Green's formula for the functions U and $\overline{U}$ in the region bounded by the scatterer, the plate, and a sphere of infinite radius R. We assume that R tends to infinity and use asymptotics (5) and (6). After separating the imaginary part, we derive

$$\frac{4\pi^2}{k}\int_0^{2\pi}\int_0^{\pi/2}|\Psi(\vartheta,\varphi)|^2\sin\vartheta\,d\vartheta\,d\varphi$$
$$+\pi\frac{D}{\rho\omega^2}(5\kappa^4 - 4\kappa^2k^2 - k_0^4)\int_0^{2\pi}|\Psi_\perp(\varphi)|^2 d\varphi \le 0. \quad (11)$$

Hence, since $\kappa > \max(k, k_0)$, we obtain

$$\Psi(\vartheta,\varphi)\equiv 0,\quad \vartheta\in[0,\pi/2],\quad \varphi\in[0,2\pi],$$
$$\Psi_\perp(\varphi)\equiv 0,\quad \varphi\in[0,2\pi].$$

Note that, for the field scattered from the irregularity, the left-hand side of inequality (11) is the scattering cross section, i.e., the scattered energy normalized by the energy per unit area of the wavefront of the incident plane wave [20].

A similar analysis for the two-dimensional case can be found in [14, 15].

Below, we will need the following two functions. One of them, Green's function for harmonic vibrations of the acoustic medium in the region $\mathbf{R}^3_+ = \{-\infty < x < +\infty, -\infty < y < +\infty, z > 0\}$ bounded by the elastic plate $\{z = 0\}$. This function is known (see, for example, [16]); it can be constructed by the Fourier method

$$G(\mathbf{r},\mathbf{r}_0) = \frac{1}{8\pi^2}\int\!\!\int_{\mathbf{R}^2}\exp(i\lambda(x-x_0)+i\mu(y-y_0))$$
$$\times\left(e^{-\gamma|z-z_0|} + \frac{\ell_+}{\ell_-}e^{-\gamma(z+z_0)}\right)\frac{d\lambda\,d\mu}{\gamma}. \quad (12)$$

Here,

$$\gamma = \sqrt{\lambda^2+\mu^2-k^2},$$
$$\ell_\pm = (D(\lambda^2+\mu^2)^2 - \rho_0 h\omega^2)\gamma \pm \rho\omega^2.$$

The other function is the surface Green function for the same problem, which describes the field of a point source located on the plate:

$$g(\mathbf{r}, x_0, y_0) = \frac{\rho\omega^2}{4\pi^2}$$
$$\times\int\!\!\int_{\mathbf{R}^2}\frac{1}{\ell_-}\exp(i\lambda(x-x_0)+i\mu(y-y_0)-\gamma z)d\lambda\,d\mu. \quad (13)$$

The integration in Eqs. (12) and (13) is performed according to the ultimate absorption principle.

By calculating the integrals at large r with the help of the saddle-point technique, one can easily verify that the functions $G(\mathbf{r}, \mathbf{r}_0)$ and $g(\mathbf{r}, x_0, y_0)$ satisfy asymptotics (5) and (6) and have the patterns

$$\Psi^{(G)} = \frac{ik}{8\pi^2}\exp(-ikx_0\cos\vartheta\cos\varphi$$
$$-iky_0\cos\vartheta\sin\varphi)\Bigg\{\exp(-ikz_0\sin\vartheta)$$
$$+\frac{ikD\sin\vartheta(k^4\cos^4\vartheta - k_0^4) - \rho\omega^2}{ikD\sin\vartheta(k^4\cos^4\vartheta - k_0^4) + \rho\omega^2}\exp(ikz_0\sin\vartheta)\Bigg\},$$
$$\Psi^{(g)} = -\frac{\partial\Psi^{(G)}(\vartheta,\varphi,x_0,y_0,0)}{\partial z_0}.$$

The surface wave patterns $\Psi_\perp^{(G)}$ and $\Psi_\perp^{(g)}$ are obtained from the patterns $\Psi^{(G)}$ and $\Psi^{(g)}$ as

$$\Psi_\perp(\varphi) = -2\pi i\frac{\kappa}{k}\operatorname*{Res}_{\vartheta=\vartheta^*}\Psi(\vartheta,\varphi)$$
$$\vartheta^* = \arccos(\kappa/k) = i\ln\left(\frac{\kappa}{k} + \sqrt{\left(\frac{\kappa}{k}\right)^2 - 1}\right). \quad (14)$$

A similar formula for two-dimensional problems was derived in [21].

We change the integration variables $\lambda = k\cos\vartheta\cos\varphi$ and $\mu = k\cos\vartheta\sin\varphi$ in Eq. (12) so that $\gamma = -ik\sin\vartheta$. Using the explicit expression for the pattern $\Psi^{(G)}$, one can easily show that the following formula is valid for $z > z_0$:

$$G(\mathbf{r},\mathbf{r}_0) = -\int\!\!\int\Psi^{(G)}(\vartheta,\varphi,\mathbf{r}_0)$$
$$\times\exp(ik(x\cos\vartheta\cos\varphi + y\cos\vartheta\sin\varphi + z\sin\vartheta))$$
$$\times\cos\vartheta\,d\vartheta\,d\varphi. \quad (15)$$

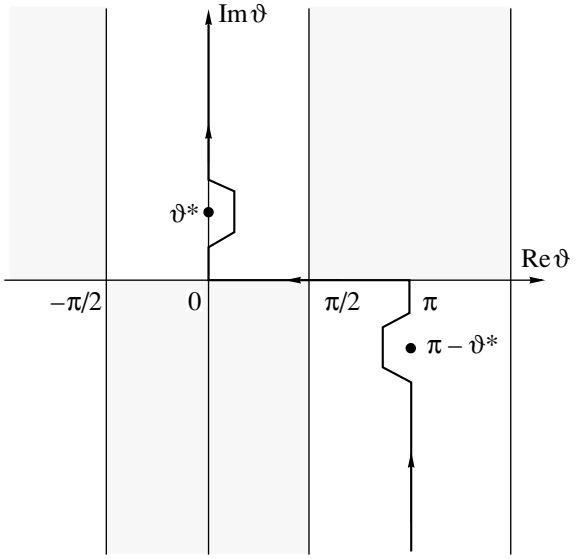

Fig. 2. Modified Sommerfeld's path.

Two versions of the integration path are possible here: (i) the integration with respect to ϑ is performed along Sommerfeld's path $(\pi - i\infty, +i\infty)$ bypassing the point $\vartheta = \pi - \vartheta^*$ on the left and the point $\vartheta = \vartheta^*$ on the right (the same path as in the two-dimensional case [15], see Fig. 2), and the integration with respect to φ is performed within $[0, \pi]$; (ii) the integration with respect to ϑ is performed along a half of Sommerfeld's path $(\pi/2, +i\infty)$ bypassing the point $\vartheta = \vartheta^*$ on the right, and the integration with respect to φ is performed within $[0, 2\pi]$.

Now, we derive a similar formula for the solution U to the boundary-value problem. We select a smooth surface Σ supported by a smooth contour Γ on the plate, so that the whole region Ω is within Σ. We consider Green's formula for the functions G and U in the region bounded by the plate, the surface Σ, and a hemisphere of large radius R. The relationship between the functions G and g, $g = -\partial G/dz_0|_{z=0}$, and condition (3) yields the identity

$$U(\mathbf{r}_0) = \int_\Sigma \left(U(\mathbf{r}) \frac{\partial G(\mathbf{r}_0, \mathbf{r})}{\partial n} - \frac{\partial U(\mathbf{r})}{\partial n} G(\mathbf{r}_0, \mathbf{r}) \right) d\Sigma$$
$$+ \int_\Gamma \left(\xi(\mathbf{r}_\perp) f_g(\mathbf{r}_0, \mathbf{r}_\perp) - f(\mathbf{r}_\perp) g(\mathbf{r}_0, \mathbf{r}_\perp) \right. \tag{16}$$
$$\left. + \frac{\partial \xi(\mathbf{r}_\perp)}{\partial \nu} m_g(\mathbf{r}_0, \mathbf{r}_\perp) - m(\mathbf{r}_\perp) \frac{\partial g(\mathbf{r}_0, \mathbf{r}_\perp)}{\partial \nu} \right) d\ell.$$

Identity (16) allows one to calculate the field U at any point outside the surface Σ if the functions U, $\partial U/\partial n$, ξ, $\partial \xi/\partial \nu$, m, and f are known at the surface Σ and at the contour Γ. In particular, when $\mathbf{r}_0$ tends to infinity, identity (16) yields the formula that expresses the pattern $\Psi(\vartheta, \varphi)$ in terms of $\Psi^{(G)}$ and $\Psi^{(g)}$:

$$\Psi(\vartheta, \varphi) = \int_\Sigma \left(U(\mathbf{r}) \frac{\partial \Psi^{(G)}(\vartheta, \varphi, \mathbf{r})}{\partial n} \right.$$
$$\left. - \frac{\partial U(\mathbf{r})}{\partial n} \Psi^{(G)}(\vartheta, \varphi, \mathbf{r}) \right) d\Sigma$$
$$+ \int_\Gamma (\xi(\mathbf{r}_\perp) \mathbf{f} \Psi^{(g)}(\vartheta, \varphi, \mathbf{r}_\perp) - f(\mathbf{r}_\perp) \Psi^{(g)}(\vartheta, \varphi, \mathbf{r}_\perp) \tag{17}$$
$$\left. + \frac{\partial \xi(\mathbf{r}_\perp)}{\partial \nu} \mathbf{m} \Psi^{(g)}(\vartheta, \varphi, \mathbf{r}_\perp) - m(\mathbf{r}_\perp) \frac{\partial \Psi^{(g)}(\vartheta, \varphi, \mathbf{r}_\perp)}{\partial \nu} \right) d\ell.$$

Here, $\mathbf{f}$ and $\mathbf{m}$ are the force and moment operators from formulas (9) and (10). In particular, Eq. (17) determines the analytical properties of the function Ψ. Since the integration is performed over a finite region, these properties are inherited from the functions $\Psi^{(G)}$ and $\Psi^{(g)}$; i.e., the function Ψ is a meromorphic function of ϑ and has poles at the points that correspond to the solutions to dispersion equation (4). The pole at $\vartheta = \vartheta^*$ corresponds to the wave propagating along the plate. The patterns Ψ and $\Psi_\perp$ comply with Eq. (14).

Using Eq. (15) for Green's functions G and g and Eq. (17), one can easily obtain a formula for U that is similar to Eq. (15):

$$U(\mathbf{r}) = -\iint \Psi(\vartheta, \varphi) \exp(ik(x\cos\vartheta\cos\varphi + y\cos\vartheta\sin\varphi + z\sin\vartheta)) \cos\vartheta \, d\vartheta \, d\varphi. \tag{18}$$

In this formula, the integration paths are the same as in Eq. (15). Formula (18) is valid at a certain distance from the plate, for $z > z^* = \max_\Sigma z$. When this condition is met, the integral with respect to ϑ converges exponentially in the semi-infinite bands that are free from shading in Fig. 2.

Note that formula (18) is known for the problems of diffraction by finite obstacles [22]. It can be used to construct a solution by the method of the pattern integral equations [22, 23].

Let us assume that two solutions, V and W, exist for the boundary-value problem determined by Eqs. (1)–(3) with a given source of the field (including the plane wave). Then, the difference $U = V - W$ is a solution to the source-free boundary-value problem. As shown above, condition (8) ensures that the patterns Ψ and $\Psi_\perp$ and the field U are zero at real observation angles. Since Ψ is analytical with respect to ϑ, Ψ is equal to zero throughout the entire complex plane ϑ and, in particular, on the integration path in Eq. (18) (see Fig. 2). Formula (18) thus shows that the function U is zero for $z > z^*$. The extension of U below z^* is zero, because, if a solution to the Helmholtz equation is zero in a certain region, it is identically zero. As a result, the solutions V and W coincide. Due to condition (3), the respective

plate displacements also coincide, which proves the following theorem:

Theorem 1. The solution to problem (1)–(3) with arbitrary boundary conditions that satisfy inequality (8) is unique.

Consider now the problem of diffraction by an isolated plate. This problem consists in constructing a solution to the equation

$$D\Delta_\perp^2\xi(x, y) - \rho_0 h\omega^2\xi(x, y) = 0 \qquad (19)$$

with certain boundary conditions imposed on the obstacle and with radiation conditions (7) at infinity.

As before, we assume that the problem is well-posed if the boundary conditions at the obstacle satisfy the inequality

$$\mathrm{Im}\left(\int\limits_{\partial\Omega_\perp}\left(f\bar{\xi} + m\frac{\partial\bar{\xi}}{\partial\nu}\right)ds + \sum_i F_i\bar{\xi}(x_i, y_i)\right) \geq 0. \qquad (20)$$

We note that inequality (20) coincides with inequality (8) when $U \equiv 0$.

The proof obtained above for the uniqueness of the solution to well-posed problem (1)–(3) relies on formula (18), which reconstructs the acoustic field from its radiation pattern. This formula is valid for the solution to the Helmholtz equation in the entire space or in a halfspace bounded by a perfect or impedance (including the generalized-impedance) baffle. A solution to Eq. (19), which describes flexural vibrations of an isolated plate, cannot be expressed by a formula similar to Eq. (18), and the question concerning the uniqueness of the solution to the boundary-value problem for the isolated plate proves to be more complicated. As before, the boundary conditions and condition (20) entail that $\Psi_\xi \equiv 0$; however, in general, the field $\xi^s(x, y)$ can be nonzero.

Let us consider the function

$$\zeta(x, y) = (\Delta_\perp - k_0^2)\xi(x, y).$$

As follows from asymptotics (7), the function $\zeta(x, y)$ satisfies condition (7) with the pattern $\Psi_\zeta = -2k_0^2\Psi_\xi$. From Eq. (19), it follows that the function $\zeta(x, y)$ also satisfies the Helmholtz equation with the wave number k_0. Thus, by virtue of the two-dimensional analog of Eq. (18) (see [15])

$$\zeta(x, y) = -\int\limits_{\pi - i\infty}^{+i\infty}\Psi_\zeta(\varphi)\exp(ik(x\cos\varphi + y\sin\varphi))d\varphi,$$

the function $\zeta(x, y)$ is identically equal to zero. Therefore, a solution to the source-free boundary-value problem satisfies the equation

$$\Delta_\perp\xi(x, y) - k_0^2\xi(x, y) = 0, \qquad (21)$$

which differs from the Helmholtz equation only in sign, with certain boundary conditions at the obstacle boundary. The number of such conditions is determined by the order of the operator in Eq. (19), which makes the boundary-value problem for Eq. (21) overdetermined.

Let us first consider the boundary conditions for a fixed or hinged edge. That is, let the condition

$$\xi = 0 \qquad (22)$$

or

$$\frac{\partial\xi}{\partial\nu} = 0 \qquad (23)$$

be valid on the entire contour $\partial\Omega_\perp$, or let condition (22) be valid on a part of the contour and condition (23) be valid on the remaining part of the contour. In this case, the solution is unique, which follows directly from Green's formula. Multiply both sides of Eq. (21) by $\bar{\xi}$ and perform the integration by parts. When field sources are absent, the integral over the circle of large radius vanishes in the limit, which leads to the identity

$$\begin{aligned} 0 &= \int\limits_{\mathbf{R}^2\setminus\Omega_\perp}\int (\Delta_\perp\xi - k_0^2\xi)\bar{\xi}dS \\ &= -\int\limits_{\mathbf{R}^2\setminus\Omega_\perp}\int (|\nabla_\perp\xi|^2 + k_0^2|\xi|^2)dS + \int\limits_{\partial\Omega_\perp}\frac{\partial\xi}{\partial\nu}\bar{\xi}d\ell. \end{aligned} \qquad (24)$$

Here, $\nabla_\perp$ is the two-dimensional gradient with respect to the coordinates x and y. By virtue of conditions (22) and (23), the contour integral vanishes and, hence, $\xi \equiv 0$. Thus, the following theorem is valid:

Theorem 2. A solution to the boundary-value problem for Eq. (19) outside an arbitrary finite region Ω is unique if the boundary conditions are such that $\xi = 0$ on a part of the boundary, Γ_1, and $\partial\xi/\partial\nu = 0$ on the remaining part of the boundary, $\Gamma_2 = \partial\Omega_\perp\setminus\Gamma_1$.

Now, let the boundary conditions for ξ be such that neither condition (22) nor condition (23) is satisfied on a part of the boundary. For example, let the edge be free:

$$f = 0, \quad m = 0$$

or, in the general case,

$$f = Z_f\xi, \quad m = Z_m\frac{\partial\xi}{\partial\nu}, \tag{25}$$

where Z_f and Z_m mean the force and moment impedances. In particular, Z_f and Z_m may be constant quantities, functions of a point of the contour, or differential operators with respect to the tangential to the contour.

To establish the uniqueness theorem for the boundary-value problem for Eq. (19) with boundary conditions (25), it is sufficient to show that, for a solution to the source-free problem, we have

$$\int\limits_{\partial\Omega_\perp}\frac{\partial\xi}{\partial\nu}\bar{\xi}d\ell \le 0. \tag{26}$$

Then, as in the case of conditions (22) and (23), identity (24) immediately implies that ξ is zero. However, it was found that, when the contour $\partial\Omega_\perp$ is of a general type and when natural assumptions are made for the impedances Z_f and Z_m, the validity of condition (26) cannot be proved, and, moreover, we provide below an example of a system in which a localized wave exists, which means that a solution to the diffraction problem is not unique.

Consider the vibrations of an elastic plate with a circular aperture of radius R and impose the impedance conditions

$$f = \omega^2 M\xi, \quad m = \omega^2 J\xi_\nu \tag{27}$$

on the edge of the aperture. Here, M and J are the per-unit-length virtual mass and moment of inertia (it is taken into account that f and m are the force and moment that act on the plate).

Let us determine the values of the impedances at which a wave localized near the aperture can exist. As shown above, such a wave must satisfy Eq. (21); i.e., it must have the form

$$\xi = K_j(k_0 r)e^{ij\varphi}, \tag{28}$$

where $K_j(k_0 r)$ is the Macdonald function.

Note that, in the general case, the solution to the problem has the form

$$(\alpha H_j^{(1)}(k_0 r) + \beta K_j(k_0 r))e^{ij\varphi}.$$

However, we will select M and J so as to make the coefficient α equal to zero. Substituting expression (28) into impedance conditions (27) and calculating the force f and the moment m from formulas (9) and (10), we obtain

$$\frac{\omega^2}{D}M = k_0^3\left\{\left[1-(1-\sigma)\frac{j^2}{(k_0R)^2}\right]\frac{K_j'(k_0R)}{K_j(k_0R)} + (1-\sigma)\frac{j^2}{(k_0R)^3}\right\},$$

$$\frac{\omega^2}{D}J = k_0\left\{\frac{1-\sigma}{k_0R} - \left[1+(1-\sigma)\frac{j^2}{(k_0R)^2}\right]\frac{K_j(k_0R)}{K_j'(k_0R)}\right\}.$$

It is convenient to compare the quantities M and J with the mass M_0 and the moment of inertia (with respect to the edge) J_0 of a circular sector $R\,d\varphi$:

$$M_0 = \frac{1}{2}h\rho_0 R^2 d\varphi, \quad J_0 = \frac{1}{12}h\rho_0 R^4 d\varphi.$$

Since $h\rho_0\omega^2/D = k_0^4$, we obtain

$$\frac{M}{M_0} = \frac{2}{k_0R}\left\{\left[1-(1-\sigma)\frac{j^2}{(k_0R)^2}\right]\frac{K_j'(k_0R)}{K_j(k_0R)} + (1-\sigma)\frac{j^2}{(k_0R)^3}\right\},$$

$$\frac{J}{J_0} = \frac{12}{(k_0R)^3}\left\{\frac{1-\sigma}{k_0R} - \left[1+(1-\sigma)\frac{j^2}{(k_0R)^2}\right]\frac{K_j(k_0R)}{K_j'(k_0R)}\right\}.$$

Figure 3 represents the mass and the moment of inertia as functions of the parameter k_0R for several first indexes j. For $j \neq 0$, the force impedance can be positive as well as negative (which corresponds to the elasticity impedance). The moment impedance is always positive. An example of a continuous natural vibration performed by an infinite plate so that it is localized near the irregularity and equal to zero in the far-field zone is given in [25].

If the plate is in contact with an acoustic medium, the uniqueness of the solution follows from the absence of the energy-carrying field components at infinity. For a plate in free space, we managed to prove the uniqueness theorem for a solution to the problem of diffraction by a finite obstacle only for the case of a fixed or hinged edge. Using an example, we showed that in the case of general-type impedance boundary conditions, the existence of a localized solution is possible, which

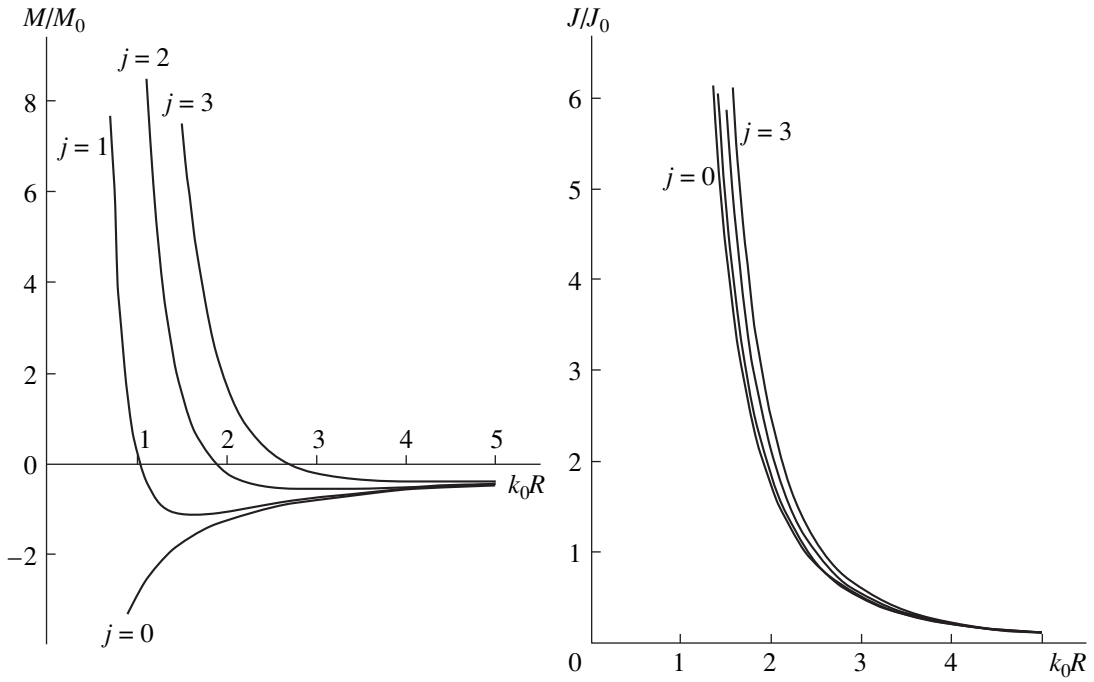

Fig. 3. Normalized mass M/M_0 and moment J/J_0 impedances versus the aperture size in terms of the wavelength at $\sigma = 1/3$.

leads to a nonuniqueness of the solution. For the localized solution to exist, the boundary conditions at the obstacle must be matched in a special manner.

ACKNOWLEDGMENTS

This work was supported by the Russian Foundation for Basic Research, project no. 99-02-16844 and, in part, by the UTC Center of Excellence in Computer Applications Scholarship.

REFERENCES

1. L. M. Lyamshev, *Sound Reflection by Thin Plates and Covers in a Liquid* (Akad. Nauk SSSR, Moscow, 1955).
2. V. N. Krasil'nikov, Prikl. Mat. Mekh. **25**, 764 (1961).
3. D. P. Kouzov, Prikl. Mat. Mekh. **27**, 1037 (1963).
4. D. P. Kouzov, Prikl. Mat. Mekh. **33**, 240 (1969).
5. B. P. Belinskiĭ, Prikl. Mat. Mekh. **42**, 486 (1978).
6. E. L. Shenderov, *Wave Problems in Hydroacoustics* (Sudostroenie, Leningrad, 1972).
7. B. P. Belinskiĭ and V. A. Veshev, Akust. Zh. **32**, 519 (1986) [Sov. Phys. Acoust. **32**, 324 (1986)].
8. G. Ya. Popov, *Concentration of Elastic Stresses near Stamps, Sections, Thin Inclusion, and Strengthenings* (Nauka, Moscow, 1982).
9. I. D. Abrahams, Proc. R. Soc. London, Ser. A **378**, 89 (1981).
10. I. V. Andronov, Prikl. Mat. Mekh. **54**, 312 (1990).
11. I. V. Andronov and B. P. Belinskiĭ, Prikl. Mat. Mekh. **61**, 202 (1997).
12. A. N. Tikhonov and A. A. Samarskiĭ, *Equations of Mathematical Physics* (Gostekhteorizdat, Moscow, 1953).
13. B. P. Belinskiĭ, Vestn. Leningr. Univ., Ser. 1: Mat., Mekh., Astron. **13** (3), 5 (1983).
14. B. P. Belinskiĭ, Zap. Nauchn. Semin. LOMI **128** (13), 21 (1983).
15. I. V. Andronov and B. P. Belinskiy, J. Phys. A: Math. Gen. **31**, L405 (1998).
16. I. V. Andronov, J. Math. Phys. **34**, 2226 (1993).
17. A. G. Kyurkchan, in *Proceedings of VIII All-Union Symposium on Difraction and Wave Propagation* (1982), Vol. 1, p. 329.
18. S. G. Mikhlin, *Variation Methods in Mathematical Physics* (GITTL, Moscow, 1957).
19. B. P. Belinskiĭ and D. P. Kouzov, Akust. Zh. **27**, 710 (1981) [Sov. Phys. Acoust. **27**, 394 (1981)].
20. I. V. Andronov, Akust. Zh. **39**, 13 (1993) [Acoust. Phys. **39**, 5 (1993)].
21. I. V. Andronov, B. P. Belinskiy, and J. P. Dauer, J. Sound Vibr. **195**, 667 (1996).
22. A. G. Kyurkchan and A. I. Kleev, *Radiotekh. Elektron.* (Moscow) **40** (6), 897 (1995).
23. A. G. Kyurkchan, Dokl. Akad. Nauk **325** (2), 273 (1992) [Sov. Phys. Dokl. **37** (7), 338 (1992)].
24. V. F. Apel'tsin and A. G. Kyurkchan, *Analytical Properties of Wave Fields* (Mosk. Gos. Univ., Moscow, 1990).
25. Yu. I. Bobrovnitskiĭ and M. P. Korotkov, Akust. Zh. **37**, 872 (1991) [Sov. Phys. Acoust. **37**, 453 (1991)].

Translated by A. Khzmalyan

Acoustical Physics, Vol. 47, No. 1, 2001, pp. 35–41. Translated from Akusticheskiĭ Zhurnal, Vol. 47, No. 1, 2001, pp. 44–51.
Original Russian Text Copyright © 2001 by Grigor'ev, Katsnel'son, Kuz'kin, Petnikov.

Characteristics of the Diffraction of Acoustic Waves in Stratified Sound Channels

V. A. Grigor'ev*, B. G. Katsnel'son*, V. M. Kuz'kin, and V. G. Petnikov****

** Voronezh State University, Universitetskaya pl. 1, Voronezh, 394693 Russia*

*** Wave Research Center, General Physics Institute, Russian Academy of Sciences, ul. Vavilova 38, Moscow, 117942 Russia*

e-mail: petnikov@kapella.gpi.ru

Received December 30, 1999

Abstract—The results of calculations performed in the framework of the approximate approach developed by the authors are presented for the diffraction of sound waves by a stiff spheroid in an acoustic waveguide. The scattered sound field is analyzed as a function of the following parameters of the problem: the spheroid dimensions, its position relative to the sound source and the receiver, the vertical profile of sound velocity in the waveguide, and the acoustic parameters of the waveguide bottom. *© 2001 MAIK "Nauka/Interperiodica".*

It is well known that the inner boundary-value problem of the wave field diffraction by spatially localized inhomogeneities in inhomogeneous waveguides is extremely complicated from the mathematical point of view. In most cases, an exact solution of this problem is impossible, and, in practice, researchers use one or another approximate method of those described in the review by Gorskiĭ *et al.* [1]. However, such methods also require much calculation. Therefore, the results obtained in this area of research [1–6] are insufficiently representative and do not allow one to study the space-time variability of the diffracted sound field as a function of the parameters of the problem, such as the wavelength, the refraction index in the waveguide, the characteristics of the halfspace underlying the waveguide, and the parameters of the inhomogeneity itself (the dimensions and the coordinates that determine its position in the waveguide). This study is intended to partially fill the aforementioned gap for oceanic sound channels.

For our calculations, we use the approximate approach [7] based on the representation of the scattering matrix of the waveguide modes in terms of the scattering amplitude of a body in free space. Such an approach is highly efficient from the computational point of view, because it allows one to divide the problem into two parts: the determination of the scattering amplitude in free space and the determination of the sound field at a given distance from the sound source.

Let us consider this approach in greater detail, because, in this study, the approach is applied in a new form, without using the WKB approximation, as in the cited paper [7]. (In our case, the range of its applicability extends to the lower frequency region.) Let the waveguide consist of a water layer of depth H with the density $\rho(z)$ and the sound velocity $c(z)$; the water layer lies on an absorbing bottom, which can be characterized by different parameters (the density, the sound velocity, and the damping factor for acoustic waves). We introduce a coordinate system fixed to the waveguide (the x–y plane coincides with the sea surface, and the z-axis is vertical and directed downward) and consider a point source and a receiver with the coordinates $(0, 0, z_0)$ and (x, y, z), respectively. We denote the radius-vector of the point of reception by $\mathbf{R}$. We also introduce a coordinate system (x', y', z') fixed to the scatterer and having its origin at a point taken as the scatterer center. Below, the coordinates of this point (x_s, y_s, z_s) will be called the scatterer coordinates (for the sake of brevity). In addition, we define the radius-vectors in the horizontal plane, $\mathbf{r}_s$ and $\mathbf{r}$, for the scatterer and receiver positions, respectively. The sound field at the reception point, $P(\mathbf{R})$, which is the object of our study, can be represented as the sum of the direct $P_0(\mathbf{R})$ and scattered $P_s(\mathbf{R})$ fields:

$$P(\mathbf{R}) = P_0(\mathbf{R}) + P_s(\mathbf{R}). \quad (1)$$

To calculate the scattered sound field, we use the following integral representation [2–4]

$$P_s(\mathbf{R}) = \int \nu(\mathbf{R}')G(\mathbf{R}, \mathbf{R}')d\mathbf{R}', \quad (2)$$

where $\nu(\mathbf{R})$ is the density of imaginary sources distributed over the surface or throughout the volume of the scatterer and $G(\mathbf{R}, \mathbf{R}')$ is Green's function. The integration is performed within the scatterer over some surface or volume, depending on the kind of the source we introduce (the surface source or the volume source). The unknown function $\nu(\mathbf{R})$ is determined from the conditions for the field at the scatterer surface $\hat{S}$. Spe-

cifically, for a perfectly rigid scatterer, this condition is as follows:

$$\frac{\partial}{\partial n}[P_i(\mathbf{R}) + \int \nu(\mathbf{R}')G(\mathbf{R}, \mathbf{R}')d\mathbf{R}']_{\mathbf{R} \in \hat{S}} = 0, \quad (3)$$

where $P_i(\mathbf{R})$ is the field incident on the scatterer.

For the diffraction problem in a waveguide, such an equation is usually solved numerically (see, e.g., [5]) using the approximation of the unknown function $\nu(\mathbf{R})$ by a step function. By contrast, our approach is based on the assumption that, in the vicinity of the scatterer, the medium varies smoothly, and, in this vicinity, we can assume that Green's function coincides with that of free space, $G_0(\mathbf{R}, \mathbf{R}')$. In this case, the source function $\nu(\mathbf{R})$ corresponds to the solution to the problem of scattering by an object in a homogeneous space and is considered to be known (we denote it by $\nu_0(\mathbf{k}_i, \mathbf{R})$). Formally, this function is the solution to the integral equation, which, for a perfectly rigid scatterer, has the form

$$\frac{\partial}{\partial n}[\exp(i\mathbf{k}_i\mathbf{R}) + \int \nu_0(\mathbf{k}_i, \mathbf{R}')G_0(\mathbf{R}, \mathbf{R}')d\mathbf{R}']_{\mathbf{R} \in \hat{S}} = 0, \quad (4)$$

where $G_0(\mathbf{R}, \mathbf{R}') = \dfrac{\exp[ik(z_s)|\mathbf{R} - \mathbf{R}'|]}{4\pi|\mathbf{R} - \mathbf{R}'|}$. In our calculations, to characterize the scattering by an object in an unbounded homogeneous medium, it will be convenient to use the scattering amplitude

$$F(\mathbf{k}_i, \mathbf{k}_s) = \frac{1}{4\pi}\int \nu_0(\mathbf{k}_i, \mathbf{R}')\exp(-i\mathbf{k}_s\mathbf{R}')d\mathbf{R}. \quad (5)$$

Here, $\mathbf{k}_i$ and $\mathbf{k}_s$ are the wave vectors of the incident and scattered waves, respectively. We note that the scattering amplitude can be expressed through the angles θ and φ in the spherical coordinate system fixed to the scatterer where these angles determine the propagation directions of the incident and scattered plane waves:

$$F(\mathbf{k}_i^{\pm}, \mathbf{k}_s^{\pm}) \equiv F(\theta_i, \varphi_i, \theta_s, \varphi_s).$$

Using the mode representation of the sound field in a waveguide [9], we represent the sound wave in the form

$$\begin{aligned} P(r, z) &= \sum_m b_m(r)\psi_m(z) \\ &= \sum_m a_m\psi_m(z)\frac{\exp[iq_m r]}{\sqrt{q_m r}}\exp[-\gamma_m r/2], \end{aligned} \quad (6)$$

where $\psi_m(z)$ and ξ_m are the eigenfunctions and eigenvalues of the Sturm–Liouville boundary-value problem ($\xi_m = q_m + i\gamma_m/2$). In the case of an omnidirectional point source of power W_0, the coefficients are expressed as $a_m = \sqrt{\rho_0 c_0 W_0}e^{i\frac{\pi}{4}}\psi_m(z_0)$ (where ρ_0 and c_0 are the density and sound velocity in the waveguide at the source site). To obtain the function $\nu(\mathbf{R})$ and, hence, the scattered field, we determine the incident field near the scatterer where the medium is assumed to be homogeneous and weakly absorbing. When the variations of the primed arguments are small, for the functions involved in the expression for the incident field, we obtain

$$\begin{aligned} \psi_m(z_s + z') &\cong a_m^+\exp(i\boldsymbol{\sigma}_m\mathbf{R}) + a_m^-\exp(-i\boldsymbol{\sigma}_m\mathbf{R}'), \\ &\frac{\exp[iq_m|\mathbf{r}_s - \mathbf{r}'|]}{\sqrt{q_m|\mathbf{r}_s - \mathbf{r}'|}}\exp(-\gamma_m|\mathbf{r}_s - \mathbf{r}'|/2) \\ &\cong \frac{\exp[iq_m r_s]}{\sqrt{q_m r_s}}\exp[i\mathbf{q}_m\mathbf{R}']\exp(-\gamma_m r_s/2). \end{aligned} \quad (7)$$

Then, we have

$$\begin{aligned} P_i(\mathbf{R}_s + \mathbf{R}') &= \sum_m a_m\psi_m(z_s + z') \\ &\times \frac{\exp[iq_m|\mathbf{r}_s - \mathbf{r}'|]}{\sqrt{q_m|\mathbf{r}_s - \mathbf{r}'|}}\exp[-\gamma_m|\mathbf{r}_s - \mathbf{r}'|/2] \\ &\cong \sum_m b_m(r_s)[a_m^+\exp(i\mathbf{k}_m^+\mathbf{R}') + a_m^-\exp(i\mathbf{k}_m^-\mathbf{R}')], \end{aligned} \quad (8)$$

where $\boldsymbol{\sigma}_m$ is a vector directed along the z axis with the magnitude $\sigma_m = \sqrt{k^2(z_s) - q_m^2}$, $a_m^{\pm} = \dfrac{1}{2}\left[\psi_m(z) \pm \dfrac{d\psi_m/dz}{i\sigma_m}\right]_{z = z_s}$, and $\mathbf{k}_m^{\pm}$ are the wave vectors with the horizontal and vertical components $(\mathbf{q}_m, \pm\boldsymbol{\sigma}_m)$, respectively. Substituting the incident field (8) into Eq. (3), which determines the condition for the unknown function $\nu(\mathbf{R})$, we derive the expression

$$\nu(\mathbf{R}) = \sum_m b_m(r_s)[a_m^+\nu_0(\mathbf{k}_m^+, \mathbf{R}') + a_m^-\nu_0(\mathbf{k}_m^-, \mathbf{R}')]. \quad (9)$$

Calculating the scattered field (2) with Green's function of the waveguide and using the approximation (7) for the eigenfunctions near the scatterer, we obtain an expression for the scattered field at the reception point:

$$\begin{aligned} P_s(\mathbf{r}, z) &= \sqrt{\frac{i}{8\pi}}\sum_\mu b_\mu(r_s)\psi_\mu(z) \\ &\times \frac{\exp[iq_m|\mathbf{r} - \mathbf{r}_s|]}{\sqrt{q_m|\mathbf{r} - \mathbf{r}_s|}}\exp[-\gamma_m|\mathbf{r} - \mathbf{r}_s|/2], \end{aligned} \quad (10)$$

where

$$b_\mu(r_s) = \sum_m S_{\mu m}b_m(r_s) \quad (11)$$

and $S_{\mu m}$ is the scattering matrix which has the form

$$\begin{aligned} S_{\mu m} &= 4\pi[a_m^+a_\mu^+F(\mathbf{k}_m^+, \mathbf{k}_\mu^+) + a_m^+a_\mu^-F(\mathbf{k}_m^+, \mathbf{k}_\mu^-) \\ &+ a_m^-a_\mu^+F(\mathbf{k}_m^-, \mathbf{k}_\mu^+) + a_m^-a_\mu^-F(\mathbf{k}_m^-, \mathbf{k}_\mu^-). \end{aligned} \quad (12)$$

We note that Eq. (12) allows one to use any known scattering amplitude for a smooth body in free space, including the one measured in the experiment.

It should be noted that the described approach is valid on condition that the effects of multiple scattering are small, and the medium is homogeneous in the vicinity of the scatterer. In other words, the scattering body must be offset from the waveguide boundary by a distance h that exceeds the horizontal dimensions of the body l (i.e., $h \geq l$), and the variations of the vertical wave vector $\boldsymbol{\sigma}_m$ that occur along the z axis at a distance equal to the vertical dimension of the body d must be small; i.e., $d < L_{\sigma_m} \equiv \dfrac{\sigma_m}{d\sigma_m/dz}$. If we take into account that the relationship $\sigma_m \cong m\pi/H$ is valid within an order of magnitude (the case of the exact equality corresponds to the Pekeris model [9]) and, in addition, we have $L_{\sigma_m} \cong \left.\dfrac{\sigma_m^2}{k|dk/dz|}\right|_{z=z_s}$, the second of the two aforementioned conditions can be represented in the form

$$d < \frac{c\lambda^2}{4H^2|dc/dz|}. \tag{13}$$

For calculating the diffraction field in a waveguide by the method described above, we selected the scattering body in the form of an acoustically stiff spheroid elongated in the horizontal plane, with the short axis d and the long axis l. The choice of the model was determined by the fact that the problem of scattering by a spheroid allows a rigorous analytical solution [10]. This makes it possible to adequately describe the fine structure of the diffraction field and to study its dependence on the scatterer dimensions.

We restrict our consideration to the case of monochromatic radiation of frequency f and assume that the scatterer changes its position in the horizontal plane by moving normally to the base line connecting the source with the receiver (Fig. 1). The horizontal distance from the point where the object crosses the base line to the source will be denoted by r_{0s}.

The scattering amplitude for a spheroid has the form [10]

$$F(k_m^{\pm}, k_\mu^{\pm}) = \frac{2i}{k}\sum_{n=0}^{\infty}\sum_{l=n}^{\infty}\varepsilon_n S_{nl}(\chi, \cos\theta_m^{\pm}) \times S_{nl}(\chi, \cos\theta_\mu^{\pm})\frac{R_{nl}^{(1)'}(\chi, \vartheta)}{R_{nl}^{(3)'}(\chi, \vartheta)}\cos[n(\varphi_m^{\pm} - \varphi_\mu^{\pm})], \tag{14}$$

where $\varepsilon_n = \begin{cases} 1, & n = 0 \\ 2, & n \neq 0 \end{cases}$ is the Neumann symbol; S_{nl}, $R_{nl}^{(1)}$, and $R_{nl}^{(3)}$ are angular and radial prolate spheroidal functions of the first and third kinds (the primes marking the radial functions mean their derivatives with respect to ϑ); $\chi = (k/2)\sqrt{l^2 - d^2}$ and $\vartheta = l/\sqrt{l^2 - d^2}$ are the parameters of the spheroid that characterize its wave dimensions and degree of elongation; and

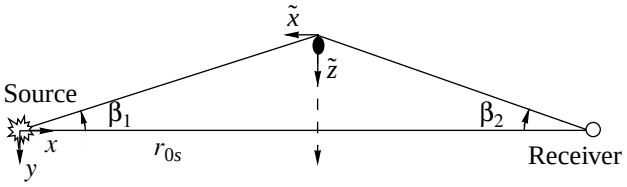

Fig. 1. Schematic diagram of the numerical experiment.

$$\begin{aligned}
\theta_m^+ &= \theta_m^- = \arccos\left(-\frac{q_m \sin\beta_1}{k}\right), \\
\theta_\mu^+ &= \theta_\mu^- = \arccos\left(\frac{q_\mu \sin\beta_2}{k}\right), \\
\varphi_m^{\pm} &= \pi \mp \arctan\left(\frac{\sigma_m}{q_m \cos\beta_1}\right) \\
\varphi_\mu^{\pm} &= \pi \mp \arctan\left(\frac{\sigma_\mu}{q_\mu \cos\beta_2}\right),
\end{aligned} \tag{15}$$

where $\beta_{1,2}$ are the azimuth angles that determine the position of the scatterer relative to the source and the receiver (Fig. 1).

When $\chi \gg 1$, we can use the following asymptotic approximation for the radial prolate spheroidal functions [11]:

$$R_{nl}^{(1)}(\chi, \vartheta) \approx \sqrt{\frac{\pi}{2\chi\vartheta}} J_n\left(\chi\zeta - \frac{2e+1}{2}\arctan\zeta\right), \tag{16}$$

$$R_{nl}^{(3)}(\chi, \vartheta) \approx \sqrt{\frac{\pi}{2\chi\vartheta}} H_n^{(1)}\left(\chi\zeta - \frac{2e+1}{2}\arctan\zeta\right), \tag{17}$$

where J_n and $H_n^{(1)}$ are the nth-order Bessel and Hankel functions, respectively; $\zeta = \sqrt{\vartheta^2 - 1}$; and $e = l - n$. In contrast to the functions $R_{nl}^{(1),(3)}$, the existing asymptotics for the angular prolate spheroidal functions S_{nl} provide no uniform convergence with the varying parameter $\eta = \cos\theta_{m,\mu}^{\pm}$. Therefore, the values of the function S_{nl} are determined by numerically solving the singular Sturm–Liouville problem [11]:

$$\left[\frac{d}{d\eta}(1-\eta^2)\frac{d}{d\eta} + \chi^2(1-\eta^2) - \frac{n^2}{1-\eta^2} + \lambda_{nl}\right] \times S_{nl}(\chi, \eta) = 0,$$

$$|\eta| \leq 1,$$

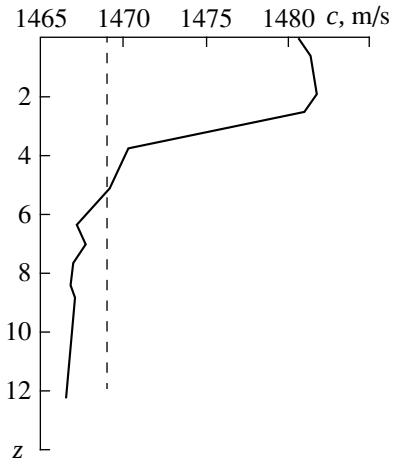

Fig. 2. Sound velocity profiles used in the calculations. The waveguide depth is expressed in units of wavelength λ.

where the function $S_{nl}(\chi, \eta)$ is limited at $\eta \longrightarrow \pm 1$ and normalized according to the formula $\int_{-1}^{1} S_{nl}^2(\chi, \eta)d\eta = 1$ and λ_{nl} are the eigenvalues.

The summation of the infinite binary series (14) is practically limited to the harmonics with the numbers $n = 0, \ldots, N_\infty$ and $l = n, \ldots, L_\infty$, where $L_\infty = [-0.5n^2 + \chi]$ and N_∞ is the maximal number at which the inequality $N_\infty \le [-0.5N_\infty^2 + \chi]$ holds (here, the square brackets denote the integral part of the number). With greater numbers of harmonics, the value of the scattering amplitude can be refined by no more than 1%.

For our numerical calculations, we selected a plane-parallel waveguide of depth $H \cong 12\lambda$ bounded from above by a free surface $z = 0$ and from below by an absorbing fluid bottom. (To provide the possibility of the generalization of the results, all linear dimensions are presented in terms of the sound wavelength λ.) We also assumed that a point sound source of power $W_0 = 270$ W was positioned at the waveguide bottom and a receiver was set at a distance of $10^3\lambda$ from it. Other parameters of the problem, namely, the receiver depth, the spheroid dimensions, the spheroid depth z_s, the distance r_{0s}, the horizontal distance y_s from the base line, the acoustic parameters of the bottom, the vertical sound velocity profile $c(z)$ in the waveguide (see Fig. 2), and the sound wavelength were varied in the course of the calculations.

In this paper, for brevity, we present only the most important results of our calculations and the main conclusions derived from the analysis of the computational data. Figure 3 shows the dependence of the quantity $dP = |P| - |P_0|$ on the distance y_s for different recep-

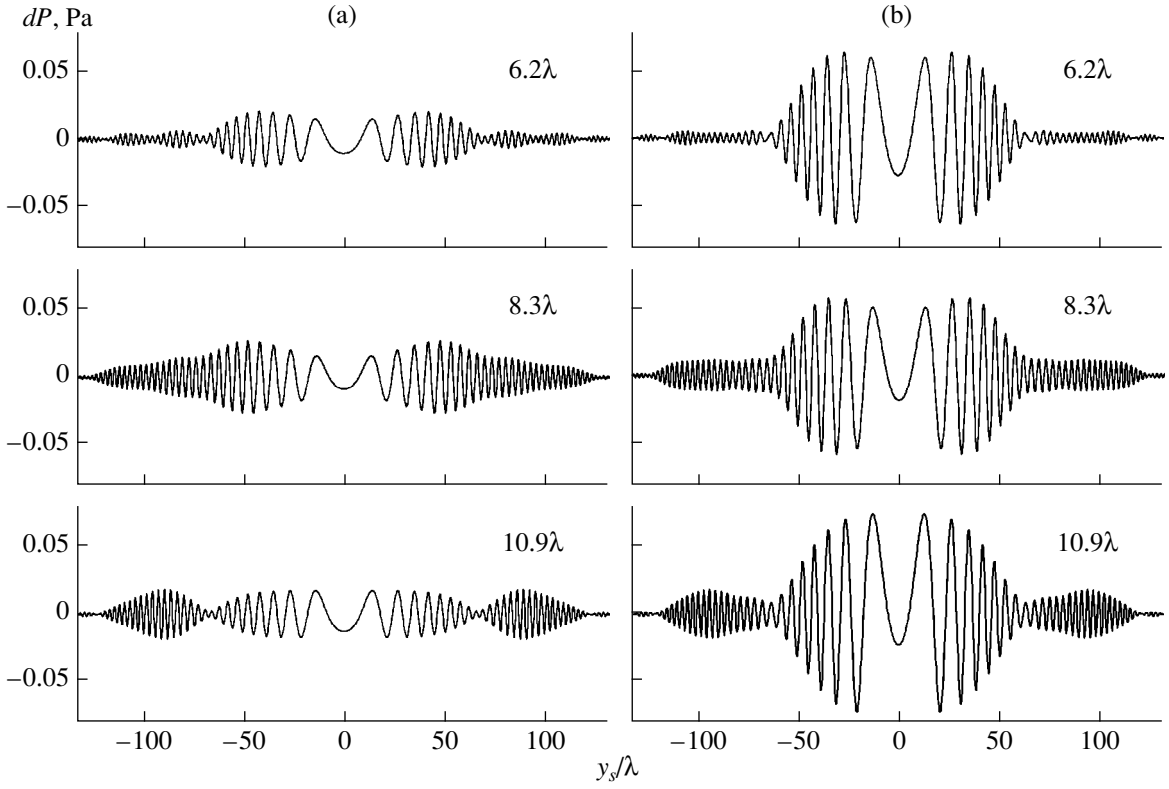

Fig. 3. Sound field variations due to the diffraction. The horizontal axis shows the distance from the scatterer to the base line. The numbers in the plots indicate the receiver depth. The spheroid dimensions are l = (a) 2.2 and (b) 4.4, d = (a) 0.3 and (b) 0.51. All distances, depths, and dimensions are given in units of wavelength λ.

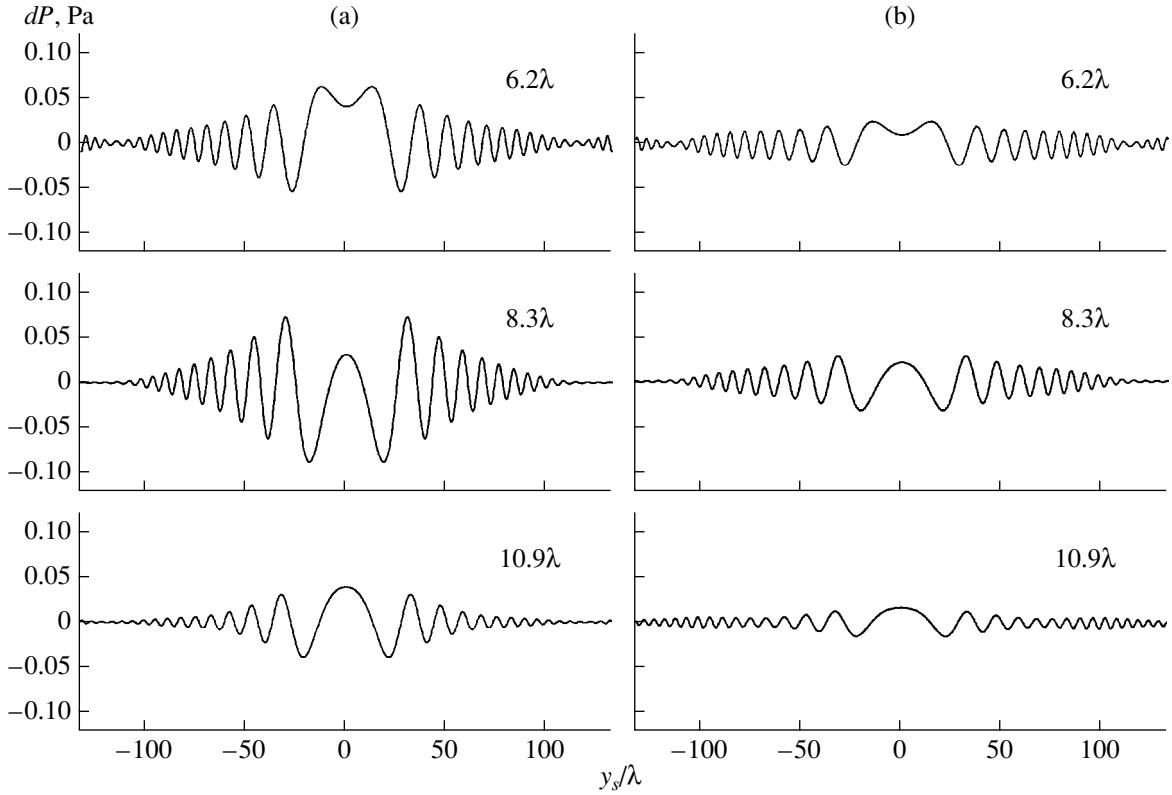

Fig. 4. Sound field variations due to the diffraction. The horizontal axis shows the distance from the scatterer to the base line. The numbers in the plots indicate the receiver depth. The spheroid dimensions are l = (a) 6.6 and (b) 4.4, d = (a) 0.73 and (b) 0.51. All distances, depths, and dimensions are in units of wavelength λ.

tion depths and for two spheroids with the dimensions: (a) $l = 2.2\lambda$, $d = 0.3\lambda$ and (b) $l = 4.4\lambda$, $d = 0.51\lambda$. We assumed that the spheroid intersected the base line halfway between the source and the receiver, i.e., at $r_{0s} = 500\lambda$, at the depth $z_s = 5.1\lambda$. The sound velocity profile used in this numerical example is shown in Fig. 2 by the solid line,[1] and the acoustic parameters of the bottom were as follows: the ratio of the ground and water densities $m_1 = 1.8$, the complex refraction index in the bottom $n = n_0(1 + i\alpha)$, $n_0 = 0.88$, and the damping factor $\alpha = 0.015$. The number of modes used in the calculations was selected individually for every numerical example based on the fact that its further increase practically did not affect the resulting scattered field. Specifically, for the calculations shown in Fig. 3, the number of modes was 15. As one can see from this figure, the value of $|dP|$ averaged over the depth is proportional to the area bounded by the shadow contour of the spheroid and the dependence of the quantity dP on the distance y_s is a quasi-harmonic one with a symmetric linear frequency modulation. Similar dependences were obtained for other acoustic parameters of the bottom (in the numerical calculations, the values of m_1 and n_0 were varied within 10% of those specified above and the value of α was varied within 100%), for another sound velocity profile in the waveguide (this dependence $c(z)$ is shown in Fig. 2 by the dashed line), for another sound wavelength λ_0 ($\lambda_0 = \lambda/2$), and for other spheroid dimensions. For example, Fig. 4 presents the results for the sound wavelength λ_0 and the spheroid dimensions (a) $l = 6.6\lambda$, $d = 0.73\lambda$ and (b) $l = 4.4\lambda$, $d = 0.51\lambda$. Here, the remaining parameters of the problem are the same as in Fig. 3, but the calculations were performed using only seven modes.

The statistical analysis of the computational data, on the one hand, confirmed the approximate expressions obtained earlier [6, 12, 13] for the variation coefficient g, the characteristic distance between the scatterer and the base line L within which the diffraction perturbation of the direct field is maximal, and the law governing the phase variation $\Delta\varphi(y_s)$ of the dependence $dP(y_s)$:

$$g \equiv \max\left(\frac{|dP|}{|P_0|}\right) \cong \frac{\tilde{S}}{2HF}, \quad L \cong \frac{2F^2}{l}, \quad \Delta\varphi \cong \frac{\pi y_s^2}{F^2}. \quad (18)$$

Here, $\tilde{S}$ is the area bounded by the shadow contour of the scatterer (in our case, $\tilde{S} = \pi ld/4$) and F is the radius of the first Fresnel zone ($F = \sqrt{r_{0s}(r - r_{0s})\lambda/r}$). On the other hand, the analysis showed that the approximate

[1] Note that this sound velocity profile was recorded in one of the full-scale experiments.

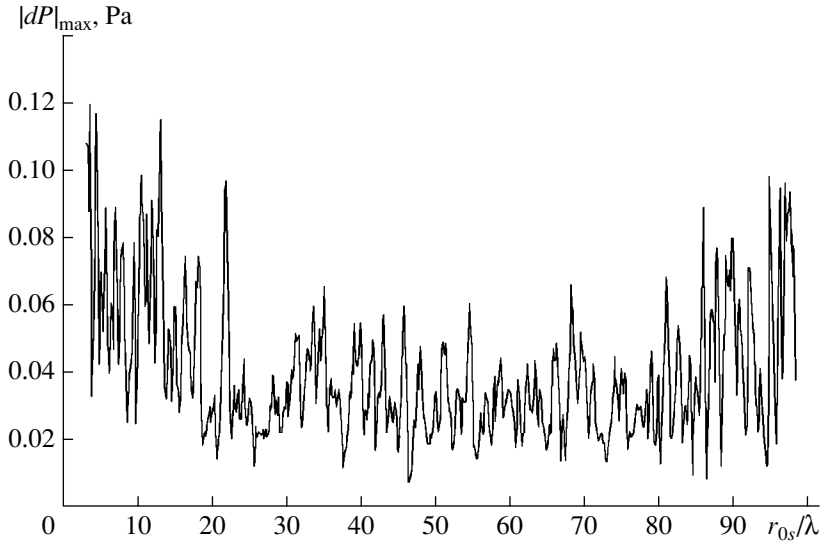

Fig. 5. Dependence of the maximal values of the sound field variations on the distance to the source in units of wavelength λ.

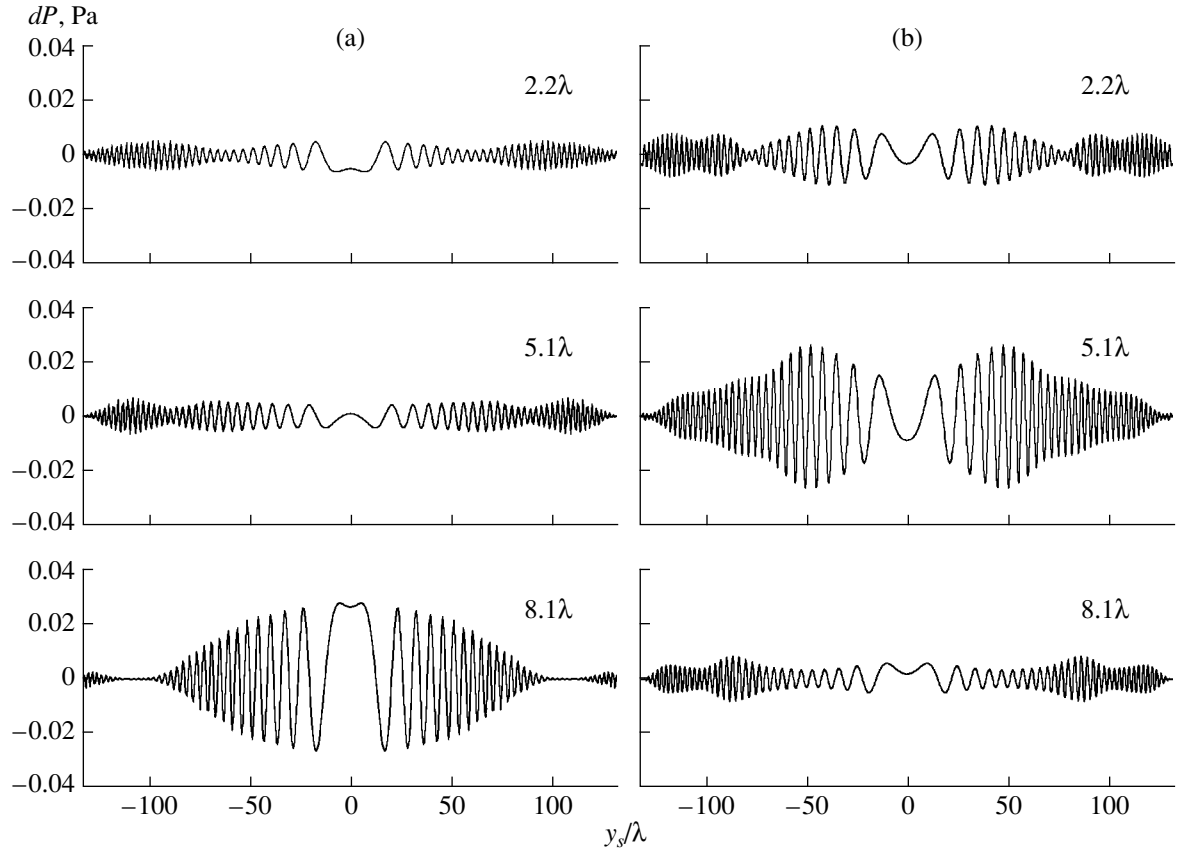

Fig. 6. Sound field variations due to the diffraction. The horizontal axis shows the distance from the scatterer to the base line. The numbers in the plots indicate the scatterer depth. The corresponding velocity profiles are shown in Fig. 2: (a) by the dashed line and (b) by the solid line. All distances and depths are in units of wavelength λ.

expressions (18) are valid only for the results averaged over the depth z_s and only for the interval of distances Δr ($D \ll \Delta r \ll r$, where D is the period of interference beats in the waveguide). For individual dependences $dP(y_s)$, these relations can fail. As an example of such a failure, we present the dependence of the maximal value $|dP|_{max}$ on the distance r_{0s} (Fig. 5) for a spheroid with the dimensions $l = 2.2\lambda$, $d = 0.3\lambda$ with the same

parameters of the waveguide and the same trajectory of the spheroid motion (normally to the base line at the depth $z_s = 5.1\lambda$) as in Fig. 3. The maximum was determined both in the reception depth, from 6.2λ to 10.9λ, and in the distance y_s, from -133λ to $+133\lambda$. One can see that the dependence $|dP|_{\max}(r_{0s})$ is oscillatory rather than monotone, and, only at small distances from the source and the receiver can one notice an increase in $|dP|_{\max}$ that should be expected according to the approximate expression (18) at a constant direct field P_0.

The complex interference structure of the sound field, which is formed in the waveguide in the vertical plane in the case of multimode propagation, masks the effect of the average depth dependence of the sound field intensity on the scattered field. To confirm this statement, in Fig. 6 we present the calculated functions $dP(y_s)$ for different depths of the scatterer z_s and for different sound velocity profiles, which determine the aforementioned dependence. Here, the dimensions of the spheroid crossing the base line at its center were assumed to be $l = 2.2\lambda$, $d = 0.3\lambda$. The depth of the waveguide and the acoustic properties of the bottom were the same as in Fig. 3. The receiver depth was 8.3λ. We note that, when the profile $c(z)$ has the form shown in Fig. 2 by the solid line, the sound field is mainly concentrated near the bottom, under the discontinuity layer; when the profile corresponds to that shown by the dashed line, the sound field is almost uniformly distributed in the waveguide depth. However, this fact did not explicitly manifest itself in the specific example shown in Fig. 6 that compares the diffraction perturbations of the sound field for the scatterer positions above and below the discontinuity layer.

In closing, we note that the calculations performed in this study demonstrate the complexity of the spatial structure of the sound field formed in the waveguide as a result of the diffraction by spatially localized inhomogeneities.

ACKNOWLEDGMENTS

This work was supported by the Russian Foundation for Basic Research, project no. 99-02-17671.

REFERENCES

1. S. M. Gorskiĭ, V. A. Zverev, and A. I. Khil'ko, in *Formation of Acoustic Fields in Oceanic Wavegides*, Ed. by V. A. Zverev (Inst. Prikl. Fiz. Akad. Nauk SSSR, Nizhni Novgorod, 1991), pp. 82–114.
2. F. Ingenito, J. Acoust. Soc. Am. **82**, 2051 (1987).
3. T. W. Dawson and J. A. Fawcett, J. Acoust. Soc. Am. **87**, 1110 (1990).
4. A. Sarkissan, J. Acoust. Soc. Am. **95**, 2340 (1994).
5. V. A. Eliseevnin and Yu. I. Tuzhilkin, Akust. Zh. **41**, 249 (1995) [Acoust. Phys. **41**, 214 (1995)].
6. V. A. Grigor'ev and V. M. Kuz'kin, Akust. Zh. **41**, 410 (1995) [Acoust. Phys. **41**, 359 (1995)].
7. Yu. A. Kravtsov, V. M. Kuz'kin, and V. G. Petnikov, Akust. Zh. **30**, 339 (1984) [Sov. Phys. Acoust. **30**, 199 (1984)].
8. A. Sarkissian, J. Acoust. Soc. Am. **102**, 825 (1997).
9. B. G. Katsnel'son and V. G. Petnikov, *Acoustics of Shallow Sea* (Nauka, Moscow, 1997).
10. N. B. Konyukhova and T. V. Pak, *Diffraction of a Plane Acoustic Wave by a Stiff Prolate Spheroid* (Vychisl. Tsentr Akad. Nauk SSSR, Moscow, 1985).
11. I. V. Komarov, L. I. Ponomarev, and S. Yu. Slavyanov, *Spheroidal and Coulomb Spheroidal Functions* (Nauka, Moscow, 1976).
12. S. M. Gorskiĭ, V. A. Zverev, A. L. Matveev, and V. V. Mityugov, Akust. Zh. **41**, 223 (1995) [Acoust. Phys. **41**, 190 (1995)].
13. V. M. Kuz'kin, Akust. Zh. **43**, 514 (1997) [Acoust. Phys. **43**, 440 (1997)].

Translated by E. Golyamina

Acoustical Physics, Vol. 47, No. 1, 2001, pp. 42–44. Translated from Akusticheskiĭ Zhurnal, Vol. 47, No. 1, 2001, pp. 52–55.
Original Russian Text Copyright © 2001 by Gulyaev, Zemlyakov, Kryshtal', Medved', Fong, Shemet.

A Tunable Gas Sensor Using an Acoustic Waveguide

Yu. V. Gulyaev*, V. E. Zemlyakov*, R. G. Kryshtal'*, A. V. Medved'*, Khoang van Fong, and V. V. Shemet***

** Institute of Radio Engineering and Electronics, Russian Academy of Sciences, pl. akademika Vvedenskogo 1, Fryazino, Moscow oblast, 141120 Russia*
e-mail: avm@ms.ire.rssi.ru

*** Technical University, Hanoi, Vietnam*

Received May 10, 2000

Abstract—A tunable gas sensor using surface acoustic waves (SAW) is described. It is designed on the basis of a waveguide delay line fabricated on a piezoelectric substrate made of 128° Y-cut $LiNbO_3$. A voltage applied between the waveguide and two electrodes causes a local change in the properties of the substrate near the waveguide and differently affects the sensor's response to the vapors of various analytes. Some results of the experimental study of the sensor, which show the change in the selectivity under the effect of voltage, are presented. The analytes used for testing include a number of alcohols and deionized water. The possibilities for employing such a sensor in the sensor arrays of gas analyzers of the electronic nose type are discussed. © *2001 MAIK "Nauka/Interperiodica".*

Gas sensors on the basis of surface acoustic waves (SAW) are widely used in gas analyzers of the electronic nose type [1]. The main part of such an analyzer is an array of sensors—a set of sensors with different sensitivities to various chemical substances. Different responses are achieved by using different sensitive coatings for different sensors of the array. The principle of operation of these sensors is described in [2]. Their main disadvantage lies in the different rate of ageing of sensitive coatings, which leads to the need for repeated calibration of an electronic nose. Anisimkin *et al.* [3] propose an array of four SAW sensors with the use of only one sensitive layer for the entire array. However, this approach makes it possible to compensate the disadvantages connected with the ageing of the sensitive coating only partially.

In this paper, we describe a tunable SAW gas sensor whose selectivity is determined not by the properties of the sensitive coating, but by the voltage applied in a certain way to the metal waveguide along which the SAW propagate.

The schematic diagram of the sensor is shown in Fig. 1. As a substrate, we used a 128° Y-cut $LiNbO_3$ piezoelectric crystal with the dimensions $12 \times 5 \times 0.25$ mm. For the excitation and reception of SAW, two interdigital transducers (IT) (*1*) were used. Every IT consists of 30 pairs of electrodes with a spatial period of 8 μm and an aperture of 110 μm. The distance between the ITs is 6.5 mm. An aluminum SAW waveguide (*2*) in the form of a narrow strip 24 μm wide and 5 mm long, together with the acoustic concentrators (*3*), and the waveguide electrodes (*4*), is located between the ITs. The electrodes are as near to the waveguide as 30 μm, which makes it possible to obtain strong electric fields in the vicinity of the waveguide at comparatively small voltages applied to it. The insertion loss of the delay line (with a SAW waveguide), which actually represents the considered SAW sensor, is 15 dB at the main frequency of 486 MHz in a 50-Ω channel without matching elements. The bandwidth at a level of 3 dB is 18 MHz. Originally, the authors of this paper used such an acoustic delay line in high-sensitivity voltage sensors and in SAW phase shifters [4, 5].

Note that the described SAW sensor does not comprise any special sensitive coatings unless the aluminum waveguide is considered as such a coating. Nevertheless, if required, this possibility is not ruled out. A sensitive layer can be applied directly on the SAW waveguide of the sensor.

For measuring the response of the sensor, we used an experimental setup shown schematically in Fig. 2. The SAW sensor in a metal housing with electric leads for the connection to the measuring instruments and with connecting pipes for feeding and removing gas was placed in a thermostat T1 in which a constant temperature of 50 ± 0.05°C was maintained. The inner vol-

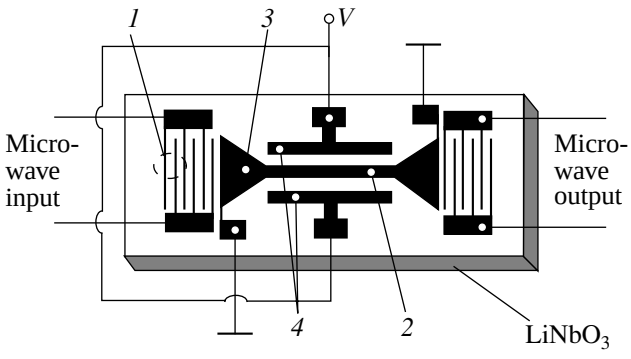

Fig. 1. Design of the SAW sensor.

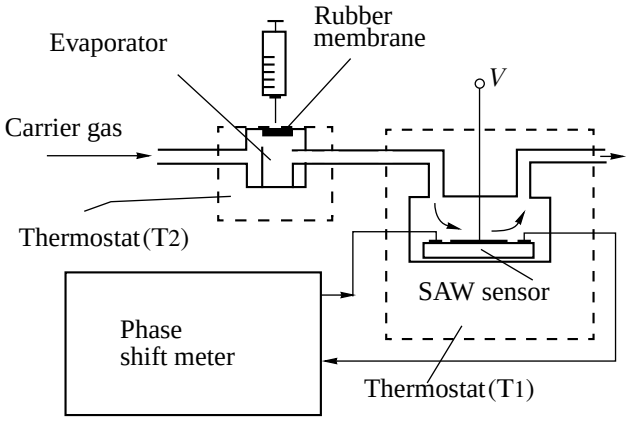

Fig. 2. Experimental setup for testing the SAW sensor.

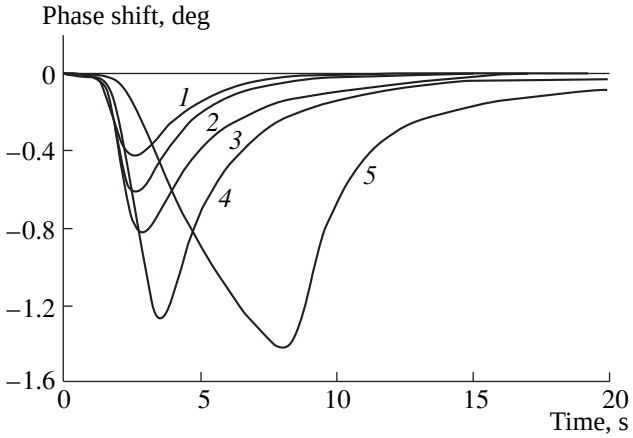

Fig. 3. Measured phase shifts of the SAW signal as a function of time (the responses of the sensor) for various alcohols in the absence of voltage across the waveguide: (*1*) methanol, (*2*) propanol-2, (*3*) ethyl alcohol, (*4*) propanol, and (*5*) isoamyl alcohol.

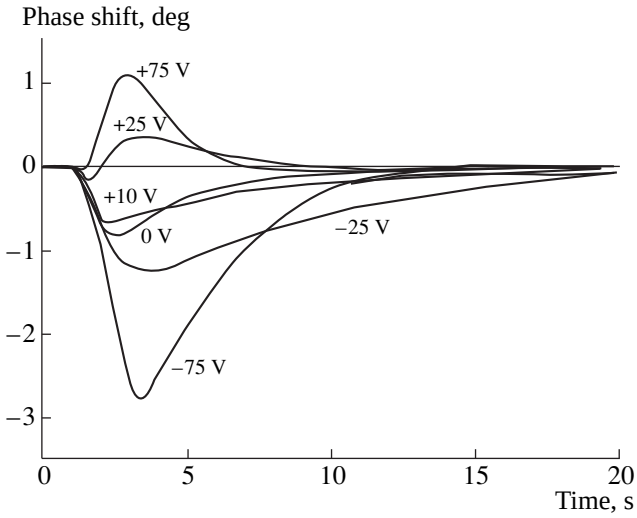

Fig. 4. Measured responses of the sensor to ethyl alcohol vapor for various voltages applied to the waveguide.

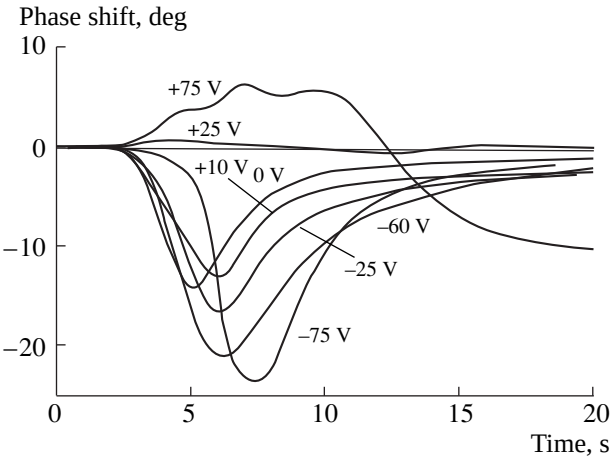

Fig. 5. Measured responses of the sensor to water vapor for various voltages applied to the waveguide.

ume of the metal housing was about 2 cm^3. Nitrogen was used as a carrier gas. The gas flow rate in the experiment was equal to 30 $cm^3/min \pm 1\%$. The liquid testing analytes of volume 0.1 μl were fed by means of a microsyringe into an evaporator, which was placed in the thermostat T2 with a constant temperature of 135°C. This temperature was higher than the boiling points of all the analytes used in the experiment.

A signal of frequency 486 MHz and power 1 mW was fed to the input IT. The output signal was taken from the output IT, and, by using a phase meter, the phase shift of this signal was measured as a function of time (the response of the SAW sensor).

In the experiment, we measured the sensor responses to vapors of alcohol (ethyl, methyl, isopropyl, propyl, and isoamyl) and of deionized water at various voltages applied to the electrodes of the waveguide.

Figure 3 displays the measured responses to various alcohols in the absence of voltage across the waveguide electrodes (in this case, the waveguide and the electrodes are short-circuited). It is seen that the SAW sensor clearly distinguishes the alcohols even without a sensitive coating. It is quite natural, because the physical properties of various alcohols (the boiling point, the density, the viscosity, and the saturation vapor pressure) are different and they variously affect the propagation of SAW in the presence of the adsorption and desorption of the molecules of alcohols.

The voltage applied to the waveguide electrodes changes the character of the responses. It is clearly seen in the examples of responses to vapors of ethyl alcohol (Fig. 4) and water (Fig. 5). A negative voltage increases and a positive voltage decreases the magnitude of the responses. If the voltage is sufficiently high, it can even change the sign of the response to the opposite. As is

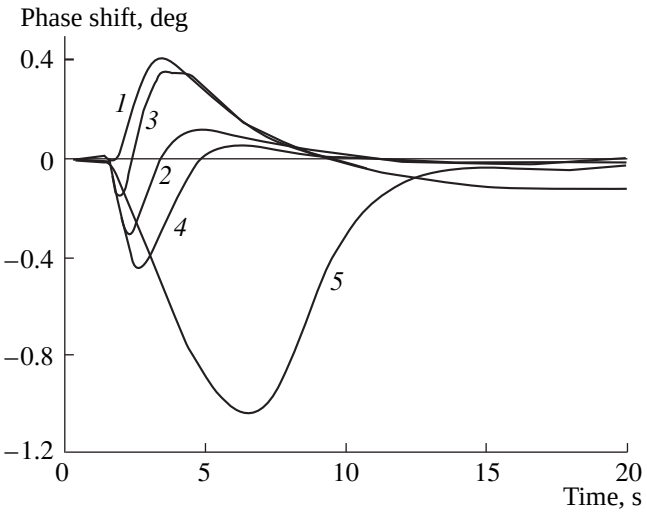

Fig. 6. Measured responses of the sensor to vapors of various alcohols at a voltage of 25 V across the waveguide electrodes: (*1*) methanol, (*2*) propanol-2, (*3*) ethyl alcohol, (*4*) propanol, and (*5*) isoamyl alcohol.

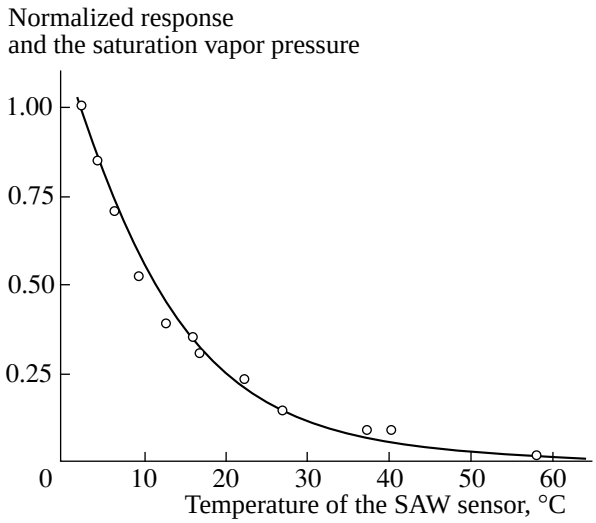

Fig. 7. Measured dependence of the sensor response on its temperature (experimental points). The analyte is ethyl alcohol. The solid line shows the calculated temperature dependence of the normalized saturation vapor pressure of ethyl alcohol.

seen from Fig. 6, the same value of the voltage (in our experiment it is equal to +25 V) applied to the waveguide affects the sensor responses to the vapors of various alcohols in different ways. It should be noted that, for every analyte, there exists a voltage at which the sensor is practically insensitive to the analyte. For instance, in our experiment, for water vapor, the value of this voltage is +25 V. This fact may be of certain interest in designing an electronic nose.

In our experiment, the temperature of the sensor was constant and equal to 50°C; however, if the temperature is reduced, the sensitivity of the sensor sharply increases. Figure 7 displays the dependence of the relative change in the sensor response on temperature for the ethyl alcohol vapor. It is seen that, at the sensor temperature of about 2.3°C, the response becomes about a hundred times greater than the response at a temperature of 50°C. Consequently, the sensitivity of the sensor increases by the same factor with cooling. In the same figure, the solid line shows the theoretical temperature dependence of the relative change in the saturation vapor pressure of ethyl alcohol. The measured values of the sensor's response (the experimental points) obtained at various temperatures for the ethyl alcohol vapor fit this dependence quite well.

The physical mechanism of the effect of the applied voltage on sensor's response is not yet completely understood. We assume that a number of factors simultaneously contribute to this effect. In our opinion, the most significant of them is the dependence of sensor's response to a specific gas on the changes that occur in the components of the mechanical displacements in SAW under the action of electric fields [6]. Among other factors, we should mention the possible influence of electric fields on the processes of adsorption and desorption of molecules of the analyte at the working surface of the sensor.

In our experiment, as the sensor's response, we measured the phase shift of the output signal. For a convenient integration with digital processing systems, it is better to measure the change in the frequency of the output signal by inserting the delay line in the feedback circuit of an amplifier, as was done in [5].

Thus, we can conclude that the proposed sensor has the property of a tunable chemical selectivity and, consequently, is well suited for use in the sensor array of an electronic nose. In particular, by assembling an array of any number of identical sensors and applying different voltages to them, it is possible to make their selectivity different.

REFERENCES

1. H. T. Nagle, S. S. Schiffman, and R. Gutierrez-Osuna, IEEE Spectr., September, 22 (1998).
2. M. Holmberg, F. Wingust, I. Lundström, *et al.*, Sens. Actuators B **35**–**36**, 528 (1996).
3. V. I. Anisimkin, R. G. Kryshtal, A. V. Medved, *et al.*, Electron. Lett. **34**, 1360 (1998).
4. Yu. V. Gulyaev, O. A. Mal'tzev, A. V. Medved, and R. A. Mishkinis, Pis'ma Zh. Tekh. Fiz. **11** (13), 824 (1985) [Sov. Tech. Phys. Lett. 11, 342 (1985)].
5. A. V. Medved, R. A. Mishkinis, and P. F. Rutkovsky, Electron. Lett. **26**, 973 (1990).
6. V. I. Anisimkin, I. M. Kotelyanskii, V. I. Fedosov, *et al.*, in *Proceedings of IEEE Ultrasonics Symposium, Seattle, 1995*, Vol. 1, p. 207.

Translated by A. Svechnikov

Acoustical Physics, Vol. 47, No. 1, 2001, pp. 45–49. Translated from Akusticheskiĭ Zhurnal, Vol. 47, No. 1, 2001, pp. 56–61.
Original Russian Text Copyright © 2001 by Gusev.

Internal Structural Symmetry of Optimal Layered Structures

E. L. Gusev

Joint Institute of Physical and Engineering Problems of the North, Yakutian Scientific Center, Siberian Division, Russian Academy of Sciences, ul. Oktyabr'skaya 1, Yakutsk, 677891 Russia
e-mail: e.l.gusev@sci.yakutia.ru
Received December 14, 1999

Abstract—Problems of the optimal synthesis of multilayer structures implementing the ultimate performance under the action of elastic waves are considered. It is required to design a multilayered structure by choosing the physical properties of materials, the thickness of the layers, their number, and the mutual arrangement of layers with different physical properties in a way such that the energy characteristics of an elastic wave be as close as possible to the desired characteristics. From an analysis of the necessary optimum conditions, it is inferred that the optimal solutions are characterized by a certain internal order in the structure parameters, i.e., by an internal symmetry. When known *a priori*, these qualitative relations considerably reduce the number of variants tested for the optimum and make it possible to efficiently design composite structures implementing the ultimate performance in terms of exhibiting the desired properties under the action of elastic waves. © *2001 MAIK "Nauka/Interperiodica".*

The design of composite materials and structures characterized by a preliminarily specified set of properties has become a problem of fundamental importance in the past few decades [1–13]. Layered media whose properties vary along a single direction form the most commonly encountered type of such inhomogeneous structures. A wave acting upon an inhomogeneous structure gives rise to a system of reflected and refracted waves, which interact with the incident wave forming a complex interference pattern. This interference pattern depends on the structure of the inhomogeneous medium. Varying the structure of the composite medium, one can control the energy characteristics of the wave process.

The problem of primary scientific interest is the determination of the limiting possibilities in controlling the energy parameters of wave processes of different physical natures (such as electromagnetic, acoustic, temperature, and elastic waves) by systematically choosing the structure of the inhomegeneous medium. Solution of this problem not only determines the efficiency of different devices based on the wave energy conversions, but also offers extended possibilities for the efficient use of the wave energy converters in new fields of physics and engineering.

The design of structures with unique properties necessarily involves the study of their ultimate performance. The latter corresponds to the limiting level achievable with a systematic control of the composition and the parameters of the structure.

The solution to the problem of studying the ultimate performance of a composite structure in controlling the energy characteristics of wave processes of different physical natures assumes an exhaustive search among all possible structures. Because the number of possible structures is very large, an exhaustive search is impracticable even with the fastest computers. The commonly used approaches to the solution of this problem consist in the search among a small subset of the whole set of all possible structure versions. However, such approaches, on the one hand, cannot ensure that the version found implements the ultimate performance and, on the other hand, give no way of estimating how wide the variant found deviates from the variant actually implementing the ultimate performance.

Thus, the commonly used approaches

(i) give no way of objectively estimating how much the designed structures used in different fields of physics and engineering differ from the structures implementing the ultimate performance and

(ii) give no way of efficiently designing structures implementing the ultimate performance.

A general point of the commonly used approaches is that they all consider the problem with no account taken of its qualitative features, in particular, the qualitative relations between the parameters in the structures implementing the ultimate performance.

In this context, we formulated the problem of developing the methods for a comprehensive investigation of the ultimate performance of composite structures. We advance the hypothesis that general regularities exist for structures implementing the ultimate performance.

In papers [1, 2], we determined the qualitative regularities for the structure of an optimal solution for the case of an oblique incidence of electromagnetic waves on a system of magnetodielectric layers, as well as for the case of an oblique incidence of acoustic waves on a

1063-7710/01/4701-0045$21.00 © 2001 MAIK "Nauka/Interperiodica"

system of layers in which the shear waves cannot propagate. We stated, in particular, that the relation between the parameters in structures implementing the ultimate performance is characterized by a certain internal order, or a certain internal symmetry, which allows one to efficiently select the total set of variants implementing the ultimate performance for the mentioned problems. It appeared that the symmetry of the same type is characteristic of the relations between the parameters in optimal structures under the action of both electromagnetic and acoustic waves. The knowledge of such qualitative regularities is of essential importance for both theory and practice [2, 4–9].

The question arises of whether the symmetry type found for the parameters in the optimal structures for the above models remains intact for the synthesis problems described by more complex models, in particular, by the models that take into account the transformation of waves of different types at the layer boundaries.

Let a set of elastic layers with different physical properties fill the gap between two halfspaces. In this case, we will observe a much more complex interference pattern, because both longitudinal and transverse waves can propagate in elastic media. In comparison with the cases considered earlier [1, 2], the complexity of the interference pattern is caused primarily by mutual transformations of the two types of waves at the layer boundaries.

Assume that it is necessary to design a multilayer structure implementing the ultimate performance in terms of the suppression of elastic waves in a specified range of angular frequencies $[\omega_{min}, \omega_{max}]$. We will assume that the halfspaces on both sides of the layered system are filled with perfect liquids. The development of efficient methods for investigating the ultimate performance for such problems are of fundamental importance for many fields, such as ultrasonic engineering, acoustoelectronics, nondestructive testing, seismology, and vibration damping.

The propagation of an elastic wave in a system of elastic layers is described by the system of equations of elastic motion

$$\mu_s \Delta u_s + (\lambda_s + 2\mu_s)\operatorname{grad}\operatorname{div} u_s = \rho_s \frac{\partial^2 u_s}{\partial t^2}, \quad (s = 1, \ldots, N). \tag{1}$$

Here, $u_s(x, y, z, t)$ is the vector of particle displacement in the sth medium, ρ_s is the density of the sth layer, λ_s and μ_s are the Lamé coefficients of the sth layer, and N is the number of layers. The vector field of displacements can be represented as the superposition of two fields [3]

$$u_s = \operatorname{grad}\Phi_s + \operatorname{rot} P_s. \tag{2}$$

Here, Φ_s and P_s are the scalar and vector potentials of the wave field. A general-type plane wave can be represented as a superposition of plane harmonic waves, i.e., as the Fourier integral

$$\Phi_s(x, y, z, t) = \frac{1}{\sqrt{2\pi}} \int_{-\infty}^{+\infty} f_s(z, \omega) \exp(i\Delta_0 x - i\omega t) d\omega,$$

$$P_s(x, y, z, t) = \frac{1}{\sqrt{2\pi}} \int_{-\infty}^{+\infty} g_s(z, \omega) \exp(i\Delta_0 x - i\omega t) d\omega, \quad (s = 1, \ldots, N). \tag{3}$$

Here, $\Delta_0 = k_0 \sin\vartheta_0$, $k_0 = \omega/c_0$ is the wave number of the incident wave, c_0 is the velocity of the wave in the first halfspace, and ϑ_0 is the angle of incidence of the elastic wave. With this representation, the problem on the propagation of an elastic wave in the system of elastic layers is reduced to the following boundary-value problem for the spectral densities of scalar and vector potentials:

$$\frac{\partial^2 f_s(z, \omega)}{\partial z^2} + (k_s^2(\omega) - \Delta_0^2(\omega)) f_s(z, \omega) = 0,$$

$$\frac{\partial^2 g_s(z, \omega)}{\partial z^2} + (\gamma_s^2(\omega) - \Delta_0^2(\omega)) g_s(z, \omega) = 0,$$

$$b_{s-1} \le z \le b_s, \quad (s = 1, \ldots, N),$$

$$f_s(b_{s-1}, \omega) = \Phi_1^s f_{s-1}(b_{s-1}, \omega) + i\Phi_2^s \frac{\partial g_{s-1}(b_{s-1}, \omega)}{\partial z},$$

$$g_s(b_{s-1}, \omega) = \Phi_1^s g_{s-1}(b_{s-1}, \omega) - i\Phi_2^s \frac{\partial f_{s-1}(b_{s-1}, \omega)}{\partial z},$$

$$\frac{\partial f_s(b_{s-1}, \omega)}{\partial z} = Q_1^s \frac{\partial f_{s-1}(b_{s-1}, \omega)}{\partial z} + iQ_2^s g_{s-1}(b_{s-1}, \omega), \tag{4}$$

$$\frac{\partial g_s(b_{s-1}, \omega)}{\partial z} = Q_1^s \frac{\partial g_{s-1}(b_{s-1}, \omega)}{\partial z} - iQ_2^s f_{s-1}(b_{s-1}, \omega),$$

$$(s = 2, \ldots, N),$$

$$\frac{\partial f_0(0, \omega)}{\partial z} = -i\cos\vartheta_0 \left[k_0 f_0(0, \omega) + \frac{2}{k_0 \rho_0 c_0^2} \right],$$

$$\frac{\partial f_{N+1}(l, \omega)}{\partial z} = ik_{N+1} \cos\vartheta_{N+1} f_{N+1}(l, \omega).$$

In this notation,

$$\Phi_1^s = \frac{\mu_{s-1}\gamma_{s-1}^2 + 2\Delta_0^2(\mu_s - \mu_{s-1})}{\mu_s \gamma_s^2},$$

$$\Phi_2^s = \frac{2\Delta_0(\mu_s - \mu_{s-1})}{\mu_s \gamma_s^2},$$

$$Q_1^s = \frac{\mu_s\gamma_s^2 - 2\Delta_0^2(\mu_s - \mu_{s-1})}{\mu_s\gamma_s^2},$$

$$Q_2^s = \Delta_0\frac{\mu_s\gamma_s^2 - \mu_{s-1}\gamma_{s-1}^2 - 2\Delta_0^2(\mu_s - \mu_{s-1})}{\mu_s\gamma_s^2},$$

$$(s = 2, \ldots, N).$$

Here, $k_s = \omega/c_s$ is the wave number of the longitudinal waves in the sth layer, c_s is the velocity of the longitudinal waves in the sth layer, $\gamma_s = \omega/d_s$ is the wave number of the shear waves in the sth layer, and $b_s(x = \overline{0, N})$ are the coordinates of the boundaries between layers with different physical properties.

Let the discrete set of materials admissible for the design be given. Different physical properties of these materials will be related through certain functional dependences rather than be independent. We choose the density ρ of the material as an independent parameter. Then, the velocities of the longitudinal and transverse waves in the material will be certain functions of density: $c = c(\rho)$, $d = d(\rho)$. These functions unambiguously determine the velocities of the longitudinal and transverse waves in admissible materials from their densities. We denote by Λ the set of densities of the admissible materials:

$$\Lambda = \{\rho_{\min} = \rho^1 < \rho^2 < \rho^3 < \ldots < \rho^m = \rho_{\max}\}.$$

It is necessary to choose the physical properties of the layer materials $\rho_s(s = 1, \ldots, N)$, the layer thickness $\Delta_s^* = b_s^* - b_{s-1}^*$ $(s = 1, \ldots, N^*)$, the number of layers N^*, and their order in the structure so that the energy transmission coefficient $T(\omega)$ of the structure under design be as close as possible to the desired function $\tilde{T}(\omega)$. Mathematically, the problem is reduced to the minimization of the quality criterion

$$J = \int_{\omega_{\min}}^{\omega_{\max}} \tau(\omega)[T(\omega) - \tilde{T}(\omega)]^2 d\omega \qquad (5)$$

on the solutions of system (4); here, $\tau(\omega)$ $(0 \le \tau(\omega) \le 1)$ is the weighting function and

$$T(\omega) = \frac{c_0\rho_0\cos\vartheta_{N+1}}{c_{N+1}\rho_{N+1}\cos\vartheta_0}|f_{N+1}(l, \omega)|^2.$$

The problem determined by Eqs. (4) and (5) is a combinatorial problem of the optimal control of composite systems. Similar problems were studied in [2], where the necessary optimum conditions were formulated for composite systems with this type of structure.

For optimal control problem (4), (5), one can formulate the necessary optimum conditions by generalizing the Pontryagin maximum principle [10] to the problems of optimal control of composite systems [2]. In this approach, the functions R_s [2] will appear as analogs of the Hamilton functions. For optimal control problem (4), (5), these functions can be represented in the form

$$R_s(;\rho)|_z = \int_{\omega_{\min}}^{\omega_{\max}} \sum_{i=1}^{8} \alpha_s^i(z, \omega)G_s^i(\omega;\rho)d\omega, \qquad (6)$$
$$b_{s-1} \le z \le b_s, \quad (s = 1, \ldots, N).$$

In this notation, the functions $\alpha_s^i(z, \omega)$ $(i = 1, \ldots, 8)$ are expressed through the solutions $f_s(z, \omega)$ and $g_s(z, \omega)$ $(b_{s-1} \le z \le b_s, s = 1, \ldots, N)$ to the initial system of Eqs. (4) and the solutions $\psi_s(z, \omega)$ and $p_s(z, \omega)$ $(b_{s-1} \le z \le b_s, s = 1, \ldots, N)$ to the system conjugate with system (4) [2] and the functions $G_s^i(\omega;\rho)$ are analytical functions of ρ.

It can be shown that the functions $\alpha_s^i(z, \omega)$ satisfy the following differential equations:

$$\frac{\partial^3\alpha_s^i(z, \omega)}{\partial z^3} + 4k_s^2(\omega)\frac{\partial\alpha_s^i(z, \omega)}{\partial z} = 0, \quad (i = 1, \ldots, 4),$$

$$\frac{\partial^4\alpha_s^i(z, \omega)}{\partial z^4} + 2(k_s^2(\omega) + \gamma_s^2(\omega) - 2\Delta_0^2(\omega))\frac{\partial^2\alpha_s^i(z, \omega)}{\partial z^2} \qquad (7)$$
$$+ (k_s^2(\omega) - \gamma_s^2(\omega))\alpha_s^i(z, \omega) = 0 \quad (i = 5, \ldots, 8),$$
$$b_{s-1} \le z \le b_s, \quad s = 1, \ldots, N.$$

Let N^* be the optimal number of layers, $\rho_s^*(s = 1, \ldots, N^*)$ be the optimal physical parameters of layers, and b_s^* $(s = 1, \ldots, N^* - 1)$ be the optimal coordinates of the layer boundaries. Then, the following condition is satisfied for the optimal solution:

$$R_s(*;\rho_s^*)\big|_z = \max_{\rho\in\Lambda} R_s(*;\rho),$$
$$b_{s-1}^* \le z \le b_s^*, \quad (s = 1, \ldots, N^*). \qquad (8)$$

(The missing arguments of the functions R_s are calculated for the optimal solution.)

We will try to find qualitative regularities in the optimal solutions to the optimum design problems set in the form of Eqs. (4) and (5). We will consider the case that is most interesting from both theoretical and practical standpoints in which the desired transmission coefficient $\tilde{T}(\omega)$ is such that its value is ultimate for every frequency $\omega \in [\omega_{\min}, \omega_{\max}]$. In other words, the desired function $\tilde{T}(\omega)$ can take on only two values: either 0 (a total reflection is desired) or 1 (a total transmission is desired).

The problem type under consideration includes the following optimum design problems:

(i) maximal damping of an elastic wave within a given frequency range $[\omega_{min}, \omega_{max}]$,

(ii) minimal reflection of an elastic wave within a given frequency range $[\omega_{min}, \omega_{max}]$,

(iii) maximal damping of an elastic wave in some spectral regions and minimal reflection in other spectral regions.

Consider first an oblique incidence of an elastic harmonic wave of frequency ω on the system of elastic layers and assume that the set of admissible materials consists of two materials.

Taking into account the structure of the differential equations (7) for the functions $\alpha_s^i(z, \omega)$ ($b_{s-1} \le z \le b_s$, $s = 1, \ldots, N$) involved in the functions $R_s(; \rho)$ given by Eq. (6) and the properties of the solutions to the initial system of Eqs. (4), we can determine the relationship between the functions $\alpha_s^i(z, \omega)$ for the nearest layers with identical physical properties, i.e., for the layers with the numbers s and $s + 2$.

This design analysis makes it possible to state that the following equalities are satisfied for the optimal solution:

$$R_{s-2}(*; \rho) = R_s(*; \rho),$$
$$b_{s-3}^* \le z \le b_{s-2}^*, \quad (s = 4, \ldots, N^* - 1). \tag{9}$$

Since the functions R_s for the internal layers with identical physical properties have identical behavior on the optimal solution, the distances between the optimal boundaries of the considered layers will also be identical. Note that the optimal coordinates of the layer boundaries are the singular points of the functions R_s, because these points correspond to the simultaneous maxima of the functions R_s for different elements of the set Λ.

Consequently, we immediately obtain from Eqs. (9)

$$\Delta_s^* = \Delta_{s-2}^*, \quad (s = 4, \ldots, N^* - 1). \tag{10}$$

Thus, the following statement is true:

Statement 1. Let a harmonic elastic wave be obliquely incident on a system of elastic layers and let the set of admissible materials consist of only two materials. Then, the internal layers with identical physical properties have identical thickness in the optimal structure.

It is clear that, for the case of an admissible set consisting of more than two materials, this statement also holds if the optimal design consists of two or less materials of the admissible set.

Consequence. Let the admissible set consist of more than two materials. If the optimal design for the case of a harmonic elastic wave obliquely incident on a system of elastic layers consists of two or less materials of the admissible set, the internal layers with identical physical properties have an identical thickness.

Thus, the relation between the parameters in an optimal elastic system shows a certain internal order, or an internal symmetry. The established internal symmetry property describes the regularities in the internal relations between different groups of parameters in the optimal structure, namely, if the physical properties of internal layers are identical in an optimal structure,

$$\rho_s^* = \rho_{s-2}^* \quad (s = 4, \ldots, N^* - 1),$$

then, these layers have identical thickness:

$$\Delta_s^* = \Delta_{s-2}^* \quad (s = 4, \ldots, N^* - 1).$$

The internal symmetry property established for the optimal structures makes it possible to considerably reduce the dimension of the initial design problem and to reduce the multiparameter design problem whose dimension is determined by the total number of layers in the optimal structure to a three-parameter problem. The three independent parameters to be varied in the design are the thickness of the internal layers with different physical properties and the thickness of one of the boundary layers. Consequently, the total set of parameters describing the structure implementing the ultimate performance can be exhaustively determined for the case under consideration.

We return to the consideration of the general case of an oblique incidence of a nonmonochromatic elastic wave on the system of elastic layers. We will consider the optimum design problem given by Eqs. (4) and (5) under the additional assumption that, at some frequency $\omega = \omega^* \in [\omega_{min}, \omega_{max}]$, the energy transmission coefficient $T(\omega)$ of the system under design necessarily takes on its ultimate value

$$T(\omega^*) = T_{\omega^*}^*(\omega^*), \tag{11}$$

where $T_{\omega^*}^*(\omega^*)$ is the ultimate value of the energy transmission coefficient at the frequency $\omega = \omega^*$.

It is obvious that the actual transmission coefficient will be closest to the desired value for the harmonic wave with the frequency $\omega = \omega^*$. Consequently, the set of globally optimal solutions to optimum design problem (4), (5) with additional condition (11) will be a subset of globally optimal solutions obtained for the harmonic wave with the frequency $\omega = \omega^*$.

Therefore, the structure of the optimal solutions for the case considered is characterized by the same properties as those obtained for harmonic wave actions.

Thus, in the more general case of elastic waves obliquely incident on the system of elastic layers, the relations between the parameters in the structures implementing the ultimate performance are governed by the same qualitative regularities as those obtained earlier for electromagnetic and acoustic waves [2] and, in particular, are characterized by the same internal symmetry type.

As a result, the formulated optimum design problem can be solved explicitly, which means that one can determine the complete set of variants of layered structures implementing the ultimate performance.

The above analysis leads to the conclusion that the necessary optimum conditions (8) contain essential information on the structure of an optimal system. Although the optimum design problem (4), (5) is characterized by fairly complex Hamilton functions, the qualitative structure of the optimal solution can be determined from an analysis of their structure.

CONCLUSIONS

1. In the case of an admissible set consisting of two materials, the elastic layered structure that is optimal for an obliquely incident harmonic elastic wave exhibits the property of internal order, or internal symmetry. This property also holds for an inharmonic elastic wave obliquely incident on the system of elastic layers under an additional assumption of the type of Eq. (11).

This property makes it possible to explicitly solve the optimum design problem for the cases considered, which means an efficient determination of the complete set of variants of structures implementing the ultimate performance.

2. The property of internal order, or the internal symmetry property, established earlier for electromagnetic and acoustic waves [2, 4] appears to be of a fairly general nature and holds for the wave processes whose interaction with inhomogeneous structures is described by models that are more complicated than those considered earlier in [2, 4]. In particular, it holds for elastic waves obliquely incident on the system of elastic layers in which shear waves can be excited.

3. The established regularities can also be used for investigating the general case of nonmonochromatic elastic waves obliquely incident on the system of elastic layers without any additional assumptions like condition (11). In this case, the preliminary search within the subset of variants selected according to the above regularities can offer efficient solutions that are quite appropriate for an initial approximation to the optimal solution for the initial design problem given by Eqs. (4) and (5).

REFERENCES

1. E. L. Gusev, Preprint, YaF SO AN SSSR (Yakutsk Branch, Siberian Division, Academy of Sciences of the USSR, 1990).
2. E. L. Gusev, *Mathematical Methods of the Synthesis of Layered Structures* (Nauka, Novosibirsk, 1993).
3. V. T. Grinchenko and V. V. Meleshko, *Harmonic Oscillations and Waves in Elastic Bodies* (Naukova Dumka, Kiev, 1981).
4. E. L. Gusev, Dokl. Akad. Nauk **346** (3), 324 (1996) [Phys. Dokl. **41** (1), 13 (1996)].
5. E. L. Gusev, Dokl. Akad. Nauk **349** (3), 329 (1996) [Phys. Dokl. **41** (7), 325 (1996)].
6. E. L. Gusev, Akust. Zh. **43**, 705 (1997) [Acoust. Phys. **43**, 612 (1997)].
7. E. L. Gusev, J. Appl. Mech. Tech. Phys. **38**, 768 (1997).
8. E. L. Gusev, in *Proceedings of International Conference on Symmetry in Natural History* (Krasnoyarsk, 1998), p. 47.
9. E. L. Gusev, Akust. Zh. **45**, 502 (1999) [Acoust. Phys. **45**, 443 (1999)].
10. A. N. Shupikov, N. V. Smetankina, and H. A. Sheludko, Meccanica **33** (6), 553 (1998).
11. J. S. Hesthaven, Comput. Phys. **142** (1), 129 (1998).
12. E. R. Michael, J. Acoust. Soc. Am. **104**, 3369 (1998).
13. J. K. Tomson, J. Sound Vib. **33** (6), 12 (1999).
14. L. S. Pontryagin, V. G. Boltyanskiĭ, R. V. Gamkrelidze, and E. F. Mishchenko, *Mathematical Theory of Optimal Processes* (Nauka, Moscow, 1983).

Translated by A. Vinogradov

Acoustical Physics, Vol. 47, No. 1, 2001, pp. 50–55. Translated from Akusticheskiĭ Zhurnal, Vol. 47, No. 1, 2001, pp. 62–68.
Original English Text Copyright © 2001 by Davydov, Lyamshev.

Electromagnetic–Acoustic Evaluation of the Permeability of Porous Media[1]

A. A. Davydov* and L. M. Lyamshev**

** Department of Geology and Geophysics, University of Adelaide, Adelaide, SA, 5000 Australia*
e-mail: dad@senet.com.au

*** Andreev Acoustics Institute, Russian Academy of Sciences,*
ul. Shvernika 4, Moscow, 117036 Russia
e-mail: lyamshev@kapella.gpi.ru

Received June 12, 2000

Abstract—The generation of ultrasound in a porous water-saturated medium subjected to rapid electromagnetic heating is considered. The irradiation provides the Joule heating of narrow and electrically high resistive pore throats, which interconnect cavities within the medium and, consequently, determine the permeability of the medium. Because of the small throat sizes, the sound generation is accompanied by considerable thermal flows going out from the throats into a relatively cold environment. Due to the latter, the output of the ultrasonic measurement allows one to estimate the rate of the thermal exchange process. A common geometric model of fluid flows and electric currents throughout a complicated network of intergranular cavities and their interconnecting throats is used for calculating the permeability of a rock on the basis of the determined values of the thermal exchange rate. *© 2001 MAIK "Nauka/Interperiodica".*

INTRODUCTION

The application of radiation exposure to a heterogeneous medium consisting of a matrix with embedded inclusions leads to the generation of acoustic waves, the characteristics of which are determined by the volume fraction, shape, size, and orientation of the inclusions [1]. In the recent past, this set of static medium parameters was extended by a dynamic parameter, which was permeability. The parameter determines the ability of a fluid or gas to penetrate through a porous structure under pressure [2]. A new method combining the electromagnetic heating of water in the pores and the detection of an acoustical response to the heating for permeability measurements in water saturated media has been proposed recently [3]. The method is based on the nonlinear effect of sound generation, when boiling occurs if the pressure of the saturated steam exceeds the sum of external and capillary pressures. Since the capillary pressure is determined by the size of pores, the size can be found by using the acoustically registered vaporization threshold. Unlike the direct but time consuming method of permeability assessment by means of mercury injections, this method [3] can be applied in field conditions, for oil exploration purposes, for example. The method of permeability control was also considered within the linear effect of ultrasound generation at low levels of electromagnetic irradiation, but with the use of primary microwave heating and subsequent radiofrequency irradiation [4]. The variant of the method using the radiofrequency range was proposed later [5].

In this paper, we investigate theoretically the process of acoustic generation resulting from the pulsed electromagnetic irradiation of a porous medium. The related inverse problem for the permeability reconstruction is solved as well.

SOUND GENERATION AND THE INVERSE PROBLEM

Let a pulse emitted by a system of electromagnetic coils propagate in the positive direction of the z axis and be incident on the surface of a porous sample at $z = 0$ (Fig.1). Then thermal sources of sound occur in the medium, the power density of which is determined by the relationship [6]

$$Q(x, y, z, t) = A\gamma J(x, y, t)\exp(-\gamma z), \qquad (1)$$

where A is the coefficient of electromagnetic wave transmission into the medium. The distribution of electromagnetic intensity $J(x, y)$ on the surface and the radiation absorption coefficient γ of the medium create a direction diagram for the space distribution of the sound sources [6]. Let the system of the electromagnetic sources provide a relatively uniform irradiation spot on the surface. Orienting toward the problems of oil exploration and taking into account typical well bore diameters of 10–30 cm, we estimate the spot to be in the diameter of 5–10 cm. We restrict the time of sound registration by the arrival time of the acoustic response coming from the spot perimeter. Then, assum-

[1] This paper was submitted by the authors in English.

ing the sound velocity $s \sim 3$–5 km/s, $t < a/2s \sim 5$–20 μs, we neglect the intensity variations across the xy-plane: $J(x, y) \approx \text{const}$. We assume the time of the electromagnetic irradiation to be short: $t_b \sim 0.1$–1 μs. After the irradiation process, $t > t_b$, electromagnetic noises cannot affect the operation of an acoustic detector placed on the front surface at the center of the irradiation spot.

Pulse irradiation of a porous medium leads to the appearance of nonuniform thermal pressure in the medium constituents, but for the problem under our consideration it can be described in terms of the effective pressure $P_e(z, t) = \Gamma_e(t)\ \overline{W}(z, t)$. Here, the Gruneisen parameter $\Gamma_e(t)$ depends on time, the kind of irradiation, and the medium parameters [7]. The density of energy deposited into the medium is determined by the power of the radiation-induced thermal sources: $\partial \overline{W}(z, t)/\partial t = Q(z, t)$. Acoustic displacements on the surface $z = 0$ originating from the exponentially decreasing effective pressure are given by the relationship

$$u(0, t) = -\frac{1}{\rho s^2}\int_0^{st} P_e\left(0, t - \frac{z''}{s}\right)\exp(-\gamma z'')dz''. \quad (2)$$

Introducing the speed of the displacements, we get

$$w(0, t) = \frac{\partial u(0, t)}{\partial t} = -\frac{1}{\rho s}P_e(0, t) - s\gamma u(0, t). \quad (3)$$

Thus, the measurements of the speed and acoustic displacements give us the time dependence of the effective pressure. By using the frequency dependence of the radiation penetration depth into the ground, it is possible to simplify the last equation further. For this purpose, we choose the radiofrequency range where the penetration depth, γ^{-1}, reaches tens of centimeters or meters [8], so the second term in the right part of Eq. (3) can be dropped.

POROUS STRUCTURE AND ELECTROMAGNETIC HEATING OF MATERIAL

In order to investigate the process of radiofrequency heating for a porous medium, we use a basic sample of wet sandstone. The permeability measurements for this mineral are very important for many applications. The mineral itself is dielectric, so electromagnetic radiation is absorbed mainly by the water-filled pores.

We treat the pore net of a cube volume of the medium having the edge length L_0 as a bundle of N_p pores, in that time a single pore is considered as a sequence of N_{ct} intergranular cavities interconnected by pore throats. The radiation loss is made up of two terms: the loss due to the lag of the polarization and the conductive loss [9]. The polarisation part $Q_d = 2\pi f\varepsilon_0\varepsilon_d'' E^2$ is determined by the electric field strength

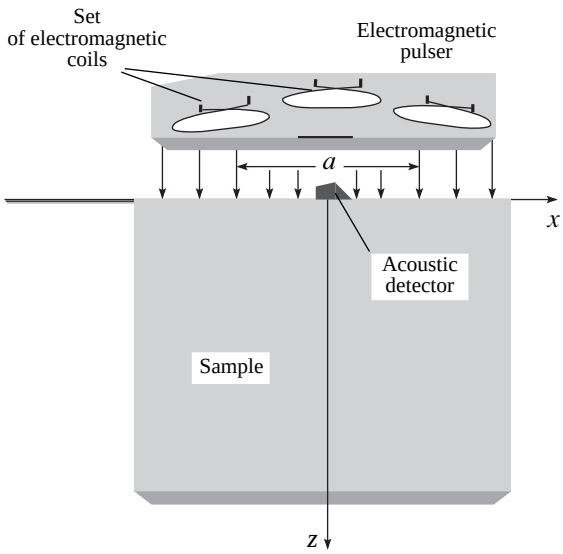

Fig. 1. The principal diagram of the electromagnetic–acoustic experiment.

E, the electromagnetic wave frequency f, and the dielectric loss factor ε_d'', and is approximately independent of pore size. The second term representing the rate of Joule heating $Q_j = \sigma_w^{-I} J^2$, is determined by the specific electric conductivity of pore the water σ_w and the eddy current density $J = I/S$. Thus, the rate of Joule heating is dependent on the pore cross-section area S. Electric current $I = U/R_p$ is the result of electric potential $U = EL_0$ induced between the opposite facets of the cube under irradiation. Pore resistivity R_p is

$$R_p = \frac{1}{\sigma_w}\int_0^L \frac{dl}{S} = \frac{L_0}{\sigma_w}\frac{1}{\langle S_1^- \rangle}, \quad (4)$$

Here and hereafter,

$$\frac{1}{\langle S_n^- \rangle} = \frac{1}{L_0}\int_0^L \frac{dl}{S^n(l)}; \quad \langle S_n \rangle = \frac{1}{L_0}\int_0^L S^n(l)dl. \quad (5)$$

The pore is longer then the edge length as a result of tortuosity: $L > L_0$. Taking into account the network of N_p paralleled pores per unit facet, $N_p/L_0^2 = \nu/\langle S_1 \rangle$, we find the specific electric conductivity of the rock:

$$\sigma = \frac{N_p}{R_p L_0} = \nu\sigma_w\frac{\langle S_1^- \rangle}{\langle S_1 \rangle}. \quad (6)$$

Here, ν is the porosity of the rock. From the above, the rate of electromagnetic heating is

$$Q_j = \frac{J^2}{\sigma_w} = \frac{1}{\sigma_w}\left(\frac{EL_0}{R_p}\right)^2\frac{1}{S^2} = \sigma_w E^2\frac{\langle S_1^- \rangle^2}{S^2}. \quad (7)$$

By the summation of the polarisation and conductive losses, we find the total rate of the heating in water-filled pores:

$$Q(S) = \bar{E}^2\left(2\pi f\varepsilon_0\varepsilon_d'' + \sigma_w\frac{\langle S_1^-\rangle^2}{S^2}\right), \quad (8)$$

where $\bar{E}^2$ represents a square electric field strength averaged over the period of the electromagnetic wave. Averaging over a pore volume gives us an equation for the rate of heating within the pore network:

$$\bar{Q} = \bar{E}^2\left(2\pi f\varepsilon_0\varepsilon_d'' + \sigma_w\frac{\langle S_1^-\rangle}{\langle S_1\rangle}\right). \quad (9)$$

Representing the square of the applied electric strength $\bar{E}^2$ in terms of the intensity of the electromagnetic radiation J^{mw}, we rewrite the Eq. (9) in the form $\bar{Q} = Q(x, y, z)\gamma^{-1}$, where Q is determined by relationship (1) and the penetration depth is [9]

$$\gamma^{-1} = \frac{c}{2^{3/2}\pi f}\frac{\sqrt{\sqrt{1 + (\varepsilon''/\varepsilon')^2} + 1}}{(\varepsilon''/\varepsilon')}. \quad (10)$$

Here, ε' is the relative dielectric constant of the medium ε'' is the loss factor, and c the speed of an electromagnetic wave in the medium. The complex dielectric constant is determined by $\varepsilon = \varepsilon_d + i\sigma/2\pi f\varepsilon_0$ and can be estimated by means of the equation [10]

$$\frac{\varepsilon_w - \varepsilon}{3\varepsilon} = (1 - \nu)\left(\frac{\varepsilon_w - \varepsilon_r}{2\varepsilon + \varepsilon_r}\right), \quad (11)$$

where ε_r represents the dielectric permittivity of the rock skeleton and ε_w is the complex dielectric constant of bound water.

The penetration depth is plotted in Fig. 2 as a function of the electromagnetic frequency in the range of 1–900 MHz. Apparently, the penetration depth depends on the water conductivity determined by the concentration of salt and the pore volume fraction, and the depth varies from several centimeters, when the volume fraction and water conductivity reach high values, up to hundreds of meters at low values of the parameters. Lowering the radiation frequency stimulates the growth of the Joule loss part relative to the polarisation losses. Even in the case of a low porosity of 5% and a water conductivity of 0.1 Sm/m, if the polarisation losses represent the main part of the total losses at a frequency of 100 MHz, the polarisation part is a third of the total losses only at a frequency of 1 MHz. Thus, the frequency tuning allows us to reduce the polarisation losses and, therefore, to neglect the first term in the brackets of Eqs. (8) and (9) and to adjust the depth of penetration. As an example, the penetration depth of a high porosity, 30%, and high conductivity, 10 Cm/m, medium is about 8.5 cm at the working frequency of 100 MHz, but it reaches up to 27 cm if the working frequency is reduced to 1 MHz.

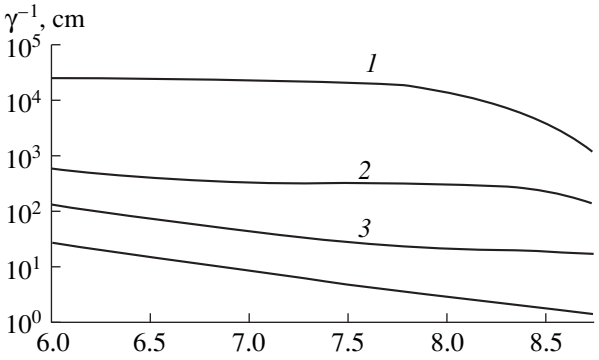

Fig. 2. Penetration depth for electromagnetic radiation at different values of the electrical conductivity of ground water and the water saturation of the ground versus the logarithm of the wave frequency. The porosity is (*1*) 5, (*2*) 15, (*3*) 20, and (*4*) 30%; σ_w = (*1*) 0.01, (*2*) 0.1, (*3*) 1, and (*4*) 10 Cm/m.

EFFECTIVE THERMAL PRESSURE AND THERMAL EXCHANGE IN A POROUS MATERIAL

Heating leads to the appearance of thermal pressure in heated pores $P_w(t) = \Gamma_w(T)\ \bar{W}_w(z, t)$, where Γ_w is the temperature dependent Gruneisen parameter of water. Another component of pressure $P_r = \Gamma_r\bar{W}r(z, t)$, where Γ_r is the Gruneisen parameter of the mineral matrix, appears in the matrix due to thermal flows going out from the heated pores and forming the density of absorbed energy $\bar{W}r(z, t)$ in the mineral. The P_p and P_r pressures together form the time dependent effective pressure used in Eqs. (2) and (3) [7]:

$$P_e(z, t) = \nu a_w P_w(z, t) + (1 - \nu)a_r P_r(z, t). \quad (13)$$

The parameter describing pressure transformations in acoustically slightly mismatched rock skeleton–wet rock structures, a_r, can be estimated by means of the relationship

$$a_r \approx \frac{3K + 4\mu}{3K_r + 4\mu_r}, \quad (14)$$

where K and μ are the effective bulk and shear moduli of the wet mineral and K_r and μ_r represent the corresponding moduli of the matrix.

Taking into account that the effective modulus K and μ are decreasing functions of the porosity ν, the coefficient of pressure transformation a_r is a decreasing function of the porosity with maximum value at $\nu = 0$. A more complicated problem is to estimate the parameter a_w dependent on the pore shape and varying from a minimum value in the case of spherical or needle-

shaped pores to a maximum value in the case of flake-like pores [11]:

$$\frac{3K + 4\mu}{3K_w + 4\mu} \le a_w \le \frac{3K + 4\mu}{3K_w}. \quad (15)$$

For sandstone, $K_r \approx 3.6 \times 10^{10}$ Pa and $\mu_r \approx 2.2 \times 10^{10}$ Pa (quartz mainly) [12], we estimate the possible variations of the ratio a_w/a_r in the range of $2 \le a_w/a_r \le 30$. Therefore, the dependence on the energy balance of the medium constituents is determined for the effective pressure by the shapes of the porous cavities forming the main volume of the pore. Substituting the obtained boundary values and taking the water's Gruneisen parameter at the well bore temperature of 40°C, $\Gamma_w \approx 0.16$, $\Gamma_r = \alpha_r K_r/\rho_r C_r = 0.6$, $\alpha_r = 3.4 \times 10^{-5}$ °C^{-1}, $\rho_r = 2.7$ g/cm^3, and $C_r = 0.74$J/g°C, we estimate the possible variations $-0.5 \le \xi \le 7$ for the parameter $\xi = a_w\Gamma_w/a_r\Gamma_r$. The parameter determines the sensitivity of the effective pressure to the variation of the mineral–pore energy balance:

$$P(z, t > t_b) = \nu a_r \Gamma_r W_w(z, t_b)\left[1 + \xi\frac{W_w(z, t)}{W_w(z, t_b)}\right]. \quad (16)$$

Here, $W_w(z, t_b)$ is the density of the energy deposited into a pore during the time of irradiation t_b and $W_w(z, t)$ represents the density of energy remaining in the pore up to time t. In order to derive the equation of the energy balance, we consider thermal flows going out from a pore segment having a cross-section area S and length l_s. Assuming that the thermal exchange is insignificant for time t_b, the approximation of instantly acting heating used is $t_b = 0$. The thermal flows from the segment boundary are maximally close to the initial thermal excitation and follow the heat conductivity law for two contacting halfspaces [13]:

$$q_T(S, t) = -Sl_s\frac{\partial W_w(S, t)}{\partial t} = -S_\perp\kappa_w\nabla W_w(S, t) \approx \frac{2}{1 + K_\varepsilon}\sqrt{\frac{\kappa_w}{t}}S_\perp W_w(S, t). \quad (17)$$

Here, $K_\varepsilon = \lambda_w\kappa_w/\lambda_r\kappa_r$, where λ_w and λ_r are the thermal conductivities and coefficients κ_w and κ_r represent the temperature conductivities of the water and the mineral. The gradient is taken normal to the boundary, and $S_\perp \approx 2(\pi S)^{1/2}l_s$ is the area of water–mineral contact. Because the flows are proportional to the density of the absorbed energy, the relative value of those is independent of the variable z and we omit the variable. The average of $W(S, t)$ along the pore

$$\overline{W_w(t)} = \frac{1}{\langle S_1\rangle}\frac{1}{L_0}\int_0^L SW_w(S, t)dl, \quad (18)$$

and the expression of the function $\overline{W}_w(t)$ as a Taylor power series of $t^{1/2}$ yield near $t = 0$

$$\frac{\overline{W_w(t)}}{\overline{W_w(0)}} \approx 1 - \frac{4\sqrt{\kappa_w t}}{(1 + K_\varepsilon)\langle S_1\rangle}\frac{1}{L_0}\int_0^L\left(\frac{S_\perp}{l_S}\right)\frac{W_w(S, t)}{\overline{W_w(0)}}dl \approx \exp\left(-\sqrt{\frac{t}{t_T}}\right). \quad (19)$$

Here, the characteristic time of thermal exchange is determined by the relationship $t_T = (1 + K_\varepsilon)^2 D_e^2/16\kappa_w$, where the length parameter is defined as an effective diameter and determined by the relation

$$\frac{1}{D_e} = \frac{2\sqrt{\pi}}{\langle S_1\rangle}\frac{1}{L_0}\int_0^L\sqrt{S}\frac{W_w(S, 0)}{\overline{W_w(0)}}dl. \quad (20)$$

Because the Joule losses provide the main heating at frequencies below 100 MHz, we have

$$D_e \approx \frac{1}{2\sqrt{\pi}}\frac{\langle S^-_{3/2}\rangle}{\langle S^-_1\rangle}. \quad (21)$$

Taking into account that in the limiting case of $t \gg t_T$ the temperatures of the water and the mineral should be equal, we get a more complicated approximate relationship:

$$\frac{\overline{W_w(t)}}{\overline{W_w(0)}} \approx \nu\frac{\rho_w C_w}{\rho C} + \left(1 - \nu\frac{\rho_w C_w}{\rho C}\right)\exp\left(-\sqrt{\frac{t}{t_T}}\right), \quad (22)$$

where $\rho C = \nu\rho_w C_w + (1 - \nu)\rho_r C_r$ is the specific heat capacity of the water-saturated mineral.

PORE STRUCTURE AND PERMEABILITY

The analysis suggests that the effective pressure and, therefore, the acoustic response on heating are dependent of the effective diameter D_e. Additionally, the fluid flow along a pore under pressure and, therefore, the permeability of the porous medium are dependent on the cross section [14]. Considering again a cubic sample with the edge length L_0, we establish a relation between the permeability and the effective diameter D_e. Within the approximation of stationary flow, the rate of the flow is constant along a pore:

$$q_p = \left(\frac{dP}{dl}\right)\frac{1}{8\pi\mu}S^2, \quad (23)$$

where dP/dl is the gradient of pressure along the pore. Using the permeability definition [2], we find the rate of the fluid flow q_{tot} throughout the system of all N_p/L_0^2 pores:

$$q_{tot} = \frac{N_p q_p}{L_0^2} = \frac{k}{\mu}\frac{\Delta P}{L_0} = \frac{k}{\mu}\frac{1}{L_0}\int_0^L\left(\frac{dP}{dl}\right)dl. \quad (24)$$

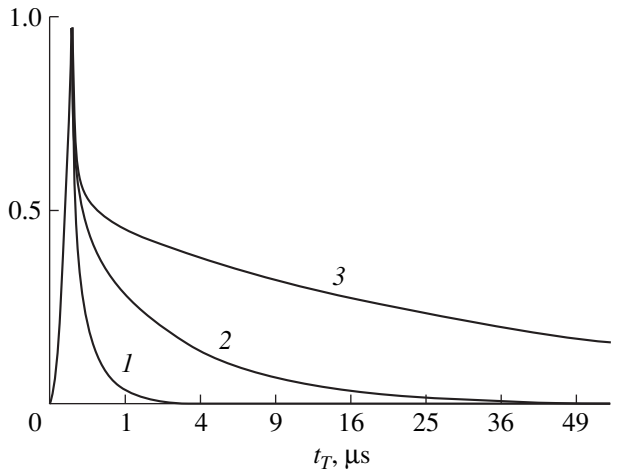

Fig. 3. The waveforms of ultrasound signals generated by electromagnetic pulses in a porous medium. After the representation of heating dynamics ($t < t_b$), on the right of the vertical dashed line, the signals show the dynamics of thermal exchange. The duration of the thermal exchange is determined by the permeability of the porous medium.

From that we derive the relationship for the coefficient of permeability:

$$k = \frac{q_p \mu N_p}{L_0 \int_0^L \left(\frac{dP}{dl}\right) dl} = \frac{N_p}{8\pi L_0^2} \langle S_2^- \rangle, \quad (25)$$

where ΔP is the difference of the pressure level applied to opposite facets of the mineral sample. Multiplying and dividing by $\langle S_1^- \rangle$, then using Eq. (6) and the approximate relation $\langle S_2^- \rangle \langle S_1^- \rangle \approx (\langle S_{3/2}^- \rangle)^2$, we write the relationship for the permeability coefficient in the form

$$k \approx \frac{\nu}{8\pi} \frac{(\langle S_{3/2}^- \rangle)^2}{\langle S_1 \rangle \langle S_1^- \rangle} = \frac{\sigma}{8\pi\sigma_w} \left(\frac{\langle S_{3/2}^- \rangle}{\langle S_1^- \rangle} \right)^2. \quad (26)$$

Thus, the permeability is determined by the effective diameter

$$k \approx \frac{\sigma}{2\sigma_w} D_e^2. \quad (27)$$

In order to estimate D_e, we substitute for conductivity σ the relationship given by Archie's law: $\sigma = \sigma_w (S_w)^n \nu^m$ [2] for a fully saturated medium, $S_w = 1$, with the empirical constant $m = 2$. This yields $D_e = (2k)^{1/2} \nu^{-1}$. Taking into account that commercial reservoirs generally have permeability ranging from a few millidarcys ($k \sim 10^{-11}$ cm^2) up to a darcy ($k = 10^{-8}$ cm^2), and porosity $\nu \approx 0.1$–0.3, we estimate that the effective diameter varies in the range from 0.2 up to 10 μm. The size is close to the diameters of pore throats determined in petrographic observations [15]. Substituting the coefficient of water temperature conductivity $\kappa_w \approx 0.0014$ cm^2/s, we find that $0.1 < t_T < 100$ μs. The size of pores is sufficiently large and distributed in the range from 40 up to 400 μm [15]. For these sizes, the thermal time t_T lies in the range from ~600 μs up to 0.24 s. Comparing that with the effective time of ultrasound generation of several microseconds, we conclude that thermal flows from overheated pore throats must be taken into account, but the pore–rock skeleton thermal exchange is insignificant.

In terms of the time of thermal exchange t_T, the permeability k is determined by

$$k = \frac{8\kappa_w}{(1 + K_\varepsilon)^2} \frac{\sigma}{\sigma_w} t_T \approx 8\kappa_w \nu^2 t_T. \quad (28)$$

Thus, on the one hand, the time of thermal exchange t_T determines the permeability coefficient and, on the other hand, it manages the time dependence of the effective pressure according to relationships (13) and (19). That gives the opportunity for acoustical measurements of time t_T. For example, in the case of low absorption $\gamma \ll 1$, the speed of displacements in a response is proportional to the effective pressure.

As follows from Eq. (16), in the case of needle-shaped inclusions, the effective pressure reaches its maximum $P_c(z) = \nu a_r \Gamma_r W_w(z, t_b)$ on the latest stages of the thermal exchange process, when $t \sim t_T$. In the case of $\zeta \approx -0.5$, the pressure for earlier stages is only half of the above pressure value. More sufficient changes are expected for flake-shaped inclusions, when $\zeta \approx 7$, and the maximum of about of 8 P_c follows the pulse of irradiation immediately. Orienting on P_c and assuming it to be equal to the relatively easily registered pressure of 100 Pa, we estimate the value of the current in electromagnetic coils which is required for getting this pressure level. As it is possible to show, for the relatively favorable conditions of high water conductivity $\sigma = 1$Cm/m and porosity of 20%, the current required in the coils is about 1KA, when the time of 10 MHz irradiation is 1 μs. As follows from Fig. 2, the depth of penetration in this case reaches 8 m, which is sufficiently long as compared to the assumed probed depth of 10 cm. It should be noted that it is also possible to apply the contact method of radio-frequency heating, where electrodes contact an investigated sample electrically. The method requires sufficiently small electric currents.

As follows from Eqs. (3) and (16), for the acceleration $a(0, t) = \partial w(0, t)/\partial t$ measured after electromagnetic irradiation (or derived numerically from the measurement of acoustic stresses), the primarily unknown parameter ξ appears as a coefficient determining the amplitude and polarity of the acoustic response only. Therefore, the analysis in terms of the acceleration looks favorable. Since the effective pressure is a function of the density of energy deposited into a medium, the complicated picture of tens of megahertz can occur in the front part of the acoustic wave responding the dynamics of density growth ($t < t_b$). We are interested in

latest stages representing the dynamics of thermal exchange, so we omit the detailed investigation of the earlier stage and just approximate the signal using Eq. (16), where $W_w(z, t < t_b) = Qt$.

Acoustic accelerations have been calculated for the surface of a sandstone sample. The result of the calculations is shown in Fig. 3, where the function $a(0, t)t^{1/2}$ is plotted instead of the acceleration function. Due to the square root dependence of the effective pressure on time, the dependence of the new function on time t_T looks more illustrative. Also the square time scale was chosen for the abscissa axis. The curves were normalized to the maximum of acceleration achieved within the approximation used at $t = t_b$. Curve *1* represents an extremely short acoustic response following the electromagnetic heating of a structure having a low permeability of about a millidarcy and, sequentially, a rapid thermal exchange during $t_T \sim 0.1$ μs. A longer pulse for the case of intermediate porosity of 0.1 darcy, $t_T = 2$ μs, is presented by curve *2*. A long acoustic response of the duration of tens microseconds, curve *3*, represents the case of high permeability of about several darcies and thermal exchange time $t_T = 40$ μs. The pulse width from t_b up to the moment where the level of the amplitude drops to exp(–1)/2 of the maximum signal value could be taken as the primary estimation of the time of thermal exchange. Together with independently determined porosity ν, it gives the estimation of permeability. In order to estimate in a more exact manner, we build the function

$$\chi(\tau_1, \tau_2) = \frac{\sqrt{t_1}a(0, t_1)}{\sqrt{t_2}a(0, t_2)} = \frac{\partial P_e(0, \tau)/\partial\tau|_{\tau = \sqrt{t_1}}}{\partial P_e(0, \tau)/\partial\tau|_{\tau = \sqrt{t_2}}} \approx \exp\left(\frac{\tau_2 - \tau_1}{\sqrt{t_T}}\right) \quad (29)$$

If a number of measurements distributed along a set of time moments are available, we get the estimation of the thermal time averaged over the measurement set:

$$\overline{\sqrt{t_T}} = \frac{1}{NM}\sum_{i=1}^{N}\sum_{j=1}^{M}\frac{\tau_j - \tau_i}{\ln(\chi(\tau_i, \tau_j))} \quad (30)$$

CONCLUSIONS

The analysis of ultrasound generation in a porous water saturated medium subjected to a rapid electromagnetic irradiation shows that the irradiation mainly provides the Joule heating of narrow and electrically high resistive pore throats. The throats interconnect cavities within the medium and, consequently, determine the permeability of the medium. Due to small throat sizes, the sound generation is accompanied by considerable thermal flows outgoing from the throats to a relatively cold environment. As a result, the output of the ultrasonic measurement represents the dynamics of the thermal exchange process and the duration of the process allows one to estimate the permeability value.

ACKNOWLEDGMENTS

The work of A. A. Davydov was supported in part by the Australian Cooperative Research Centre and the National Centre for Petroleum Geology and Geophysics (Australia). The work of L. M. Lyamshev was supported by the Russian Foundation for Basic Research (project no. 99-02-16334).

REFERENCES

1. A. A. Davydov, Zh. Tekh. Fiz. **61** (3), 186 (1991) [Sov. Phys. Tech. Phys. **36**, 365 (1991)].
2. W. W. Telford, L. P. Geldart, R. E. Sheriff, and D. A. Keys, *Applied Geophysics* (Cambridge Univ. Press, Cambridge, 1976).
3. A. A. Davydov and J. K. Applegate, Australian Provisional Patent Application PO 1760 (1996).
4. A. A. Davydov, *Annual Report* (Nat. Centre Petroleum Geolog. Geophys., Univ. of Adelaide, South Australia, 1997), p. 24.
5. A. A. Davydov and S. A. Greenhalgh, Australian Provisional Patent Application PQ 0755 (1999).
6. L. M. Lyamshev, *Radiation Acoustics* (Nauka, Moscow, 1996).
7. A. A. Davydov and V. T. Lazurik, Akust. Zh. **31**, 705 (1985) [Sov. Phys. Acoust. **31**, 432 (1985)].
8. J. L. Davis and A. P. Annan, Geophys. Prospect. **37**, 531 (1989).
9. A. C. Metaxas and R. J. Meredith, *Industrial Microwave Heating* (Peter Peregrinus, London, 1988).
10. J. D. Hasted, *Aqueous Dielectrics* (Chapmen and Hall, New York, 1973).
11. A. A. Davydov, A. I. Kalinichenko, and V. T. Lazurik, Probl. Yad. Fiz. Kosm. Lucheĭ, No. 21, 43 (1984).
12. *Tables of Physical Data: Handbook*, Ed. by I. K. Kikoin (Atomizdat, Moscow, 1976).
13. A. V. Lykov, *Analytical Heat Diffusion Theory* (Vysshaya Shkola, Moscow, 1967; Academic, New York, 1968).
14. L. D. Landau and E. M. Lifshitz, *Course of Theoretical Physics*, Vol. 6: *Fluid Mechanics* (Nauka, Moscow, 1986; Pergamon, New York, 1987).
15. M. R. Rezaee and N. M. Lemon, Aust. PESA J. **24**, 116 (1996).

Acoustical Physics, Vol. 47, No. 1, 2001, pp. 56–61. Translated from Akusticheskiĭ Zhurnal, Vol. 47, No. 1, 2001, pp. 69–75.
Original Russian Text Copyright © 2001 by El'meshkin, Shevyakhov.

Mode Spectrum of Noncollinear Electroacoustic Boundary-Guided Waves in a Ferroelectric with a Moving Strip Domain

O. Yu. El'meshkin and N. S. Shevyakhov

Institute of Radio Engineering and Electronics (Ul'yanovsk Branch), Russian Academy of Sciences, ul. Goncharova 48, Ul'yanovsk, 432011 Russia
e-mail: ufire@mv.ru

Received November 12, 1999

Abstract—The mode spectrum of electroacoustic boundary waves guided by a strip domain uniformly moving in a 4-mm ferroelectric is considered in the quasi-static approximation. The motion of the strip domain is found to cause the wave vector of the electroacoustic wave to be noncollinear with the guiding boundaries. The frequency dependences of the phase velocity are presented for the symmetric and antisymmetric modes of the electroacoustic wave. These dependences are compared in the reference system fixed to the strip domain and in the laboratory reference system. It is shown that, at low and moderate frequencies, the symmetric mode of the electroacoustic wave is more efficiently localized by a moving strip domain than by a single domain wall. *© 2001 MAIK "Nauka/Interperiodica".*

The Gulyaev–Bleustein [1, 2] electroacoustic boundary waves are efficiently guided by single domain walls [3–5], as well as by systems of parallel domain boundaries in ferroelectric crystals [6–8]. The steady interest in such systems, which can be treated as periodic media (superlattices) when the number of domain walls (DWs) is great, is partly associated with the progress in acoustics of solid layered structures [9, 10] in relation to the new possibilities of synthesizing them by computer-aided techniques. Another stimulus to study these structures is the promising possibility of purposefully changing the regular ferroelectric domain structure by an external action (electric field, mechanical load, heating, etc.) in processing devices based on acoustic waves in order to control their characteristics [11].

Experimental achievements [12] opened up possibilities for practical applications of these effects. However, except for [13], theoretical studies were limited to stationary (fixed) DWs. At the same time, it is clear that, in general, one should allow for the DWs motion due to the rearrangement of the ferroelectric domain structure that accompanies switching of acoustodomain devices. For example, the motion of DWs can result from breaking the crystal domain structure when the device operates in a nonstationary abnormal mode of operation. In order to extend the field of application and to find additional signal-processing possibilities in acoustodomain devices, it is even more interesting to consider the DWs motion as the forced one, caused purposefully by a control action.

This paper continues the study [13] of electroacoustic boundary waves guided by moving DW. Specifically, it analyzes the effect of a uniform motion of a strip domain (SD) of thickness $d \gg \Delta$ (Δ is the thickness of a 180° DW) on the propagation of electroacoustic boundary waves along this domain in the (001) plane of a 4-mm tetragonal ferroelectric. Evaluation of waveguide properties of the moving SD seems most important, because it usually represents the main element of the regular domain structure of polydomain ferroelectric materials [14]. On the other hand, in controlled acoustodomain devices, crystals with a single SD are preferred.

As in the previous paper [13], we assume that the ferroelectric has a crystallographic orientation with the tetrad axis being parallel to the z-axis of the laboratory coordinate system $x0yz$, but it has two, rather than one, parallel 180° domain walls of a very small wave thickness $k\Delta \ll 1$, where k is the wave number of the electroacoustic wave. These DWs lie in equispaced (010) planes of the crystal at $y_1 = V_D t$ and $y_2 = V_D t + d$, where t is the time, thus forming a strip domain moving at a constant speed $\mathbf{V}_D \| y \|$ [010]. We assume that the DW is described by a structureless model and that it, as well as the thermodynamic state of the crystal and the SD motion, comply with the constraints imposed in [13].

As usual (see [3, 4, 6–8]), we treat the ferroelectric as a piezoelectric crystal symmetric with respect to the planes $y = y_{1,2}$ and represent the effective piezoelectric modulus e_{15} inside and outside the SD as $e_{15} = e$ for $y_1 < y < y_2$ and $e_{15} = -e$ for $y < y_1$ and $y > y_2$, where e is the piezoelectric modulus of a single-domain ferroelectric. Then, we use the quasi-static approximation and change to the coordinate system $\tilde{x}0\tilde{y}\tilde{z}$ fixed to the SD and related to the laboratory coordinate system through the Galilean transformation

$$\tilde{x} = x, \quad \tilde{y} = y - V_D t, \quad \tilde{z} = z, \quad \tilde{t} = t. \qquad (1)$$

1063-7710/01/4701-0056$21.00 © 2001 MAIK "Nauka/Interperiodica"

As a result, for the shear displacements $\mathbf{u}$ and $\mathbf{u}_j \parallel z$ ($j = 1$ for $\tilde{y} < 0$ and $j = 2$ for $\tilde{y} > d$) and for the electric potentials

$$\varphi = \frac{4\pi e}{\varepsilon}u + \Phi, \quad \varphi_j = -\frac{4\pi e}{\varepsilon}u_j + \Phi_j, \tag{2}$$

we obtain the relationships

$$\left[\frac{1}{c_t^2}\left(\frac{\partial}{\partial\tilde{t}} - V_D\frac{\partial}{\partial\tilde{y}}\right)^2 - \tilde{\nabla}^2\right]\begin{pmatrix} u \\ u_j \end{pmatrix} = 0, \quad \tilde{\nabla}^2\begin{pmatrix} \Phi \\ \Phi_j \end{pmatrix} = 0. \tag{3}$$

These relationships are derived from equations obtained in [3, 6, 7, 13]. In Eqs. (2) and (3), $\tilde{\nabla} = \partial^2/\partial\tilde{x}^2 + \partial^2/\partial\tilde{y}^2$; Φ and Φ_j are the potentials of the electrostatic leakage fields induced from the SD surfaces into its volume and into external regions by the piezopolarization charges; $c_t = (\lambda^*/\rho)^{1/2}$ is the shear wave velocity; $\lambda^* = \lambda + 4\pi e^2/\varepsilon$; ε is the permittivity; λ is the shear modulus; and ρ is the crystal density.

The conventional boundary conditions [1–8], which require that the displacements, the potentials, the shear stresses, and the normal components of the electric induction be continuous, do not contain time derivatives, and, therefore, they retain their form after we change to the SD-fixed coordinates. One should bear in mind only that they are transferred to the planes $\tilde{y}_j = (j-1)d$, $j = 1, 2$.

By virtue of Eq. (2), the boundary conditions can be written in the form

$$\begin{aligned} &(u - u_j)\big|_{\tilde{y}=\tilde{y}_j} = 0, \quad \left(\frac{\partial\Phi}{\partial\tilde{y}} - \frac{\partial\Phi_j}{\partial\tilde{y}}\right)\Big|_{\tilde{y}=\tilde{y}_j} = 0, \\ &\left(\frac{4\pi e}{\varepsilon}u + \Phi\right)\Big|_{\tilde{y}=\tilde{y}_j} = \left(-\frac{4\pi e}{\varepsilon}u_j + \Phi_j\right)\Big|_{\tilde{y}=\tilde{y}_j}, \\ &\left(\lambda^*\frac{\partial u}{\partial\tilde{y}} + e\frac{\partial\Phi}{\partial\tilde{y}}\right)\Big|_{\tilde{y}=\tilde{y}_j} = \left(\lambda^*\frac{\partial u_j}{\partial\tilde{y}} - e\frac{\partial\Phi_j}{\partial\tilde{y}}\right)\Big|_{\tilde{y}=\tilde{y}_j}. \end{aligned} \tag{4}$$

Aiming to construct the solutions to Eqs. (3) in the form $\exp i(k_\parallel\tilde{x} - \Omega\tilde{t})$, we obtain the following equations for the characteristic coefficients q:

$$(1-\beta^2)q^2 - i2\frac{\Omega}{c_t}\beta q - \left(k_\parallel^2 - \frac{\Omega^2}{c_t^2}\right) = 0, \; q^2 - k_\parallel^2 = 0, \tag{5}$$

where $\beta = V_D/c_t$.

Since u, Φ, u_j, and Φ_j must be finite in their domains of definition, Eqs. (5) yield

$$\begin{aligned} u_j &= U_j e^{i\xi}e^{ik_\perp\tilde{y}}\exp[(-1)^{j+1}s\tilde{y}], \\ u &= e^{i\xi}e^{ik_\perp\tilde{y}}(Ve^{-s\tilde{y}} + We^{s\tilde{y}}), \\ \Phi_j &= F_j e^{i\xi}\exp[(-1)^{j+1}k_\parallel\tilde{y}], \\ \Phi &= e^{i\xi}(Ae^{-k_\parallel\tilde{y}} + Be^{k_\parallel\tilde{y}}). \end{aligned} \tag{6}$$

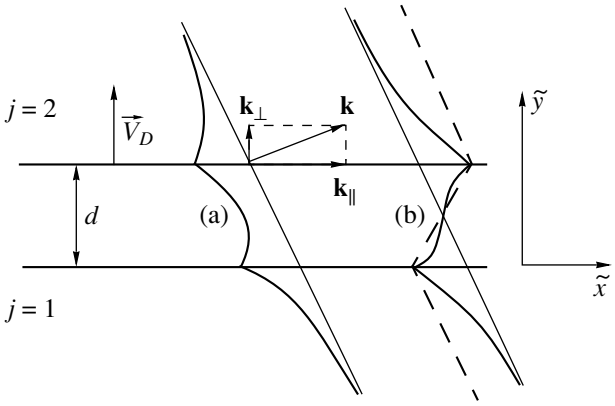

Fig. 1. SD-fixed coordinate system and the distribution of shear displacements along a sloping wavefront of a noncollinear electroacoustic wave: (a) the symmetric mode and (b) the antisymmetric mode.

In Eqs. (6), $\xi = k_\parallel\tilde{x} - \Omega\tilde{t}$ is the phase of the electroacoustic wave measured along the SD; Ω is the frequency in the SD-fixed coordinate system; and $k_\parallel$ and $k_\perp$ are the longitudinal and transverse components of the electroacoustic wave number $\mathbf{k} = \mathbf{k}_\parallel + \mathbf{k}_\perp$ (see Fig. 1). In view of the constraint $\beta < 1$, we obtain

$$k_\perp = \frac{\Omega}{c_t}\frac{\beta}{1-\beta^2}, \quad s = \frac{1}{1-\beta^2}\sqrt{k_\parallel^2(1-\beta^2) - \frac{\Omega^2}{c_t^2}}. \tag{7}$$

In addition to Eqs. (7), we find a relationship that is characteristic particularly of the electroacoustic waves and relates the amplitude attenuation factor s and the spectral parameters $k_\parallel$, $k_\perp$, and Ω; this relationship can be found by numerically solving the transcendental equation

$$\begin{aligned} &\mathcal{K}^4\frac{\kappa^2}{\sigma^2}(1-e^{-2\kappa})(1-e^{-2\sigma}) \\ &-2\mathcal{K}^2\frac{\kappa}{\sigma}(1-e^{-\sigma}e^{-\kappa}\cos k_\perp d) + 1 = 0. \end{aligned} \tag{8}$$

It represents the solvability condition for the system of homogeneous algebraic equations in the amplitudes of displacements U_j, V, and W and potentials F_j, A, and B, which results from substituting Eqs. (6) into Eqs. (4). According to the established terminology [1–6], Eq. (8) can be called the dispersion relationship for the electroacoustic wave guided by the moving SD. In Eq. (8), $\mathcal{K}^2 = 4\pi e^2(\varepsilon\lambda^*)^{-1}$ is the squared electromechanical coupling coefficient, $\kappa = k_\parallel d$, and $\sigma = sd$.

To calculate the electroacoustic wave spectrum, one should determine the function $\sigma = \sigma(\kappa)$ from Eq. (8), where $k_\perp d = [\kappa^2\beta^2(1-\beta^2)^{-1} - \sigma^2]^{1/2}$ as a result of eliminating $\tilde{\Omega}$ from Eqs. (7). This function together with Eqs. (7) and the relationship between Ω and the wave frequency ω in the laboratory coordinate system determines any characteristic of the electroacoustic wave in

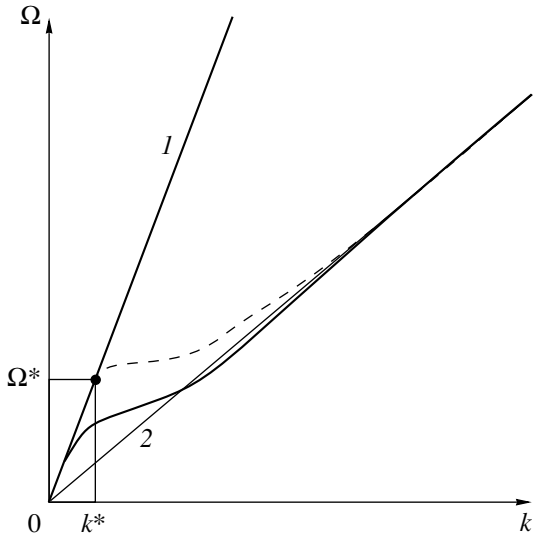

Fig. 2. General form of the electroacoustic wave spectrum: the symmetric mode (solid line) and the antisymmetric mode (dashed line).

the SD-fixed coordinate system and in the laboratory coordinate system. Before discussing the numerical results, we give a general description of the electroacoustic wave on the basis of the analysis of Eqs. (6)–(8).

At $\beta = 0$ ($k_\perp = 0$), Eq. (8) takes a known simplified form [6]

$$\sigma = \kappa\mathcal{K}^2(1 \pm e^{-\sigma})(1 \mp e^{-\kappa}). \qquad (9)$$

The upper and lower signs in Eq. (9) correspond to the symmetric and antisymmetric modes of the electroacoustic wave, respectively; these modes received their names in compliance with the distribution of the displacements u from Eqs. (6) with respect to the SD middle plane $\tilde{y} = d/2$. The conclusion that the two modes are present is also valid for $\beta \neq 0$, because biquadratic equation (8) has two roots $(\mathcal{K}^2\kappa/\sigma)_{1,2}$. Typical profiles of the displacements u and u_j are shown in Fig. 1, where (a) the symmetric mode is determined by the root of Eq. (8) with a higher ratio σ/κ, and the antisymmetric mode (b) corresponds to the root of Eq. (8) with the smaller ratio σ/κ.

The motion of the SD changes the structure of the electroacoustic wave so that its wave vector **k** becomes noncollinear with respect to the guiding surfaces $\tilde{y} = 0$ and $\tilde{y} = d$. For waves guided by stationary (fixed) boundaries, this property is observed in the leaky or quasi-surface acoustic waves [15]; it always indicates that the wave loses its energy due to the radiation into the underlying halfspace or into the adjacent external medium. When the SD moves, the electroacoustic wave can be formally associated with the decaying leaky wave only on one side of the SD, for $\tilde{y} > d$. On the other side ($\tilde{y} < 0$), the wave concentrates near the boundaries, which is a property not typical of the known types of surface or boundary waves. Thus, an energy flux exists in this wave that flows through the DW with a component collinear with the SD motion, which eliminates the possibility of losing or accumulating the energy at the guiding surfaces.

The inclination of the electroacoustic wavefront (Fig. 1) in the direction of the SD motion and the formation of the transverse component of the wave vector $\mathbf{k}_\perp \neq 0$ can be considered as a response to the "ether wind." In fact, from the viewpoint of the observer connected with the SD, the medium, due to its drift, transfers energy in the direction opposite to the actual SD motion. For the electroacoustic wave propagation to be stationary ($k_\parallel > 0$, $k_\perp > 0$, and $\Omega > 0$), the wave must compensate for this effect by the transverse component of the energy flux. This component arises when $\mathbf{k}_\perp \neq 0$ and characterizes the power spent by the external source (it is present implicitly because of the presence of the SD motion) for the motion of the electroacoustic wave connected with the SD through the piezopolarization charges.

Figure 2 shows a typical mode spectrum of the electroacoustic wave guided by the SD. The SD motion manifests itself primarily as a change in the slope of asymptotes 1 and 2. In particular, as follows from the first equation of Eqs. (3) and Eq. (7) for $k_\perp$, the low-frequency asymptote 1 of the symmetric mode, which represents the dispersion law for the bulk shear waves in a single-domain crystal, has the form $\Omega = kc_t(1 - \beta^2)$ with allowance for the medium drift. The high-frequency asymptote 2, which is common for the two modes, represents the dispersion law for the electroacoustic wave guided by a single moving DW [13] (the Maerfeld–Tournois mode [3]) modified by virtue of Eq. (7) due to the medium drift:

$$\Omega = kc_t(1-\beta^2)\left[\frac{1-\mathcal{K}^4(1-\beta^2)}{1-\mathcal{K}^4\beta^2(1-\beta^2)}\right]^{1/2}. \qquad (10)$$

This law is obtained in the limit $d \longrightarrow \infty$ ($\sigma \longrightarrow \infty$, $\kappa \longrightarrow \infty$) from Eq. (8).

The heavy dot in Fig. 2 (k^*, Ω^*), at which the antisymmetric wave originates, also belongs to asymptote 1, and, therefore, $\Omega^* = k^*c_t(1 - \beta^2)$ and $\sigma^* = \sigma(\kappa^*) \equiv 0$. Delocalization of the oscillations of shear displacements u_j from Eqs. (6) indicates that the antisymmetric mode degenerates into the simplest one and, as becomes clear from the error found in [16], the only possible form of the discrete spatial spectrum of the so-called plane homogeneous waves associated with (better to say, captured by) the SD. Since the first of the characteristic equations (5) has multiple roots at $\Omega = \Omega^*$ and $k = k^*$, the field of the shear displacements u inside the SD will contain a linear function of $\tilde{y}$ in parentheses in Eqs. (6) rather than a combination of exponential functions. The corresponding distribution

of the shear displacements of the antisymmetric mode is plotted in Fig. 1 with a dashed broken line.

At the point (k^*, Ω^*), according to Eq. (7), we have $k_\perp = k_\parallel\beta(1-\beta^2)^{-1/2}$ and $k^* = k_\parallel(1-\beta^2)^{-1/2}$. Using the substitutions $e^{-\sigma} \approx 1-\sigma$ and $e^{-2\sigma} \approx 1-2\sigma$ in Eq. (8), in the limit $\sigma \longrightarrow 0$, we obtain

$$\mathcal{K}^2(1-\beta^2)^{1/2}k^*d[1-e^{-2(1-\beta^2)^{1/2}k^*d}] = 1-e^{-(1-\beta^2)^{1/2}k^*d}\cos(\beta k^*d). \quad (11)$$

Our calculations have shown that, due to the constraint $\mathcal{K}^2 < 0.5$ inherent in ferroelectrics far from the phase transition, the roots of Eq. (11) almost always comply with the condition $k^*d > 2$. When $\mathcal{K}^2 \ll 1$ and $\beta \ll 1$, an approximate relationship $k^*d \approx 1/\mathcal{K}^2$ follows from Eq. (11) with a good accuracy. As $\beta \longrightarrow 1$ at a fixed $\mathcal{K}^2$, k^*d grows unboundedly. The same result was obtained in [6] for the case $\mathcal{K}^2 \longrightarrow 0$. Thus, the antisymmetric mode disappears when the acoustodomain interaction is absent ($\mathcal{K}^2 = 0$) or vanishes ($\mathcal{K}^2 \neq 0$, $\beta \longrightarrow 1$). The latter property follows from the fact that, as $\beta \longrightarrow 1$, asymptotes 1 and 2 of the mode spectrum converge (Fig. 2), and, hence, the electroacoustic wave degenerates into a wave that propagates in the bulk of the crystal at the frequency $\Omega = kc_t(1-\beta^2) \longrightarrow 0$ with the wave vector components $k_\parallel = k(1-\beta^2)^{1/2} \longrightarrow 0$ and $k_\perp = k\beta \longrightarrow k$. This follows from Eq. (7) according to the condition $s = 0$. Since the wavefront of this wave is parallel to the domain walls ($\mathbf{k} \parallel \mathbf{V}_D$), this wave cannot produce piezopolarization charges on them[1] and is actually uncoupled with the SD.

Strictly speaking, for $\beta \longrightarrow 1$ ($\Omega \longrightarrow 0$, $s \longrightarrow 0$, $k_\parallel \longrightarrow 0$), solution (6) describes not a propagating wave, but a static field of shear displacements in the entire unbounded crystal, $u_0 = U\exp ik_\perp\tilde{y}$, where U is any of the amplitudes U_j or $V + W$. However, by changing to the laboratory coordinate system, one can easily show that this solution really has the form of a plane homogeneous wave $u_0 = U\exp i(k_\perp y - \omega t)$ with the frequency $\omega = k_\perp V_D$. It is clear that, by virtue of the passage to the limit $\beta \longrightarrow 1$, the phase velocity $v = \omega/k_\perp = V_D$ coincides with c_t.

At an arbitrary $\beta < 1$, the comparison between Eqs. (6) in different coordinate systems with allowance for Eqs. (1) yields the rule for transforming the mode spectrum of the electroacoustic wave

$$\omega = \Omega + \mathbf{k}\mathbf{V}_D. \quad (12)$$

This expression and Eq. (7) for $k_\perp$ give the relationship

$$\omega = \frac{\Omega}{1-\beta^2}, \quad (13)$$

which predicts a positive frequency shift $\omega - \Omega > 0$ independently of the receiver position relative to the moving SD. This can be explained by the fact that the source is not explicitly defined in the natural wave problems, and its role can be assigned, if at all, to the electroacoustic wave itself, rather than to the SD. Being present at all points of the space, the wave becomes connected with the SD and involves the medium into the motion along the y axis equally everywhere and acts on the receiver as an approaching source.[2]

By virtue of Eq. (13), asymptote 1 in Fig. 2 takes the form $\omega = kc_t$ in the laboratory coordinate system and no longer changes its slope with β. On the contrary, it can easily be seen from Eq. (10) that the slope of asymptote 2 decreases as $\beta \longrightarrow 1$ until it entirely converges with asymptote 1. Therefore, though the mode spectrum in the laboratory coordinate system, $\omega = \omega(k)$, formally resembles the one in Fig. 2, its transformation due to the SD motion proceeds in a qualitatively different manner. The differences in the mode spectrum behavior due to the choice of the coordinate system reveal the relativity of the spectral representation of the wave fields in the form of Eqs. (6) in view of Eq. (13). This property is particularly clearly seen in the frequency dependences of the mode phase velocities $v(\Omega) = \Omega/k$ (in the SD-fixed coordinates; Fig. 3) and $v(\omega) = \omega/k$ (in the laboratory coordinate system; Fig. 4) obtained for the $BaTiO_3$ crystal. In calculations, we took into account the equality

$$kd = \left[\frac{\kappa^2}{1-\beta^2} - \beta^2\sigma^2(\kappa)\right]^{1/2}, \quad (14)$$

which follows from Eq. (7) for s. By virtue of Eqs. (13) and (14) and the first formula of Eqs. (7), the functions $v(\Omega)$ and $v(\omega)$ can be represented in the parametric form

$$v(\omega) = \frac{v(\Omega)}{1-\beta^2} \equiv c_t\left[\frac{\kappa^2 - \sigma^2(\kappa)(1-\beta^2)}{\kappa^2 - \sigma^2(\kappa)\beta^2(1-\beta^2)}\right]^{1/2}, \quad \omega = \frac{c_t}{d}\left[\frac{\kappa^2}{1-\beta^2} - \sigma^2(\kappa)\right]^{1/2}, \quad (15)$$

where κ is the parameter and $\sigma = \sigma(\kappa)$ is determined in the course of the numerical solution of Eq. (8).

From Figs. 3 and 4 and from Eqs. (8) and (15) considered simultaneously, it follows that, independently of the choice of the coordinate system, the electroacoustic wave guided by the moving SD exhibits the property inherent in all boundary-guided (surface) waves, namely, a slow propagation velocity: $v \leq c_t$. In

[1] According to Eqs. (6), for $\beta \longrightarrow 1$ ($\Omega \longrightarrow 0$, $k_\parallel \longrightarrow 0$), we obtain Φ, Φ_j = const, which means that there are no piezopolarization charges on the SD boundaries.

[2] The only difference follows from the fact that the electroacoustic wave can be localized by the SD boundaries. It consists in that, when the receiver is in the region $\tilde{y} > d$, since the SD is approaching the receiver, the latter records growing oscillations, while, when the receiver is in the region $\tilde{y} < 0$, it records decreasing oscillations (carried away by the SD).

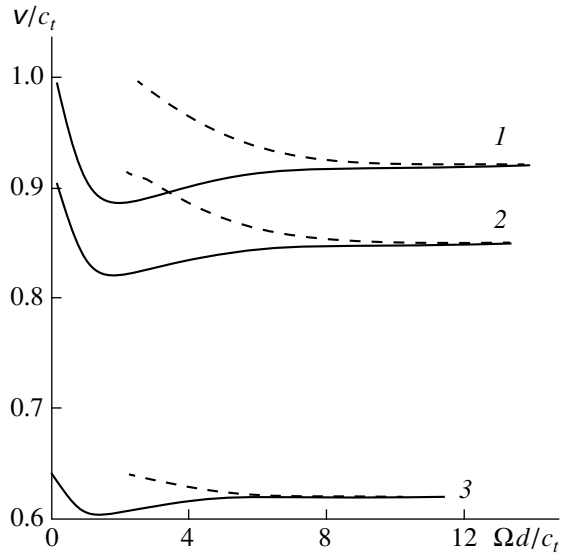

Fig. 3. Phase velocity of the electroacoustic wave guided by an SD in $BaTiO_3$ ($\mathcal{K}^2 = 0.38$) in the SD-fixed coordinate system versus frequency for $\beta = (1)\ 0, (2)\ 0.3$, and $(3)\ 0.6$: the symmetric mode (solid line) and the antisymmetric mode (dashed line).

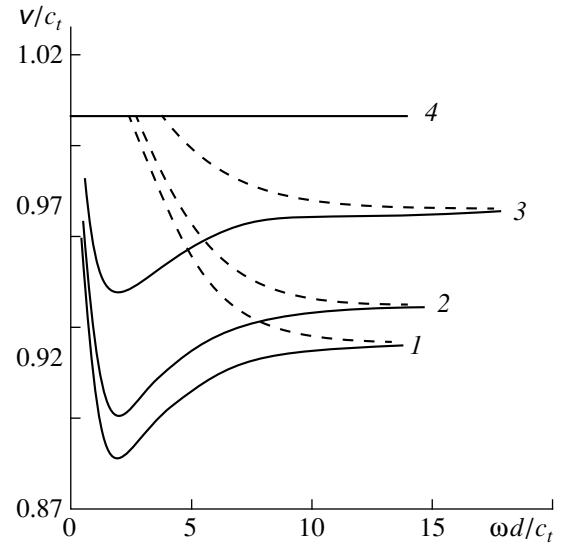

Fig. 4. Phase velocity of the electroacoustic wave guided by an SD in $BaTiO_3$ ($\mathcal{K}^2 = 0.38$) in the laboratory coordinate system versus frequency for $\beta = (1)\ 0, (2)\ 0.3, (3)\ 0.6$, and $(4)\ 1$: the symmetric mode (solid line) and the antisymmetric mode (dashed line).

the SD-fixed coordinate system (Fig. 3), this property of the electroacoustic wave becomes more pronounced with increasing β, because the observer does not perceive its transverse transfer. In the limit $\beta \longrightarrow 1$, when the longitudinal propagation terminates, the wave looks completely decelerated ($v \longrightarrow 0$). Conversely, in the laboratory coordinate system (Fig. 4), the deceleration of the electroacoustic wave due to the SD motion completely disappears as $\beta \longrightarrow 1$ ($v \longrightarrow c_t$; see straight line *4* in Fig. 4). This results from both the longitudinal propagation and the transverse transfer. Therefore, when $\beta \longrightarrow 1$, although the wave propagation in the longitudinal direction terminates, a possibility of the transverse wave motion remains when, in view of the above-mentioned uncoupling of the electroacoustic wave with the SD, the wave degenerates into a homogeneous plane wave.

Since the modes exhibit a frequency dispersion, along with the phase velocities it is reasonable to consider the group velocities $\mathbf{V}_{g\Omega} = \partial\Omega/\partial\mathbf{k}$ (in the SD-fixed coordinates, $\mathbf{k} = \mathbf{k}(\Omega)$) and $\mathbf{V}_{g\omega} = \partial\omega/\partial\mathbf{k}$ (in the laboratory coordinate system, $\mathbf{k} = \mathbf{k}(\omega)$). By virtue of Eq. (12), the relationship between them is given by the formula

$$\mathbf{V}_{g\omega} = \mathbf{V}_{g\Omega} + \mathbf{V}_D, \tag{16}$$

where the Galilean velocity composition law is clearly seen. This formula reveals the twofold effect of the SD motion on the signal transmission by the electroacoustic wave. First, as a result of the SD motion, the spectrum of the wave is modified, which affects the delay of the transmitted signal and is characterized by the first term in Eq. (16). Second, the transverse drift of the signal by the moving SD takes place, which is represented by the second term in Eq. (16). The nature of the transverse signal drift clearly manifests itself when $\beta \ll 1$. In this case, the SD motion primarily governs the orientation of the vector $\mathbf{V}_{g\Omega}$ and the component $V_{g\Omega}^{\perp} \sim \beta$ can be considered as a measure of the increase in the longitudinal signal delay: an increase in β favors an increase in $V_{g\Omega}^{\perp}$ and also causes a decrease in $V_{g\Omega}^{\parallel}$, thereby increasing the delay.

In view of Eq. (14) and frequency representations (13) and (15), the quantities $V_{g\Omega}$ and $V_{g\omega}$ can be reduced to the form

$$V_{g\Omega} = V_{g\omega}(1-\beta^2),$$

$$V_{g\omega} = c_t \frac{[\kappa^2 - \beta^2(1-\beta^2)\sigma^2(\kappa)]^{1/2}}{[\kappa^2 - (1-\beta^2)\sigma^2(\kappa)]^{1/2}} \times \frac{\kappa - (1-\beta^2)\sigma(\kappa)\sigma'(\kappa)}{\kappa - \beta^2(1-\beta^2)\sigma(\kappa)\sigma'(\kappa)}. \tag{17}$$

Equations (17) (which require that not only the function $\sigma = \sigma(\kappa)$, but also its derivative $\sigma'(\kappa)$, be determined numerically) along with Eqs. (13) and (15) for the frequencies allow one to calculate the group velocities as functions of the frequency. Their difference in the SD-fixed and laboratory coordinate systems is basically similar to that for the phase velocities (see Figs. 3, 4). However, the quantities $V_{g\Omega}$ and $V_{g\omega}$ approach the high-frequency limit in a different manner: in the high-frequency asymptotics, the group velocities of the symmetric and antisymmetric modes exchange their places.

Since real crystals have finite dimensions, in order to find whether it is possible to use the effect of the translational transfer of the electroacoustic wave by the moving SD, it is important to estimate the degree of its boundary localization $\Gamma = s/k$ defined as the ratio of the wavelength to the scale (length) of the mode boundary localization $\Lambda = 2\pi/s$ outside the SD. In the case under study, $\Gamma = \sigma(\kappa)/kd$; in view of Eq. (14), we obtain

$$\Gamma = \frac{\sigma(\kappa)(1-\beta^2)^{1/2}}{[\kappa^2 - \beta^2(1-\beta^2)\sigma^2(\kappa)]^{1/2}}. \quad (18)$$

This expression is invariant under transformation (1), which allows us to limit the study to analyzing it in one of the two coordinate systems. In particular, when used with Eq. (15) for ω, Eq. (18) yields a parametric representation for $\Gamma(\omega)$ in the laboratory coordinate system. The quantity $\Gamma(\Omega)$ can be obtained through the Doppler frequency shift.

Our calculations show that the SD motion slightly decreases the electroacoustic wave localization coefficient. This effect is more pronounced at lower frequencies for the antisymmetric mode. For the symmetric mode, the localization coefficient exhibits a maximum whose frequency is almost independent of β in the laboratory coordinate system. The localization length is a little greater than two wavelengths; therefore, at a distance from the SD of, e.g., three wavelengths, the symmetric mode of the electroacoustic wave will be virtually absent. At this and longer distances between the SD and the external boundaries of the crystal, a self-contained propagation of the electroacoustic wave and the possibility of its translation by a moving SD become real. It should be noted that, under the considered conditions, the localization of the symmetric mode of the electroacoustic wave by an SD is always higher than that by a single moving DW.

ACKNOWLEDGMENTS

This work was supported by the Federal Specific-Purpose Program "Integratsiya," project no. A 0066.

REFERENCES

1. J. L. Bleustein, Appl. Phys. Lett. **13**, 412 (1968).
2. Yu. V. Gulyaev, Pis'ma Zh. Eksp. Teor. Fiz. **9**, 63 (1969) [JETP Lett. **9**, 37 (1969)].
3. C. Maerfeld and P. Tournois, Appl. Phys. Lett. **19**, 117 (1971).
4. J. C. Peuzin, Solid State Commun. **9**, 1639 (1971).
5. G. G. Kessenikh, V. N. Lyubimov, and D. G. Sannikov, Kristallografiya **17**, 591 (1972) [Sov. Phys. Crystallogr. **17**, 512 (1972)].
6. V. N. Lyubimov and D. G. Sannikov, Kristallografiya **24**, 5 (1979) [Sov. Phys. Crystallogr. **24**, 1 (1979)].
7. Xingjiao Li, J. Appl. Phys. **61**, 2327 (1987).
8. Xingjiao Li, Yibing Li, Yiwu Lei, and L. E. Cross, J. Appl. Phys. **70**, 3209 (1991).
9. J. T. Stewart and Y. K. Yong, IEEE Trans. Ultrason. Ferroelectr. Freq. Control **41**, 375 (1994).
10. H. Kato, J. Acoust. Soc. Am. **101**, 1380 (1997).
11. A. N. Alekseev, Izv. Akad. Nauk, Ser. Fiz. **57**, 92 (1993).
12. A. N. Alekseev, Izv. Akad. Nauk, Ser. Fiz. **56**, 172 (1992).
13. N. S. Shevyakhov, Akust. Zh. **45**, 570 (1999) [Acoust. Phys. **45**, 509 (1999)].
14. A. S. Sonin and B. A. Strukov, *Introduction to Ferroelectricity* (Vysshaya Shkola, Moscow, 1970).
15. S. V. Biryukov, Yu. V. Gulyaev, V. V. Krylov, and V. P. Plesskiĭ, *Surface Acoustic Waves in Inhomogeneous Media* (Nauka, Moscow, 1991).
16. L. M. Lyamshev and N. S. Shevyakhov, Pis'ma Zh. Tekh. Fiz. **17** (17), 13 (1991) [Sov. Tech. Phys. Lett. **17**, 611 (1991)].

Translated by A. Khzmalyan

Acoustical Physics, Vol. 47, No. 1, 2001, pp. 62–67. Translated from Akusticheskiĭ Zhurnal, Vol. 47, No. 1, 2001, pp. 76–82.
Original Russian Text Copyright © 2001 by Zverev, Pavlenko, Sokolov, Sharonov.

Blind Dereverberation in the Deep Sea

V. A. Zverev, A. A. Pavlenko, A. D. Sokolov, and G. A. Sharonov

Institute of Applied Physics, Russian Academy of Sciences,
ul. Ul'yanova 46, Nizhni Novgorod, 603600 Russia
e-mail: zverev@hydro.appl.sci-nnov.ru

Received May 10, 2000

Abstract—Experimental data are presented on the blind dereverberation of the noise-type signal generated by a sound source moving in the deep sea. The noise emitted by a towed source is received by a drifting hydrophone with a high excess of the signal over the ambient noise, which results in a stable interference pattern of high contrast. The observed interference structure indicates that the signal arrives at the receiver along different paths. With the use of the blind dereverberation technique for the signal processing and without any *a priori* information on the properties of the propagation channel, the parameters (the delay, the amplitude, and the phase) of each of the seven interfering signals are determined. From the data obtained, the frequency response of the filter that provides a strong suppression of the reverberation is calculated and the spectrum of the received signal is obtained without any interference distortions. © *2001 MAIK "Nauka/Interperiodica"*.

INTRODUCTION

An important feature of the process of the sound field formation in oceanic waveguides is the interference caused by the surface and bottom reflections and by the layered structure of the water bulk. The interference effects lead to the reverberation, which consists in the fact that, in addition to the main signal, multiple signals are received that propagate over different paths and arrive at the receiver with different delays. The reverberation-caused distortions of the signal are equivalent to the action of a nonlinear filter whose parameters are completely determined by the delays, amplitudes, and phases of the reflected signals.

The only way to get rid of the reverberation distortions is to filter the signal. For this purpose, one should construct a filter with a frequency response that is inverse with respect to that of a filter equivalent to the reverberation distortions. To construct the reverberation-suppressing filter, special-purpose measurements are usually carried out. For example, the reverberation distortions can be measured for a precisely known signal. The process that leads to eliminating the reverberation distortions is called dereverberation. The dereverberation is regarded as blind when no additional measurements are performed, and all the necessary information is extracted from the received distorted signal of an *a priori* unknown shape.

A method of blind dereverberation based on the mathematical properties of the signal is known [1]. In this method, the frequency response of the filter that is inverse to the reverberation is found from the principle of minimal phase shift for two receivers. However, this method is now at the stage of development and is not always applicable [2, 3].

Another method of blind dereverberation has been developed by us and successfully applied to the in-sea measurements. This method is based on the direct extraction of the required information on the parameters of the delayed signals from the received distorted signal. We managed to do so by taking into account the specific features of the interference structure formation [4–9]. It was found that, from the spectrum of the interference-modulated received signal, the information can be extracted on values of the signal delays with an accuracy of several fractions of the digitizing unit. Based on the measured delays, we developed a technique for the determination of the signal amplitudes and phases to a required accuracy. From these parameters, we determined the frequency response of the filter that eliminates the particular reverberation distortions.

The method is verified by both numerical and in-sea experiments. The latter were carried out in a deep sea ($Z = 3100$ m), with the reception of the noise (within the frequency band 10–4000 Hz) generated by a towed sound source that passed the receiving hydrophone at a distance of about 700 m. In these measurements, according to the interference pattern, the level of the emitted noise was much higher than that of the ambient noise. The entire interference structure of the near sound field is published in [9], and a fragment of it is presented below. With a single experimental realization of the received noise, 1 s in duration, the parameters were determined of seven delayed signals, two of which proved to have opposite phases, the others being in phase with the most rapid and intense signal. The amplitudes of the delayed signals were within 20–30% of the amplitude of the maximal signal. By applying the inverse-reverberation filter, we considerably suppressed the observed interference pattern.

The parameters of the delayed signals, which were theoretically estimated for the specific conditions of the

1063-7710/01/4701-0062$21.00 © 2001 MAIK "Nauka/Interperiodica"

experimental site, correlate with the parameters obtained from the experiment.

THEORY

We use the following model of the received signal. An initial signal $F(t)$ is repeated at time intervals τ_n with changed amplitudes a_n, which can be positive or negative. Later, this model can be complicated by introducing a varying phase that is the same for all spectral frequencies of $F(t)$. With this model, the received signal $P(t)$ can be expressed as

$$P(t) = F(t) + \sum_n a_n F(t-\tau_n). \quad (1)$$

Expression (1) is a particular case of a more general expression

$$P(t) = \int_{-\infty}^{t} F(\tau)S(t-\tau)d\tau, \quad (2)$$

where $S(t)$ is the response of a linear filter to an excitation in the form of a δ-pulse. In our case, with the specified model of the signal, the quantity $S(t)$ is the following sum of δ-functions:

$$S(t) = \delta(0) + \sum_n a_n \delta(t-\tau_n). \quad (3)$$

From the theory of linear filters, the spectrum of $P(t)$ is a product of the spectra of $F(t)$ and $S(t)$:

$$G_P(\omega) = G_F(\omega)G_S(\omega). \quad (4)$$

Here, the spectrum means the result of a complex Fourier transform of the function indicated by the subscript of G. With the model at hand, by substituting Eq. (3) in Eq. (4), we obtain the following initial expression:

$$G_P(\omega) = G_F(\omega)\left[1 + \sum_n a_n \exp(i\varphi_n)\exp(i\omega\tau_n)\right]. \quad (5)$$

In Eq. (5), we performed the aforementioned generalization by introducing the phase φ_n of the delayed signal, which is the same for all values of ω.

The form of Eq. (5) suggests how one can obtain the signal $F(t)$ from $P(t)$ thereby having suppressed the distortions caused by the signal repetitions, i.e., by the reverberation. To do so, one should produce three operations: (a) to determine the spectrum $G_P(\omega)$ of the received signal by applying the Fourier transform; (b) to divide this spectrum by the square-bracketed expression in Eq. (5), i.e., by the frequency response of the equivalent linear filter; and (c) to apply the inverse Fourier transform. These operations cause no problems if the filter frequency response is known.

The problem is how to determine the frequency response of the equivalent linear filter solely by using the signal $P(t)$ without any other measurements (the blind dereverberation). We show the way to do so with the specified model for the signal $P(t)$. According to Eq. (5), it is sufficient to determine the values of the quantities τ_n, a_n, and φ_n.

First, the values of the signal delays τ_n must be determined with the maximal possible accuracy. This can be done by the spectral analysis of the logarithm of the absolute value of the spectrum of the received signal. This procedure has different applications and is called the cepstral analysis [1]. By taking the logarithm of Eq. (5), we obtain

$$\ln(|G_P(\omega)|) = \ln(|G_F(\omega)|) + \ln\left(\left|1 + \sum_n a_n \exp(i\varphi_n)\exp(i\omega\tau_n)\right|\right). \quad (6)$$

According to Eq. (6), in the spectrum (cepstrum) of the logarithm of the modulus of the spectrum of the received signal, spectral lines must present at frequencies ("quefrencies") that are equal to the signal delays. In such a way, one can both establish the fact that discrete delays are present in the signal (from the existence of the associated maximum in spectrum (6)) and determine the delay times of the signal (from the position of this maximum). False maximums that correspond to the first term in Eq. (6) may also occur. However, this fact can easily be established at the next stage of signal processing, in the procedure of determining the coefficients. For spectral components of the first term in Eq. (6), zero-valued amplitudes are obtained.

The values of the coefficients a_n and φ_n are separately determined for each delay. To do so, a set of reference functions is constructed. To make this procedure clear, let us consider the determination of the only coefficient a_1. The following function is taken as reference:

$$W_n(t) = P(t) - kP(t-\tau_n), \quad (7)$$

where k is so far an arbitrary number and τ_n is the previously estimated signal delay.

In view of Eq. (1), the logarithm of spectrum (7) can be represented as

$$\ln[G_W(\omega)] = \ln[1 + B_1\exp(i\omega\tau_1) + B_2 + MB_3] + \ln[G_F(\omega)], \quad (8)$$

where

$$B_1 = a_1\exp(i\varphi_1) - k, \quad (9)$$

$$B_2 = ka_1\exp(i\varphi_1)\exp(i\omega 2\tau_1), \quad (10)$$

$$B_3 = 1 - k\exp(i\omega\tau_1), \quad (11)$$

$$M = \sum_{n=2}^{n=N} a_n \exp(i\omega\tau_n). \quad (12)$$

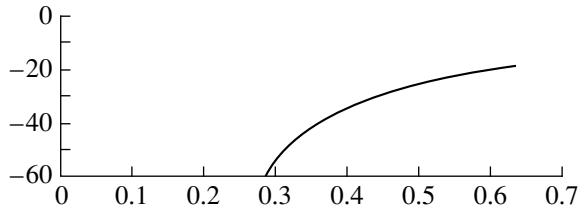

Fig. 1. Amplitude of the quefrency τ_1 in the first term of Eq. (8) at $B_1 = 0$ versus the amplitudes of the delayed signals. The values of the parameters are indicated in Table 1.

When expression (9) is equal to zero, Eq. (8) explicitly involves no exponential terms of the form $\exp(i\omega\tau_1)$. This means that, if the logarithm in Eq. (8) can be linearized, there will be no components of spectrum (cepstrum) (8) at quefrencies τ_1. However, the logarithm in Eq. (8) can be linearized if the amplitudes of the delayed signals are sufficiently low. Below, this condition is presented in a numerical form. Here and further, we assume that the amplitudes of the delayed signals are sufficiently small. In this case, by assigning different complex values to the coefficient k, one can achieve a situation when B_1 becomes either zero or reaches some minimal absolute value. A finite minimal value means that the corresponding quefrency occurs in the last term in Eq. (8). Thus, all parameters of the reverberation frequency response which are involved in Eq. (5) can be successively determined.

Now, to eliminate the reverberation distortions, it is sufficient to divide the spectrum of the received signal by the frequency response with the determined parameters of the delay signals substituted in it. Then, the inverse Fourier transform can be applied. Again, the cepstral analysis can be used to prove that the problem is correctly and completely solved. The cepstrum of the reconstructed signal should not involve any intense discrete components.

EXPERIMENTAL RESULTS

Prior to processing the experimental data, we numerically calculated the limits of possible amplitudes of the delayed signals. The calculations were carried out according to the first term in expression (8). Into this expression, specific values were substituted for five delayed signals. These values are shown in Table 1. The amplitudes of the signals corresponding to all delays except for the first one were multiplied by the factor q varying from 0 to 0.7. The coefficient k was specified to be precisely equal to a_1. The spectrum of the first term in Eq. (8) (cepstrum) was measured at a single frequency that corresponds to a fixed delay τ_1. The results are presented in Fig. 1. A sharp boundary can be seen in the amplitude values of the delayed signal: below it, there is no signal of the quefrency for which condition (9) is valid. The sharpness of this boundary is an important fact, which evidences that the condition of low delayed signals does lead to accurate estimates of their amplitudes if the proposed method is used.

Table 1

τ_n	a_n
38	1
59	0.8
77	0.5
83	0.3

In our experiment on blind dereverberation, a broadband source of noise-like sound was used. The obtained signal was represented as a sequence of 24 realizations. The current spectrum of the received noise is shown in Fig. 2 in the coordinates of frequency and time (and number of realization). The duration of the realization that was spectrally analyzed was 0.5 s with the 8192-Hz frequency of the signal digitization. Thus, the signal spectrum ranged from 0 to 4096 Hz. In the current spectrum, interference lines that indicate the interfering modulation of intense spectral components due to the reverberation are pronounced.

The cepstrum (spectrum of the logarithm of the modulus of the spectrum) is shown in Fig. 3 for this signal in the coordinates of quefrency (from 0 to 10 ms) and number of realization. The vertical lines are well pronounced; these lines correspond to the delay times of the signal arrivals relative to the signal arriving first.

To determine the delays τ_n, amplitudes a_n, and phases φ_n of the interfering components, further processing was performed with the use of Eqs. (7)–(9) for a single realization (no. 8) at the seven most intense quefrencies. The obtained results are summarized in Table 2.

The accuracy attained in determining the maximums of quefrencies was up to 0.125 of the step of the time grid. It was done by adding zeros to the spectrum of the function (for details, see [10]). The amplitudes and phases were also fairly reliably determined. The reliability can be confirmed by Fig. 4 where the variation of the quefrency in Eq. (8) is shown for a varying coefficient k at the quefrency 1.282 ms. The plot shown in Fig. 4 is typical. The depth of the minimum was always no less than 50 dB.

Figures 5 and 6 show the spectrum and cepstrum of the signal before and after the dereverberation procedure. The parameters of the filter were the same for all realizations. It can be seen from the figures that these parameters are appropriate for other realizations: the eighth row in Figs. 5 and 6 does not differ from the others. This fact is evidence of the stability of the propagation conditions for all 24 rows of data, i.e., for the 12-s duration of the measurements. The cross-sections of the current spectra are shown in Fig. 7 before the processing (the thick curve) and after it (the thin curve). The cross-sections are plotted for the selected realization

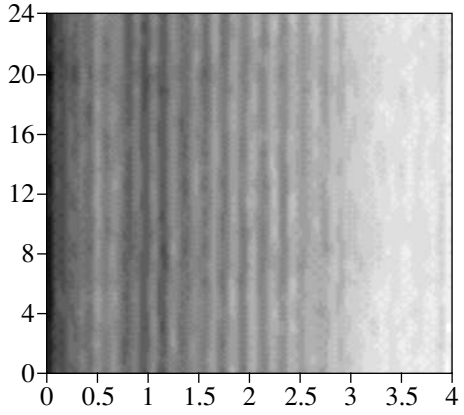

Fig. 2. Modulus of the current spectrum of the analyzed signal. The abscissa and ordinate axes represent the frequency (in kHz) and the ordinal number of the realization, respectively.

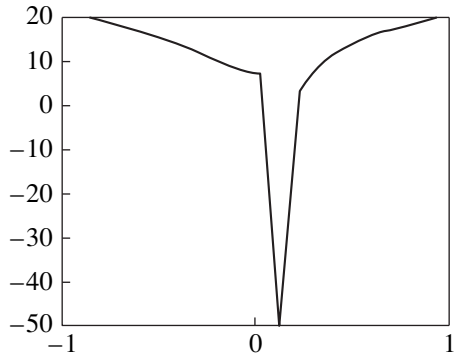

Fig. 4. Cepstrum of function (8) (in dB) at the quefrency 1.282 ms versus the coefficient k involved in Eq. (8). The absolute value of the coefficient k is plotted along the horizontal axis.

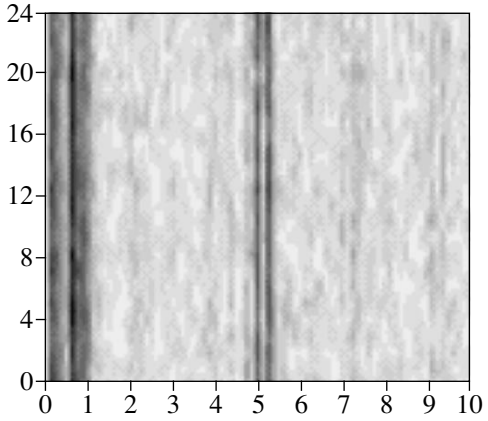

Fig. 3. Current cepstrum for the analyzed signal. The abscissa and ordinate axes represent the quefrency (in ms) and the ordinal number of the realization.

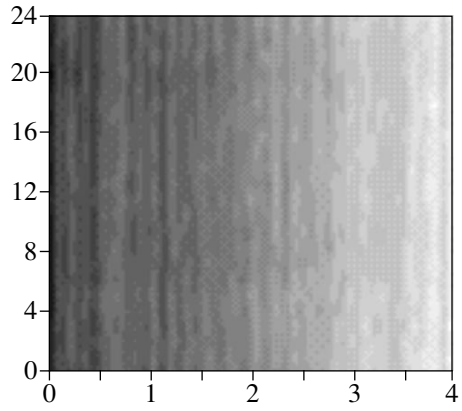

Fig. 5. Same as in Fig. 2 after the elimination of the reverberation.

no. 8. As a result of the dereverberation, the spectrum of the received signal has become smoother.

DISCUSSION

In considering the interference effects that occur when sound propagates in an acoustic waveguide, it is common practice to use the analogy between wave processes and oscillations. Then, the problem of interference in the propagation channel is reduced to that of signal transmission through the linear filter that is represented by the medium itself. If the nonlinear phenomena caused by high sound levels are neglected, the use of transfer functions is quite justified in describing the channel of the sound propagation.

The transfer functions $S[\omega, r, z_s, z_r, C(r, z), t]$ of an underwater channel depend on the relative positions of the source and receiver (r is the distance between them, z_s and z_r are their depths), the distribution $C(r, z)$ of the sound speed, the properties of the bottom, the sea state, the inhomogeneities of the water bulk and the sea floor, and so on. Most of these factors can vary in time, though the key ones governing the formation of the sound field (such as the medium stratification, the parameters of the waveguide boundaries and currents)

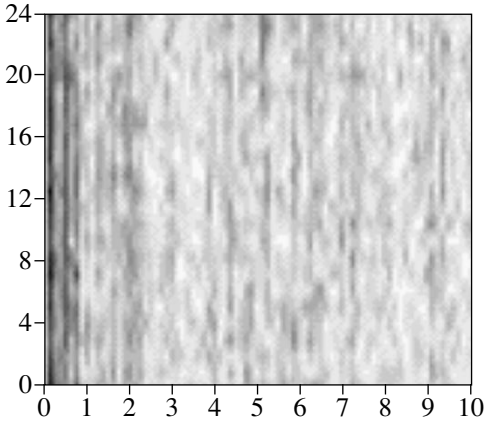

Fig. 6. Same as in Fig. 3 after the dereverberation.

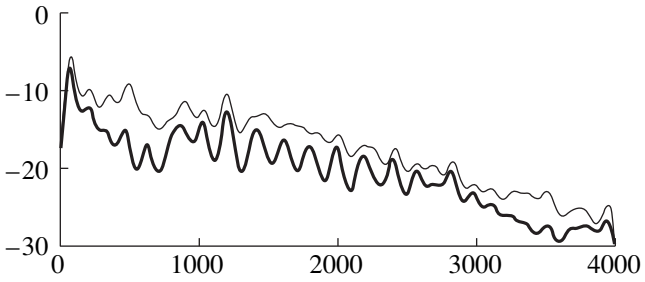

Fig. 7. Modulus of the spectrum of the analyzed signal of realization no. 8 before (the thick curve) and after (the thin curve) the dereverberation processing. The modulus of the spectrum is frequency averaged.

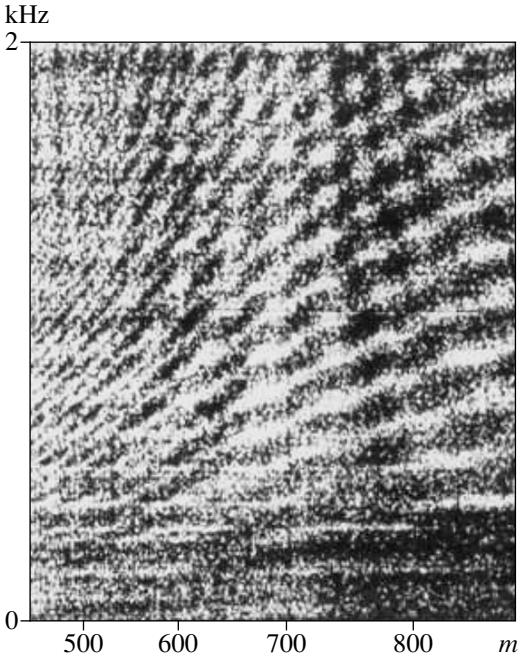

Fig. 8. Interference structure of the sound field of the received signal (0–2.0 kHz) generated by a moving source of broadband sound in the deep-sea experiment. The depths of the source and the receiver are 100 and 78 m, respectively.

are characterized by much weaker (or slower) time dependences.

To study the transfer characteristics of underwater sound waveguides treated as multichannel linear systems that have a great number of inputs and outputs with the corresponding number of the transfer functions, the well-known methods of measuring the impulse and frequency responses are applicable. These methods are based on the use of pulsed, cw, or noise-type signals for sounding the underwater sound channel.

Table 2

τ_n, ms	A_n	φ_n, deg
0.214	0.232	180
0.32	0.179	0
0.778	0.242	0
1.022	0.223	0
1.282	0.123	0
4.974	0.202	0
5.264	0.2	180

In our deep-sea experiment, we used the noise transmission within the frequency band 10–4000 Hz. The signals were generated by a broadband sound source that was towed at a depth of 100 m with a constant speed relative to the receiver, which slowly drifted at a depth of 78 m. A continuous sensing of the waveguide by the noise signal allowed us to measure the squared modulus of the frequency transfer function for various distances r from the source.

Figure 8 shows a fragment of the interference structure of the sound field, which was experimentally observed at the distances 500 to 800 m from the source within the frequency band 0–2 kHz. This figure illustrates the main features and laws of the sound field formation in a deep sea with the deep-axis underwater channel. As has been mentioned above, the formation of the interference structure of the sound field produced by a broadband sound source in a deep sea is associated with the signals that arrive at the receiver along different paths, with different delays τ relative to each other.

To determine the parameters of the interfering components (the relative delays, amplitudes, and phases), we applied the blind dereverberation processing to the signals that were received by the hydrophone at the distances around 700 m from the source, with weakly varying path lengths (the source moved nearly perpendicularly to the propagation path).

To compare the measured parameters of the interference-modulated spectrum of the received signal (see Table 2), calculations were carried out for the interference structure of the sound field of a point source in view of the experimental conditions. In the calculations, we used the ray theory with the measured depth dependence $C(z)$ of the sound speed (Fig. 9a), the source and receiver depths equal to z_s = 100 m and z_r = 78 m, and the distances r varying up to 1000 m. Figure 9b shows the calculated delays (measured from the first arrival) for the signals of the ray groups that participate in forming the interference structure. The results are plotted versus the distance (the τ–r diagram).

The τ–r diagram presents the main groups of curves that are associated with the following types of rays interfering at the reception point: the rays refracted below the channel axis (with the minimal propagation times) and reflected from the surface (with delays that weakly depend on the distance), the rays refracted in the deeper channel (the monotonically decaying curve of relative delays), and the rays refracted above the channel axis and reflected from the surface (the set of curves with small delays at the distances longer than 500 m). In other words, the interfering surface-reflected

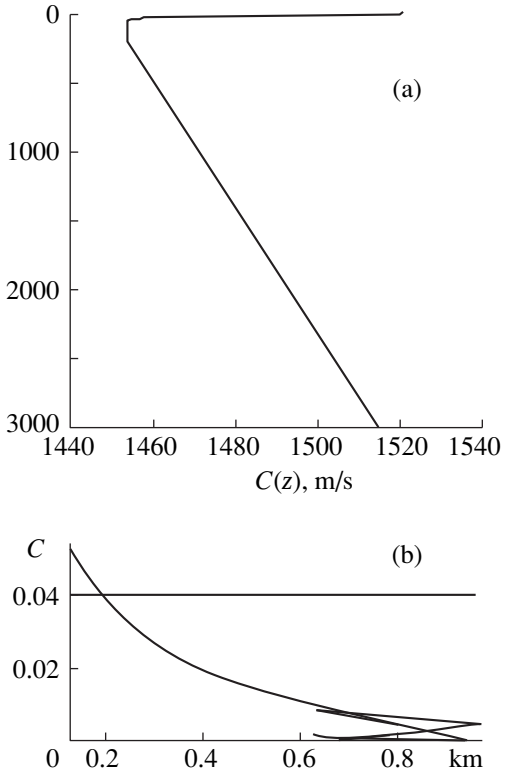

Fig. 9. (a) Measured vertical profiles $C(z)$ of the sound speed up to the depth 3000 m; (b) calculated relative delays of the signals versus the distance from the sound source.

rays are added to the classical "quartets" of rays, which are typical of the underwater sound channel. Obviously, the different types of rays contribute differently to the energy of the received signal. Some of them can have a low intensity, the bottom-reflected rays being an example for a deep sea. At a distance of about 720 m, the spectrum of the calculated delays agrees well with that of the measured delays presented in Table 2. It is worth mentioning that the insufficient precision of the available hydrological data prevents one from calculating the relative delays to an accuracy that can be attained in the measurements based on the described dereverberation method.

An important advantage of the proposed method is the possibility to determine the relative phases of the signals with different delays. By doing so, one can distinguish between the signals propagating along the rays that have even or odd numbers of surface reflections, provided that the signal is first to arrive without any surface reflections or with an even number of them. A phase change of $\pi/2$ also occurs if the ray has turning points. If reflections from the elastic bottom exist, the determination of the relative phase will allow one to measure the complex-valued reflection coefficient.

The existence of the interference structure in the sound field confirms the coherence of the interfering rays, and the possibility of determining the signal amplitudes for different delays, in fact, allows one to determine the degree of coherence for the interacting components.

CONCLUSIONS

This study opens the prospects for determining the structure of sound signals (the delays of modes or rays, their amplitudes and phases) from the parameters of the nearly arbitrary sound signals that can be observed in a sufficiently broad frequency band. The accuracy of determining the delays is the key characteristic in, e.g., ocean tomography, and the elimination of the interference distortions is important in nearly all acoustic measurements.

ACKNOWLEDGMENTS

This work was supported by the Russian Foundation for Basic Research, project nos. 99-02-16401 and 00-15-9674.

REFERENCES

1. M. H. Hayes, J. S. Lim, and A. V. Oppenheim, IEEE Trans. Acoust., Speech, Signal Process. **28** (1980).
2. S. Subramaniam, A. P. Petropulu, and C. Wendt, IEEE Trans. Speech Audio Process. (September 1996).
3. A. P. Petropulu and C. L. Nikias, IEEE Trans. Signal Process. **41** (6), 2088 (1993).
4. V. N. Golubev, V. I. Il'ichev, E. F. Orlov, *et al.*, in *Acoustic Waves in the Ocean*, Ed. by L. M. Brekhovskikh and I. B. Andreeva (Nauka, Moscow, 1987), pp. 100–111.
5. *Interference of Broadband Sound in the Ocean*, Ed. by V. A. Zverev and E. F. Orlov (Inst. Prikl. Fiz., Akad. Nauk SSSR, Gorkiĭ, 1984).
6. E. F. Orlov, V. N. Fokin, and G. A. Sharonov, Akust. Zh. **34**, 902 (1988) [Sov. Phys. Acoust. **34**, 520 (1988)].
7. E. F. Orlov and G. A. Sharonov, *Interference of Sound Waves in the Ocean*, (Dal'nauka, Vladivostok, 1998).
8. *Acoustic Interferometry in the Ocean*, Ed. by E. F. Orlov and G. A. Sharonov (Dal'nauka, Vladivostok, 1993).
9. A. D. Sokolov, V. N. Fokin, and G. A. Sharonov, Izv. Vyssh. Uchebn. Zaved., Radiofiz. **38** (8), 817 (1995).
10. *Formation of Acoustic Fields in Oceanic Waveguides*, Ed. by V. A. Zverev (Inst. Prikl. Fiz., Akad. Nauk SSSR, Nizhni Novgorod, 1991).

Translated by E. Kopyl

Acoustical Physics, Vol. 47, No. 1, 2001, pp. 68–75. Translated from Akusticheskiĭ Zhurnal, Vol. 47, No. 1, 2001, pp. 83–91.
Original Russian Text Copyright © 2001 by Ivanov.

Damping of the Acoustic Diffraction and Radiation Fields Produced by a Convex Body

V. P. Ivanov

Scientific Center of Nonlinear Wave Mechanics and Technologies, Russian Academy of Sciences, ul. Bardina 4, Moscow, 117334 Russia

e-mail: office@nwmtc.ac.ru

Received April 7, 1999

Abstract—The problem of active damping of the acoustic radiation and diffraction fields produced by a convex body is solved using a discrete array of receivers and radiators of nonzero wave dimensions.
© 2001 MAIK "Nauka/Interperiodica".

The development of science and technology and, especially, the ecological problems which have become most topical in recent years often require unconventional approaches for their solution. An example is the method of active noise control [1–8]. This method consists in the damping of the extraneous acoustic field in a given spatial region or in the damping of the field of a radiating body with the help of auxiliary radiators that operate in antiphase with the primary sources. The method of active field control is formalized as an inverse diffraction problem for acoustic fields in a region with an unknown boundary. According to Glasko [9], the general property of inverse problems is that they are physically unrealizable. This paper studies the inverse problem for a physically realizable model of the process of active damping of acoustic fields. The paper presents a three-dimensional generalization of the results obtained earlier [10].

FORMULATION OF THE PROBLEM

We consider the case of low-frequency diffraction, when the characteristic wave dimensions of the body are of the order of unity. Proceeding from the requirements of physical realizability, we define the velocity field potential U excited by the extraneous sources F, the auxiliary radiators, the radiation of the body itself, and the field of diffraction by bodies as the solution to the following problem. We set the origin of coordinates inside a convex body bounded by the surface S_{01} and arrange the centers of spherical receivers S_{jm} ($m = 1, \ldots, M_j$) of radius a_1 on the spheres with the radii R_j, where $j = 1, 2$. On a sphere of radius R_3, where $R_1 < R_2 < R_3$, we place the centers of auxiliary spherical radiators S_{3m} of radius a_2. The body S_{01} lies inside the sphere of radius R_1; outside the sphere of radius $R > R_3$, we have a spatial region F where extraneous sources with the volume velocity f are located. We take into account that the receivers average the results of measurements of the total field U over their surfaces. The function f is unknown, and the field generated by extraneous sources and described by this function should be determined in the vicinity of the body S_{01}. Another unknown quantity is the distribution of the normal velocity f_{01} of the surface S_{01} which characterizes the field of the self-radiation of the body. We assume that the known quantities are

$$Q_{01}^* = \int_{S_{01}} |\mu_{01}^*| dS_{01}, \quad Q_F = \int_F |f| dF,$$

where μ_{01}^* is the density of the potential of the self-radiation field of the body S_{01}. We define the potential U in the region outside the bodies S_{jm} ($j = 0, \ldots, 3$, $m = 1, \ldots, M_j$, and $M_0 = 1$) as the solution to the problem

$$(\Delta + k^2)U = -4\pi f, \quad k = \omega/c = \text{const}, \quad \text{suppf} \subseteq F,$$
$$\partial U/\partial n|_{S_{jm}} = f_{jm}, \quad j = 0, \ldots, 3, \qquad (1)$$
$$f_{jm} = 0 \text{ for } j = 1, 2,$$

where $\partial/\partial n$ is the derivative with respect to the normal to the surface S_{jm}. We assume that the radiation condition, or the decay condition, is satisfied at infinity. We denote by U_∂ the diffraction and radiation fields produced by the bodies S_{jm}, $j = 0, \ldots, 3$. It is necessary to determine the spatial arrangement and the number M_3 of the auxiliary radiators S_{3m} and the complex amplitudes f_{3m} so as to satisfy the following inequality for all points outside the sphere of radius R:

$$\sup|U_\partial| < \varepsilon, \qquad (2)$$

where ε is sufficiently small.

We assume that the wave number k is not a resonance one for the regions bounded by the surface S_{01} and the spheres S_{jm} and S_{3m}. From the substitution specified above, it follows that the damping problem represents an inverse diffraction problem in a region with an unknown boundary, because, firstly, we seek the functions f_{3m}, and, secondly, we do not know the spatial arrangement, the total number, and the wave dimen-

sions of the receivers and auxiliary radiators. We denote the incident field of extraneous sources by U_F and define it as the solution to Eq. (1) in free space with the radiation condition. To solve the problem given by Eq. (1) with condition (2), it is necessary to consider an auxiliary problem of measuring and separating the fields, namely, to determine the numbers M_j ($j = 1, 2$), the wave dimension ka_1, and the spatial arrangement of the receivers so as to make it possible from the measurements of the normal velocity induced by the total field at the surfaces S_{jm} of these receivers to calculate the field U_F inside the sphere of radius R_1 and the diffraction and radiation field U_∂ outside the sphere of radius R_2 with a predetermined accuracy.

SOLUTION OF THE PROBLEM OF MEASURING AND SEPARATING THE FIELDS

We solve the problem of the field measurement on the assumption that the type of auxiliary radiators realizing the damping problem is set beforehand. The density of the field potential at the surface of such an auxiliary radiator S_{3m} is determined by the self-radiation field and the field of diffraction and secondary diffraction by the surface S_{3m}. For the selected type of radiators, this quantity is considered as constant. Setting $ka_1 \ll 1$ and using the aforementioned condition for the wave number, we seek the field U, $U = U_\partial + U_F$, in the form of a sum of simple layer potentials set at the surfaces S_{jm}, where $j = 0, \ldots, 3$, and the volume potential U_F set in the region F'. These potentials have the form

$$U_\partial = \sum_{j=0}^{3} \sum_{m=1}^{M_j} \int_{S_{jm}} \mu_{jm} \frac{\exp(ikR_{jm})}{R_{jm}} dS_{jm},$$
$$U_F = \iint_F f \frac{\exp(ikR_F)}{R_F} dF, \tag{3}$$

where μ_{jm} are continuous densities of the velocity potential that are induced by the total field at the surfaces S_{jm} and R_{jm} and R_F are the distances from the observation point to the points of the surfaces S_{jm} and the region F. We substitute Eqs. (3) for the field U into the boundary conditions at the surfaces S_{jm} ($j = 1, 2$) and integrate the result over the surfaces S_{jm}, because each receiver averages the measured value over its surface. As a result, we obtain a finite system of algebraic equations that relate an infinite number of amplitudes of the spatial harmonics $g_{1n\alpha}$ of the diffraction and self-radiation field of the body S_{01} to the amplitudes $g_{2n\alpha}$ of the incident field of extraneous sources and the field formed by the radiation of auxiliary radiators and diffraction by these radiators:

$$\sum_{n=0}^{\infty} \sum_{\alpha=-n}^{n} [g_{1n\alpha} h_n^{(1)}(kR_q) + g_{2n\alpha} \psi_n(kR_q)] \times P_n^\alpha(\cos\theta_{qp}^0) \exp(i\alpha\varphi_{qp}^0)$$
$$= -\frac{\psi_0(ka_1) h_0^{(1)'}(ka_1)}{\psi_0'(ka_1)} b_{qp}(1 + \delta_{qp}) = c_{qp}, \tag{4}$$
$$q = 1, 2, \quad p = 1, \ldots, M_q.$$

In Eq. (4), we used the following notation:

$$g_{1n\alpha} = (2n+1)\frac{(n-\alpha)!}{(n+\alpha)!} \int_{S_{01}} \mu_{01} \psi_n(kr_{01}) \times P_n^\alpha(\cos\theta_{01}) \exp(-i\alpha\varphi_{01}) dS_{01};$$

$$g_{2n\alpha} = (2n+1)\frac{(n-\alpha)!}{(n+\alpha)!} \iint_F f h_n^{(1)}(kr_F) P_n^\alpha(\cos\theta_F) \times \exp(-i\alpha\varphi_F) dF + \sum_{m=1}^{M_3} d_{3m}(2n+1) h_n^{(1)}(kR_3) \times P_n^{-\alpha}(\cos\theta_{3m}^0) e^{-i\alpha\varphi_{3m}^0}, \quad b_{qp} = \int_{S_{qp}} \mu_{qp} dS_{qp};$$

$$d_{3m} = 4\pi a_2^2 \psi_0(ka_2) d_{3m}^0 = \text{const}, \quad m = 1, \ldots, M_3;$$

b_{qp} are the directly measured quantities; δ_{qp} is the measurement error due to the finiteness of the receiver system and the method of the field measurement at the surface S_{qp}; d_{3m}^0 is the zeroth harmonic of μ_{3m}; $\psi_n(x)$ and $h_n^{(1)}(x)$ are Bessel and Hankel spherical functions; $P_n^m(x)$ are associated Legendre polynomials; $(r_{01}, \theta_{01}, \varphi_{01})$ are the spherical coordinates of a point of the surface S_{01} in the basic coordinate system; $(r_F, \theta_F, \varphi_F)$ are the spherical coordinates of a point of the region F; $(R_q, \theta_{qp}^0, \varphi_{qp}^0)$ are the coordinates of the receiver centers; and $(R_3, \theta_{3p}^0, \varphi_{3p}^0)$ are the coordinates of the radiator centers in the basic coordinate system. In the case of low-frequency fields and a uniform distribution of the receiver centers over the spheres of radius R_q, the following estimate is valid for the measurement error related to the secondary diffraction field:

$$\delta_{qp} \le \frac{4b^*}{|b_{qp}|} \left| \frac{\psi_0'(ka_1)}{\psi_0(ka_1) h_0^{(1)'}(ka_1)} \right| \frac{(N+1)^2 + (N+1)\ln N}{kR_1} \times (1 + O(ka_1)) = \delta_{qp}^* < \delta, \tag{5}$$

where $b^* = \max_{q,p} |b_{qp}|$, $a_1/R_{qpjm}^* < 1/4$, δ is a sufficiently small number, and R_{qpjm}^* is the minimal distance between the centers of the receivers S_{qp} and S_{jm}. In Eq. (5), we used

the assumption that $M_1 = M_2 = (N+1)^2$. For the selected method of measurement, the following considerations should be taken into account. In this method, only the zeroth harmonic of the field induced at the receiver surface is measured in the coordinate system related to the center of the receiver. If the method allows one to measure other harmonics as well, which provides extra information on the field [11], an additional error arises at every receiver because of the unknown number of the neglected harmonics of the field induced at the receiver. From condition (5) with a given N, it is easy to obtain an estimate for the allowed receiver size by replacing the Bessel functions with their asymptotics corresponding to $ka_1 \longrightarrow 0$:

$$ka_1 \leq [3\delta|b_{qp}|kR_1/(8b^*((N+1)^2 + (N+1)\ln N))]^{1/3}. \quad (6)$$

The number N will be determined in the course of solving the damping problem. From formula (6), we obtain the upper estimate of the receiver wave dimension, which, in the case of a uniform distribution of receivers over the sphere S_j, provides a small measurement error related to the secondary diffraction field. On the other hand, for the wave dimension of the receiver, the following relationship should hold:

$$ka_1 \geq ka_1^*, \quad (7)$$

where the parameter ka_1^* is assumed to be preset. This condition should be satisfied, because the field induced at the receiver must exceed some threshold value determined by the receiver sensitivity. The system of Eqs. (4) has an infinite number of solutions. In the case $kR_1 \cong 1.0$, the field due to the diffraction by the bodies S_{jm} ($j = 0, \ldots, 3$) is determined with fairly high accuracy by the first $(N+1)^2$ spatial harmonics. Therefore, we seek the solution to system (4) in the form $g^*_{jn\alpha} = g_{jn\alpha}$ for $0 \leq n \leq N$, $-n \leq \alpha \leq n$, and $g^*_{jn\alpha} = 0$ for $n \geq N+1$, where $j = 1, 2$. Then, we have

$$\sum_{n=0}^{N}\sum_{\alpha=-n}^{n}[g^*_{1n\alpha}h_n^{(1)}(kR_q) + g^*_{2n\alpha}\psi_n(kR_q)] \times P_n^{\alpha}(\cos\theta^0_{qp})\exp(i\alpha\varphi^0_{qp}) = c_{qp}, \quad q = 1, 2, \quad p = 1, \ldots, (N+1)^2. \quad (8)$$

In the previous publication [12], it was shown that, with a certain arrangement of the receiver centers on the spheres of radii R_1 and R_2, the solution to system (8) exists for an arbitrary N, provided that the relations

$$A^m_{n,N-n}(\cos\theta^0_{q,N-n}) \neq 0, \quad n = 0, \ldots, N, \quad (9)$$

introduced in the cited paper hold and the wave number k is not a resonance one for the layer $R_1 \leq r \leq R_2$ with perfectly compliant walls; i.e.,

$$C_n = \psi_n(kR_2)h_n^{(1)}(kR_1) - \psi_n(kR_1)h_n^{(1)}(kR_2) \neq 0 \text{ for } n = 0, \ldots, N. \quad (10)$$

The physical interpretation of condition (9) at $n = 0$ is quite simple: the centers of the receivers must not lie at the points corresponding to the zero values of the associated polynomials $P_n^m(x)$ where the spherical harmonics are equal to zero. When conditions (9) and (10) are fulfilled, the solution to system (8) exists for any N and any right-hand side, and this solution has the form

$$g^*_{1n\alpha} = C_n^{-1}[\psi_n(kR_2)X_{1n\alpha} - \psi_n(kR_1)X_{2n\alpha}],$$
$$g^*_{2n\alpha} = C_n^{-1}[h_n^{(1)}(kR_1)X_{2n\alpha} - h_n^{(1)}(kR_2)X_{1n\alpha}], \quad (11)$$
$$n = 1, \ldots, N, \quad -n \leq \alpha \leq n,$$

where the unknown quantities $X_{qn\alpha}$ are determined by the formulas

$$X_{qn\alpha} = \sum_{m=0}^{N-|\alpha|}\sum_{j=-j_1}^{j_2}(-1)^{m^2+m+j}\frac{D^{\alpha+j(2|\alpha|+1)}_{N-|a|,|\alpha|}(\cos\theta_{q,|\alpha|})\Delta_{m+|\alpha|}(c_q)\Delta^{-1}_{m+|\alpha|}}{B^{\alpha}_{N-|a|,|\alpha|}(\cos\theta^0_{q,|\alpha|})B^{\alpha+j(2|\alpha|+1)}_{N-|a|-m,|\alpha|+m}(\cos\theta^0_{q,m+|\alpha|})}.$$

Here, Δ_m is the Vandermonde determinant of the $2m+1$ matrix formed by the elements $\{\exp[2\pi ijs/(2m+1)]\}$; $j = 0, \ldots, 2m$; $-m \leq s \leq m$;

$$j_1 = E\left(\frac{(1+\operatorname{sgn}\alpha)|\alpha|+m}{2|\alpha|+1}\right);$$

$$j_2 = E\left(\frac{(1-\operatorname{sgn}\alpha)|\alpha|+m}{2|\alpha|+1}\right);$$

$E(x)$ is the integral part of a number x; $\operatorname{sgn} x = 1$ for $x > 0$; and $\operatorname{sgn} x = -1$ for $x < 0$. The quantity $\Delta_{m+|\alpha|}(c_q)$ denotes the Vandermonde determinant of the matrix $\Delta_{m+|\alpha|}$ in which the column of number $\alpha + j(2|\alpha|+1)$ is replaced by the part of the column of constant terms $c_{q,m+|\alpha|,\nu}$, this matrix corresponding to the set of rows with the number $|\alpha| + m$. The coefficients $B^j_{\alpha\beta}$ and $D^j_{\alpha\beta}$ are determined by the recurrence relations given in the appendix to the cited paper [12]. In Eq. (11), the number N is not yet determined. It will be calculated later with the use of condition (2). Thus, we determined the approximate values of the amplitudes of the first $(N+1)^2$ spatial harmonics of the incident field produced by the extraneous source and the auxiliary radiators in the vicinity of the body S_{01} and the approximate values of

the amplitudes of harmonics of the diffraction and radiation field produced by the body S_{01} outside the sphere of radius R_2.

SOLUTION OF THE PROBLEM OF DAMPING THE DIFFRACTION AND RADIATION FIELDS PRODUCED BY THE BODY

One of the approaches used for solving the damping problem is as follows. The wave dimensions of radiators are selected to be small; the radiator array is sufficiently sparse; and, with the aim to increase the intensity of the radiated field, radiators of monopole and dipole types are selected. We note that the wave dimensions of auxiliary radiators that provide the solution of the damping problem cannot be as small as one likes, because the intensity of the radiated field depends on these dimensions. Let us consider an auxiliary radiator in the form of a spherical shell with a spherically symmetric distribution of normal velocity over the surface. The displacement or inflection of this shell in the radial direction u_r is limited by the value u_r^*, which is determined by the condition that the stresses and strains in the shell material do not exceed the allowed values within which oscillations of the shell occur without the shell fracture. The value u_r^* decreases with decreasing r. Under a spherically symmetric load, the normal velocity of the surface is $v = -i\omega u_r$, and, hence, for the functions f_{3p}, we have a limitation:

$$|f_{3p}| \le |\omega u_r^*|. \tag{12}$$

The upper estimate for the function f_{3p} is assumed to be preset. Other methods of damping can be related to the choice of a more complex structure of the density of the field potential μ_{3p} and to the use of auxiliary radiators of tripole, quadrupole, or higher-order types.

We begin to solve the damping problem for the field U_∂ on the assumption that $ka_2 \ll 1$. We represent the diffraction field U_∂ plus the field V for $r \ge R$ in the form

$$U_\partial = ik\sum_{n=0}^{\infty}\sum_{\alpha=-n}^{n} P_n^{-\alpha}(\cos\theta)\exp(-i\alpha\varphi)h_n^{(1)}(kr)$$
$$\times\left[g_{1n(-\alpha)} + (2n+1)\psi_n(kR_3)(-1)^\alpha\sum_{m=1}^{M_3} d_{3m}P_n^\alpha\right. \tag{13}$$
$$\left.\times(\cos\theta_{3m}^0)\exp(i\alpha\varphi_{3m}^0)\right] + V,$$

where V is the field of diffraction by the receiver system, $(R_3, \theta_{3m}^0, \varphi_{3m}^0)$ are the coordinates of the center of an auxiliary radiator S_{3m}, and (r, θ, φ) are the coordinates of the current point in the basic coordinate system. For condition (2) to be satisfied, i.e., for the field U_∂ to be small in magnitude, we use the following approach. The field V can be made small in magnitude by choosing a sufficiently small wave dimension ka_1. The first term in the expression for the diffraction field can be made small in magnitude by setting the first $(N+1)^2$ spatial harmonics involved in the bracketed part of Eq. (13) equal to zero by selecting the appropriate reduced amplitudes d_{3m} and the necessary number of auxiliary radiators. However, this can be made only approximately, because we know the approximate values $g_{1n\alpha}^*$ of the coefficients $g_{1n\alpha}$ obtained by solving the problem of measuring and separating the fields. We set $M_3 = (N+1)^2$ and impose the requirement that the equations

$$\sum_{m=1}^{(N+1)^2} d_{3m}P_n^\alpha(\cos\theta_{3m}^0)\exp(i\alpha\varphi_{3m}^0)$$
$$= -\frac{(-1)^\alpha g_{1n(-\alpha)}^*}{(2n+1)\psi_n(kR_3)} = \beta_{n\alpha}, \tag{14}$$
$$n = 0, \ldots, N, \quad -n \le \alpha \le n$$

be satisfied on condition that $\psi_n(kR_3) \ne 0$ for $n = 0, 1, \ldots, N$. The choice of the amplitudes d_{3m} in the form of constants can be rigorously justified if we formulate the problem of active damping by radiators of small wave dimensions as the optimal-power problem. Let us assume that μ_{3m} contains a finite number of harmonics. To solve the damping problem, we additionally require that the following condition be satisfied

$$\sum_{m=0}^{M_3}\int_{F_{3m}} |\mu_{3m}|^2 dF_{3m} \longrightarrow \min,$$

or, with the use of the Parseval equality, the condition

$$\sum_{m=0}^{M_3}\sum_{n=0}^{\infty}\sum_{j=-n}^{n} |\mu_{3mnj}|\frac{2}{2n+1}\frac{(n-j)!}{n!} \longrightarrow \max_{n,j}$$

be satisfied, where μ_{3mnj} represents the reduced amplitudes of spherical harmonics of the density μ_{3m}. If a solution to such a problem does exist, it is realized with the zeroth harmonics of the density, μ_{3m00}, because when the field is damped by small-wave-size radiators, we have $|\mu_{3m00}/\mu_{3mnj}| = 0[(ka_2)^n]$, where $n = 1, 2, \ldots$, for $ka_2 \longrightarrow 0$. Let us show that, for a special arrangement of the radiator centers on the sphere of radius R_3, the solution to system (14) exists for an arbitrary N and any right-hand side. We place the centers of the auxiliary radiators in the latitudes $\theta_{3\beta}^0$, $\beta = 0, \ldots, N$, so as to satisfy the condition $\cos\theta_{3\beta}^0 = 1 - 2(\beta+1)/(N+3) + \delta_\beta$, where $0 \le \delta_\beta \le 1/(N+3)$; in every latitude, the radiators are distributed uniformly along the longitude $\varphi_{3\beta\nu}^0 = 2\pi\nu/(2\beta+1)$, $\nu = 0, \ldots, 2\beta$. We change the numbers of

the sought quantities so that $d_{3m} = d_{3p\nu}$ when $p^2 \le m \le (p+1)^2$, $m = p^2 + \nu$, and apply the condition of solvability (9). For such an arrangement of the radiator centers, system (14) takes the form

$$\sum_{p=0}^{N}\sum_{\nu=0}^{2p} d_{3p\nu} P_n^{\alpha}(\cos\theta_{3p}^0)\exp(i\alpha\varphi_{3m}^0) = \beta_{n\alpha}, \quad n = 0, \ldots, N, \quad -n \le \alpha \le n. \tag{15}$$

The solution to system (15) can be represented in an explicit form for arbitrary N and $\beta_{n\alpha}$:

$$d_{3p\nu} = \sum_{n=0}^{P}\sum_{\alpha=-n}^{n}\beta_{n\alpha}\sum_{i=i_1}^{i_2}\Delta_p^*(\alpha + i(2|\alpha|+1)) \times D_{N-|\alpha|,|\alpha|}^{\alpha+i(2|\alpha|+1)}(\cos\theta_{|\alpha|}^0)[\Delta_p B_{N-|\alpha|,|\alpha|}^{\alpha}(\cos\theta_{|\alpha|}^0) \times B_{N-p,p}^{\alpha+i(2|\alpha|+1)}(\cos\theta_{\beta}^0)]^{-1},$$

where $i_1 = -E\left(\frac{|p|+\alpha}{2|\alpha|+1}\right)$, $i_2 = E\left(\frac{|p|-\alpha}{2|\alpha|+1}\right)$, $p = 0, 1, \ldots, N$, and $\nu = 0, 1, \ldots, 2p$.

The quantity $\Delta_p^*(\alpha + i(2|\alpha|+1))$ represents the Vandermonde determinant of the matrix Δ_p in which the column of number $\alpha + i(2|\alpha|+1)$ is replaced by a column consisting of zeros with the exception of unity standing in the νth row of the group of rows with the number p. Thus, we determined the amplitudes $d_{3p\nu}$ of the density of the velocity field potential at the surface $S_{3p\nu}$.

Now, let us determine the type of the auxiliary radiators that realize the damping problem. This type is determined by the function $f_{3p\nu}$ describing the distribution of the normal velocity over the surface $S_{3p\nu}$. We substitute representation (3) for the field U in the boundary conditions at the radiator surface S_{3p} (to simplify the formulas, we return to the old notation). We use the properties of the simple layer potential. As a result, we obtain a functional relation between the distribution of the normal velocity f_{3p} over the surface S_{3p}, the amplitudes d_{3p}, and other components of the field U:

$$f_{3p} = ik^2 h_0^{(1)'}(ka_2)d_{3p} + \int_F f\frac{\partial}{\partial n}\frac{\exp(ikR_{3pF})}{R_{3pF}}dF + \int_{S_{01}}\mu_{01}\frac{\partial}{\partial n}\frac{\exp(ikR_{3p01})}{R_{3p01}}dS_{01} + \sum_{j=1}^{2}\sum_{m=1}^{M_j}\int_{S_{jm}}\mu_{jm}\frac{\partial}{\partial n}\frac{\exp(ikR_{3pjm})}{R_{3pjm}}dS_{jm} + \sum_{m=1(m\ne p)}^{M_3}\int_{S_{3m}}\mu_{3m}\frac{\partial}{\partial n}\frac{\exp(ikR_{3p3m})}{R_{3p3m}}dS_{3m}. \tag{16}$$

Here, R_{3pF}, R_{3p01}, R_{3pjm}, and R_{3p3m} are the distances from a point of the surface S_{3p} to a point of the region F and points of the surfaces S_{01}, S_{jm}, and S_{3m}, respectively; $\partial/\partial n$ denotes the derivative with respect to the normal to the surface S_{3p}. From Eq. (16), it follows that the function f_{3p} can be calculated only approximately, because the coefficients $g_{1n\alpha}$ and $g_{2n\alpha}$, which determine the values of the two last integrals on the right-hand side of Eq. (16), are calculated approximately, and only the zeroth harmonics of the density of potential are measured at the receivers S_{jm} ($j = 1, 2$). With the use of the summation theorems for the spherical wave functions and their representations in different coordinate systems, the integration on the right-hand side of the expression for f_{3p} yields:

$$f_{3p} = ik^2\left\{-\frac{id_{3p}}{(ka)^2} + \sum_{m=-1}^{1}\frac{(1-m)!}{(1+m)!}\psi_0(ka_2)P_1^m \times(\cos\theta_{3p})e^{-im\varphi_{3p}}\left[\sum_{s=0}^{N}\sum_{q=-s-m}^{s+m}\frac{(s+q)!}{(s-q)!(2s+1)} \times g_{2sq}^* R_{m-q,s,m,1}^{(1)} + \sum_{s=0}^{N}\sum_{q=-s}^{s}\frac{g_{1sq}^*}{(2s+1)}Q_{qsm1}^{(1)} + \sum_{n=1(n\ne p)}^{(N+1)^2} d_{3n}h_1^{(1)}(kR_{3p3n})P_1^m(\cos\theta_{3p3n}^0)e^{im\varphi_{3p3n}^0}\right]\right\} \times(1 + O(ka_1, ka_2)). \tag{17}$$

Here, $(a_2, \theta_{3p}, \varphi_{3p})$ are the coordinates of a point on the sphere S_{3p}; $(R_{3p3n}, \theta_{3p3n}^0, \varphi_{3p3n}^0)$ are the spherical coordinates of the center of the radiator S_{3n} relative to the center of the radiator S_{3p}; and $R_{nmpq}^{(1)}$ and $Q_{nmpq}^{(1)}$ are the conversion constants of the Bessel spherical functions in different coordinate systems (these constants were determined in [13]). For an auxiliary radiator to provide a constant density of potential at its surface in the process of active damping, the normal velocity f_{3p} should have the following structure. By virtue of Eq. (15), the monopole component of the normal velocity depends only on the radiation and diffraction field produced by the body S_{01}. According to Eq. (17), the normal velocity components varying with θ_{3p} and φ_{3p}, i.e., the components that can be interpreted as dipoles, depend on the field of extraneous sources, the radiation and diffraction field produced by the body S_{01}, and the radiation field of all other auxiliary radiators. We denote by f_{3p}^* the principal part of the function f_{3p}.

DETERMINATION OF THE NUMBER N

To determine the number N, we use representation (13) for the field U. With allowance for the transformations described above, it takes the form

$$U_\partial = U_1 + U_2 + U_3 + V, \tag{18}$$

where

$$U_1 = ik\sum_{n=0}^{\infty}\sum_{\alpha=-n}^{n} h_n^{(1)}(kr)P_n^{-\alpha}(\cos\theta) \times \exp(-i\alpha\varphi)[g_{1n(-\alpha)} - (g^*_{1n(-\alpha)})];$$

$$U_2 = ik\sum_{n=N+1}^{\infty}\sum_{\alpha=-n}^{n} (-1)^\alpha(2n+1)\psi_n(kR_3)h_n^{(1)} \times (kr)P_n^{-\alpha}(\cos\theta)\exp(-i\alpha\varphi) \times \sum_{\beta=0}^{N}\sum_{\nu=0}^{2\beta} d^*_{3\beta\nu}P_n^\alpha(\cos\theta^0_{3\beta})\exp(-ia\varphi^0_{3\beta\nu});$$

$$U_3 = ik\sum_{n=0}^{N}\sum_{\alpha=-n}^{n} (-1)^\alpha(2n+1)\psi_n(kR_3)h_n^{(1)} \times (kr)P_n^{-\alpha}(\cos\theta)\exp(-i\alpha\varphi) \times \sum_{\beta=0}^{N}\sum_{\nu=0}^{2\beta} (d^*_{3\beta\nu} - d_{3\beta\nu})P_n^\alpha(\cos\theta^0_{3\beta})\exp(-ia\varphi^0_{3\beta\nu});$$

V is the field of diffraction by the receiver system; and $d^*_{3p\nu}$ is the reduced density of potential at the surface of an auxiliary radiator, this density being generated by the function $f^*_{3p\nu}$. We consider the first term U_1 on the right-hand side of Eq. (18). Analysis of this term shows that the number of receivers $(N+1)^2$ should be selected in such a way that the readings of the receivers provide the reconstruction of the measured field with sufficient accuracy. Intuition suggests that the choice is related to the approximation of the function by its values given for a set of points from the domain of definition of this function. However, according to condition (7), the field cannot be measured at a point; moreover, it cannot be extended using the continuity condition beyond the receiver boundary because of the specific features of the diffraction field within the region bounded by the sphere S_{jm}. Therefore, it is necessary first to formalize the physical problem of the field measurement as the problem of approximation of some specially introduced function. We introduce the functions

$$\Phi(r,\theta,\varphi) = ik\sum_{n=0}^{\infty}\sum_{\alpha=-n}^{n} h_n^{(1)}(kr)P_n^\alpha(\cos\theta)\exp(i\alpha\varphi)g_{1n\alpha},$$

$$\Phi_N(r,\theta,\varphi) = ik\sum_{n=0}^{\infty}\sum_{\alpha=-n}^{n} h_n^{(1)}(kr)P_n^\alpha(\cos\theta)\exp(i\alpha\varphi)g^*_{1n\alpha}.$$

The function $\Phi(r,\theta,\varphi)$ cannot be interpreted as the measured field, because this function is defined on the entire sphere R_j and the field is undefined on the sphere part lying inside the receivers $S_{jm}, j = 1, 2$. Let $\Phi(r,\theta,\varphi)$ represent a smooth function bounded together with its Nth derivatives, which corresponds to the case of low-frequency diffraction. Analysis of the solution to system (8) shows that the function Φ_N approximates the function Φ given at the points $(R_q, \theta^0_{qm}, \varphi^0_{qm})$. We require that the magnitude of the field U_1 be no greater than ε_1. According to Kushnirenko [14], when the positions of the receiver centers $(R_q, \theta^0_{q\alpha}, \varphi^0_{q\alpha\beta})$ lie in the vicinity of the points

$$\theta^0_{q\alpha} = \pi\alpha/(N+2), \quad \alpha = 1, \ldots, N+1 \text{ for odd } N,$$

$$\theta^0_{q\alpha} = \pi\alpha/(N+1), \alpha = 0,\ldots, N \text{ for even } N,$$

$$\varphi^0_{q\alpha\beta} = 2\pi\beta/(2\alpha+1), \beta = 0, \ldots, 2\alpha$$

with the coordinates $\theta^0_{q\alpha}$ simultaneously satisfying condition (9), the number of receivers that provide a given accuracy of the field measurement is calculated by the formula

$$N = E\left(\left[\frac{\pi^2}{2\varepsilon_1}\sum_{n=1}^{\infty}((n+1)n)\left|h_n^{(1)}(kR_1)\psi_n(kr^*_{01})\right|Q_{01}\right]^{1/2}\right) - 1. \tag{19}$$

Here, Q_{01} is the integral of the magnitude of the total density of potential at the body S_{01}, $E(x)$ is the integral part of the number x, and r^*_{01} is the maximal distance from the origin of coordinates to the points of the surface S_{01}. The constant Q_{01} is determined by the relationship

$$Q_{01} = Q^*_{01} + Q_{01F} + Q_{011} + Q_{012},$$

where

$$Q_{01F} = \int_{S_{01}}|\mu_{01F}|dS_{01}, \quad Q_{011} = \int_{S_{01}}|\mu_{011}|dS_{01},$$

$$Q_{012} = \int_{S_{01}}|\mu_{012}|dS_{01},$$

μ_{01F} is the density of potential induced at the body S_{01} by the field of extraneous sources, μ_{011} is the density of potential induced at the body S_{01} by the field of diffraction by the receiver array, and μ_{012} is the density of potential induced at the body S_{01} by the field of auxil-

iary sources. Using the integral equation of the diffraction problem of the extraneous field diffraction by only the body S_{01} to estimate Q_{01F} and taking into account the results obtained by Steklov [15], we obtain the expression

$$\int_{S_{01}} |\mu_{01F}|\,dS_{01} \le \frac{1 + k(r_F^* - r_{01}^*)}{(r_F - r_{01}^*)^2}\frac{Q_F}{\pi} \times \left[1 + \frac{I_{S_{01}} + D_0}{D_0}\right] K_{S_{01}}|S_{01}|.$$

The term Q_{012} is estimated using the integral equation of the diffraction problem for the field generated by auxiliary radiators and diffracted by the body S_{01}. In this case, we also take into account the following consideration. Since the diffraction and radiation field produced by the body should be damped as a result of the interference of this field with the field of auxiliary radiators, the magnitude of the field of auxiliary radiators outside the sphere of radius R should be equal to the magnitude of the field of extraneous sources and the magnitude of the field of the self-radiation of the body S_{01}. Thus, we have

$$\int_{S_{01}} |\mu_{012}|\,dS_{01} \le \frac{[1 + k(r_F^* - r_{01}^*)1](R - R_3)}{(R - r_{01}^*)^2\pi} \times \left[1 + \frac{I_{S_{01}} + D_0}{D_0}\right] K_{S_{01}}|S_{01}|\left[\frac{Q_F}{r_F^* - R} + \frac{Q_{01}^*}{R - r_{01}^*}\right],$$

where r_F^* is the distance from the origin of coordinates to the region F.

The term Q_{011} is estimated using the integral equation that describes the diffraction by the body S_{01} for the secondary diffraction field caused by the receiver array, with the extra condition $(R_1 - r_{01}^*)/R_1 \ll 1$ and with allowance for relation (5):

$$\int_{S_{01}} |\mu_{011}|\,dS_{01} \le \frac{1 + k(R_2 - r_{01}^*)}{R_1}\frac{Q_F}{\pi} \times \left[1 + \frac{I_{S_{01}} + D_0}{D_0}\right] K_{S_{01}}|S_{01}|\left|\frac{\psi_0(ka_1)h_0^{(1)'}(ka_1)}{\psi_0'(ka_1)}\right| b^* k\varepsilon_1,$$

where $I_{S_{01}}$, D_0, and $K_{S_{01}}$ are determined by the formulas

$$1/D_0 = \max(1/D,\, d\sqrt{3}),$$

$$I_{S_{01}} = \max_{S_{01}} \int_{S_{01}} \frac{dS_{01}}{2\pi R(s, s_1)},$$

$$K_{S_{01}} = 1 + \left|\frac{\lambda_1}{1 - \lambda_1}\right| \left[\max_{S_{01}} \int_{S_{01}} |K_1(s, s_1)|^2 dS_{01}\right].$$

Here, d and D are the Lyapunov constants of the surface S_{01}, $R(s, s_1)$ is the distance between arbitrary points of the surface S_{01}, $K_1(s, s_1)$ is the symmetrized kernel for $\partial/\partial n(\exp(ikR)/R)$, λ_1 is the first eigenvalue of the integral equation with the kernel $K_1(s, s_1)$, and $|S_{01}|$ is the area of the surface S_{01}. To determine the parameter λ_1, we can use the results obtained by Mikhlin and Smolitskiĭ [16]:

$$\lambda_1 = \sqrt{A_{2m}/A_{2m+2}}, \quad A_m = \iint K_m^2(x, s)\,dx\,ds,$$

where K_m is the mth iteration of the kernel K_1 and m is large.

For the aforementioned arrangement of the receiver centers and for the number N selected according to Eq. (19), we obtain the close-to-minimal measurement error related to the arrangement of the receivers on the spheres R_j, $j = 1, 2$.

The second term of the sum on the right-hand side of Eq. (18) corresponds to the uncompensated part of the spatial harmonics of the field with the numbers $n \ge (N + 1)$, its presence being related to the finite number of auxiliary radiators. With allowance for the comment made in estimating the term Q_{012}, we obtain that $|U_2|$ satisfies the inequality

$$|U_2| \le \frac{(N+1)^2}{2kR}\left(\frac{R_3}{R}\right)^{N+1} \frac{1}{\left|h_0^{(1)}(k(R - R_2))\right|} \times \left[\frac{Q_{01}^*}{R - r_{01}^*} + \frac{Q_F}{r_F^* - R}\right] = U_2^*(N) = \varepsilon_2. \tag{20}$$

The field U_3 takes into account the total radiation field discrepancy related to the use of only monopole- and dipole-type auxiliary radiators instead of the n-pole-type ones. In estimating the third term in the sum on the right-hand side of Eq. (18), we require that the following additional conditions be satisfied:

$$kR \ge kR_3 + 0.1,$$

$$\max_p |d_{3p}^* - d_{3p}| \frac{1}{\left|h_0^{(1)}(k(R - R_2))\right|} \times \left[\frac{Q_{01}^*}{R - r_0^*} + \frac{Q_F}{r_F^* - R}\right](ka_2)^4 \ll 1. \tag{21}$$

In this case, for U_3, we obtain the estimate

$$|U_3| \le \frac{3\pi k(N+1)^2}{\left|h_0^{(1)}(k(R - R_2))\right|}\left[\frac{Q_{01}^*}{R - r_0^*} + \frac{Q_F}{r_F^* - R}\right](ka_2)^4 = U_3^*(N), \quad U_3^*(N) = \varepsilon_3. \tag{22}$$

The contribution made by the field of diffraction by the receivers to the total diffraction field satisfies the inequality

$$|V| \le \left|\frac{\psi_0'(ka_1)Q_F}{\psi_0(ka_1)h_0^{(1)'}(ka_1)}\right| \left\{\frac{Q_F}{k(r_F^* - R_2)} + \frac{R - R_3}{k(R_3 - R_2)}\right.$$

$$\times\left[\frac{Q_F}{r_F^*-R}+\frac{Q_{01}^*}{R-r_{01}^*}\right]+\left\{Q_{01}+\left(1+\frac{I_{S_{01}}+D_0}{D_0}\right)\right.$$

$$\times K_{S_{01}}|S_{01}|\left[\frac{Q_F(1+k(r_F^*-r_{01}^*))}{\pi(r_F-r_{01}^*)^2}\right.$$

$$\left.\left.+\frac{(1+k(R-r_{01}^*))(R_3-R)}{\pi(R-r_{01}^*)^2}\left[\frac{Q_F}{r_F^*-R}+\frac{Q_{01}^*}{R-r_{01}^*}\right]\right]\right\} \quad (23)$$

$$\times\frac{(N+1)^2+(N+1)\ln N}{R_1}=V^*(N)\Bigg\}V^*(N),$$

$$V^*(N)=\varepsilon_4.$$

For condition (2) to be satisfied, we require that the following equality be valid:

$$\sum_{j=1}^{4}\varepsilon_j=\varepsilon.$$

Inequality (6) and relationships (19), (20), (22), and (23) form a nonlinear system of equalities and inequalities for the determination of the number N, the wave dimensions ka_1 and ka_2, and the radii R and R_j, $j = 1, 2, 3$. This system can be solved by iterations according to the following algorithm. First, we select the radii $R_1 > r_{01}^*$ and $R > R_3 > R_2 > R_1$. Since, with increasing N, we have $U_2^*(N) \longrightarrow 0$, the solution to Eq. (20), which is nonlinear in N, exists and can be found by the Newton method or by the bisection method. Then, from Eq. (7), we determine the parameter ka_1. From Eq. (19), we calculate the value of $N = N'$ and select $N = \max(N, N')$. We calculate the parameter ka_2 from Eq. (22) and verify condition (20). Then, we verify the conditions

$$R_1 > (N+1)a_1/\sqrt{\pi}, \quad R_3 > (N+1)a_2/\sqrt{\pi},$$

which mean the possibility to arrange $(N+1)^2$ receivers on the sphere of radius R_1 and $(N+1)^2$ radiators on the sphere of radius R_3 so that $a_1/R_{qpjm}^* < 1/4$ and $a_2/R_{3p3q}^* < 1/4$, where R_{3p3q}^* is the minimal distance between the centers of the radiators S_{3p} and S_{3q} on the sphere of radius R_3. We refine the value of the radius R_1 as the maximum of the values $R_1 > r_{01}^* + a_1$ and $R_1 > (N+1)a_1/\sqrt{\pi}$; we take $R_2 > R_1 + 2a_1$; the value of the radius R_3 is refined as the maximum of the values $R_3 > R_2 + a_1 + a_2$ and $R_3 > (N+1)a_2/\sqrt{\pi}$; and, finally, we take $R > R_3 + a_2$ and $R > R_3 + 0.1/k$. Using the values of the radii R_j and R refined as described above, from Eq. (22) we calculate the wave dimension ka_2, and, from Eq. (23) in which the Bessel spherical functions are replaced by their asymptotics in the small parameter, we calculate the wave dimension ka_1. We compare the latter with the value of ka_1 calculated by formula (7), and select the minimal value of these two.

Thus, the diffraction problem of active damping is completely solved. The physical realization of the problem is determined by conditions (7) and (12): if the solution of the diffraction problem yields the parameter $ka_1 \geq ka_1^*$ and the condition $|f_{3p}| \leq |\omega u_r^*|$ is satisfied for the function f_{3p}, the problem of active field control is physically realizable. If these conditions fail, the problem is physically unrealizable within the class of receivers and radiators determined by conditions (7) and (12).

REFERENCES

1. G. D. Malyuzhinets, Tr. Akust. Inst. Akad. Nauk SSSR, No. 15, 124 (1971).
2. I. A. Urusovskiĭ, Akust. Zh. **23**, 304 (1977) [Sov. Phys. Acoust. **23**, 170 (1977)].
3. A. A. Mazanikov, V. V. Tyutekin, and M. V. Fedoryuk, Akust. Zh. **26**, 759 (1980) [Sov. Phys. Acoust. **26**, 428 (1980)].
4. I. A. Urusovskiĭ, Akust. Zh. **27**, 585 (1981) [Sov. Phys. Acoust. **27**, 325 (1981)].
5. S. J. Elliott and P. A. Nelson, Noise/News Int. **2** (2), (1994).
6. G. V. Alekseev, Akust. Zh. **43**, 737 (1997) [Acoust. Phys. **43**, 639 (1997)].
7. V. V. Tyutekin, Akust. Zh. **43**, 238 (1997) [Acoust. Phys. **43**, 202 (1997)].
8. S. J. Elliott, in *Proceedings of the International Symposium "Active 99," 1999*, p. 3.
9. V. B. Glasko, *Inverse Problems of Mathematical Physics* (Mosk. Gos. Univ., Moscow, 1984).
10. A. I. Boĭko and V. P. Ivanov, Zh. Vychisl. Mat. Mat. Fiz. **16**, 152 (1976).
11. *Vector-Phase Methods in Acoustics*, Ed. by V. I. Il'ichev, (Nauka, Moscow, 1989).
12. V. P. Ivanov, Akust. Zh. **36**, 872 (1990) [Sov. Phys. Acoust. **36**, 487 (1990)].
13. E. A. Ivanov, *Electromagnetic Wave Diffraction by Two Bodies* (Nauka i Tekhnika, Minsk, 1968).
14. G. G. Kushnirenko, Vestn. Khark. Politekh. Inst. **25** (3), 3 (1959).
15. V. A. Steklov, *Principal Problems of Mathematical Physics* (Fizmatgiz, Moscow, 1983).
16. S. G. Mikhlin and Kh. D. Smolitskiĭ, *Approximate Methods of Differential and Integral Equation Solutions* (Nauka, Moscow, 1965).

Translated by E. Golyamina

Acoustical Physics, Vol. 47, No. 1, 2001, pp. 76–84. Translated from Akusticheskiĭ Zhurnal, Vol. 47, No. 1, 2001, pp. 92–100.
Original Russian Text Copyright © 2001 by Krivonosova, Rinkevich, Smorodinskiĭ .

Acoustic Fields Detected by a Laser Interferometer in Aluminum Single Crystals

A. S. Krivonosova, A. B. Rinkevich, and Ya. G. Smorodinskiĭ

Institute of Metal Physics, Ural Division, Russian Academy of Sciences,
ul. Kovalevskoĭ 18, Yekaterinburg, 620219 Russia
e-mail: rin@imp.uran.ru

Received December 29, 1999

Abstract—Elastic fields in aluminum single crystals are studied using the laser interferometry technique. The measurements are conducted at a frequency of 10 MHz for the case of the wave propagation along the [001] and [111] axes and also for small deviations from the [111] axis. The energy distribution is measured in the transition region between the near and far fields. The energy of transverse elastic waves in the case of the propagation along the [111]-axis is distributed within a sector. The deviation of the propagation direction from this axis leads to radical changes in the energy distribution. © *2001 MAIK "Nauka/Interperiodica".*

The study of the elastic energy distribution in a beam propagating in an anisotropic medium is an important problem of crystal acoustics. The propagation of ultrasonic beams in crystals was treated theoretically in detail by Khatkevich [1]. The particular features of the polarization of elastic waves near acoustic axes were studied by Al'shits and Shuvalov [2]. Quasi-transverse waves propagating near the [111]-axis of a cubic crystal are of special interest. The velocities of transverse modes are degenerate in the case of the propagation strictly along this axis. At the same time, the plane perpendicular to the axis is not a plane of bilateral symmetry. Therefore, the energy flux of elastic waves deviates from the axis. The deviation angle depends on the radiator polarization. If the initial polarization is rotated through some angle, the energy flux deviates through a twofold angle and it performs a complete revolution when the radiator polarization is rotated through $\pm\pi$; the energy flux vector circumscribes a conical surface. This is the effect of internal conical refraction [3]. The cone of internal conical refraction is circular in cubic crystals. The distribution of the beam energy in the conditions of the conical refraction was investigated experimentally in a germanium single crystal [4]. It was demonstrated that, in the case of the ultrasonic propagation strictly along the [111]-axis, the energy is distributed within a wide crescent-shaped area in conformity with the theory [1]. The deviation of the beam from the axis leads to the elimination of the velocity degeneracy and to the mode splitting. Two sharp peaks were observed in the energy distribution. Anisimkin and Morozov [4] suggested a very strict criterion for the angle of beam deviation within which the observation of the effect of internal conical refraction is possible.

The utilization of the laser detection technique provides an opportunity to study in detail the distribution of the elastic energy. The methods for measuring the components of elastic displacements in the plane of a reflecting surface and normally to it were developed by Monchalin *et al.* [5], and a method for evaluating the three components of the elastic displacements was proposed by Bayon and Rasolofosaon [6]. The detection of ultrasound with the help of a confocal Fabry–Perot interferometer using a phase-modulated radiation was performed by Nakano *et al*. [7]. We investigate the elastic fields excited in an aluminum crystal by a piezoelectric transducer. The detection of waves transmitted through the sample is performed with the help of a Doppler laser interferometer. Aluminum single crystals are selected as the objects of investigation. They have a high degree of structural perfection. This is especially important for studying the effect of conical refraction, when even small changes in the crystallographic orientation of grains can affect the energy distribution in the beam. We study the fields of longitudinal and transverse (quasi-transverse) waves in the cases of their propagation along the [001] and [111] axes of the crystal and for small deviations from the [111]-axis.

The measurements were performed using a laser interferometer of the Institute of Nondestructive Testing (Dresden, Germany). Elastic waves were excited in crystals by piezoelectric transducers with the resonance frequency f = 10 MHz. The piezoelectric plates were shaped as disks with the diameters 5 mm in the case of longitudinal waves and 6 mm in the case of transverse waves. The piezoelectric transducer for transverse waves had a buffer made of fused quartz. Taking into account the sample length (about 17 mm), the buffer length, the wave frequency, and the piezoelectric plate dimensions, we can conclude that the measurements were conducted within either the near field of radiation or the transition region between the near and far fields. A sounding signal with the duration $\tau = 0.4$ μs was gen-

1063-7710/01/4701-0076$21.00 © 2001 MAIK "Nauka/Interperiodica"

erated by a USIP-12 ultrasonic flaw detector manufactured by the Krautkrämer company. A decaying series of pulses corresponding to the ultrasonic wave reflection in the sample was observed with the help of the flaw detector. A beam of elastic waves propagating in the crystal reached the opposite face and was reflected by it. The field of elastic displacements was measured by an OFV 3000S Doppler laser interferometer made by the Polytec Company. The output signal of the interferometer was observed using an LC 334A oscilloscope (LeCroy) and digitized by it. The data were analyzed by the LabView 5.0 computer code. This software set up the mode of scanning: the scanning field (most often 16×19 mm) and the scanning interval of 0.125 or 0.25 mm. In addition, the number of measurement cycles, within which the measurement data were averaged at each point of the scanning field, was set up. The number of cycles was selected depending on the signal-to-noise ratio, and, as a rule, 50 or 100 cycles of averaging were used. The information on the time dependence of the received signal amplitude was stored and remained accessible for further analysis.

The LabView 5.0 code allows one to observe the time dependence of the amplitude at any selected point of the scanning field (the A-scan). Moreover, it is possible to analyze the B-scan, i.e., the set of the time dependences of the amplitude measured along a selected direction (either along the scanning direction or perpendicular to it). Further, the amplitude distribution of the interferometer signal over the scanning field (the C-scan) is represented by a diagram. The LabView 5.0 code provides the possibility to select the time interval within which the C-scan is plotted. This allows us to separate the waves of interest.

The samples used for our measurements were aluminum single crystals grown at the Institute of Metal Physics, Ural Division, Russian Academy of Sciences. The sample for the [001] direction was a rectangular prism with faces coincident with the (001) crystallographic faces within 1°–2°. The samples for the [111] direction were cut from a cylindrical ingot with the diameter 20–22 mm. The sample length was approximately 17 mm. Two samples were cut from this ingot in such a way that the normal to the plane-parallel faces of one of them formed an angle of 1.5° with the [111] direction, and, for the other sample, this angle was 5°. The plane facets of the samples were polished in such way that the average height of roughness was 8 μm. The distance between two irregularities in the sample plane was from 30 to 100 μm.

The single crystals were grown from aluminum of 99.999% purity using the Bridgeman technique. One of the main criteria of perfection of pure metal single crystals is the presence of dislocations in them. The density of the growth dislocations in the bulk of the crystal was revealed by the method of etch pits and constituted about 10^3 cm^{-2}. The dislocations were freely distributed in crystals in the form of a three-dimensional grid, or they were arranged in rows forming small-angle boundaries. An X-ray topogram of a single crystal with the orientation [111] is given in Fig. 1. Only two crystallites with the misorientation not exceeding 20' are observed within the whole cross-section of the single crystal. The X-ray alignment of the sample along the [111] direction was performed especially carefully: the normal to the face plane deviates from the axis within no more than 0.5°.

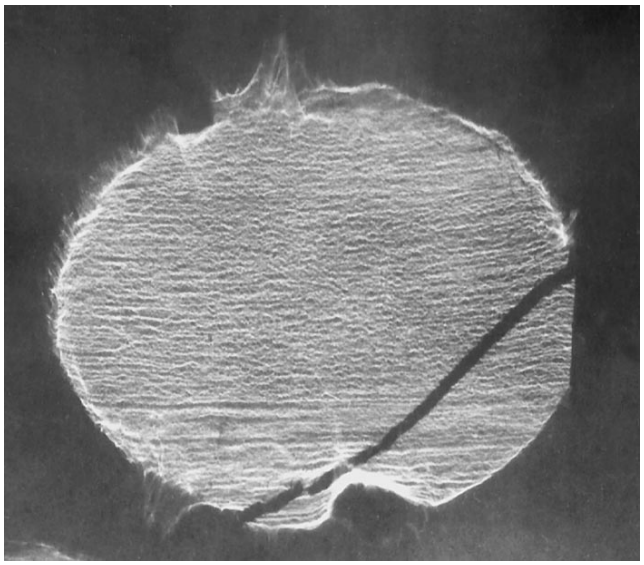

Fig. 1. X-ray topogram of an aluminum single crystal from which the samples with the [111] orientation were cut out.

Let us first consider the results of the measurements for a single crystal with the [001] orientation. A B-scan obtained using longitudinal waves is shown in Fig. 2a for the direction of the *Y*-axis in the (001) plane along the direction of scanning. The line, along which the B-scan was measured, passes through the center of the projection of the piezoelectric plate onto the opposite face of the sample. Two systems of lines are clearly visible. They correspond to the values 1.00–1.50 and 6.00–6.50 on the abscissa axis of the B-scan. The abscissa is the time axis calibrated in microseconds with the arbitrarily selected origin. The aforementioned systems of lines correspond to longitudinal waves transmitted through the sample one and three times. One can notice the curvature of the lines that is caused by the difference between the pulse arrival times at different points of the beam cross-section. The less distinct sloping lines correspond to the radiation part reflected from the lateral faces of the sample.

Figure 2b demonstrates a B-scan obtained in the case of scanning in the *X* direction. The scanning line in this case passes not through the beam center but is shifted by the distance equal to the radius of the piezoelectric plate. The distortion of the lines in this case is more evident, especially at the beam periphery. In both figures, the systems of lines have the form of alternat-

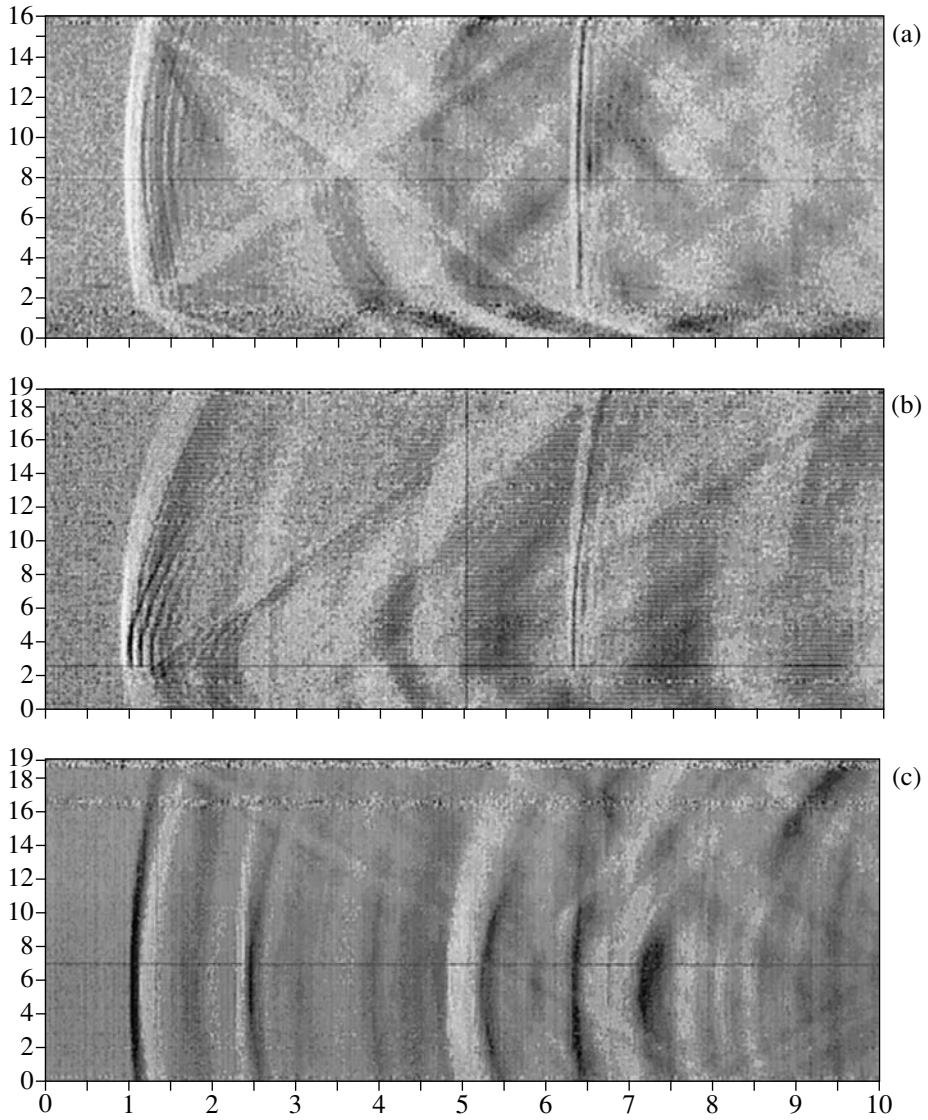

Fig. 2. B-type scans obtained for a single crystal with the [001] orientation: (a) longitudinal waves, the direction of scanning is the *Y*-axis; (b) longitudinal waves, the direction of scanning is the *X*-axis; and (c) transverse waves, the direction of scanning is the *X*-axis.

ing light and dark stripes. Light stripes correspond to the positive half-period of the received signal and dark stripes, to the negative one. The B-scan obtained in the case of wave excitation by a transverse wave transducer is presented in Fig. 2c. Here, the direction of scanning is the *X*-axis. The observed pattern is interpreted as follows. The line within the interval 1.00–1.50 μs corresponds in the arrival time to the longitudinal wave excited by the piezoelectric plate as a parasitic signal. The parasitic signal of a longitudinal wave, which was possibly caused by insufficient damping of the piezoelectric plate, was observed near the point 2.50 μs. The position of the distorted line within the interval 4.70–5.50 μs approximately corresponds to a delay in the propagation of transverse waves. The laser interferometer measures the elastic displacements normal to the plane of the reflecting face. The origin of the signal of a transverse wave whose elastic displacements lie in the face plane will be discussed below.

A C-scan corresponding to transverse waves in the [001] crystal is shown in Fig. 3. The radiation spot of irregular shape has the transverse dimension ≈10.00–2.00 = 8 mm along the abscissa axis. This is somewhat greater than the piezoelectric plate diameter (6 mm). Figure 3 demonstrates the structure of the radiation field in the case of coincidence of the beam axis with the crystallographic axis in the absence of the effect of conical refraction.

Let us turn to the results of measurements of the fields of ultrasonic waves for the [111] propagation direction and the directions close to this axis. Images of the B-type for transverse waves in the *X* direction perpendicular to the direction of scanning are shown in

Fig. 4, where, in the case (a), the central ray of the beam with the wave vector $\mathbf{k}_0$ is parallel to the axis: $\mathbf{k}_0$//[111]; in the case (b), it deviates from this direction by 1.5°; and, in the case (c), it deviates by 5°. The intervals from 5.5 to 18.5 cm (see Fig. 4a) and from 2 to 16.8 cm (see Fig. 4b) on the ordinate axis correspond to the plane face of the sample. The total field of the B-scan in Fig. 4c corresponds to the plane face of the sample. The sloping lines in Fig. 4a, which are located beyond the indicated interval, are formed by the radiation part coming out to the lateral surface of the sample. The lines caused by the parasitic radiation of longitudinal waves by the transverse-wave transducer are present in the initial portion of the measurement interval on the abscissa axis in the diagrams of Fig. 4. For example, in Fig. 4a, the lines observed from 0 to 3.5 μs correspond to the longitudinal waves. Despite the small amplitude of the parasitic radiation (its level is 20–25 dB less than the level of the transverse waves), these signals can be distinguished in Fig. 4 due to the high sensitivity of the laser interferometer to the displacements normal to the surface. We are interested in the signals caused by transverse waves in the interval 4.50–6.00 μs. The amplitude distributions shown in Figs. 4a and 4c agree qualitatively with the energy distribution pattern in the conditions of internal conical refraction [1]. According to the theory, the radiation energy is distributed along almost all generatrices of the refraction cone. In the cross-section by a straight line, this part of the radiation must give a B-scan with the arrival time of the signal varying nonmonotonically along the ordinate axis. At the same time, Fig. 4a contains a radiation component whose arrival time is approximately constant along the whole line of the B-scan section. The deviation from the axis must lead to the elimination of the velocity degeneracy of the quasi-transverse waves. However, the deviation by 1.5° from the [111] axis does not lead to radical changes in the energy distribution (Fig. 4b). The diagram of the B-scan for the deviation angle 5° looks entirely different (Fig. 4c). It exhibits no distinct pattern of signals within the interval 4.50–6.00 μs. The pattern of the energy distribution can be observed more illustratively in the C-scans.

The distribution for the direction exactly along the [111] axis is given in Fig. 5a. The time interval of observation corresponds to the arrival time 4.50–6.00 μs for transverse waves. The oval line in the figure is the boundary of the plane face of the sample. One can see that radiation is distributed within a conical sector. Two amplitude peaks are visible within this sector. The energy distribution under the conditions of internal conical refraction differs radically from the one given in Fig. 3. The radiation distribution in a crystal inclined at an angle of 1.5° to the [111]-axis is shown in Fig. 5b. One can see that a considerable part of the elastic energy is distributed over a wide region of the sample with the area far exceeding the area of the radiator. However, in Fig. 5b, it is difficult to connect any definite radius of the energy distribution with the radius of

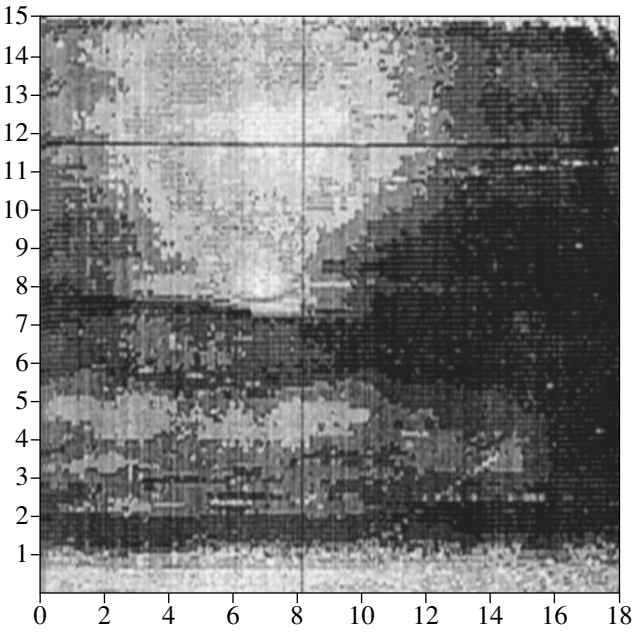

Fig. 3. C-type scan in a [001] single crystal, transverse waves.

the cone of internal conical refraction. Two more distinct peaks are present in Fig. 5b apart from the distributed part of the energy. One of the peaks is very close to the sample center.

The presence of the part of the radiation energy that is distributed over the circular arcs testifies to the fact that, in both cases corresponding to Figs. 5a and 5b, the effect of internal conical refraction distorted by the presence of additional peaks is observed. The additional peaks are probably caused by small deviations of the central ray of the beam from the [111] axis and by the presence of the lateral rays of the beam, which are deflected from the axis through considerable angles in the conditions of our experiment. It is necessary to take into account that, in our case, we have the ratio $\lambda/a \approx 0.1$ (λ is the wavelength and a is the radiator radius). With such a ratio, the diffraction divergence causes deviations up to ~6° from the central ray.

Evidently, an increase in the deviation angle from the [111]-axis must lead to the disappearance of the effect of internal conical refraction and, hence, to radical changes in the energy distribution. For large deviation angles, the velocity degeneracy of the natural quasi-transverse waves is eliminated and the beam is split into two beams corresponding to two modes. In the limiting case of large deviations, two peaks were observed without traces of energy spreading between them [4]. In our case, the measurements were conducted at a relatively low frequency 10 MHz. When the deviation angle is 5° (Fig. 5c), the radiation energy is divided between the two peaks formed by two quasi-transverse modes. However, even in this case, the radi-

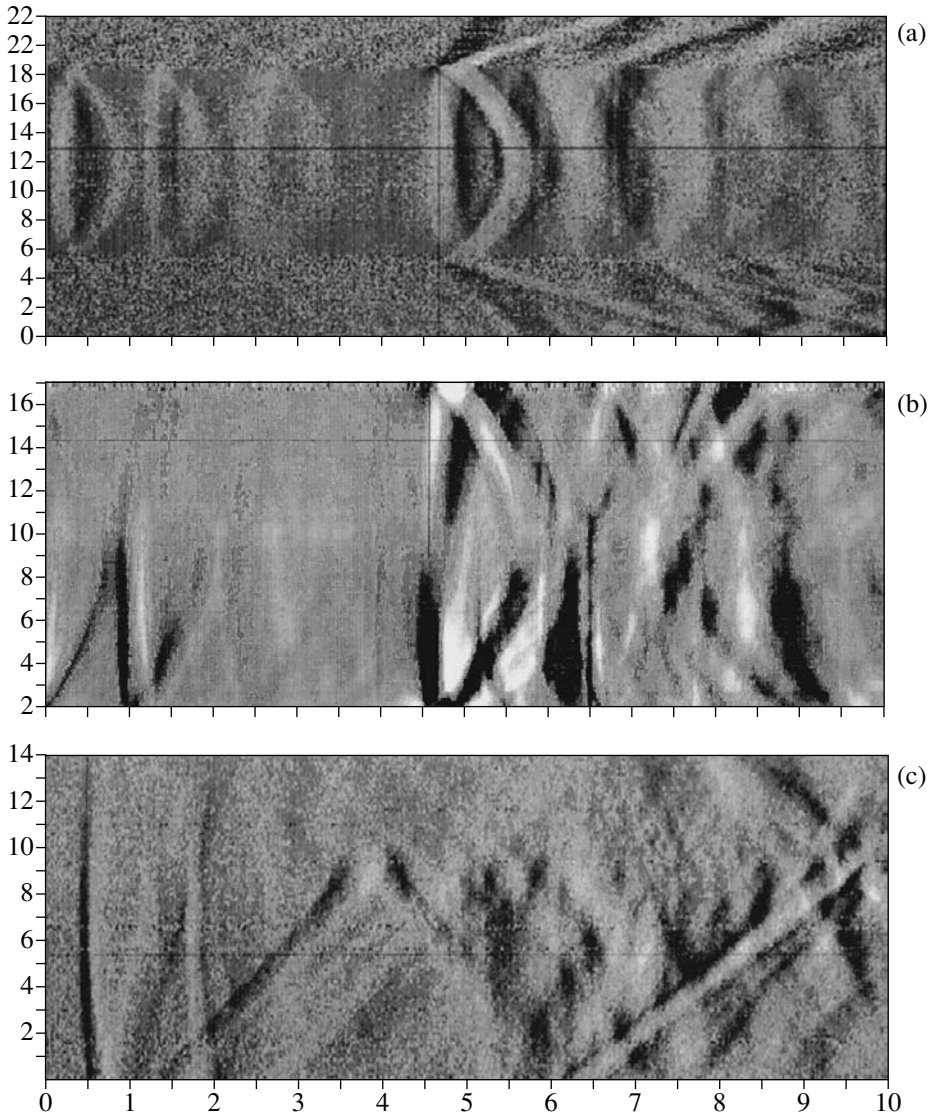

Fig. 4. B-type scan in the direction of the *X*-axis in the case of the excitation by a transverse wave transducer when (a) $\mathbf{k}_0$//[111] and when the wave vector is deflected from the [111]-axis through the angles (b) 1.5° and (c) 5°.

ation energy corresponding to the beam lying far from the center is distributed over a circular arc.

The question about the maximal deviation angle at which the internal conical refraction is still observable was treated by Artman [8] and Anisimkin and Morozov [4]. Artman [8] suggested the condition that the maximal possible angle of deviation Δ from the acoustic axis is less than the angle of beam divergence $\delta \sim \lambda/a$. According to the measurements by Anisimkin and Morozov [4], the observation criterion was made more strict: $\Delta < 0.1\delta$. In fact, the measurements can be conducted in both far and near wave fields of radiation. Therefore, in addition to the wavelength and the radiator radius, a more exact condition must also include the sample length, the size of the near zone of radiation $\sim a_2/\lambda$, and, probably, the cone angle of internal conical refraction calculated according to the theory of plane waves.

Let us discuss the factors that determine the signal of the laser interferometer in the case of the normal incidence of a shear wave on the sample surface. As we know, in the first approximation, the interferometer is sensitive to the displacements normal to the reflecting surface [9]. In analyzing the experimental results, we have to take into account the surface roughness, the deviation of the beam wavefront from a plane, and the presence of widely deflected rays of the beam in the conditions of the internal conical refraction.

According to Vinogradova *et al.* [10], the wavefront of the field of a disk-shaped radiator near the acoustic axis can be approximated by a spherical surface of the

radius $R = a\left(\frac{1+D^2}{D}\right)^{1/2}$, where a is the radiator radius, $D = \frac{2Z}{qa^2}$, Z is the sample length, and q is the wave number. In our conditions, the wavelength is $\lambda = 0.3$ mm for transverse waves and the size of the near wave zone is $x_n = 30$ mm. The phase difference between the center of the radiator projection and the point at a distance a from the radiation axis is $\Delta\phi = a^2/2\lambda R$, and, in our conditions, it is $\approx\pi/2$. The deviation of the wavefront from the plane of the sample surface gives rise to a component of elastic displacements that is normal to the sample surface plane. We estimate their value on the basis of calculations [11]. The radiation deflected through the angle θ from the [111] crystal axis splits into two quasi-shear waves. These waves contain the longitudinal oscillation components $A_3^{(i)}$, which are different for the modes $i = 1$ and $i = 2$. The components depend on the polar β and axial θ angles:

$$A_3^{(1)} = \frac{1}{3}(2K_3 - 3)\theta\cos\frac{\beta}{2}\left(4\sin^2\frac{\beta}{2} - 1\right),$$
$$A_3^{(2)} = \frac{1}{3}(2K_3 - 3)\theta\sin\frac{\beta}{2}\left(1 - 4\cos^2\frac{\beta}{2}\right). \quad (1)$$

Here, $K_3 = \frac{C_{11} - C_{12} - 2C_{44}}{C_{12} + C_{44}} + \frac{3}{2}$ and $C_{i,j}$ are the components of the elastic constant tensor of the crystal. The estimates give the maximal value of the ratio of the longitudinal and transverse components $\approx 0.08\theta$. The cone angle of internal conical refraction ϑ_{VCR} calculated for plane waves constitutes 6° for aluminum. For the rays corresponding to this angle, the relative value of the longitudinal component of elastic displacements does not exceed 0.008. This value is too small to explain the results of Fig. 5a, where the intensity of signals with the deviation angles 4°–8° is very large. The angle of the diffraction divergence of the beam $\theta_d \cong \lambda/2a$ constitutes 3° for our conditions. At the same time, in Fig. 5a, one can see the rays deflected through greater angles, up to 20°–25°. The share of the longitudinal component of displacements constitutes up to 0.03 for these rays. The existence of such rays is a consequence of conical refraction [1].

Let us take into account the influence of the roughness of the sample surface on the output signal of the interferometer in order to explain the experimental results. For this purpose, we separate two rays, 1 and 2, in the beam incident on the sample surface (Fig. 6). We introduce the angles $\alpha_{1,2}$ between the ray and the tangent to the surface at the points of incidence. We assume that the surface structure is such that $|\cot\alpha_{1,2}| \leq 1$. Let N roughness elements of the average height Δh occur within 1 cm of the surface length. Then, we have the average value $\langle|\cot\alpha_{1,2}|\rangle \sim \Delta hN$. For a sample the normal to which corresponds to the [111]-axis, the product ΔhN is approximately equal to 0.5. An elastic wave causes a displacement of the reflecting surface from the position I to the position II with the normal

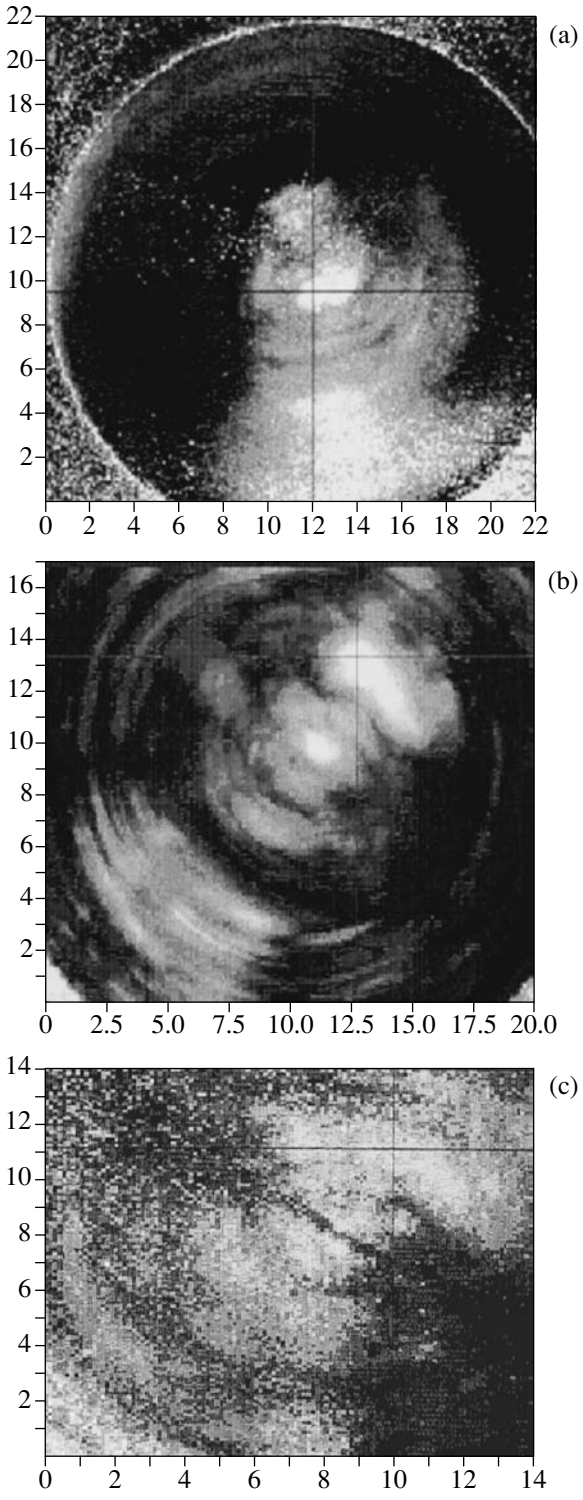

Fig. 5. Distribution of the energy of elastic waves when (a) $\mathbf{k}_0$//[111] and when the wave vector is deflected from the [111]-axis through the angles (b) 1.5° and (c) 5°.

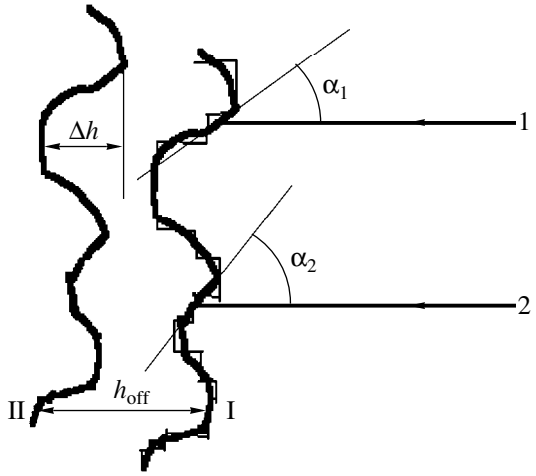

Fig. 6. Schematic diagram of the rough surface with rays 1 and 2 incident on it.

component of the displacement h_{off}. We approximate the surface section by a stepped line. Then, the contribution made by the elastic wave displacements to the signal phase will be $\phi_S = 2h_{\text{off}}2\pi/\lambda$. The rays reflected from the sample A_f and the reference signal A_r enter the interferometer photodetector:

$$A_r = A_{ro}\exp(i\phi r),$$
$$A_f = A_{fo(1)}\exp[i(\phi 1 + \phi s2)] + A_{fo(2)}\exp[i(\phi 2 + \phi s2)],$$

where A_{ro} and ϕ_r are the amplitude and phase of the reference signal and $A_{fo(i)}$ and ϕ_i are the same quantities for the signal resulting from the reflection of the ith ray (i = 1, 2). The phase ϕ_{si} in the reflected ith ray is caused by the surface displacement due to the elastic wave. The calculation is conducted for the properly normalized intensity I:

$$\begin{aligned} I &= A_t A_t^* \\ &= I_r + I_f + 2A_{fo(1)}\cos(\phi_1 - \phi_2 + \phi_{s1} - \phi_{s2}) \\ &\quad + 2A_{ro}[A_{fo(1)}\cos(\phi_r - \phi_1 - \phi_{s1})] \\ &\quad + A_{fo(2)}\cos(\phi_r - \phi_2 - \phi_{s2}), \end{aligned} \tag{2}$$

where $I_r = (A_{ro})^2$ and $I_f = (A_{fo(1)})^2 + (A_{fo(2)})^2$.

For the longitudinal elastic waves, the contributions to the phase ϕ_{s1} and ϕ_{s2} are equal: $\phi_{s1} = \phi_{s2} = \phi_s = \frac{2\pi}{\lambda}u_0\cos\omega_s t$, where ω_s is the circular frequency of the elastic wave and $h_{\text{off}} = u_0\cos w_s t$. From Eq. (2), we obtain

$$\begin{aligned} I &= I_0 + 2[I_r(I_f + I_h)]^{1/2} \\ &\quad \times (1 + \cos 2\varphi_r \cos 2\varphi)^{1/2}\cos(\varphi_s + \varphi_l). \end{aligned} \tag{3}$$

In Eq. (3), I_0 is the intensity of the illumination of a given point of the sample in the absence of elastic waves, $I_0 = I_r + I_f + I_h$, and $I_h = 2A_{f0(1)}A_{f0(2)}\cos(\varphi_1 - \varphi_2)$. The angles φ and φ_l are determined as follows:

$$\begin{aligned} \tan\varphi &= \frac{A_{fo(1)}\sin\phi_1 + A_{fo(2)}\sin\phi_2}{A_{fo(2)}\cos\phi_1 + A_{fo(1)}\cos\phi_2}, \\ \tan\varphi_l &= \frac{\cos(\phi_r + \varphi)}{\cos(\phi_r - \varphi)}. \end{aligned} \tag{4}$$

It is possible to tune the interferometer in such a way that $\varphi_r = \pi/4$. In the case of a sufficiently smooth surface $\Delta h \ll \lambda$, the phase difference is $|\phi_1 - \phi_2| \ll \pi/2$. In this case, the alternating component of intensity I_h is proportional to the amplitude of the elastic wave. A speckle pattern is absent.

In the case of transverse waves, the situation is different. Here, the contribution to the phase of reflection of the rays 1 and 2 depends on the details of the surface structure: $\phi_{s1,2} = \frac{4\pi}{\lambda}u_0\cot\alpha_{1,2}\cos\omega_s t$. Since the amplitude of elastic waves is small, $\frac{4\pi}{\lambda}u_0 \ll 1$, and $|\cot\alpha_{1,2}| \leq 1$, the phase difference $\delta = \phi_{s1} - \phi_{s2}$ is small, $|\delta| \ll 1$. In this approximation, from Eq. (3) we obtain

$$I = I_0 + 2[I_r(I_f + I_h)]^{1/2}(1 + \delta\kappa)\cos(\phi_{s1} + \phi_t), \tag{5}$$

where

$$\kappa = \frac{A_{fo(1)}A_{fo(2)}\sin(\phi_2 - \phi_1)}{(I_f + I_h)^{1/2}}, \quad \tan\varphi_1 = \tan\varphi - \delta\frac{A_{fo(2)} + A_{fo(1)}\cos(\phi_2 + \phi_1)}{[A_{fo(1)}\cos(\phi_r - \phi_1) + A_{fo(2)}\cos(\phi_r - \phi_2)]^2},$$

and the angle φ is determined by Eq. (4). By tuning the interferometer, it is possible to obtain $\varphi_t \approx 0$. We take into account that $\delta = \frac{4\pi}{\lambda}u_0(\cot\alpha_2 - \cot\alpha_1)\cos\omega_s t$. In the accepted approximation of small wave amplitudes, the alternating component of intensity is

$$\begin{aligned} I_{\sim} &\sim \frac{8\pi u_0}{\lambda}I_r^{1/2}(I_f + I_h)^{1/2} \\ &\quad \times \cot\alpha_1\left[\cos\omega_s t + \frac{4\pi u_0}{\lambda}\kappa(\cot\alpha_1 - \cot\alpha_2)\cos^2\omega_s t\right]. \end{aligned} \tag{6}$$

It is necessary to average Eq. (6) over the beam cross-section to obtain the contribution of the whole laser beam to the intensity. Then, the factor $\cot\alpha_1$ will be replaced by the averaged quantity $\langle|\cot\alpha_1|\rangle \approx \Delta hN$. The alternating component in Eq. (6) depends on the surface structure and demonstrates speckles in the scanned reflections. Note that, in addition to the harmonic component, the signal contains a component $\sim\cos^2\omega_s t$, which leads to distortions of the radio pulse

shape and to its asymmetry. The time dependence of the amplitude (the A-scan) in the case of transverse waves contains low-frequency components. A typical oscillogram is given in Fig. 7. The interval 4.5–6.5 μs corresponds to quasi-transverse waves. In order to understand the origin of the low-frequency components, it is necessary to recall that the excitation is performed by a pulsed signal. The partial amplitude $A_{f0(i)}$ of the wave reflected from the ith point of the reflecting surface of the sample is expressed by the product of the spectral density $S(\Omega)$ by the local value of the reflection coefficient $R_{(i)}$: $A_{f0(i)} = S(\Omega)R_{(i)}$. The spectrum of a train of radio pulses contains spectral components with the frequency Ω proportional to the repetition frequency F of the radio pulses. The major part of the pulse energy is concentrated within the spectral interval of width $2/\tau$ centered at the carrier frequency of the radio pulses. This interval contains $2/F\tau$ spectral components. We restrict our consideration to two spectral components for the sake of simplicity. In this case, the expression for the amplitude of the wave reflected from the sample takes the form

$$\begin{aligned} A_f &= A_{f0(1)}\exp[i(\phi_1 + \phi_{s1})] \\ &+ A'_{f0(1)}\exp[i(\phi_1 + \phi'_{s1})] \\ &+ A_{f0(2)}\exp[i(\phi_2 + \phi_{s2})] + A'_{f0(2)}\exp[i(\phi_2 + \phi'_{s2})], \end{aligned}$$

where the subscripts (1) and (2) refer to the two selected rays. The terms proportional to $A_{f0(i)}$ and $A'_{f0(i)}$ belong to the spectral components of a pulse of the elastic wave with different frequencies; they introduce the phases ϕ_{si} and ϕ'_{si}. Calculating (as above) the intensity $I = A_t A_t^*$ and restricting ourselves to considering only the low-frequency terms with the difference frequencies, we obtain

$$\begin{aligned} I_{lf} \approx 2\{&[(A_{f0(1)}A'_{f0(1)} + A_{f0(2)}A'_{f0(2)}) \\ &+ (A_{f0(1)}A'_{f0(2)} + A_{f0(2)}A'_{f0(1)})\cos(\phi_1 - \phi_2)]^2 \\ &+ (A_{f0(1)}A'_{f0(2)} - A_{f0(2)}A'_{f0(1)})^2\sin^2(\phi_1 - \phi_2)\}^{1/2}. \end{aligned} \quad (7)$$

The amplitude of the spectral component of intensity I_{lf}, which corresponds to the difference frequency $\Omega_1 - \Omega_2 = (n_1 - n_2)F$, is proportional to $2[A^2_{f0(1)} + A^2_{f0(2)} + 2A_{f0(1)}A_{f0(2)}\cos(\phi_1 - \phi_2)]$. One more source of low-frequency signals at the interferometer output is the interaction of the spectral components of the reference signal and the signal reflected from the sample. The spectral component $A_{r0}\exp[i(\phi + \Omega_r t)]$ of the reference signal combined with the component $A_{f0(i)}\exp[i(\phi_i + \Omega_{s(i)}t)]$ reflected from the ith point of the sample leads to the intensity component with the frequency $\Omega_{s(i)} - \Omega_r$ and the amplitude proportional to $A_{f0(i)}A_{r0}\cos(\phi_i - \phi_r)$. Thus, the alternating component of the intensity of transverse waves contains a low-frequency component

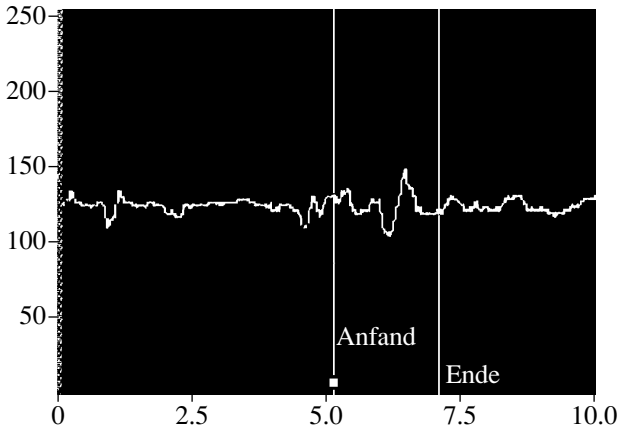

Fig. 7. Oscillogram of oscillations in a single crystal with the orientation at 1.5° to the [111]-axis; the excitation by a transverse wave transducer.

which depends on the product $u_0\langle\cot\alpha\rangle$. The C-scan obtained with the help of the laser interferometer reflects both the distribution of the elastic field and the roughness of the reflecting surface.

The above analysis is needed only to qualitatively demonstrate the presence of the interferometer signal and its connection with the amplitude of the elastic wave as applied to a shear wave in the conditions of the internal conical refraction. For a quantitative comparison of the results with the experiment, in addition to averaging Eqs. (6) and (7), it is necessary to take into account the interference with the longitudinal component of elastic displacements, which is considerable for the lateral rays of the beam. At the same time, there is no need to account for the variation of the delay time of the pulse over the beam cross-section because of the small width of the laser beam $d \ll \lambda$.

In conclusion, we summarize the main results of this work. The distributions of the elastic fields in an aluminum single crystal are obtained by the laser interferometry technique. The distribution of the elastic energy within a wide sector shifted from the radiator projection is observed in the conditions of the internal conical refraction. The sector area far exceeds the area of the piezoelectric radiator. The deflection of the central beam through 1.5° from the [111] axis distorts the energy distribution, and the deflection through 5° leads to a radical change in the distribution pattern. In the latter case, the internal conical refraction is absent. The response of the laser interferometer to the displacements of the reflecting surface due to a normally incident transverse wave is analyzed. The effect of roughness of the reflecting surface and the presence of rays widely deflected from the normal in the conditions of internal conical refraction are taken into account. It is demonstrated that the response of the laser interferometer is proportional to the amplitude of elastic displacements multiplied by the average (over the cross-section

of the laser beam) value of the absolute value of the cotangent of the angle between the beam and the tangent to the surface. The interferometer response to transverse waves contains low-frequency components with the frequencies much lower than the carrier frequency of the pulse of the ultrasonic wave.

ACKNOWLEDGMENTS

The work is supported by the Russian Foundation for Basic Research and the German Research Society. We are grateful to M. Kröning for the opportunity to conduct the measurements with the equipment that belongs to the Institute of Nondestructive Testing and to B. Köler for his assistance in the measurements.

REFERENCES

1. A. G. Khatkevich, Kristallografiya **31**, 629 (1986) [Sov. Phys. Crystallogr. **31**, 371 (1986)].
2. V. I. Al'shits and A. L. Shuvalov, Kristallografiya **29**, 629 (1984) [Sov. Phys. Crystallogr. **29**, 373 (1984)].
3. J. de Klerk and M. I. P. Musgrave, Proc. Phys. Soc. London, Sect. B **68** (422), 81 (1955).
4. V. I. Anisimkin and A. I. Morozov, Fiz. Tverd. Tela (Leningrad) **17**, 3006 (1975) [Sov. Phys. Solid State **17**, 1994 (1975)].
5. J.-P. Monchalin *et al.*, J. Nondestruct. Eval. **8** (2), 121 (1989).
6. A. Bayon and P. N. J. Rasolofosaon, J. Acoust. Soc. Am. **99**, 954 (1996).
7. H. Nakano, Y. Matsuda, and S. Nagai, Ultrasonics **37**, 257 (1999).
8. R. A. Artman, J. Acoust. Soc. Am. **33**, 493 (1966).
9. I.-P. Monchalin and R. Heon, Mater. Eval. **44**, 1231 (1986).
10. M. B. Vinogradova, O. V. Rudenko, and A. P. Sukhorukov, *The Theory of Waves* (Nauka, Moscow, 1979).
11. R. Truell, C. Elbaum, and B. B. Chick, *Ultrasonic Methods in Solid State Physics* (Academic Press, New York, 1969; Mir, Moscow, 1972).

Translated by M. Lyamshev

Acoustical Physics, Vol. 47, No. 1, 2001, pp. 85–92. Translated from Akusticheskiĭ Zhurnal, Vol. 47, No. 1, 2001, pp. 101–109.
Original Russian Text Copyright © 2001 by Kryazhev, Kudryashov.

Spatial Structure of the Coherence Parameter of the Sound Field in an Irregular Arctic Waveguide

F. I. Kryazhev and V. M. Kudryashov

Andreev Acoustics Institute, Russian Academy of Sciences, ul. Shvernika 4, Moscow, 117036 Russia
e-mail: bvp@akin.ru

Received July 5, 1999

Abstract—Results of numerical simulation of the total and coherent sound fields and the coherence parameter for a multimode acoustic signal excited by a monochromatic sound source and propagating in an irregular arctic waveguide are presented. Expressions used as the basis for the algorithm of the sound field calculation by the method of coupled normal modes are given. Both regular and stochastic sound scattering by horizontal inhomogeneities of the bottom, water medium, and ice cover are taken into account. It is found that, in the course of sound propagation in an arctic waveguide, an anomalous variation of the energy coherence parameter of the sound field as a function of distance is observed. This variation manifests itself in the form of local peaks of the field coherence parameter. This fact should be taken into account in both the measurements of the ice cover characteristics by acoustic methods and the evaluation of the efficiency of the operation of receiving arrays.
© 2001 MAIK "Nauka/Interperiodica".

Long-range sound propagation in an underwater waveguide is accompanied by sound scattering from the horizontal inhomogeneities of the waveguide [1–4]. These inhomogeneities are commonly divided into stochastic and regular ones. Regular inhomogeneities are smooth and large-scale in character (the horizontal scale is within tens or hundreds of kilometers). They can be described by piecewise-analytical functions. The sound field scattered by them has a distinct phase structure. Regular scattering takes part in the formation of the coherent component $\langle p(\mathbf{r}, z, t)\rangle$ of the sound pressure $p(\mathbf{r}, z, t)$. Here, $\mathbf{r} = \mathbf{e}_x x + \mathbf{e}_y y$; x, y, z are the Cartesian coordinates with the z axis directed downwards and originating ($z = 0$) at the free water surface; t is time; and the angular brackets mean the operation of statistical averaging over the statistical ensemble of stochastic scatterers.

Stochastic inhomogeneities, when considered within sufficiently long parts of the waveguide, are adequately described by the statistical theory. The sound pressure component formed as a result of the scattering by these inhomogeneities, $\tilde{p}(\mathbf{r}, z, t)$, is called the stochastic component. The coherence parameter is determined by the ratio

$$K_i = |\langle p(\mathbf{r}, z, t)\rangle|^2 / \langle |p(\mathbf{r}, z, t)|^2\rangle \quad (1)$$

and characterizes the degree of coherence of the sound field. By virtue of the statistical independence of coherent and stochastic pressures, we have

$$\langle |p(\mathbf{r}, z, t)|^2\rangle = |\langle p(\mathbf{r}, z, t)\rangle|^2 + \langle |\tilde{p}(\mathbf{r}, z, t)|^2\rangle.$$

The coherence parameter is usually introduced for a sound field excited by a harmonic source. This field has interference spatial fluctuations about the average level, which is called the energy level. The horizontal (with respect to $\mathbf{r}$) scale of the interference fluctuations (the distance between the neighboring minimums or maximums of the interference pattern [2, 5]) is approximately equal to the ratio of the average wavelength of the wave cycle forming the sound field at a given interval of the sound propagation track to the number of these waves. The energy level of the sound field is obtained as a result of averaging of the magnitude of the squared sound pressure over the coordinate $\mathbf{r}$ within a track part that covers an interval of distances $\Delta\mathbf{r}$ exceeding several interference scales.

The quantity K_i fluctuates in accordance with the interference variations of the levels of $|\langle p(\mathbf{r}, z, t)\rangle|^2$ and $\langle |p(\mathbf{r}, z, t)|^2\rangle$. Therefore, we introduce the concept of the energy coherence parameter K_e, which is determined by the formula of the type of Eq. (1), but with the magnitudes of the squared sound pressures for the coherent and total sound fields being replaced by their energy values. The stochastically scattered component of sound pressure usually plays the role of interference in acoustic measurements. Since $\tilde{p}(\mathbf{r}, z, t)$ carries certain information on the source of sound, it can be used, e.g., to reveal the fact of the presence of an operating radiator, which is an example of effective utilization of the stochastically scattered component of the field.

Monitoring of a signal from a sound source can be performed at a single point of reception (by a single hydrophone). However, spatially extended receiving systems (arrays) are used in practice [6, 7]. If a horizontal linear array is located in the far wave zone of a radiator, the array can be rotated (or compensated) in such way that it will be positioned along the phase front of the coherent field, which corresponds to the maximum

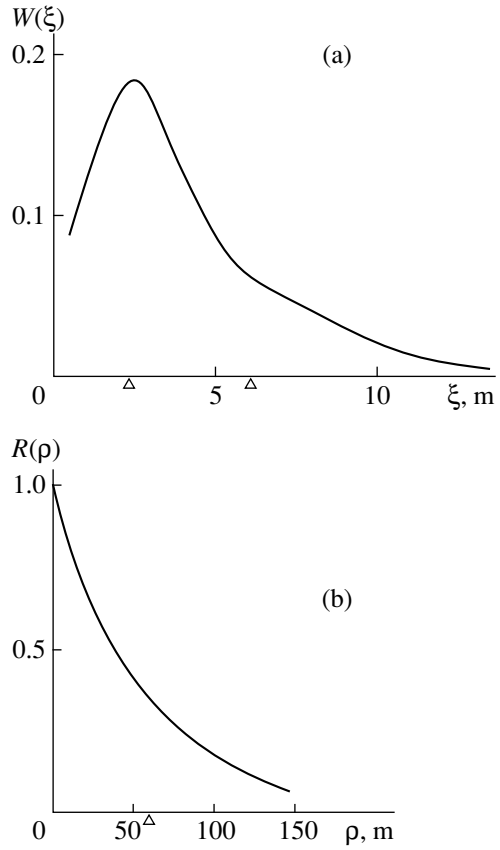

Fig. 1. (a) Probability density of draught for the lower surface of the ice cover. (b) Normalized correlation function of roughness of the lower ice surface.

of the array directivity pattern and to the maximal signal amplification for the coherent component of the field. In this case, the stochastic component of sound pressure at the array aperture also fluctuates in phase in a wide range with the horizontal correlation scale ρ. In arctic sound channels at frequencies up to 100 Hz, the correlation scale ρ has the order of magnitude from several tens up to one hundred meters [8]. If the length L of the array far exceeds ρ, the array amplification for the stochastic component is L/ρ times less than for the coherent one and the stochastic component itself, which has a random phase, plays the role of interference like the noise field of the medium. The maximal increase in the ratio $|\langle p(\mathbf{r}, z, t)\rangle|^2/\langle|\tilde{p}(\mathbf{r}, z, t)|^2\rangle$ at a linear array can attain the value equal to the number of hydrophones in the linear array. A method of separation of the coherent field from the total field with the help of an array is grounded on this fact [8, 9, 10]. Knowing the response of an array to the total field with strong suppression of the stochastically scattered component and knowing the level of the signal at a single hydrophone, one can measure the coherence parameter. If the monitored object moves along the sound propagation track, the energy coherence parameter can be measured by averaging the signal over the time interval during which the signal passes through several interference maximums.

The practical significance of the energy parameter of coherence lies in the fact that it provides an opportunity to evaluate the efficiency of the array operation in the field of the signal containing a stochastically scattered component. We should note that the majority of papers concerned with stochastic scattering in a sound channel do not consider the coherence parameter of the field.

In an arctic sound channel, temporal variations in the medium of sound propagation are fairly weak. One can discuss only the effect of spatial averaging of stochastically scattered sound on long propagation tracks at low (up to several hundreds of hertz) frequencies of sound by using the spatial analog of an ergodic theorem, which allows one to replace averaging over the ensemble of rough boundaries by spatial averaging over a single realization [11].

This paper considers the stochastic scattering of sound only by the rough ice cover. This roughness is assumed to be statistically homogeneous and isotropic within sufficiently long regions of the ice cover (with the length about tens and hundreds of kilometers). Histograms of the displacements of the ice–water interface are plotted on the basis of experimental data, from which the probability density functions are obtained for the ice draught relative to the zero level (Fig. 1a), and the spatial correlation functions of roughness are determined (Fig. 1b). In calculating the characteristics of the sound field, we use the model of floating ice [12, 13]. The relation between the roughness characteristics of the upper and lower ice boundaries can be found in [12–14].

In the stochastic component of the field, first, we have the accumulation of sound energy (in the case of the modal representation of the sound field) in the energy component $\langle|\tilde{p}(\mathbf{r}, z, t)|^2\rangle$ and the suppression of the interference component of the stochastic component.

Second, scattering leads to a redistribution of sound energy between the modes.

If we ignore the backscattering of sound or take it into account under the approximation of multiple forward scattering and single backscattering [15, 16], the spatial variability of the mode intensity of the total field can be described in the framework of the transfer equation [1, 16, 17].

Regular sound scattering by horizontal inhomogeneities of the waveguide has been much studied theoretically [18–20]. We take it into account in the framework of the "stepwise" model [18–20] under the assumption that the variations in the waveguide depth and in the vertical profile of sound velocity occur rather slowly, i.e., they have small gradients in **r**, and the parameters of the eigenfunctions of the waveguide vary only weakly within the intervals of distances

about the wave cycle length. We attribute all small-scale variations in the waveguide parameters to the class of stochastic scatterers.

We consider the regular scattering of waves according to the next scheme: vertical modes experience horizontal refraction determined by the mode rays [18]. Mode rays lie in the horizontal plane and are described by an equation analogous to the eikonal equation [2, 5] for common rays, but, on the right-hand side of the equation, the longitudinal wave number of a mode $\zeta_m(\mathbf{r})$, where m is the mode number, stands instead of the wave number of the medium. This means that mode rays can be constructed according to the common ray algorithm. If the track between the sound source and the observation point deviates only slightly from the direction of the vector of the general variation of the regular parameters of the medium, the horizontal refraction of mode rays is weak, since the bend points of these rays correspond to the values of $\zeta_m(\mathbf{r})$ close to zero, and such waves cannot exist in a real waveguide, because $|\Delta\zeta_m(\mathbf{r})| \ll |\zeta_m(\mathbf{r})|$ for all trapped modes.

We represent the sound pressure as a superposition of $M(\mathbf{r})$ modes:

$$p(\mathbf{r}, z, t) = \sum_{m=1}^{M} P_m(\mathbf{r}, t)\Phi_m(z), \tag{2}$$

where $\Phi_m(z)$ is the eigenfunction of the reference waveguide [5] at the distance $\mathbf{r}$, which corresponds to the wave number $\zeta_m(r)$. We have for the coherent field

$$\langle p(\mathbf{r}, z, t)\rangle = \sum_{m=1}^{M} \langle P_m(\mathbf{r}, t)\rangle\Phi_m(z). \tag{3}$$

If the condition

$$P_{\substack{r\to 0\\ z\to z_0}}(\mathbf{r}, z, t) = \frac{\exp[ik_0(r^2 + (z-z_0)^2)^{1/2} - i\omega t]}{(r^2 + (z-z_0)^2)^{1/2}}$$

is valid near a point sound source ($r = 0$, $z = z_0$), then, in the adiabatic approximation, we can take [18]

$$P_m(\mathbf{r}, z) = i\pi\Phi_m(z_0)H_0^{(1)}\left(\int_0^{\mathbf{r}}\zeta_m(\eta)d\eta\right)\exp(-i\omega t). \tag{4}$$

Here, $K_0 = \omega/c(0, z_0)$, $\omega = 2\pi f$, f is the sound frequency, and $c(r, z)$ is the sound velocity in water. In an irregular waveguide, we use the expression

$$P_m(\mathbf{r}, z) = C_m(\mathbf{r})\zeta_m^{-1/2}(r)\exp(-i\omega t). \tag{5}$$

It is easy to verify that $|C_m(\mathbf{r})|^2$ describes the energy flux in a mode through the waveguide cross-section in the horizontal direction along the mode ray.

If we assume that, for the modes forming the sound field at observation points along the sound propagation track, the horizontal refraction of mode rays is expressed weakly, we can replace the initial model of the waveguide by a stepwise working model; i.e., we can divide the waveguide along the track into segments, within which the waveguide parameters do not change, and they change in steps at the segment boundaries. It is assumed that a step is sufficiently small for the sound field in the new model not to differ significantly from the sound field calculated for the initial model. In our code, this fact was taken into account automatically by the algorithm that determined the segment length. In the working model, the sound field within a segment is calculated by a common code for a plane-layered waveguide, which allows for stochastic scattering [15, 16]. The sound field at the segment boundaries is matched by the conditions of continuity of the sound pressure and the longitudinal component of the vector of particle velocity and controlled by the condition of continuity of the total sound energy flux through the waveguide cross-section.

The eigenfunctions $\Phi_m(z)$ of the waveguide constitute a complete orthonormalized set. We write the condition for the mode normalization in the form

$$[\mu(z)\Phi_m(z)\Phi_n(z)] = \delta_{mn}, \tag{6}$$

where δ_{mn} is the Kronecker delta and $\mu(z)$ is the relative density of the medium. In the waveguide, we have

$$[\mu(z)\Phi_m(z)\Phi_n(z)] = \int_{-\infty}^{\infty}\mu(z)\Phi_m(z)\Phi_n(z)dz. \tag{7}$$

If in the neighboring segments of the waveguide condition (6) is not valid for some modes, a mutual transformation (scattering) of these modes occurs. Indeed, according to the condition of continuity of sound pressure on both sides of the step

$$P^{(+)}(\mathbf{r}, z, t) = P^{(-)}(\mathbf{r}, z, t),$$

where the plus sign corresponds to the "after" state and the minus sign corresponds to the "before" state, we obtain

$$\sum_n P_n^{(-)}(\mathbf{r}, t)\Phi_n^{(-)}(z) = \sum_m P_m^{(+)}(\mathbf{r}, t)\Phi_m^{(+)}(z).$$

We multiply both sides of this equality by $\mu(z)\Phi_N^{(+)}(z)$ and perform the operation of normalization. We obtain

$$P_N^{(+)}(\mathbf{r}, t) = \sum_n P_n^{(-)}(\mathbf{r}, t)[\mu(z)\Phi_n^{(-)}(z)\Phi_N^{(+)}(z)]. \tag{8}$$

Similarly, from the condition of continuity of the particle velocity, we obtain

$$P_N^{(+)}(\mathbf{r}, t) = \sum_n \frac{\zeta_n(\mathbf{r})}{\zeta_N(\mathbf{r})}P_n^{(-)}(\mathbf{r}, t)[\mu\Phi_n^{(-)}\Phi_N^{(+)}]. \tag{9}$$

Using Eqs. (6), (8), and (9), at the step we obtain

$$P_N^{(+)}(\mathbf{r}, t) = \sum_n \frac{\zeta_n + \zeta_N}{2\sqrt{\zeta_n \zeta_N}} [\mu \Phi_n^{(-)} \Phi_N^{(+)}] P_n^{(-)}(\mathbf{r}, t), \quad (10)$$

where the term at the right before $P_n^{(-)}$ is the coefficient of regular transformation of modes $D_{nN}^{(\mathbf{r})}$.

Stochastic scattering occurs within the limits of the plane-layered segment. We assume that, in the vicinity of the step, the parameters of the waveguide coincide with those of a waveguide without stochastic roughness. For a plane-layered segment of the sound channel, we solve the next equation for the total field:

$$\mathbf{e}_r \nabla |C_N(\mathbf{r})|^2 = -2 \mathrm{Jm}\, \zeta_N(\mathbf{r}) |C_N(\mathbf{r})|^2 + \sum_{n=1}^{M} |C_n(\mathbf{r})|^2 B_{nN}(\mathbf{r}), \quad (11)$$

where $\mathbf{e}_r$ is the unit vector directed along the direction of wave propagation. The coefficient of stochastic scattering along the energy flux B_{nN} has been considered in [11, 21].

Equations (10) and (11) form the basis of the algorithm for calculating the total and coherent sound fields, the coherent field obeying the condition

$$\mathrm{Jm}\, \zeta_N(\mathbf{r}) = \mathrm{Jm}\, \zeta_N^0(\mathbf{r}) + 0.5 \sum_{n=1}^{M} B_{nN}(\mathbf{r}), \quad (12)$$

where $\mathrm{Jm}\, \zeta_N^0$ is the imaginary part of the wave number in the waveguide without stochastic scatterers.

There are no inflow of energy into the resulting sound fields and no loss of energy from them at the transition through the step, and this allows one to control the possible error of calculation by the condition of continuity of the total energy fluxes through the waveguide cross-section.

The energy level of the sound fields corresponds to the relationships

$$\langle |p(\mathbf{r}, z, t)|^2 \rangle = \sum_{m=1}^{M} \langle |P_m(\mathbf{r}, t)|^2 \rangle |\Phi_m(z)|^2$$

and

$$|\langle p(\mathbf{r}, z, t) \rangle|^2 = \sum_{m=1}^{M} |\langle P_m(\mathbf{r}, t) \rangle|^2 |\Phi_m(z)|^2,$$

and the interference value of the total field is determined by the relationship

$$\langle |p(r, z, t)|^2 \rangle = \sum_{m=1}^{M} \langle |P_m(\mathbf{r}, t)|^2 \rangle |\Phi_m(z)|^2 + \sum_{m=1}^{M} \sum_{n \neq m n=1}^{M} \langle P_m(\mathrm{r}, t) \rangle \langle P_n(\mathbf{r}, t) \rangle^* \Phi_m(z) \Phi_n^*(z). \quad (13)$$

The anomalies of propagation of the total and regular fields are calculated along with these quantities. These anomalies are equal to $10 \log(\langle |p(\mathbf{r}, z, t)^2 \rangle / r^2)$ and $10 \log(|\langle p(\mathbf{r}, z, t) \rangle|^2 r^2)$. The anomalies of sound propagation do not depend on the power of the sound source, i.e., the result of anomaly calculation can easily be recalculated for the source of any power.

The energy coherence parameter is determined by the expression

$$\mathrm{K_e} = \left(\sum_{m=1}^{M} |\langle P_m(\mathbf{r}, t) \rangle|^2 \times |\Phi_m(z)|^2 \right) \Big/ \left(\sum_{m=1}^{M} \langle |P_m(\mathbf{r}, t)|^2 \rangle |\Phi_m(z)|^2 \right). \quad (14)$$

We calculate the sound fields and the coherence parameter using the code developed by Kudryashov.

Let us consider some results of sound field calculations. The ice cover is an elastic body, which has the velocity of longitudinal waves equal to 3500 $(1 - i0.04)$ m/s, the velocity of shear waves equal to 1800 $(1 - i0.04)$ m/s, and the ice density relative to that of water equal to 0.91. Inhomogeneities of the ice–water interface and their correlation function are given in Figs. 1a and 1b. It follows from these plots that the average thickness of the ice cover is 4 m and the rms deviation σ of the rough lower ice boundary from the average level is equal to 2.91 m. The roughness of the upper ice boundary is characterized by $\tilde{\sigma} = 0.73$ m. The code permits a piecewise change of the parameters of the ice cover along the track. At the segment of the sound propagation track where the change of the sound channel depth occurs and which imitates the coastal slope, we consider the ice cover as statistically homogeneous and smooth with an average thickness of 2 m, $\sigma = 1.2$ m, $\tilde{\sigma} = 0.3$ m, and the horizontal correlation scale of roughness $\rho_0 = 75$ m. According to Fig. 1b, within the deep-water segment, $\rho_0 = 57$ m. We assume the bottom to be elastic with the velocity of longitudinal waves being 1850 $(1 - i0.01)$ m/s, the velocity of transverse waves 350 $(1 - i0.01)$ m/s, and the relative density $\mu = 1.8$.

The propagation track consists of two main parts: the part with a constant depth of 2500 m and the part where the depth changes linearly with distance from 2500 to 450 m and the sound velocity changes from the

deep-water profile to a constant value in shallow water. The latter part is located either after the deep-water part or before it.

In this paper, we do not intend to perform the calculation by a model that is close to some specific case. An example of such calculation was given in [12]: the signal propagation along the track 2650 km long was calculated for a frequency of 20 Hz at which the level of the total field differed little from the coherent one.

In this paper, the calculation is conducted for a monochromatic sound signal with the frequency 90 Hz, which propagates along a track with the length of the deep-water part 500 km and the length of the irregular part 60 km. The source depth is 50 m. The reception is performed at a depth of 50 m. In these conditions, it is possible to observe a combined effect of both stochastic and regular scattering of sound on the sound field.

The coherence parameter in a deep-water sound channel usually decreases monotonically with distance. In an arctic waveguide, the change of the coherence parameter of the sound field with distance is nonmonotone because of the singularity in the distribution of sound velocity in water with depth and the presence of the ice cover. The sound field in a deep-water arctic waveguide is formed by two groups of modes. The first group is concentrated in the water layer lying next to the ice cover over the layer of Atlantic waters. These modes have small cycle lengths and large coefficients of attenuation and stochastic scattering. The second group of modes refracts below the layer of the Atlantic waters. They have greater cycle lengths and small coefficients of attenuation and stochastic scattering. The ratios of these quantities for a sound channel with the depth 2500 m are approximately one to five. Therefore, within the deep-water part of the track, the process of leveling of the mode energy fluxes in the stochastically scattered component of the sound field can occur slower than the attenuation of the modes of the first group. As a result, an inflection appears in the plot of the energy coherence parameter K_e as a function of r [22]. At first, K_e decreases with increasing r at initial distances where the sound field is formed by the waves of the first group (if the radiator and the observation horizon lie in the layer adjacent to the ice). As r increases, we enter the region where the waves of the first group are strongly attenuated, and the main contribution to the sound field is made by the waves of the second group. The parameter K_e attains the local minimum in the transition region; then, the coherence parameter of the field increases and, then, monotonically decreases with further distance growth. In this situation, the waves reflected from the bottom almost do not affect the parameter K_e. If the observation horizon lies deeper than the layer adjacent to the ice, K_e monotonically decreases with distance from the source. The transition from the deep-water part of the sound channel to the irregular part, where the depth decreases monotonically with distance and the vertical profile of the sound velocity transforms into a constant velocity with the increase in r, is often accompanied by an increase in the coherence parameter. Then, the region of decrease in K_e with the growth of r begins. A situation is possible when, within the deep-water part of the track, K_e is constant or decreases as r increases. The appearance of the region of local increase in K_e approximately coincides with the appearance of the local maximum of the anomaly of sound propagation. In practice, this fact means that zones of enhanced and reduced audibility for the useful signal are present in the coastal slope region, especially if one takes into account that the spatial variability of the level of the noise interference produced by the medium obeys almost the same laws as the stochastic component (this fact will be studied separately).

Figure 2 presents (*1*) the plot of the dependence of the coherent sound pressure level (in dB) on the distance in a deep-water sound channel and (*2*) the energy level of the sound pressure. One can see that the energy level almost coincides with the distance-average level of the sound field (on the interval exceeding the period of interference fluctuations of sound pressure).

Figure 3 shows the dependence of the propagation anomaly for (*1*) the total and (*2*) coherent sound fields for a propagation track starting with a shallow-water part. Within the shallow-water part, the total field almost coincides with the coherent field, which is caused by weak sound scattering by an area of smooth ice cover. The transition to the deep-water part of the sound channel with a thick and rough ice cover is accompanied by the accumulation of sound energy in the stochastically scattered component of the field. The change in the coherence parameter K_e in this case is shown in Fig. 4. In the shallow-water region, the value of K_e is close to unity. Then, starting from a distance of 60 km, the decrease in the coherence parameter K_e with distance occurs at the place of transition to the deep-water region. The part of the sound channel where the anomalous variation of K_e with the local maximum occurs begins at a distance of approximately 350 km. The rise of such a maximum is possible on the deep-water propagation track because of the reasons discussed earlier. This maximum manifests itself most distinctly when the track begins in the deep-water region.

Figure 5 presents the change of the coherence parameter of the sound field at a frequency of 90 Hz in a homogeneous (along the track) arctic waveguide with the depth 3500 m. The depths of transmission and reception are the same: 50 m. The parameters of the ice cover are the same as in the case of the waveguide 2500 m deep. Circles present the experimental values of the coherence parameter for the same frequency in the case of the signal reception by a horizontal array; these data were obtained in the experiment at the SP-13F station.

In the experiment, the correlation coefficient of the sound field was determined for the case of receiving elements separated in the horizontal plane, perpendicu-

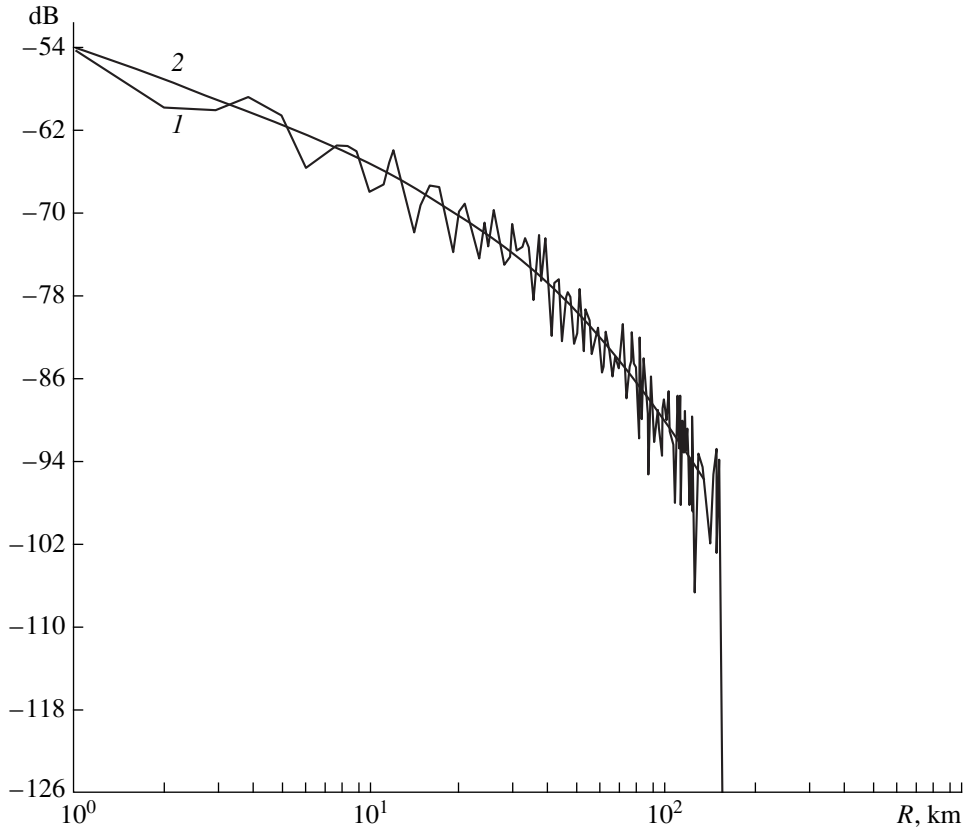

Fig. 2. Coherent sound pressure versus the distance in a deep-water sound channel: (*1*) interference level and (*2*) energy level.

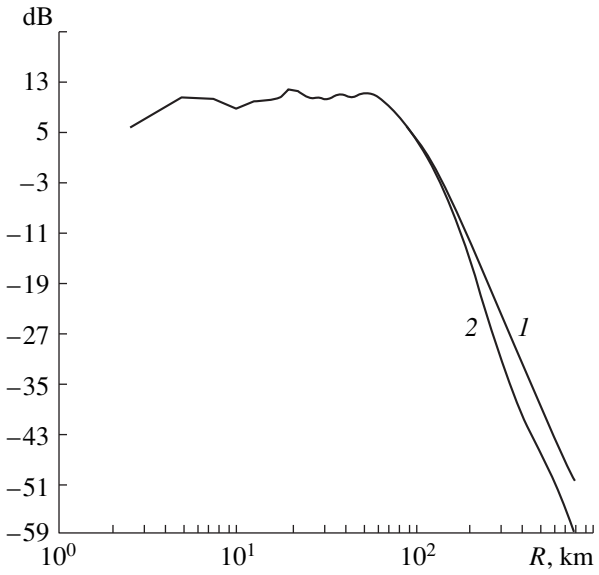

Fig. 3. Propagation anomaly on the propagation track beginning in the shallow-water region: (*1*) total field and (*2*) coherent field.

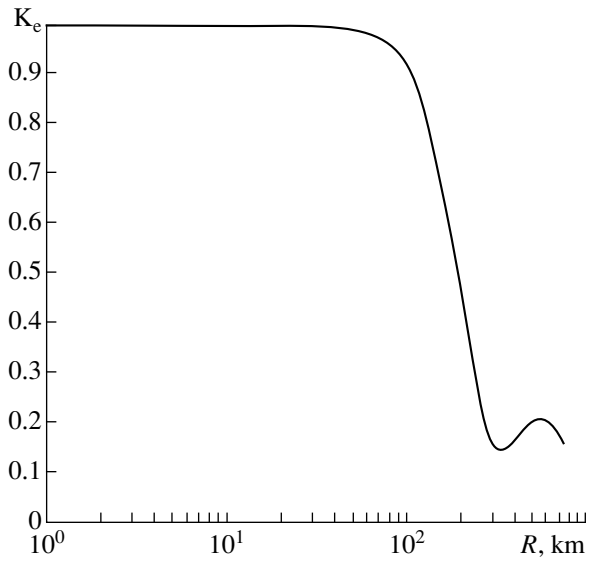

Fig. 4. Coherence parameter of the field on the propagation track beginning in the shallow-water region.

larly to the direction toward the sound source. In the case of increasing distance between the reference receiver and the receiving elements of the array, the correlation coefficient of the sound field decreases from unity to a certain value depending on the distance to the sound source and the frequency; with further increase in the distance between the reference receiver and the array elements, the correlation coefficient remains

almost constant. This provides an opportunity to determine the difference between the coherent component of the field and the total field by the value of the correlation coefficient of the sound field with allowance for the scattered component. Therefore, it is possible to determine the coherence parameter of the field according to the intensity ratio of the coherent component of the field to the total field.

Analyzing the data given in Fig. 5, we first notice the good agreement of experimental and calculated values of the coherence parameter of the field. Second, one can see that the value of the coherence parameter of the field in this waveguide is greater than in the waveguide with the depth 2500 m (Fig. 4). Large values of the coherence parameter of the field in the 3500 m deep waveguide are caused by the fact that the cycle lengths are somewhat greater than those in the sound channel with the depth 2500 m, and, therefore, the coherent component of the field at the same distances is greater than in the waveguide with lesser depth.

Let us consider a propagation track beginning in a deep-water sound channel and ending in a shallow-water region. The interference pattern for this case is shown in Fig. 2. The dependence of the propagation anomaly on the distance is plotted in Fig. 6. One can see that, in the deep-water region, a distinct divergence of the levels of the total and coherent fields takes place, which persists also with the transition to shallow water. As one can see from Fig. 4, there is no accumulation of energy of the stochastically scattered component in shallow water. However, the energy already existing is retained, because the sound field cannot attenuate faster than with the attenuation coefficient of the coherent field. The increase in the propagation anomaly of both the total and coherent sound fields is observed approximately in the middle of the variable-depth part of the sound channel. After that, the anomalies decrease with distance, because the effects of sound attenuation start to dominate over a certain increase in the sound energy flux density due to the narrowing of the sound channel. With varying distance, both regular sound scattering and the change in the eigenfunctions of the sound channel play their roles. Figure 7 shows the dependence of the energy parameter of coherence K_e on distance for a waveguide starting with a deep-water part. The presence of the local maximum of K_e in the deep-water part of the track, at a distance of 350 km, can be seen distinctly in curve *1* corresponding to the track under consideration. The transition to shallow water is accompanied by the local maximum of K_e due to the regular transformation of modes and the related change in the ratio of sound intensities of the total and coherent sound fields at the observation horizon. Curve *2* corresponds to the calculation for a shortened track: the length of the deep-water part of the track is reduced to 100 km. Higher sound intensity at the beginning of the irregular part leads to a more distinct maximum of K_e in this region (120 km).

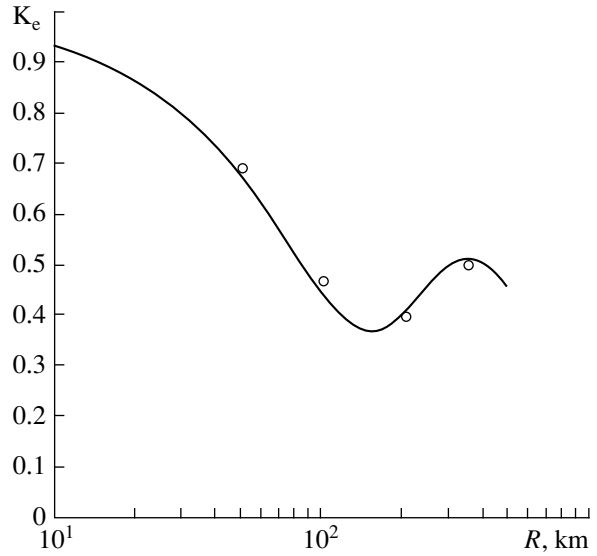

Fig. 5. Coherence parameter of the field in a sound channel with the depth 3500 m.

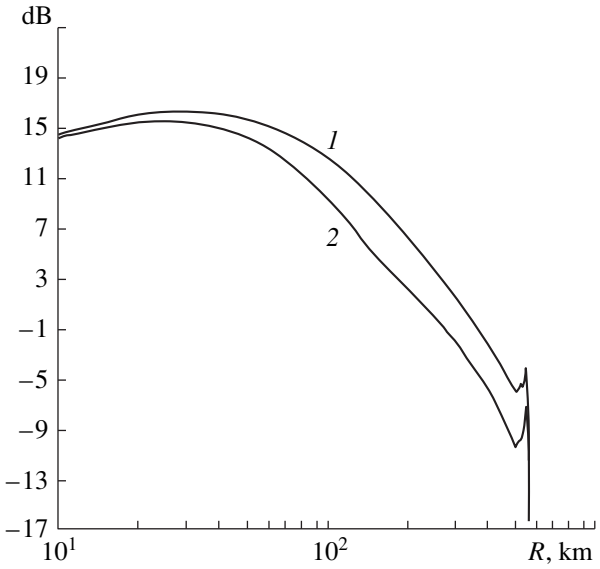

Fig. 6. Propagation anomaly on the propagation track beginning in the deep-water region: (*1*) total field and (*2*) coherent field.

In conclusion, we summarize the results:

(1) A code providing the calculation of the sound field with allowance for both regular and stochastic sound scattering in an arctic waveguide is developed; the waveguide is assumed to be inhomogeneous along the propagation track, and the ice cover roughness is represented by a two-scale model.

(2) It is found that, in the conditions of sound propagation along irregular arctic sound channels, the appearance of anomalous effects connected with stochastic sound scattering is possible.

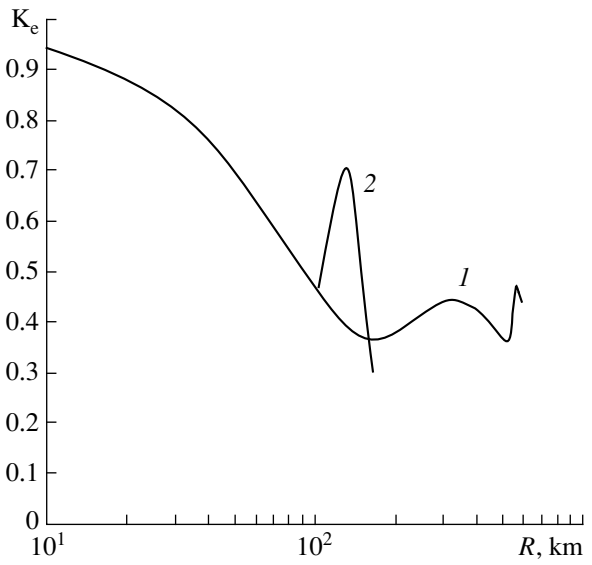

Fig. 7. Coherence parameter on the propagation track beginning in the deep-water region: the length of the deep-water part of the track is (*1*) 500 and (*2*) 100 km.

(3) The energy parameter of coherence of a monochromatic sound field decreases monotonically with distance. However, it can have local maximums in an arctic waveguide. This fact must be taken into account when estimating the state of the ice cover by acoustic data, as well as the efficiency of array operation.

ACKNOWLEDGMENTS

This work was supported by the Russian Foundation for Basic Research, project no. 99-02-18359.

REFERENCES

1. F. G. Bass and I. M. Fuks, *Wave Scattering by a Statically Rough Surface* (Nauka, Moscow, 1972).
2. L. M. Brekhovskikh and Yu. P. Lysanov, *Fundamentals of Ocean Acoustics* (Gidrometeoizdat, Leningrad, 1982; Springer, New York, 1991).
3. Yu. P. Lysanov, in *Ocean Acoustics*, Ed. by L. M. Brekhovskikh (Nauka, Moscow, 1974), pp. 232–330.
4. R. Berridge and H. Weinberg, in *Wave Propagation and Underwater Acoustics*, Ed. by J. B. Keller and J. S. Papadakis (Springer, New York, 1977; Mir, Moscow, 1980).
5. L. M. Brekhovskikh, *Waves in Layered Media* (Nauka, Moscow, 1973; Academic, New York, 1980).
6. G. S. Gabidulin, A. M. Tyurin, and V. I. Nesterenko, *Scanner Assemblies of Underwater Acoustic Means and Their Elements: Fundamentals of the Theory of Underwater Acoustic Scanner Assemblies* (Leningrad, 1982).
7. *A Handbook on Underwater Acoustics*, Ed. by A. E. Kolesnikov (Sudostroenie, Leningrad, 1988).
8. F. I. Kryazhev and V. M. Kudryashov, Akust. Zh. **30**, 790 (1984) [Sov. Phys. Acoust. **30**, 469 (1984)].
9. E. Yu. Gorodetskaya, A. I. Malekhanov, A. G. Sazontov, and V. A. Farfel', Akust. Zh. **42**, 615 (1996) [Acoust. Phys. **42**, 543 (1996)].
10. V. M. Kudryashov, in *Proceedings of the 5th Workshop "Acoustic Statistical Models of the Ocean," Moscow, 1985*, pp. 19–23.
11. V. M. Kudryashov, in *Representation Methods and Instrumental Analysis of Random Processes and Fields* (Leningrad, 1970), Vol. 3, No. 2, pp. 53–62.
12. V. M. Kudryashov, Akust. Zh. **42**, 438 (1996) [Acoust. Phys. **42**, 386 (1996)].
13. F. I. Kryazhev and V. M. Kudryashov, Akust. Zh. **43**, 203 (1997) [Acoust. Phys. **43**, 172 (1997)].
14. E. B. Chernyavskiĭ, Prom. Okeanolog. **9** (1), 71 (1971).
15. V. M. Kudryashov, in *Mathematical Problems in Geophysics* (Novorossiĭsk, 1973), Vol. 4, p. 256.
16. V. M. Kudryashov, in *Proceedings of the 4th Workshop "Acoustic Statistical Models of the Ocean," Moscow, 1982*, pp. 40–51.
17. M. J. Beran and S. Frankenthal, J. Acoust. Soc. Am. **100**, 1463 (1996).
18. R. Berridge and H. Weinberg, in *Wave Propagation and Underwater Acoustics*, Ed. by J. B. Keller and J. S. Papadakis (Springer, New York, 1977; Mir, Moscow, 1980).
19. V. M. Kudryashov, Akust. Zh. **33**, 55 (1987) [Sov. Phys. Acoust. **33**, 32 (1987)].
20. V. M. Kudryashov, Akust. Zh. **34**, 117 (1988) [Sov. Phys. Acoust. **34**, 63 (1988)].
21. V. M. Kudryashov, Akust. Zh. **42**, 247 (1996) [Acoust. Phys. **42**, 215 (1996)].
22. F. I. Kryazhev and V. M. Kudryashov, Vopr. Sudostr., Ser.: Akust., No. 10, 21 (1978).

Translated by M. Lyamshev

Acoustical Physics, Vol. 47, No. 1, 2001, pp. 93–101. Translated from Akusticheskiĭ Zhurnal, Vol. 47, No. 1, 2001, pp. 110–118.
Original Russian Text Copyright © 2001 by Maksimov.

Spectrum of Acoustic Radiation Caused by Cavitation: Analytical Model

A. O. Maksimov

Institute of Marine Technology Problems, Far East Division, Russian Academy of Sciences, ul. Sukhanova 5a, Vladivostok, 690600 Russia
e-mail: pacific@online.marine.su

Received January 27, 2000

Abstract—Nonlinear dynamics of bubbles in liquid in the presence of the resonance and noise acoustic fields is analyzed. The effect of fluctuations associated with the random field component is found to be most pronounced in the vicinity of the bifurcation values of the field amplitude and detuning, these values corresponding to changes in the number of stable oscillatory states of a bubble. The radiation spectrum of a single bubble in the vicinity of the fundamental resonance is determined. In the framework of the proposed model, a comparison of this spectrum with the real spectrum of acoustic radiation caused by cavitation is performed.
© 2001 MAIK "Nauka/Interperiodica".

The spectrum of the radiation caused by acoustic cavitation in liquid has the form of single lines rising above a noise base. The positions of the lines correspond to harmonics, subharmonics, and ultrasubharmonics of the excitation frequency. As an example, Fig. 1 shows the spectrum of the acoustic power generated by a cavitation region in liquid as a result of its excitation by a cylindrical piezoceramic transducer at a fundamental resonance frequency of 10 kHz [1]. The presence of single lines in the spectrum is related to the strongly nonlinear dynamics of single gas bubbles that occur in the field of an intense acoustic wave and experience a series of bifurcations of period doubling or even a transition to dynamic chaos [2–4]. The commonly accepted explanation for the presence of the noise base is the generation of short pulses accompanying the collapse of single inclusions [5–9].

Individual spectral lines of the cavitation radiation are characterized by a finite width and even by a definite shape. So far, the nature of these measurable characteristics has been poorly understood. The real spectrum of the acoustic pressure (Fig. 1) that causes fluctuations of single bubbles in the sheet noticeably differs from the spectrum used in theoretical calculations, which usually takes into account only the fundamental harmonic. A step toward the generalization of the conventional model was the inclusion of noise, i.e., the analysis of the nonlinear dynamics of a bubble in the field of an intense harmonic signal in the presence of a random component of much lower intensity [10].

In this case, in the Rayleigh–Plesset equation describing the radial fluctuations of a bubble

$$R\ddot{R} + \frac{3}{2}\dot{R}^2 + \frac{P_0}{\rho_0}\left[1 - \left(\frac{R_0}{R}\right)^{3\gamma}\right] + 2\delta R_0\dot{R} = -\frac{P - P_0}{\rho_0}, \quad (1)$$

only the expression for the external force P changes. Here, P_0, ρ_0, R_0, P, and R represent the equilibrium and current values of the pressure, the density of the liquid, and the bubble radius; γ is the polytropic index; and δ is the damping constant that allows for the viscous and thermal dissipation processes and the radiation damping.

The noise component is described by the additional term in the expression for the external field acting on the bubble $P(t) = P_0 + p_m\sin(\omega_p t) + p_N(t)$ (where $p_N(t)$ is the random component). To make the problem a closed one, it is necessary to describe the characteristics of the random force. We use the most simple force model in the form of a delta-correlated random process $\langle p_N(t)p_N(t+\tau)\rangle = 2\pi S\delta(\tau)$, where S is the spectral power of noise. The comparison with the real spectrum of the cavitation noise shows that, in the vicinity of resonances, such a model is not too rough.

The bubbles with radii exceeding 10^{-5} m (which are the kind of bubbles we will consider in this paper) are high-Q oscillatory systems that suppress the oscillation spectrum outside a narrow band near the fundamental frequency $\Omega_0 = (3\gamma P_0/\rho_0 R_0^2)^{1/2}$; i.e., they play the role of bandpass filters. Therefore, the noise can be approximated by the expression $p_N(t) = \Pi_N(t)\cos[\Omega_0 t + \varphi_N(t)]$ [11]. Let us change from the random amplitudes Π_N and phases φ_N to the expressions $\pi_N(t) = \Pi_N(t)\cos[\varphi_N(t)]$ and $\bar{\pi}_N(t) = -\Pi_N(t)\sin[\varphi_N(t)]$, which have simpler correlation functions $\langle\pi_N(t)\pi_N(t+\tau)\rangle = \langle\bar{\pi}_N(t)\bar{\pi}_N(t+\tau)\rangle = 2\pi S(\Omega_0)\delta(\tau)$ (here, $S(\Omega_0)$ is the spectral power of noise at the resonance frequency) and $\langle\pi_N(t)\bar{\pi}_N(t+\tau)\rangle = \langle\bar{\pi}_N(t)\pi_N(t+\tau)\rangle = 0$. In this case, the expression for the noise component acting on a bubble has the form $p_N(t) = \cos(\Omega_0 t)\pi_N(t) + \sin(\Omega_0 t)\bar{\pi}_N(t)$.

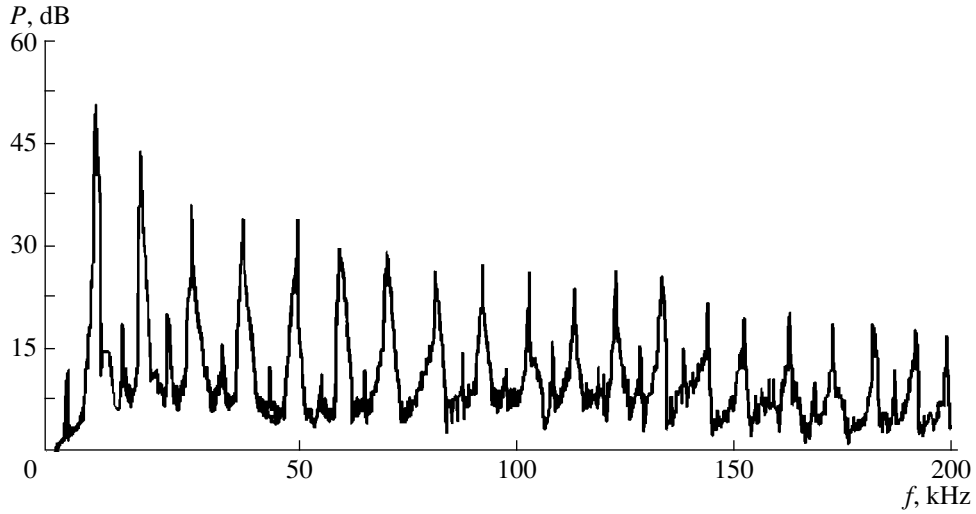

Fig. 1. Shape of the spectrum of acoustic cavitation in water. The excitation frequency is $f = 10$ kHz, and the pressure amplitude of the ultrasonic field is $p_m = 8 \times 10^4$ Pa [1].

Solving Eq. (1) with the use of an asymptotic expansion in the small parameter $|R - R_0|/R_0 \ll 1$ [12], we arrive at a system of "reduced" equations for slowly varying amplitudes a and phases ϑ:

$$(R - R_0)/R_0 = \frac{1}{2}(a\exp(-i\omega_p t + i\vartheta) + \text{c.c.})$$

$$+ \varepsilon u_1(a, \vartheta, t) + \varepsilon^2 u_2(a, \vartheta, t) + \ldots.$$

Here, ε is a small dimensionless parameter introduced for describing the order of the nonlinear terms and $u_1(a, \vartheta, t)$ and $u_2(a, \vartheta, t)$ are the higher-order terms of the expansion; only the dependence on the "fast" time, which describes the variations on the scale of the external field period, is given in an explicit form.

Correct to third-order terms, we can perform the analysis in the vicinities of the fundamental resonance, the first and second harmonics, and the first and second subharmonics. Generally speaking, the structure of the "reduced" equations in each of these regions should be different. In this paper, we restrict ourselves to describing the spectrum only in the vicinity of the fundamental resonance ($\omega_p \sim \Omega_0$).

In this region, the system of the "reduced" equations describes the bubble dynamics on the time scale that exceeds the period of the external field $2\pi/\omega_p$. Expressing this system in terms of the variables $u(t) = a(t)\cos[\vartheta(t)]$ and $v(t) = a(t)\sin[\vartheta(t)]$ with allowance for the random component, we obtain [10, 12]

$$\frac{du}{dt} = \frac{p_m + \bar{\pi}_N(t)}{2\rho_0\omega_p R_0^2} - \delta u$$

$$+ (\omega_p - \Omega_0)v + \kappa\Omega_0 v(u^2 + v^2),$$

$$\frac{dv}{dt} = -\delta v - (\omega_p - \Omega_0)u \tag{2}$$

$$- \kappa\Omega_0 u(u^2 + v^2) + \frac{\pi_N(t)}{2\rho_0\omega_p R_0^2}.$$

The system of Eqs. (2) is an example of stochastic differential equations. The description of the evolution of this system is based on the solution of the Einstein–Fokker–Planck (EFP) equation for the probability density of the dynamic states [11, 13]:

$$W(u, v) = \langle\delta(u - u(t))\delta(v - v(t))\rangle,$$

where the averaging is performed over the random force ensemble. For the case under study, the EFP equation has the form [13, 10, 14]

$$\frac{\partial W}{\partial t} + \frac{\partial}{\partial u}(PW) + \frac{\partial}{\partial v}(QW) = D\left(\frac{\partial^2 W}{\partial u^2} + \frac{\partial^2 W}{\partial v^2}\right),$$

where

$$P(u, v) = \frac{p_m}{2\rho_0\omega_p R_0^2} - \delta u$$

$$+ (\omega_p - \Omega_0)v + \kappa\Omega_0 v(u^2 + v^2), \tag{3}$$

$$Q(u, v) = -\delta v - (\omega_p - \Omega_0)u - \kappa\Omega_0 u(u^2 + v^2),$$

$$D = \frac{\pi}{4}\Omega_0\frac{S(\Omega_0)\Omega_0}{(\rho_0 R_0^2\Omega_0^2)}.$$

The presence of a small random perturbation leads to noticeable effects only near singular dynamic states of the bubble. In fact, it is easy to obtain a stationary solution to Eq. (3) in the region of the existence of a single solution to Eq. (2) in the absence of random force ($P(u_\bullet, v_\bullet) = 0, Q(u_\bullet, v_\bullet) = 0$). Expanding the coefficients $P(u, v)$ and $Q(u, v)$ near the stationary values $u_* = a_*\cos\vartheta_*$ and $v_* = a_*\sin\vartheta_*$ to the second-order terms inclusive, we arrive at the EFP equation for the Orn-

stein–Zernicke process. The solution to the latter equation has a Gaussian form [13]

$$W_{eq} = \exp[-\Phi(u, v)/D],$$

where

$$\Phi(u, v) = \Phi_0 + 1/2[c_{11}(u-u_\bullet)^2 + 2c_{12}(u-u_\bullet)(v-v_\bullet) + c_{22}(v-v_\bullet)(v-v_\bullet)];$$
$$c_{11} = -\Lambda(b_{12}^2 + b_{22}^2 + b_{11}b_{22} - b_{12}b_{21}),$$
$$c_{22} = \Lambda(b_{11}^2 + b_{21}^2 + b_{11}b_{22} - b_{12}b_{21}),$$
$$c_{12} = \Lambda(b_{11}b_{12} + b_{21}b_{22}), \quad (4)$$
$$\Lambda = (b_{11} + b_{22})/[(b_{11} + b_{22})^2 + (b_{12} - b_{21})^2];$$
$$b_{11} = (\partial P(u, v)/\partial u)_{u=u_*, v=v_*},$$
$$b_{12} = (\partial P(u, v)/\partial v)_{u=u_*, v=v_*},$$
$$b_{21} = (\partial Q(u, v)/\partial u)_{u=u_*, v=v_*},$$
$$b_{22} = (\partial Q(u, v)/\partial v)_{u=u_*, v=v_*};$$

here, $\Phi_0 = D\ln[2\pi D/(c_{11}c_{22} - c_{12}c_{12})]$ is the normalization constant determined from the condition $\int_{-\infty}^{+\infty}\int_{-\infty}^{+\infty} du\,dv W_{eq}(u, v) = 1$;

$$a_*^2[(\omega_p - \Omega_0 + \kappa\Omega_0 a_*^2)^2 + \delta^2] = \frac{p_m^2}{4\rho_0^2\omega_p^2 R_0^4},$$
$$\cos\vartheta_* = \frac{2\rho_0 R_0^2\omega_p^2(\delta/\Omega_0)}{p_m}a_*. \quad (5)$$

Using the probability density W_{eq} in the form obtained above, we determine the mean and the mean square values of the dynamic variables

$$\langle u\rangle = u_\bullet, \quad \langle v\rangle = v_\bullet, \quad \langle a\rangle = a_\bullet, \quad \langle\vartheta\rangle = \vartheta_\bullet,$$
$$\langle(a - \langle a\rangle)^2\rangle = \frac{\delta^2 + [\omega_p - \Omega_0 + \kappa\Omega_0 a_*^2][\omega_p - \Omega_0 + 2\kappa\Omega_0 a_*^2]}{\delta^2 + [\omega_p - \Omega_0 + \kappa\Omega_0 a_*^2][\omega_p - \Omega_0 + 3\kappa\Omega_0 a_*^2]}\frac{D}{\delta};$$
$$a_*^2\langle(\vartheta - \langle\vartheta\rangle)^2\rangle = \frac{\delta^2 + [\omega_p - \Omega_0 + 2\kappa\Omega_0 a_*^2][\omega_p - \Omega_0 + 3\kappa\Omega_0 a_*^2]}{\delta^2 + [\omega_p - \Omega_0 + \kappa\Omega_0 a_*^2][\omega_p - \Omega_0 + 3\kappa\Omega_0 a_*^2]}\frac{D}{\delta}; \quad (6)$$
$$a_*\langle(a - \langle a\rangle)(\vartheta - \langle\vartheta\rangle)\rangle = \frac{-\delta\kappa\Omega_0 a_*^2}{\delta^2 + [\omega_p - \Omega_0 + \kappa\Omega_0 a_*^2][\omega_p - \Omega_0 + 3\kappa\Omega_0 a_*^2]}\frac{D}{\delta}.$$

The domain of applicability of Eqs. (6) is determined by the condition of smallness of the fluctuations as compared to the mean values [13]. This imposes an important limitation on the noise intensity at which the dynamic features of the bubble behavior near the resonance will not be smeared by the fluctuations: $D \ll \delta$.

In addition, special consideration should be given to the vicinities of the bifurcation curves of the dynamic system (2), i.e., the curves on which the denominator in Eqs. (6) becomes zero. Figures 2a and 2b show the amplitude–frequency characteristic of bubble oscillations in the vicinity of the fundamental resonance (i.e., the characteristic described by Eq. (5)) and the bifurcation curves B_1 and B_2 in the plane of the determining parameters p_m/p_k, $(\omega_p - \Omega_0)/\omega_p$ and $p_k^2 = (32/3\sqrt{3}\,\kappa)\delta^3\rho_0^2 R_0^4\Omega_0$, where

$$\frac{p_{mB}^2}{p_k^2} = \frac{1}{12\sqrt{3}\delta^3}\{-(\omega_p - \Omega_0)[(\omega_p - \Omega_0)^2 + 9\delta^2] \pm [(\omega_p - \Omega_0)^2 - 3\delta^2]^{3/2}\}, \quad (7)$$
$$(\omega_p - \Omega_0) \le -\sqrt{3}\delta.$$

Here, the plus sign corresponds to the curve B_2 and the minus sign, to the curve B_1.

In the absence of noise, the singular points of the dynamic system (2), which correspond to the stationary states ($\dot u = 0$, $\dot v = 0$), are described by Eq. (5), so that the stable states correspond to nodes and the unstable states correspond to the saddle points in the u–v phase plane. The bistability, i.e., the existence of two stable stationary states, is the distinctive feature of solution (5).

First of all, we note that, in the bistability region bounded by the curves B_1 and B_2 (see Fig. 2), though not too close to these curves, the behavior of the solutions in the vicinity of each of the two stationary states corresponding to the nodal points of the dynamic system (2) has the form of Eq. (4). However, from the local expansion of the probability density, one cannot determine the occupancy numbers of these states:

$$N_{1,2} = \frac{2\pi D}{\mathrm{Det}(\hat c)}\exp\left[-\frac{\Phi(u_{*1,2}, v_{*1,2})}{D}\right]$$
$$= \left(\frac{\delta^2 + [\omega_p - \Omega_0 + 2\kappa\Omega_0 a_{*1,2}^2]^2}{\delta^2 + (\omega_p - \Omega_0)^2 + 4(\omega_p - \Omega_0)\kappa\Omega_0 a_{*1,2}^2 + 3(\kappa\Omega_0 a_*^2)^2}\right)^{1/2}\frac{2\pi D}{\delta}\exp\left[-\frac{\Phi(u_{*1,2}, v_{*1,2})}{D}\right]. \quad (8)$$

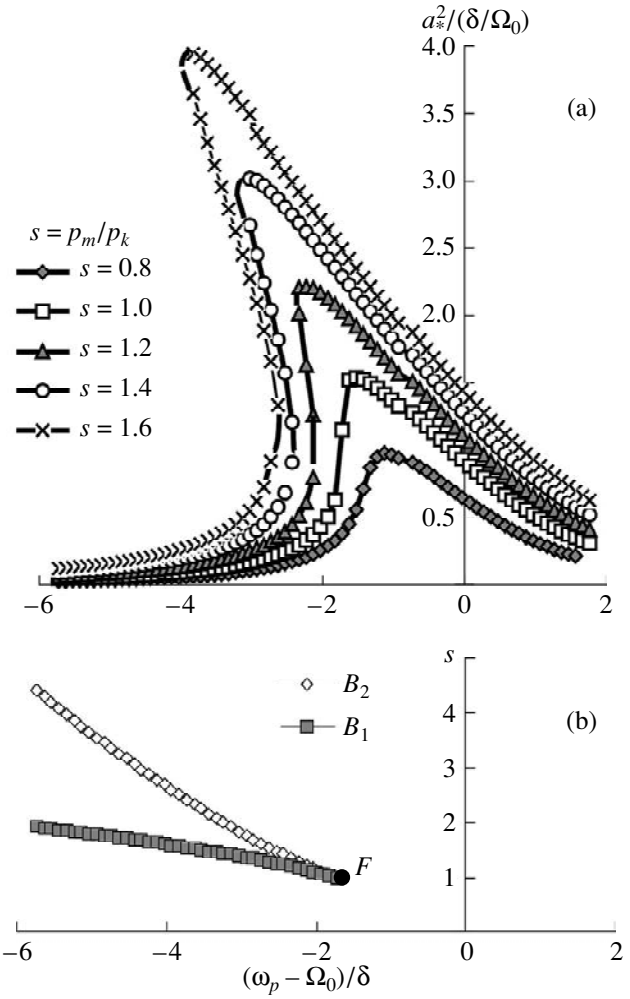

Fig. 2. (a) Amplitude-frequency characteristic of bubble oscillations in a periodic field and (b) the bifurcation curves. The hysteretic features of the nonlinear resonance manifest themselves in the bistability region bounded by the curves B_1 and B_2. The point F is the critical one at which all singularities (two nodes and one saddle point) of the dynamic system (2) merge.

Nevertheless, one simple relation between N_1 and N_2 follows from the normalization condition for the probability density W_{eq}:

$$N_1 + N_2 \approx \int_{-\infty}^{+\infty}\int_{-\infty}^{+\infty} du dv W_{eq}(u, v) = 1. \qquad (9)$$

The curve lying in the plane of the determining parameters (the detuning and the pumping amplitude) and corresponding to $N_1 = N_2$ is an analog of a binodal. For all points not on this curve, one of the states is truly equilibrium, and the other is metastable. For low-intensity noise $D \ll \delta$, the occupancy numbers of the metastable states are exponentially small everywhere except for the vicinity of the binodal. In the lowest order in $D/\delta \ll 1$, the position of the binodal does not depend on the noise intensity. In this case, we have $W_{eq} \approx \exp(-\Phi^{(0)}(u, v)/D)$, where $\Phi^{(0)}$ is determined by the equation

$$\left(\frac{\partial^2\Phi^{(0)}}{\partial u^2} + \frac{\partial^2\Phi^{(0)}}{\partial v^2}\right) + P\frac{\partial\Phi^{(0)}}{\partial u} + Q\frac{\partial\Phi^{(0)}}{\partial v} = 0. \qquad (10)$$

Since, in the case under study, the probability flux of the steady-state solution is nonzero [13] and the coefficients P and Q cannot be expressed through the introduction of the potential as $P = \partial H/\partial u$ and $Q = \partial H/\partial v$, the determination of the analytical solution to Eq. (10) is difficult and the only possible way of solving this equation is the numerical integration.

Let us consider the solution in the case of intersecting bifurcation curves. We start from the region of parameters to the left of the curve B_1 and increase the detuning at a constant pressure amplitude. According to Fig. 2b, this case corresponds to the lower branch of the amplitude–frequency characteristic. No singularities in the form of solution (4) occur in this case. This state corresponds to the true equilibrium. By contrast, for the amplitude values corresponding to the upper curve in Fig. 2a, the denominator in Eqs. (6) becomes zero. The behavior of this metastable state can be analyzed in sufficient detail [12, 14], but, in this paper, we consider only the steady-state solutions.

With further increase in the detuning, the occupancy number of the equilibrium state can be considered equal to unity everywhere up to the vicinity of the binodal. Simultaneously, the lifetime of the metastable state increases, but the occupancy number of this locally equilibrium state will be small. After passing the binodal, we obtain a different situation. Now, the state corresponding to the upper curve of the amplitude–frequency characteristic will be an equilibrium one with the occupancy number close to unity, and the state corresponding to the lower curve will have a very small occupancy number. The equilibrium state that corresponds to the amplitude on the upper curve will simply intersect the bifurcation curve B_2, while the state corresponding to the lower curve will lead to a singularity in Eqs. (6).

The above situation can be completely analytically described in the vicinity of the critical point F at which all singular points (two nodes and the saddle) of the dynamic system (2) merge. When $|p_m - p_k| \ll p_k$ and $|\omega_p - \omega_k| \ll \omega_k$ (in the determining parameter region bounded by the curves B_1 and B_2), the distance between these singular points is small. In this region, the bubble dynamics is governed by two different time scales. Their existence is related to the following factors. At the very point of bifurcation, one of the two Lyapunov exponents that determine the stability of the nodal point corresponding to the metastable state becomes zero. The two independent variables in the u–v phase plane, which correspond to these characteristic values, describe the fast and slow (for the zero exponent) motions in the vicinity of the metastable state.

For the slow variable $\eta = u - u_k$ (the fast variable is described by the expression $\xi = (v - v_k) - (1/\sqrt{3})(u - u_k)$, where $u_k = [(\sqrt{3}/2)\delta(\kappa\Omega_0)]^{1/2}$ and $v_k = [(1/2\sqrt{3})\delta/(\kappa\Omega_0)]^{1/2}$), with the use of the subordination principle [15], the EFP equation is reduced to the form

$$\frac{\partial \overline{W}}{\partial t} - \frac{\partial}{\partial \eta}\left(\frac{\partial F}{\partial \eta}\overline{W}\right) = D\frac{\partial^2 \overline{W}}{\partial \eta^2}, \quad \overline{W}(\eta) = \int W(u, v)d\xi, \tag{11}$$

$$F(\eta) = -\left[\frac{\Delta p}{2\rho_0 R_0^2 \Omega_0} + \Delta\Omega\left(\frac{\delta}{2\sqrt{3}\kappa\Omega_0}\right)^{1/2}\right]\eta + \frac{\Delta\Omega}{2\sqrt{3}}\eta^2 + \frac{1}{3\sqrt{3}}\kappa\Omega_0\eta^4,$$

$$\Delta\Omega = (\omega_p - \omega_k) = (\omega_p - \Omega_0) + \sqrt{3}\delta, \quad \Delta p = p_m - p_k.$$

In the steady-state mode, the oscillatory states of a bubble will be described by the equilibrium distribution function

$$\overline{W}_{eq}(\eta) = \frac{1}{Z}\exp\left[-\frac{F(\eta)}{D}\right], \qquad Z = \int_{-\infty}^{+\infty} d\eta \exp\left[-\frac{F(\eta)}{D}\right]. \tag{12}$$

The analysis of the dependence of the distribution function on the controlling parameters $\Delta\Omega$ and Δp can be simplified by introducing the normalized variables

$$\tilde{\eta} = \eta[|\Delta\Omega|/(\kappa\Omega_0)]^{-1/2},$$

$$\Delta_n = 2^{3/2}3^{3/4}\left(\frac{\delta}{|\Delta\Omega|}\right)^{3/2}\left[\frac{\Delta p}{p_k} + \frac{4}{\sqrt{3}}\frac{\Delta\Omega}{\delta}\right],$$

$$F(\eta) = F(\tilde{\eta}) = \frac{\Omega_0}{3\sqrt{3}\kappa}\left(\frac{\Delta\Omega}{\Omega_0}\right)^2\left[\tilde{\eta}^4 + \frac{3}{2}\tilde{\eta}^2 - \Delta_n\tilde{\eta}\right].$$

In this case, the region bounded by the curves B_1 and B_2 is determined by the simple inequality $|\Delta_n| \le 1$, because the curve B_1 is described by the equation $\Delta_n = -1$ and the curve B_2, by $\Delta_n = 1$.

The character of the fluctuations largely depends on the closeness of the determining parameters to the point F. When $\Delta\Omega^2 \gg D\Omega_0$, the distribution function $\overline{W}_{eq}$ has two sharp maxima for the values $|\Delta_n| \le 1$ (and one for $|\Delta_n| > 1$). In this case, the bubble fluctuates about one of the stationary states thus remaining for a long time near it and only rarely jumping to the other state.

From Eq. (12), we can determine the "occupancy" of the stationary states, i.e., the values of the function $\overline{W}_{eq}$ in the vicinities of the nodal points

$$\tilde{\eta}_1 = \cos[\arccos(\Delta_n/3)]$$

and

$$\tilde{\eta}_2 = \cos[\arccos(\Delta_n/3 + 2\pi/3)].$$

The equation $\Delta_n = 0$ determines the curve that is an analog of the binodal: for the corresponding values of the determining parameters, the bubble is with equal probability in each of the stationary states. For all points not on this curve, one of the states is truly equilibrium and the other is metastable.

In the immediate vicinity of the critical point, $\Delta\Omega^2 \ll D\Omega_0$, the distribution maxima are spread, which hinders the analytical calculation of the mean characteristics of the system. In this case, the dynamical characteristics of the system can be described by the correlation functions $\langle\eta(t)\eta(0)\rangle$, which, in their turn, are expressed through the nonstationary solutions to the EFP equation (11):

$$\overline{W}(\eta, t) = \sum_{n=0}^{\infty} a_n \exp(-\lambda_n t) \times \exp(-F(\eta)/2D)\Psi_n(\eta), \tag{13}$$

where Ψ_n is the eigenfunction and λ_n is the eigenvalue of the equation

$$D\frac{d^2\Psi_n}{d\eta^2} + \left[\frac{1}{2}\frac{d^2F}{d\eta^2} - \frac{1}{4D}\left(\frac{dF}{d\eta}\right)^2\right]\Psi_n + \lambda_n\Psi_n = 0. \tag{14}$$

The asymptotic behavior of the correlation function is governed by the first eigenvalue of Eq. (14):

$$\{\langle\eta(t)\eta(0)\rangle - \langle\eta^2(0)\rangle\} \sim \exp(-\lambda_1 t).$$

The numerical solution of Eq. (14) can be found in [16, 17]. At the critical point, the first eigenvalue is $\lambda_1 = 1.75(\kappa\Omega_0 D)^{1/2}$. The value of the diffusion coefficient depends on the spectral density of the noise. For $S(\Omega_0) \approx 10^4$ (Pa^2/Hz) [5–7], we obtain $D \approx 8.7\Omega_0(\Omega_0/1\text{ Hz}) \times 10^{-8}$, and for $\Omega_0 = 2\pi \times 5 \times 10^4$ Hz, we have $\lambda_1 \approx 7.5 \times 10^3$ Hz.

The results obtained above allow us to describe the spectral characteristics of the radiation generated by a fluctuating bubble. The monopole component of the radiation of a bubble located at the point $\mathbf{r}'$ has the form

$$p_r(\mathbf{r}, t) = \rho_0\frac{1}{|\mathbf{r} - \mathbf{r}'|} \times [\ddot{R}(\tau)R(\tau)^2 + 2\dot{R}(\tau)^2R(\tau)]_{\tau = t - |\mathbf{r} - \mathbf{r}'|}, \tag{15}$$

where $\mathbf{r}$ is the radius-vector of the observation point. The radiation spectrum observed at the point $\mathbf{r}$ is determined by the expression

$$S(\omega, \mathbf{r}) = \frac{1}{2\pi}\int_{-\infty}^{+\infty} d\tau \exp(-i\omega\tau)\langle(p_m(\mathbf{r})\sin(\omega_p t) + p_N(\mathbf{r}, t) + p_r(\mathbf{r}, t))(p_m(\mathbf{r})\sin[\omega_p(t + \tau)] + p_N(\mathbf{r}, t + \tau) + p_r(\mathbf{r}, t + \tau))\rangle. \tag{16}$$

This spectrum is formed by the correlations of four different types: the autocorrelation function of the external field, the correlators between the noise and the bubble radiation, the autocorrelation function of the noise, and the autocorrelation function of the radiation. It is essential that the contribution of the terms corresponding to the first two types is of a purely coherent nature (proportional to $\delta(\omega + \omega_p)$ and $\delta(\omega - \omega_p)$). The autocorrelation function of noise is frequency independent and describes the constant base of the spectrum. The shape of the radiation spectrum is exclusively determined by the contribution of the autocorrelation function of the radiation.

Substituting the asymptotic expansion for the bubble radius in Eq. (15) and retaining only the leading terms in Eq. (16), we derive

$$S_r(\mathbf{r}, \omega) = \frac{\rho_0^2 R_0^6 \omega_p^4}{2\pi|\mathbf{r} - \mathbf{r}'|^2} \int_{-\infty}^{+\infty} d\tau \exp(-i\omega\tau)$$

$$\times \langle a(t)[\cos(\vartheta(t))\cos(\omega_p t) - \sin(\vartheta(t))\sin(\omega_p t)]$$

$$\times a(t+\tau)[\cos(\vartheta(t+\tau))\cos(\omega_p(t+\tau)) \quad (17)$$

$$- \sin(\vartheta(t+\tau))\sin(\omega_p(t+\tau))]\rangle$$

$$= \frac{R_0^2}{|\mathbf{r} - \mathbf{r}'|^2}(\rho_0^2 R_0^4 \omega_p^4)[\tilde{S}_c(\omega) + \tilde{S}_n(\omega)],$$

where

$$\tilde{S}_c(\omega) = \frac{1}{4}(\langle u\rangle^2 + \langle v\rangle^2)[\delta(\omega + \omega_p) + \delta(\omega - \omega_p)] \quad (18)$$

$$= \frac{a_*^2}{4}[\delta(\omega + \omega_p) + \delta(\omega - \omega_p)],$$

$$\tilde{S}_n(\omega) = \frac{1}{4}\{\tilde{S}_{uu}(\omega - \omega_p) + \tilde{S}_{uu}(\omega + \omega_p)$$

$$+ \tilde{S}_{vv}(\omega - \omega_p) + \tilde{S}_{vv}(\omega + \omega_p)$$

$$+ i[\tilde{S}_{vu}(\omega - \omega_p) - \tilde{S}_{uv}(\omega - \omega_p)] \quad (19)$$

$$+ i[\tilde{S}_{vu}(\omega + \omega_p) + \tilde{S}_{uv}(\omega + \omega_p)]\}.$$

Here, $\tilde{S}_{uu}(\omega) = \frac{1}{2\pi}\int_{-\infty}^{+\infty} d\tau \exp(-i\omega\tau)\langle \tilde{u}(t)\tilde{u}(t+\tau)\rangle$ and $\tilde{u} = u - \langle u\rangle$. The correlators of other types are calculated in a similar way.

For reference, we presented above the explicit expression (18) for the coherent contribution to the spectral density. Such a simple expression is valid at not too small distances from the critical point. In addition, in the bistability region, for the detuning less than its values on the binodal, the amplitude values substituted in Eq. (18) should be those corresponding to the lower branch of dependence (5) and, correspondingly, the values belonging to the upper branch should be used for the detuning values lying to the right of the binodal.

Outside the vicinity of the critical point, where the amplitude and phase fluctuations can be described by the Ornstein–Zernicke process [13], the expression (19) for the incoherent contribution to the spectral density can be reduced to the following form (for definiteness, we select the vicinity $\omega \sim \omega_p$):

$$\tilde{S}_n(\omega) = \frac{D}{2}\frac{[(\omega - \omega_p)^2 + (\omega - \omega_p)(b_{12} - b_{21}) + (1/2)(b_{11}^2 + b_{12}^2 + b_{21}^2 + b_{22}^2)]}{[(\omega - \omega_p)^2 - (b_{11}b_{22} - b_{12}b_{21}) + i(\omega - \omega_p)(b_{11} + b_{22})][\text{c.c.}]}, \quad (20)$$

where (see definition (4)) $b_{11} = -\delta + 2\kappa\Omega_0 u_* v_*$, $b_{22} = -\delta - 2\kappa\Omega_0 u_* v_*$, $b_{12} = [(\omega_p - \Omega_0) + \kappa\Omega_0(u_*^2 + 3v_*^2)]$, $b_{21} = -[(\omega_p - \Omega_0) + \kappa\Omega_0(3u_*^2 + v_*^2)]$.

Expression (20) describes the main result of this study, namely, the shape of the spectrum of the bubble radiation in the cavitation region. In the strongly nonlinear mode under study when $\kappa\Omega_0 a_*^2 \geq \delta$, this shape widely deviates from the Lorentz one $\tilde{S}_n(\omega) \approx (D/2)[(\omega - 2\omega_p + \Omega_0)^2 + \delta^2]^{-1}$, to which it is reduced when the nonlinear terms are neglected.

For illustration, Fig. 3 shows the dependence of the normalized spectral density S_N ($\tilde{S}_n = (D/2\delta^2)S_N$) on the dimensionless variables $\Delta = (\omega - \omega_p)/\delta$ and $\eta = (\omega_p - \Omega_0)/\delta$ for the external pressure amplitude $p_m = 1.4p_k$. An important fact is that the magnitude and the halfwidth of the spectral density of radiation are determined by the stability of the nonlinear dynamic state of the bubble, because $(b_{11}b_{22} - b_{12}b_{21})$ is the product of the corresponding Lyapunov exponents of system (2) in the absence of noise.

An abrupt change in the spectral density in the vicinity of the detuning η_b corresponding to the binodal

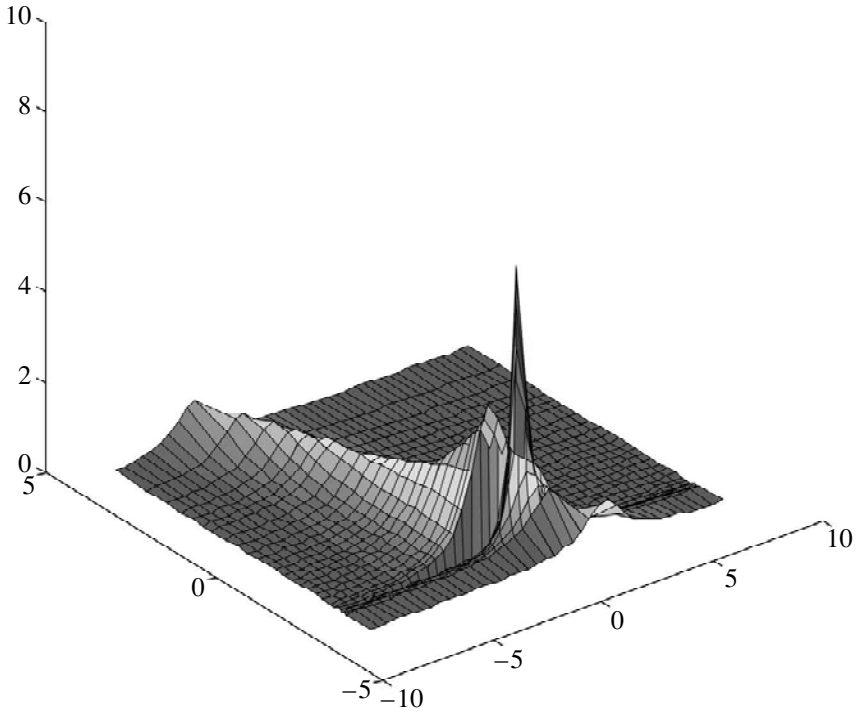

Fig. 3. Spectral density of the bubble radiation S_N as a function of the dimensionless variables $\eta = (\omega_p - \Omega_0)/\delta$ and $\Delta = (\omega - \omega_p)/\delta$ at $p_m = 1.4\ p_k$. The values of η are plotted along the y-axis, and Δ is represented by the x-axis.

is related to the change in the amplitude of the bubble oscillations due to the transition from the lower branch of the amplitude–frequency characteristic to the upper one. For the given amplitude of the external field, the transition point is fairly close to the bifurcation curve B_2 on which the Lyapunov exponent for the states belonging to the lower branch becomes zero. The oscillations corresponding to these states will be much less stable. Being affected by the external noise, they will build up to a considerably greater amplitude, which gives rise to the sharp peak in the spectral density.

The shift of the spectral density peak to lower frequencies with increasing detuning η is related to the fact that an increase in the detuning at a fixed frequency of the external field corresponds to the contribution of bubbles with greater equilibrium radii and, hence, with lower natural frequencies. Since, as was mentioned above, for the external noise, a bubble represents a bandpass filter near the natural frequency (the bandwidth is determined by its Q-factor), a decrease in the natural frequency evidently leads to a corresponding shift of the spectral density peak.

The numerical solution of the Rayleigh equation for large external pressure amplitudes showed [4, 18, 19] that the asymptotic solution (2), which takes into account only the terms up to the third order, adequately describes all qualitative features of the nonlinear resonance far beyond the region of the formal validity of this solution, $|R - R_0|/R_0 \ll 1$. One can expect that this result will also be valid in the presence of noise. The application of numerical methods in analyzing the nonlinear dynamics of a bubble in the resonance and noise fields is a natural and necessary continuation of this study.

Another problem consists in taking into account the contribution of a set of bubbles with different radii that are present in the cavitation zone. Figure 4 shows the experimental dependences obtained by different researchers [1, 20, 21] and demonstrating the stable features of the shape of the cavitation radiation spectrum in the vicinity of the fundamental frequency. These features include the presence of narrow spectral components resting on a wide base, which is asymmetric in shape and passes into the noise background. Evidently, the narrow lines are caused by the coherent contribution to the spectral density. The description of the shape of the asymmetric base is of special interest, but the direct use of expression (20) derived for the radiation spectrum of a single bubble presents considerable difficulties.

In the general case, in expression (17), we have a sum of the "diagonal" terms, i.e., the autocorrelation functions (20), and the "off-diagonal" terms, which describe the pair correlations between the radiation produced by different bubbles. Generally speaking, it is unjustified to neglect the contribution of the latter. However, for their determination, one should use the

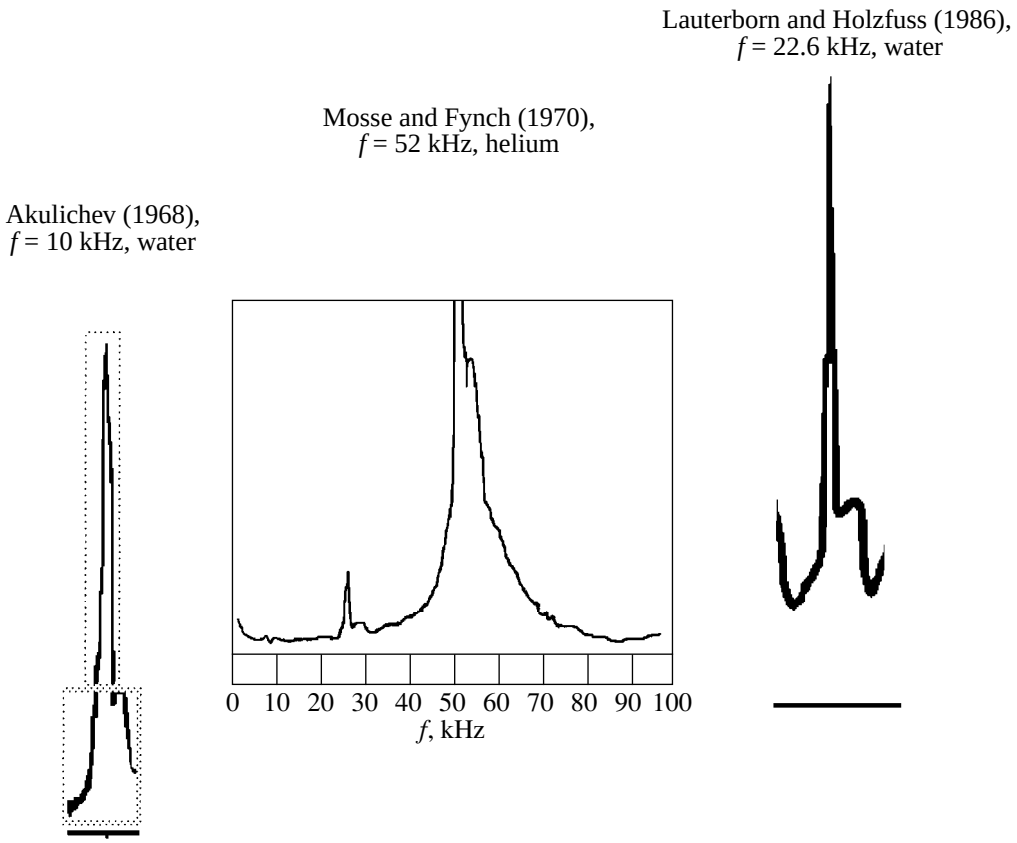

Fig. 4. Shape of the spectrum of the cavitation radiation near the fundamental frequency [1, 20. 21]. The specific features, namely, the narrow components rising over a wide base, are indicated by the dotted lines for the data taken from [1]. The asymmetric base deviates from the Lorentz form and retains its shape in widely different experimental conditions.

data on the spatial spectrum of fluctuations in the cavitation region and such data are practically absent.

At the same time, some of the specific features of the dependences shown in Fig. 4 can be understood on the basis of Eq. (20) (or its graphic representation in Fig. 3). Firstly, it is the halfwidth of the bases $\Delta\omega$ far exceeding the value of δ: the contribution of only the "diagonal" terms, which can be obtained by integrating Eq. (20) with respect to the detuning η, leads to the value $\Delta\omega \sim 5\delta$. Secondly, it is the asymmetry of the resulting spectrum about ω_p: this asymmetry is a natural result of the asymmetry of the radiation of a single bubble. Finally, the fact that the shape of the spectrum is determined by the stability of the dynamic states of the bubbles allows one to predict the changes that occur in the spectrum near the bifurcation values of the external pressure amplitude that correspond to the loss of stability.

REFERENCES

1. V. A. Akulichev, in *High-Intensity Ultrasonic Fields*, Ed. by L. D. Rozenberg (Nauka, Moscow, 1968; Plenum, New York, 1971).
2. W. Lauterborn and E. Cramer, Phys. Rev. Lett. **47**, 1445 (1981).
3. W. Lauterborn and E. Cramer, Acustica **49**, 280 (1981).
4. W. Lauterborn and U. Parlitz, in *Problems of Nonlinear Acoustics* (Inst. Gidrodin., Novosibirsk, 1987), pp. 71–80.
5. M. Harrison, J. Acoust. Soc. Am. **24**, 776 (1952).
6. V. P. Il'in, V. I. Zhukov, Yu. L. Levkovskiĭ, and A. D. Pernik, Tr. NTO Sudproma **106**, 95 (1968).
7. V. P. Morozov, Akust. Zh. **14**, 435 (1968) [Sov. Phys. Acoust. **14**, 361 (1968)].
8. Yu. L. Levkovskiĭ, Akust. Zh. **19**, 200 (1973) [Sov. Phys. Acoust. **19**, 301 (1973)].
9. R. Latorre, Acust. Acta Acust. **73**, 424 (1997).
10. A. O. Maksimov, Preprint TOI (Pacific Institute of Oceanology, Far East Division, Russian Academy of Sciences, Vladivostok, 1985).
11. S. M. Rytov, in *Introduction to Statistical Radiophysics*, Part 1: *Random Fields* (Nauka, Moscow, 1976), p. 204.
12. A. Prosperetty, J. Acoust. Soc. Am. **57**, 810 (1975).

13. C. W. Gardiner, *Handbook of Stochastic Methods for Physics, Chemistry, and the Natural Sciences* (Springer, Berlin, 1985; Mir, Moscow, 1986).
14. M. I. Dykman and M. A. Krivoglaz, Physica A (Amsterdam) **104**, 480 (1980).
15. H. Haken, *Advanced Synergetics: Instability Hierarchies of Self-Organizing Systems and Devices* (Springer, New York, 1983; Mir, Moscow, 1985).
16. H. Tomita, A. Ito, and H. Kidachi, Prog. Theor. Phys. **56**, 786 (1976).
17. M. I. Dykman and M. A. Krivoglaz, Physica A (Amsterdam) **104**, 495 (1980).
18. W. Lauterborn and E. Cramer, Acustica **49**, 226 (1981).
19. V. Kamath and A. Prosperetti, J. Acoust. Soc. Am. **85**, 1538 (1989).
20. A. Mosse and R. Finch, J. Acoust. Soc. Am. **49**, 156 (1971).
21. W. Lauterborn and J. Holzfuss, Phys. Lett. A **115**, 369 (1986).

Translated by E. Golyamina